

การประดิษฐ์ โครงสร้าง และสมบัติทางไฟฟ้าเคมีของเส้นใยนาโนคอมโพสิต
ของแม่เหล็กเฟอไรต์/คาร์บอน

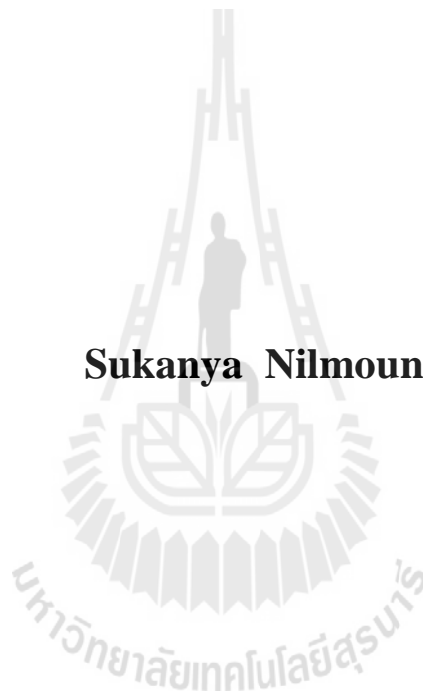


นางสาวสุกัญญา นิลม่วง

วิทยานิพนธ์นี้เป็นส่วนหนึ่งของการศึกษาตามหลักสูตรปริญญาวิทยาศาสตรดุษฎีบัณฑิต
สาขาวิชาฟิสิกส์
มหาวิทยาลัยเทคโนโลยีสุรนารี
ปีการศึกษา 2557

**FABRICATION, STRUCTURE, AND
ELECTROCHEMICAL PROPERTIES OF
ELECTROSPUN MAGNETIC FERRITE/CARBON
COMPOSITE NANOFIBERS**

Sukanya Nilmoung



**A Thesis Submitted in Partial Fulfillment of the Requirements for
the Degree of Doctor of Philosophy in Physics**

Suranaree University of Technology

Academic Year 2014

**FABRICATION, STRUCTURE, AND ELECTROCHEMICAL
PROPERTIES OF ELECTROSPUN MAGNETIC
FERRITE/CARBON COMPOSITE NANOFIBER**

Suranaree University of Technology has approved this thesis submitted in partial fulfillment of the requirements for the Degree of Doctor of Philosophy.

Thesis Examining Committee

(Asst. Prof. Dr. Worawat Meevasana)

Chairperson

(Prof. Dr. Santi Maensiri)

Member (Thesis Advisor)

(Assoc. Prof. Dr. Rattikorn Yimnirun)

Member

(Dr. Saroj Rujirawat)

Member

(Asst. Prof. Dr. Montree Sawangphruk)

Member

(Prof. Dr. Sukit Limpijumnong)

Vice Rector for Academic Affairs
and Innovation

(Assoc. Prof. Dr. Prapun Manyum)

Dean of Institute of Science

สฤกษ์ญา นิลม่วง : การประดิษฐ์ โครงสร้าง และสมบัติทางไฟฟ้าเคมี ของเส้นใยนาโนคอมโพสิตของแม่เหล็กเฟอร์ไรต์/คาร์บอน (FABRICATION, STRUCTURE, AND ELECTROCHEMICAL PROPERTIES OF ELECTROSPUN MAGNETIC FERRITE/CARBON COMPOSITE NANOFIBERS) อาจารย์ที่ปรึกษา : ศาสตราจารย์ ดร.สันติ แม้นศิริ, 245 หน้า.

ในงานวิจัยนี้ได้ทำการประดิษฐ์เส้นใยนาโนคาร์บอนคอมโพสิตกับอนุภาคเฟอร์ไรต์ จำนวน 3 กลุ่มคือ คาร์บอน/คอปเปอร์เฟอร์ไรต์ คาร์บอน/โคบอลต์เฟอร์ไรต์ และคาร์บอน/นิกเกิลเฟอร์ไรต์ ด้วยเทคนิคการปั่นด้วยไฟฟ้าร่วมกับการคาร์บอนในเซชันที่อุณหภูมิ 535 องศาเซลเซียสภายใต้บรรยากาศผสมของอากาศปรกติและก๊าซอาร์กอน การเตรียมวัสดุคอมโพสิตในแต่ละกลุ่มประกอบไปด้วย 4 ตัวอย่าง ที่มีอัตราส่วนระหว่างแหล่งพอลิเมอร์กับแหล่งโลหะแตกต่างกันคือ 100/0 80/20 60/40 และ 40/60 แทนด้วย CNF C/MFe₂O₄ 0.2 C/MFe₂O₄ 0.4 และ C/MFe₂O₄ 0.6 ตามลำดับ (เมื่อ M คือ Cu Co และ Ni) แล้วทำการศึกษาลักษณะเฉพาะโดยใช้เทคนิค TGA XRD SEM TEM Raman spectroscopy BET XAS VSM CV GCD และ EIS ผลการศึกษาพบว่า วัสดุตัวอย่างทั้งหมดที่เตรียมได้มีโครงสร้างผสมของคาร์บอนอสัณฐาน และโครงสร้างลูกบาศก์ชนิดอินเวอร์ส สปิเนล โดยตัวอย่างที่มีแหล่งโลหะ 20 และ 40 เปอร์เซ็นต์โดยน้ำหนัก (C/MFe₂O₄ 0.2 และ C/MFe₂O₄ 0.4) มีโครงสร้างเป็นอินเวอร์ส สปิเนลแบบสมบูรณ์ (ไอออน M²⁺ ทั้งหมดอยู่ที่ตำแหน่งออกตะฮีดรอล) ในขณะที่ตัวอย่างที่มีแหล่งโลหะ 60 เปอร์เซ็นต์โดยน้ำหนัก (C/MFe₂O₄ 0.6) มีโครงสร้างแบบอินเวอร์สสปิเนลแบบไม่สมบูรณ์ โดยพบไอออน M²⁺ อยู่ที่ตำแหน่งเตตระฮีดรอลและออกตะฮีดรอล ในปริมาณ 45.3 และ 54.7 เปอร์เซ็นต์ สำหรับ C/CuFe₂O₄ 0.6 58.9 และ 41.1 เปอร์เซ็นต์ สำหรับ C/CoFe₂O₄ 0.6 50.5 และ 49.5 เปอร์เซ็นต์ สำหรับ C/NiFe₂O₄ 0.6 อนุภาคนาโนเฟอร์ไรต์ที่เตรียมได้มีขนาดของผลึกโดยเฉลี่ยระหว่าง 20-55 นาโนเมตร เลขออกซิเดชันของเหล็ก (Fe) และโลหะ (Cu Co และ Ni) ในโครงสร้างอินเวอร์สสปิเนลเฟอร์ไรต์ของทุกกลุ่มตัวอย่าง เป็น 3+ และ 2+ ตามลำดับ ยกเว้นตัวอย่างคาร์บอน/โคบอลต์เฟอร์ไรต์ที่มีแหล่งโลหะ 60 เปอร์เซ็นต์โดยน้ำหนัก (C/CoFe₂O₄ 0.6) ที่เลขออกซิเดชันของโคบอลต์ เป็นการผสมระหว่าง 2+ และ 3+ การศึกษาโครงสร้างทางจุลภาค พบว่าเส้นใยทั้ง 3 กลุ่มมีขนาดเส้นผ่านศูนย์กลางลดลงประมาณ 20-35 เปอร์เซ็นต์ หลังการคาร์บอนในเซชัน เนื่องจากการสลายตัวของสารพอลิเมอร์และสารโลหะตั้งต้น นอกจากนี้ยังพบว่าตัวอย่างของทุกกลุ่มศึกษาที่ประกอบด้วยแหล่งโลหะ 60 เปอร์เซ็นต์ (C/MFe₂O₄ 0.6) เส้นใยเกิดการหลอมรวมกัน การศึกษาพื้นที่ผิวของเส้นใยนาโนคอมโพสิตทุกเงื่อนไขพบว่า มีค่าอยู่ระหว่าง 60-210 ตารางเมตรต่อกรัม โดยมีค่าเพิ่มขึ้นอย่างมากเมื่อเทียบกับเส้น

ไยนาโนคาร์บอนบริสุทธิ์ (30 ตารางเมตรต่อกรัม) ผลการศึกษาสมบัติทางแม่เหล็กที่อุณหภูมิห้องพบว่า เส้นไยนาโนคาร์บอนบริสุทธิ์แสดงพฤติกรรมแม่เหล็กแบบไดอะ ในขณะทีเส้นไยนาโนคอมโพสิตทุกเงื่อนไขแสดงพฤติกรรมแม่เหล็กแบบเฟอร์รี ซึ่งสัมพันธ์กับการกระจายตัวของไอออนบวกที่ตำแหน่งเตตระฮีดรอลและออกตะฮีดรอล ทุกกลุ่มวัสดุคอมโพสิตมีค่าแมกเนไตเซชันอิมเพิ่มขึ้นตามการเพิ่มขึ้นของปริมาณโลหะคอมโพสิต โดยตัวอย่างคาร์บอน/คอปเปอร์เฟร์ไรต์คอมโพสิต คาร์บอน/โคบอลต์เฟร์ไรต์คอมโพสิต และคาร์บอน/นิกเกิลเฟร์ไรต์คอมโพสิต แสดงค่าแมกเนไตเซชันอิมตัวในช่วง 0.3-12 0.2-43 และ 0.2-25 emu/g ตามลำดับ ซึ่งค่าเหล่านี้มีค่าต่ำกว่าค่าปกติของวัสดุเฟร์ไรต์ แต่ละชนิด อันเป็นผลจากการมีอยู่ของเนื้อคาร์บอน ผลการศึกษาสมบัติทางไฟฟ้าเคมีพบว่ากลไกการกักเก็บประจุของวัสดุขั้วคาร์บอนบริสุทธิ์เป็นแบบการสะสมแบบสองชั้นที่ผิวต่อระหว่างวัสดุขั้วและอิเล็กโทรไลต์ (EDLC) ในขณะที่วัสดุขั้วคาร์บอน/เฟร์ไรต์คอมโพสิต และวัสดุขั้วเฟร์ไรต์บริสุทธิ์ กักเก็บประจุผ่านกลไกการถ่ายโอนอิเล็กตรอน ร่วมกับกลไกการเก็บประจุแบบ EDLC ค่าความหนาแน่นการกักเก็บพลังงาน มีค่าเพิ่มขึ้นในทุกกลุ่มวัสดุขั้วคาร์บอน/เฟร์ไรต์คอมโพสิต โดยที่ความหนาแน่นกระแสไฟฟ้า 1 แอมแปร์ต่อกรัม ค่าความหนาแน่นการกักเก็บพลังงานมีค่าเพิ่มขึ้นประมาณ 2 9 และ 64 เปอร์เซ็นต์ หลังการคอมโพสิตเส้นใยคาร์บอนด้วยคอปเปอร์เฟร์ไรต์ โคบอลต์เฟร์ไรต์ และ นิกเกิลเฟร์ไรต์ ตามลำดับ การเพิ่มขึ้นดังกล่าวนี้สืบเนื่องจากค่าการเก็บประจุผ่านกลไกการเก็บประจุทั้งสองแบบรวมกันคือ EDLC และแบบซูโดคาร์ปาคิแตนซ์ นอกจากนี้ค่าความหนาแน่นการกักเก็บประจุของวัสดุขั้วคาร์บอน/เฟร์ไรต์คอมโพสิตยังมีค่าเพิ่มขึ้นโดยประมาณ 42 62 และ 79 เปอร์เซ็นต์เมื่อเทียบกับวัสดุขั้วคอปเปอร์เฟร์ไรต์ โคบอลต์เฟร์ไรต์ และ นิกเกิลเฟร์ไรต์บริสุทธิ์ ตามลำดับ ซึ่งน่าจะเป็นผลเนื่องจากการลดลงของค่าความต้านทานการส่งผ่านประจุ อันเนื่องจากอนุภาคนาโนของเฟร์ไรต์ที่เสริมเข้าไป โดยพื้นที่ผิวที่เพิ่มขึ้นพร้อมกับลักษณะช่องว่างระหว่างเส้นใยนาโนคาร์บอนกับอนุภาคนาโนเฟร์ไรต์อาจเป็นตัวแปรสนับสนุนการแทรกตัวของไอออนของอิเล็กโทรไลต์รวมถึงอัตราเร็วของการเคลื่อนที่ในช่องรูพรุน

สาขาวิชาฟิสิกส์

ปีการศึกษา 2557

ลายมือชื่อนักศึกษา _____

ลายมือชื่ออาจารย์ที่ปรึกษา _____

ลายมือชื่ออาจารย์ที่ปรึกษาร่วม _____

ลายมือชื่ออาจารย์ที่ปรึกษาร่วม _____

SUKANYA NILMOUNG : FABRICATION, STRUCTURE, AND
ELECTROCHEMICAL PROPERTIES OF ELECTROSPUN MAGNETIC
FERRITE/CARBON COMPOSITE NANOFIBERS. THESIS ADVISOR :
PROF. SANTI MAENSIRI, Ph.D. 245 PP.

SPINEL FERRITE/CARBON NANOFIBERS/CARBON/MFE₂O₄ COMPOSITE
NANOFIBERS/ELECTROSPINNING/ELECTROCHEMICAL CAPACITOR

In this work, three series of carbon/MFe₂O₄ (M = Cu, Co and Ni) composite nanofibers were synthesized by electrospinning technique followed by carbonization at 535 °C under mixed air and argon atmosphere. In each composite system, four sets of samples with different weight ratio of polymer and magnetic source of 100/0, 80/20, 60/40 and 40/60 abbreviated as CNF, C/MFe₂O₄_0.2, C/MFe₂O₄_0.4, and C/MFe₂O₄_0.6, respectively, were fabricated. The prepared samples were characterized by TGA, XRD, SEM, TEM, Raman spectroscopy, BET, XAS, VSM CV, GCD and EIS techniques. The structure of all C/MFe₂O₄ samples showed composite phase between cubic MFe₂O₄ and amorphous carbon. All C/MFe₂O₄_0.2 and C/MFe₂O₄_0.4 samples have inverse spinel structure (M²⁺ ions occupied octahedral site), while C/MFe₂O₄_0.6 samples exhibit partially inverse spinel structure with a portion of M²⁺ ions in A and B site of about 45.3 and 54.7% for C/CuFe₂O₄_0.6, 58.9 and 41.1% for C/CoFe₂O₄_0.6, 50.5 and 49.5% for C/NiFe₂O₄_0.6. The average crystallite size of the MFe₂O₄ nanoparticles is in the range of ~20-55 nm. The oxidation state of Fe and M ions in MFe₂O₄ structure is, respectively +3 and +2, except that the oxidation state of Co in C/CoFe₂O₄_0.6 is

mixed between +2 and +3. The as spun C/MFe₂O₄ nanofibers exhibit the shrinkage of about 20-35% after carbonization due to the combustion of PAN and magnetic source. The uniformity fiber was observed for all C/MFe₂O₄_0.6 samples. The specific surface areas of the composite nanofibers are about 60-210 m²/g. The values are higher than that of 30 m²/g of pure CNF. CNFs exhibit diamagnetic, while all C/MFe₂O₄ composite samples show ferrimagnetic behavior related to the distribution of cations over tetrahedral and octahedral sites. The M_s values of ~0.3-12, ~0.2-43, and ~0.2-25 emu/g for C/CuFe₂O₄, C/CoFe₂O₄, and C/NiFe₂O₄, respectively, are lower than those of the bulk MFe₂O₄, possibly due to the existence of CNF matrix. The charge storage mechanism of CNF electrode is electric double layer capacitance (EDLC), while C/MFe₂O₄ and MFe₂O₄ electrodes also store energy via electron transfer. The energy density at 1 A/g for C/MFe₂O₄ is improved by ~2, 9, and 64% after adding the CuFe₂O₄, CoFe₂O₄ and NiFe₂O₄, respectively, into CNF matrix. The enhancement may results from the combination of EDLC and pseudocapacitance. Moreover, the improvement of ~42, 62, and 79% as compared to pure MFe₂O₄ electrode is achieved. This is possibly due to the reduction of the charge transfer resistance resulting from the MFe₂O₄ nanoparticles. Large surface area with free space between MFe₂O₄ and CNF may well support the insertion of electrolyte ions and speed up transportation rate inside the pores.

School of Physics

Student's Signature _____

Academic Year 2014

Advisor's Signature _____

Co-advisor's Signature _____

Co-advisor's Signature _____

ACKNOWLEDGMENTS

All through this thesis work, I have got a lot of help from many people. First of all, I would like to express my deepest and sincere gratitude to my supervisor and co-advisor, Prof. Dr. Santi Maensiri, Assoc. Prof. Dr. Rattikorn Yimnirun and Dr. Saroj Rujirawat, for their long term guidance on all problems, chance and financial support for research presentation both in and outside of country, and more importantly for the inspiration they provided to ensure the completion of this work. I am also grateful to the lecturers of the School of Physics, Institute of science, Suranaree University of Technology for teaching me in all graduate courses. I would like to especially thank Dr. Montree Sawangphruk and members of his research group in Kasetsart University for introducing the area of electrochemical measurement. I wish to thank Advanced Materials Physics (AMP) laboratory, and the Center for Scientific and Technological Equipment, Suranaree University of Technology for research facilities support. I would like to thank to AMP group members for their friendship, friendly support and guidance during work. Finally, I would like to thank my parents for their never-ending support and encouragement over all the years of my life. Finally, I thank the Rajamangala University of Technology Isan and NANOTEC-SUT Center of Excellence on Advanced Functional Nanomaterials, Suranaree University of Technology for the scholarship support.

Sukanya Nilmoung

CONTENTS

	Page
ABSTRACT IN THAI.....	I
ABSTRACT IN ENGLISH	III
ACKNOWLEDGEMENTS	V
CONTENTS.....	VI
LIST OF TABLES	X
LIST OF FIGURES	XIV
LIST OF ABBREVIATIONS.....	XXIII
CHAPTER	
I INTRODUCTION.....	1
1.1 Background and motivation	1
1.2 Objectives of the research	4
1.3 Limitations of study	4
1.4 Location of the research	5
1.5 Anticipated outcomes.....	5
1.6 Outline of thesis	5
II LITERATURE REVIEWS.....	6
2.1 The spinel ferrite (MFe ₂ O ₄) material	6
2.1.1 Ferrite structure	6
2.1.2 The synthesis methods	8

CONTENTS (Continued)

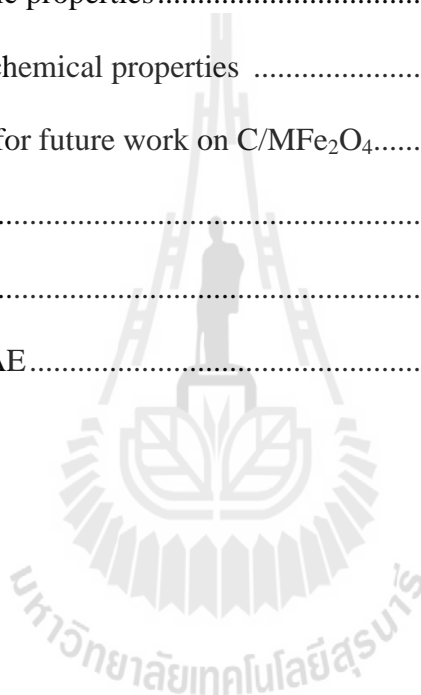
	Page
2.1.3 Applications of spinel ferrites	10
2.2 Carbon nanofibers	12
2.2.1 Carbon naofibers structure	12
2.2.2 The synthesis methods	13
2.2.3 Applications of carbon naofibers	15
2.3 Carbon composite nanofibers.....	16
2.3.1 Structure of carbon composite nanofibers	16
2.3.2 The synthesis methods	17
2.3.3 Applications of carbon composite nanofibers.....	17
2.4 Theoretical approach.....	20
2.4.1 Magnetic properties of materials.....	20
2.4.2 Electrochemical properties of materials.....	22
III RESEARCH METHODOLOGY.....	27
3.1 Fabrication of C/MFe ₂ O ₄ composite nanofibers	27
3.1.1 The precursor preparation	27
3.1.2 Fabrication of electrospun PAN/MFe ₂ O ₄ composite nanofibers.....	30
3.1.3 Fabrication of C/MFe ₂ O ₄ composite nanofibers	33
3.2 Material characterization.....	36
3.2.1 Thermo gravimetric analyzer	36
3.2.2 X-ray diffraction.....	37

CONTENTS (Continued)

	Page
3.2.3 Scanning electron microscopy.....	39
3.2.4 Transmission electron microscopy.....	39
3.2.5 Raman spectroscopy.....	40
3.2.6 Brunauer-Emmett-Teller	41
3.2.7 X-ray absorption spectroscopy.....	43
3.2.8 Magnetic measurements	45
3.2.9 Electrochemical measurements	47
IV RESULTS AND DISCUSSION.....	57
4.1 C/CuFe ₂ O ₄ composite nanofibers	58
4.1.1 Structural and morphology characterization.	58
4.1.2 Magnetic properties of C/CuFe ₂ O ₄ composite nanofibers.....	79
4.1.3 Electrochemical properties of C/CuFe ₂ O ₄ composite nanofibers ...	86
4.2 C/CoFe ₂ O ₄ composite nanofibers	100
4.2.1 Structural and morphology characterization	100
4.2.2 Magnetic properties of C/CoFe ₂ O ₄ composite nanofibers.....	122
4.2.3 Electrochemical properties of C/CoFe ₂ O ₄ composite nanofibers .	128
4.3 C/NiFe ₂ O ₄ composite nanofibers	138
4.3.1 Structural and morphology characterization	138
4.3.2 Magnetic properties of C/NiFe ₂ O ₄ composite nanofibers.....	160
4.3.3 Electrochemical properties of C/NiFe ₂ O ₄ composite nanofibers..	167

CONTENTS (Continued)

	Page
V CONCLUSIONS.....	177
5.1 The structure and morphology characterization.....	177
5.2 The magnetic properties.....	179
5.3 The electrochemical properties	181
5.4 Suggestion for future work on C/MFe ₂ O ₄	184
REFERENCES	185
APPENDIX.....	215
CURRICULUM VITAE.....	218



LIST OF TABLES

Table	Page
2.1	Details of site in spinel structure..... 8
2.2	The synthesis of MFe_2O_4 in the past decade..... 9
2.3	Typical values for electrochemical capacitance of carbon nanofibers..... 16
2.4	Lists of carbon nanofibers composite (CNFC) for used as supercapacitor electrode..... 19
2.5	Electrolytes that are used often..... 26
3.1	List of material used as starting materials for C/MFe_2O_4 composite nanofiber preparation, and their source and purity 28
3.2	List of starting raw metallic materials for the preparation of C/MFe_2O_4 system ($M = Cu, Co, Ni$)..... 29
3.3	List of electrospinning process parameters and heat treatment conditions..... 32
3.4	Circuit elements used in the equivalent models..... 56
4.1	Lists of Raman peak height, Raman peak width, R value (I_D/I_G) and in plane graphite crystallite size (L_a) of CNF and $C/CuFe_2O_4$ composite nanofibers with different magnetic source concentration..... 67
4.2	Summary of mean pore diameter, surface area and total pore volume of CNF and $C/CuFe_2O_4$ composite nanofibers with different metal source concentration..... 69

LIST OF TABLES (Continued)

Table	Page
4.3	Edge energies and oxidation state of all C/CuFe ₂ O ₄ composite nanofibers along with the standard samples 72
4.4	Lists of coordinate number (N), amplitude reduction (S_0^2), Debye-Waller factor (σ^2), interatomic distances (R), and R-factor obtained by fitting the experimental EXAFS data at Fe and Cu K-edge for C/CuFe ₂ O ₄ _0.2..... 76
4.5	Lists of coordinate number (N), amplitude reduction (S_0^2), Debye-Waller factor (σ^2), interatomic distances (R), and R-factor obtained by fitting the experimental EXAFS data at Fe and Cu K-edge for C/CuFe ₂ O ₄ _0.4..... 77
4.6	Lists of coordinate number (N), amplitude reduction (S_0^2), Debye-Waller factor (σ^2), interatomic distances (R), and R-factor obtained by fitting the experimental EXAFS data at Fe and Cu K-edge for C/CuFe ₂ O ₄ _0.6..... 78
4.7	Lists of the magnetic parameters: coercivity (H_c), saturation magnetization (M_s), squareness ratio (M_r/M_s) and blocking temperature (T_B) of C/CuFe ₂ O ₄ composite nanofibers with different magnetic source concentration..... 85
4.8	Lists of anodic and cathodic potential of C/CuFe ₂ O ₄ 88
4.9	Lists of Raman peak height, Raman peak width, R value (I_D/I_G) and in plane graphite crystallite size (L_a) of CNF and C/CoFe ₂ O ₄ composite nanofibers with different magnetic source concentration 109

LIST OF TABLES (Continued)

Table	Page
4.10 Summary of mean pore diameter, surface area and total pore volume of CNF and C/CoFe ₂ O ₄ composite nanofibers with different metal source concentration.....	111
4.11 Edge energies and oxidation states of all C/CoFe ₂ O ₄ composite nanofibers along with the standard samples	113
4.12 Lists of coordinate number (N), amplitude reduction (S_0^2), Debye-Waller factor (σ^2), interatomic distances (R), and R-factor obtained by fitting the experimental EXAFS data at Fe and Co K-edge for C/CoFe ₂ O ₄ _0.2.....	119
4.13 Lists of coordinate number (N), amplitude reduction (S_0^2), Debye-Waller factor (σ^2), interatomic distances (R), and R-factor obtained by fitting the experimental EXAFS data at Fe and Co K-edge for C/CoFe ₂ O ₄ _0.4.....	120
4.14 Lists of coordinate number (N), amplitude reduction (S_0^2), Debye-Waller factor (σ^2), interatomic distances (R), and R-factor obtained by fitting the experimental EXAFS data at Fe and Co K-edge for C/CoFe ₂ O ₄ _0.6.....	121
4.15 Lists of the magnetic parameters: coercivity (H_c), saturation magnetization (M_s), squareness ratio (M_r/M_s) and blocking temperature (T_B) of C/CoFe ₂ O ₄ composite nanofibers with different magnetic source concentration.....	127
4.16 Lists of Raman peak height, Raman peak width, R value (I_D/I_G) and in plane graphite crystallite size (L_a) of CNF and C/NiFe ₂ O ₄ composite nanofibers with different magnetic source concentration	146

LIST OF TABLES (Continued)

Table	Page
4.17 Summary of mean pore diameter, surface area, and total pore volume of CNF and C/NiFe ₂ O ₄ composite nanofibers with different metal source concentration.....	149
4.18 Edge energies and oxidation states of all C/NiFe ₂ O ₄ composite nanofibers along with the standard samples	152
4.19 Lists of coordinate number (N), amplitude reduction (S_0^2), Debye-Waller factor (σ^2), interatomic distances (R), and R-factor obtained by fitting the experimental EXAFS data at Fe and Ni K-edge for C/NiFe ₂ O ₄ _0.2.....	157
4.20 Lists of coordinate number (N), amplitude reduction (S_0^2), Debye-Waller factor (σ^2), interatomic distances (R), and R-factor obtained by fitting the experimental EXAFS data at Fe and Ni K-edge for C/NiFe ₂ O ₄ _0.4.....	158
4.21 Lists of coordinate number (N), amplitude reduction (S_0^2), Debye-Waller factor (σ^2), interatomic distances (R), and R-factor obtained by fitting the experimental EXAFS data at Fe and Ni K-edge for C/NiFe ₂ O ₄ _0.6.....	159
4.22 Lists of the magnetic parameters: coercivity (H_c), saturation magnetization (M_s), squareness ratio (M_r/M_s) and blocking temperature (T_B) of C/NiFe ₂ O ₄ composite nanofibers with different magnetic source concentration.....	166

LIST OF FIGURES

Figure	Page
1.1 The Ragone plot showing the comparison of the operational characteristics of energy storage and conversion devices.....	2
2.1 Schematic view of the MFe_2O_4 cubic structure	8
2.2 Schematic comparison of the carbon nanofiber (CNF) and carbon fiber (CF).....	13
2.3 Hysteresis loop of a ferromagnetic behavior	22
2.4 The principle charge storage mechanism of (a) EDLC (b) Pseudocapacitor ...	23
3.1 Schematic illustration of electrospinning set up	31
3.2 Schematic illustration of the fabrication process and the formation of C/ MFe_2O_4 composite nanofibers	34
3.3 Diagram showing the preparation and characterization of C/ MFe_2O_4 composite nanofibers (M = Cu, Co and Ni).....	35
3.4 Schematic principle of XRD equipment	37
3.5 Categories of gas adsorption loops (IUPAC).....	42
3.6 Schematic diagram of the VSM.....	46
3.7 (a) The potential waveform applied to the working electrode in the cycle voltammetry experiment (b) Cyclic voltammogram of three different electrochemical capacitors: ideal, resistive, faradaic capacitors.....	49

LIST OF FIGURES (Continued)

Figure	Page
3.8	The Nyquist plot with its equivalent Randle circuit for (a) an electrochemical reaction under kinetic control (b) an electrochemical system under kinetics and diffusion..... 56
4.1	TGA curves of CNF and C/CuFe ₂ O ₄ composite nanofibers under N ₂ atmosphere and air atmosphere (in set) 59
4.2	XRD patterns of (a) CNF, (b) C/CuFe ₂ O ₄ _0.2, (c) C/CuFe ₂ O ₄ _0.4 and (d) C/CuFe ₂ O ₄ _0.6 composite nanofibers..... 61
4.3	SEM micrographs of the electrospun C/CuFe ₂ O ₄ composite nanofibers before carbonization (left), the fibers after carbonization (middle) and their FE-SEM images (right), respectively of (a) pure CNF, (b) C/CuFe ₂ O ₄ _0.2 (c), C/CuFe ₂ O ₄ _0.4, and (d) C/CuFe ₂ O ₄ _0.6 composite nanofibers 63
4.4	TEM bright field images (left) with the corresponding SAED pattern (right) of (a) pure CNF, (b) C/CuFe ₂ O ₄ _0.2, (c) C/CuFe ₂ O ₄ _0.4, and (d)C/CuFe ₂ O ₄ _0.6 composite nanofibers..... 64
4.5	Raman spectra of (a) pure CNF, (b) C/CuFe ₂ O ₄ _0.2, (c) C/CuFe ₂ O ₄ _0.4, and (d) C/CuFe ₂ O ₄ _0.6 composite nanofiber 66
4.6	N ₂ adsorption/desorption isotherms of (a) pure CNF, (b) C/CuFe ₂ O ₄ _0.2, (c) C/CuFe ₂ O ₄ _0.4, and (d) C/CuFe ₂ O ₄ _0.6 composite nanofibers 69

LIST OF FIGURES (Continued)

Figure	Page
4.7 XANE spectra, pre-edge peak, and corresponding first derivatives plot, respectively of C/CuFe ₂ O ₄ composite nanofibers at Fe K-edge (a, b, c) and at Cu K-edge (c, e, f).....	71
4.8 (a, b) Fourier transform in R-space of three different composite samples at Fe and Cu k-edge, respectively. (c, d) Fourier transform in R-space with the corresponding fitted spectra. (e, f) The k ² (χ(k)) plots with the corresponding fitting spectra at Fe and Cu K-edge, respectively	75
4.9 (a) Room temperature magnetization of CNF and three types of C/CuFe ₂ O ₄ composite nanofibers carbonized at 535 °C for 1 h, (b) the variation of the coercivity (H _c) and the remanence ratio (M _r /M _s) with crystallite size at room temperature	81
4.10 The measuring temperature dependence of magnetization and their corresponding zero field-cooled and field-cooled (ZFC-FC) for (a) C/CuFe ₂ O ₄ _0.2 (b) C/CuFe ₂ O ₄ _0.4 (c) C/CuFe ₂ O ₄ _0.6 composite nanofibers.....	83
4.11 The dependence of M _r /M _s on the measurement temperature for C/CuFe ₂ O ₄ _0.2, C/CuFe ₂ O ₄ _0.4, and C/CuFe ₂ O ₄ _0.6 composite nanofibers.....	84

LIST OF FIGURES (Continued)

Figure	Page
4.12 Cyclic voltammograms (CV) in 0.5 M Na ₂ SO ₄ at different scan rates of (a) CNF, (b) C/CuFe ₂ O ₄ , and (c) CuFe ₂ O ₄ , respectively. (d) The corresponding specific capacitance at different scan rates of CNF, C/CuFe ₂ O ₄ and pure CuFe ₂ O ₄	88
4.13 Cyclic voltammograms (CV) at different scan rates of (a) CNF, (b) C/CuFe ₂ O ₄ , and (c) CuFe ₂ O ₄ electrodes in 1.0 M KOH electrolyte. (d) The corresponding specific capacitance at different scan rates. (e) The specific capacity retention of CNF, C/CuFe ₂ O ₄ and CuFe ₂ O ₄ electrodes at 1000 cycles	92
4.14 Galvanostatic charge/discharge curves of (a) CNF, (b) C/CuFe ₂ O ₄ , and (c) CuFe ₂ O ₄ electrodes at current densities of 0.1, 0.25, 0.5, 0.75 and 1.0 A/g in 1 M KOH electrolyte solution. (d) The corresponding Regone plot	94
4.15 Nyquist impedance plots at a frequency range of 0.1 Hz-100 kHz in 1 M KOH electrolyte solution for (a) CNF, (b) C/CuFe ₂ O ₄ , and (c) CuFe ₂ O ₄ electrodes.....	96
4.16 Bode plots of (a) frequency dependence of phase angle (b) impedance dependence on frequency of CNF, C/CuFe ₂ O ₄ and CuFe ₂ O ₄ electrodes	99

LIST OF FIGURES (Continued)

Figure	Page
4.17 TGA curves of CNF and C/CoFe ₂ O ₄ composite nanofibers under N ₂ atmosphere and air atmosphere (in set)	101
4.18 XRD patterns of (a) CNF, (b) C/CoFe ₂ O _{4_0.2} , (c) C/CoFe ₂ O _{4_0.4} and (d) C/CoFe ₂ O _{4_0.6} composite nanofibers.....	103
4.19 SEM micrographs of the electrospun C/CoFe ₂ O ₄ composite nanofibers before carbonization (left), the fibers after carbonization (middle) and their Fe-SEM images (right), respectively of (a) pure CNF, (b) C/CoFe ₂ O _{4_0.2} (c), C/CoFe ₂ O _{4_0.4} , and (d) C/CoFe ₂ O _{4_0.6}	105
4.20 TEM bright field images (left) with the corresponding SAED pattern (right) of (a) pure CNF, (b) C/CoFe ₂ O _{4_0.2} , (c) C/CoFe ₂ O _{4_0.4} , and (d) C/CoFe ₂ O _{4_0.6} composite nanofibers.....	106
4.21 Raman spectra of (a) pure CNF, (b) C/CoFe ₂ O _{4_0.2} , (c) C/CoFe ₂ O _{4_0.4} , and (d) C/CoFe ₂ O _{4_0.6} composite nanofiber	108
4.22 N ₂ adsorption/desorption isotherms of (a) pure CNF, (b) C/CoFe ₂ O _{4_0.2} , (c) C/CoFe ₂ O _{4_0.4} , and (d) C/CoFe ₂ O _{4_0.6} composite nanofibers	110
4.23 XANE spectra, pre-edge peak, and corresponding first derivatives plot, respectively of C/CoFe ₂ O ₄ composite nanofibers at Fe K-edge (a, b, c) and at Co K-edge (d, e, f)	114

LIST OF FIGURES (Continued)

Figure	Page
4.24	(a, b) Fourier transform in R-space of three different composite samples at Fe and Co k-edge, respectively. (c, d) Fourier transform in R-space with the corresponding fitted spectra. (e, f) The $k^2(\chi(k))$ plots with the corresponding fitting spectra at Fe and Co K-edge, respectively 118
4.25	(a) Room temperature magnetization of CNF and three types of C/CoFe ₂ O ₄ composite nanofibers carbonized at 535 °C for 1 h, (b) the variation of the coercivity (H_c) and the remanence ratio (M_r/M_s) with crystallite size at room temperature 124
4.26	The measuring temperature dependence of magnetization and their corresponding zero field-cooled and field-cooled (ZFC-FC) for (a) C/CoFe ₂ O ₄ _0.2 (b) C/CoFe ₂ O ₄ _0.4 (c) C/CoFe ₂ O ₄ _0.6 composite nanofibers 126
4.27	The dependence of M_r/M_s on the measurement temperature for C/CoFe ₂ O ₄ _0.2, C/CoFe ₂ O ₄ _0.4, and C/CoFe ₂ O ₄ _0.6 composite nanofibers..... 127
4.28	Cyclic voltammograms (CV) at different scan rates of (a) CNF, (b) C/CoFe ₂ O ₄ , and (c) CoFe ₂ O ₄ electrodes in 1.0 M KOH electrolyte. (d) The corresponding specific capacitance at different scan rates. (e) The specific capacity retention of CNF, C/CoFe ₂ O ₄ and CoFe ₂ O ₄ electrodes at 1000 cycles 131

LIST OF FIGURES (Continued)

Figure	Page
4.29 Galvanostatic charge/discharge curves of (a) CNF, (b) C/CoFe ₂ O ₄ , and (c) CoFe ₂ O ₄ electrodes at current densities of 0.1, 0.25, 0.5, 0.75 and 1.0 A/g in 1 M KOH electrolyte solution. (d) The corresponding Regone plot	133
4.30 Nyquist impedance plots at a frequency range of 0.1 Hz-100 kHz in 1 M KOH electrolyte solution for (a) CNF, (b) C/CoFe ₂ O ₄ and (c) CoFe ₂ O ₄ electrodes	135
4.31 Bode plots of (a) frequency dependence of phase angle (b) impedance dependence on frequency of CNF, C/CoFe ₂ O ₄ and CoFe ₂ O ₄ electrodes	137
4.32 TGA curves of CNF and C/NiFe ₂ O ₄ composite nanofibers under N ₂ atmosphere and air atmosphere (in set)	139
4.33 XRD patterns of (a) CNF, (b) C/NiFe ₂ O ₄ _0.2, (c) C/NiFe ₂ O ₄ _0.4 and (d) C/NiFe ₂ O ₄ _0.6 composite nanofibers	141
4.34 SEM micrographs of the electrospun C/NiFe ₂ O ₄ composite nanofibers before carbonization (left), the fibers after carbonization (middle) and their FE-SEM images (right), respectively of (a) pure CNF, (b) C/NiFe ₂ O ₄ _0.2 (c), C/NiFe ₂ O ₄ _0.4, and (d) C/NiFe ₂ O ₄ _0.6.....	143
4.35 TEM bright field images (left) with the corresponding SAED pattern (right) of (a) pure CNF, (b) C/NiFe ₂ O ₄ _0.2, (c) C/NiFe ₂ O ₄ _0.4, and (d) C/NiFe ₂ O ₄ _0.6 composite nanofibers	144

LIST OF FIGURES (Continued)

Figure	Page
4.36 Raman spectra of (a) pure CNF, (b) C/NiFe ₂ O ₄ _0.2, (c) C/NiFe ₂ O ₄ _0.4, and (d) C/NiFe ₂ O ₄ _0.6 composite nanofiber	147
4.37 N ₂ adsorption/desorption isotherms of (a) pure CNF, (b) C/NiFe ₂ O ₄ _0.2, (c) C/NiFe ₂ O ₄ _0.4, and (d) C/NiFe ₂ O ₄ _0.6 composite nanofibers.....	149
4.38 XANE spectra, the corresponding first derivatives plot and the pre-edge peak, respectively of C/NiFe ₂ O ₄ composite nanofibers at Fe K-edge (a, b, e) and at Ni K-edge (c, d, f)	151
4.39 (a, b) Fourier transform in R-space of three different composite samples at Fe and Ni k-edge, respectively. (c, d) Fourier transform in R-space with the corresponding fitted spectra. (e, f) The k ² (χ(k)) plots with the corresponding fitting spectra at Fe and Ni K-edge, respectively.....	153
4.40 (a) Room temperature magnetization of CNF and three types of C/NiFe ₂ O ₄ composite nanofibers carbonized at 535 °C for 1 h, (b) the variation of the coercivity (H _c) and the remanence ratio (M _r /M _s) with crystallite size at room temperature	162
4.41 The measuring temperature dependence of Magnetization and their corresponding zero field-cooled and field-cooled (ZFC-FC) for (a) C/NiFe ₂ O ₄ _0.2 (b) C/NiFe ₂ O ₄ _0.4 (c) C/NiFe ₂ O ₄ _0.6 composite nanofibers.....	163

LIST OF FIGURES (Continued)

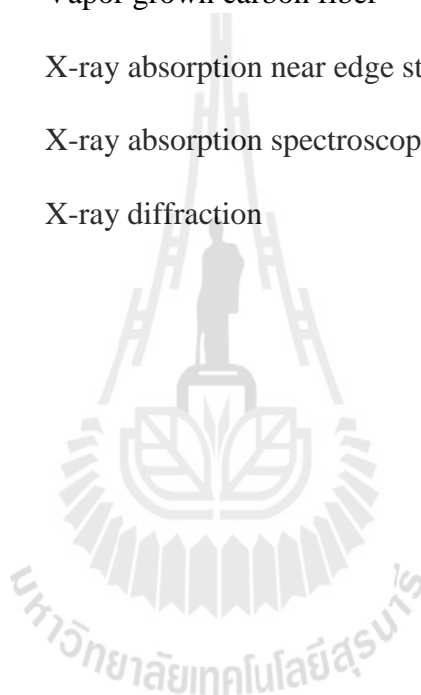
Figure	Page
4.42	The dependence of M_r/M_s on the measurement temperature for C/NiFe ₂ O ₄ _0.2, C/NiFe ₂ O ₄ _0.4, and C/NiFe ₂ O ₄ _0.6 composite nanofibers.....
	165
4.43	Cyclic voltammograms (CV) at different scan rates of (a) CNF, (b) C/NiFe ₂ O ₄ , and (c) NiFe ₂ O ₄ electrodes in 1.0 M KOH electrolyte. (d) The corresponding specific capacitance at different scan rates. (e) The specific capacity retention of CNF, C/NiFe ₂ O ₄ and NiFe ₂ O ₄ electrodes at 1000 cycles
	170
4.44	Galvanostatic charge/discharge curves of (a) CNF, (b) C/NiFe ₂ O ₄ , and (c) NiFe ₂ O ₄ electrodes at current densities of 0.05, 0.1, 0.25, 0.5, 0.75 and 1.0 A/g in 1 M KOH electrolyte solution. (d) The corresponding Regone plot
	172
4.45	Nyquist impedance plots at a frequency range of 0.1 Hz-100 kHz in 1 M KOH electrolyte solution for (a) CNF, (b) C/NiFe ₂ O ₄ and (c) NiFe ₂ O ₄ electrodes.....
	175
4.46	Bode plots of (a) frequency dependence of phase angle (b) impedance dependence on frequency of CNF, C/NiFe ₂ O ₄ and NiFe ₂ O ₄ electrodes.....
	176

LIST OF ABBREVIATIONS

BET	=	Brunauer emmett teller
CB	=	Carbon black
CF	=	Carbon fiber
CNF	=	Carbon nanofiber
CCNF	=	Carbon composite nanofiber
CNT	=	Carbon nanotube
CV	=	Cyclic voltammetry
DMF	=	<i>N, N</i> -dimethylformamide
ES	=	Electrospinning
EIS	=	Electrochemical impedance spectroscopy
EXAFS	=	Extended X-ray absorption fine structure
FE-SEM	=	High resolution scanning electron microscopy
GCD	=	Galvanostatic charge/discharge
GDL	=	Gas diffusion layer
PVA	=	Poly (vinyl alcohol)
PAN	=	Polyacrylonitrile
PVP	=	polyvinyl alcohol
PEO	=	Polyethylene Oxide
PVDF	=	Poly (vinylidene fluoride)
SEM	=	Scanning electron microscopy

LIST OF ABBREVIATIONS (Continued)

TEM	=	Transmission electron microscopy
TGA	=	Thermo gravimetric analysis
VSM	=	Vibrating sample magnetometer
VGCF	=	Vapor grown carbon fiber
XANE	=	X-ray absorption near edge structure
XAS	=	X-ray absorption spectroscopy
XRD	=	X-ray diffraction



CHAPTER I

INTRODUCTION

1.1 Background and motivation

Carbon composite nanofiber (CCNF) is an important member of carbon nanofibers (CNFs) that has been investigated in both fundamental scientific research and practical applications. It is the materials that enable to be applied as promising materials in many fields, such as electrode materials for energy storage devices (batteries and electrochemical capacitor), sensors, electrical devices, etc. More in details about the structure, synthesis method, and potential applications of CCNF are presented in section 2.3.

In the electrochemical capacitor (EC), carbon materials in different form have played important used as material electrode. EC is an energy storage device that provides high power density (>10 kW/kg) due to their ability to release energy more easily from surface, and high number of charge/discharge life cycles ($>10^6$ cycles) without damage due to non-faradaic process. Moreover, it has higher energy density than the conventional capacitor due to the double capacitor layer effect. These advantages have made them currently popular as the energy sources for mobile phones, lab top computers, and so on (Jayalakshmi *et al.*, 2008). Up to now, the energy density of EC was not so high compared to batteries as seen in Figure 1.1. Therefore, recently, many researchers have focused on modification of carbonaceous materials or designing new materials to solve such a problem.

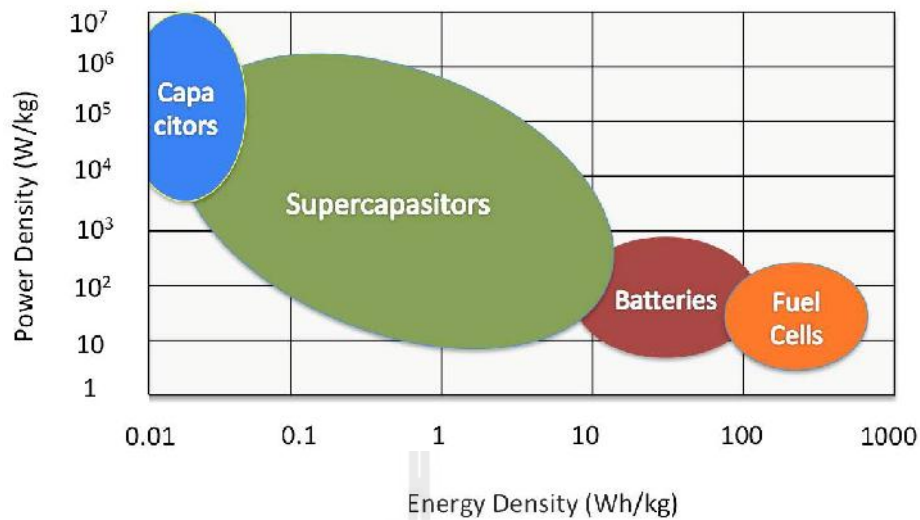


Figure 1.1 The Ragone plot showing the comparison of the operational characteristics of energy storage and conversion devices (Adapted from Simon *et al.*, 2008).

To date, there have been many researches that focus on improving materials that offer large surface area and high conductivity, which could provide the higher values of capacitance and also the energy density. Various carbonaceous materials from these works such as activated carbon (Qu *et al.*, 1998), carbon nanotubes (CNTs) (Chen *et al.*, 2004), carbon nanofibers (CNFs) (Merino *et al.*, 2005), and graphene (Vivekchand *et al.*, 2008) are the commonly used materials. In addition, composites based on one-dimensional carbon material such as carbon nanotubes composite (Fan *et al.*, 2007), carbon composite nanofibers (Yan *et al.*, 2011, Kim *et al.*, 2013) also have been widely used to improve overall performance of ECs. However, the application of one-dimension carbon materials as an electrode of electrochemical capacitor is still limited due to the low energy. New materials are needed to overcome the drawbacks of activated carbon electrode materials to improve the performances for supercapacitors. Especially for CNF, researchers have put attention to modifying

CNF in a variety of ways, such as increasing impactful surface area and introduction of other electroactive material.

In this work, non woven PAN-based carbon composite nanofibers reinforced with the crystalline ferrite nanoparticles (having formula MFe_2O_4 , where M are Ni^{2+} , Co^{2+} and Cu^{2+}) were studied to observe the morphology, structure, magnetic and electrochemical properties. The aim of work is divided in to two main parts. Firstly, the effect of magnetic/carbon concentration ratio on the morphology, structure and magnetic properties was investigation. Secondly, how the electrochemical properties of CNF improve after the introduction of ferrite nanoparticle. Normally, metal-oxides present an attractive alternative as an electrode material because of their high specific capacitance and conductivity making them easier to construct high-energy and high-power densities. However, bare MFe_2O_4 exhibits low conductivity. Therefore non woven carbon nanofibers have been considered as the promising conductive support for MFe_2O_4 . High surface area with large pore volume of CNF efficient ion diffusion pathways and enhance the penetration of the ion electrolyte. Moreover, MFe_2O_4 is a metal oxide that can generate the Faradaic reactions. This reaction taking place in the charge storage mechanism, in which supported pseudo capacitance (Winter and Brodd, 2004; Bard and Faulkner, 2001). Therefore, adding magnetic nanoparticle into CNFs matrix is a promising approach to combine the electrochemical double layer and pseudo capacitance, and thus improving the capacitance of an electrochemical capacitor.

1.2 Objectives of research

The general objective of this PhD thesis is to contribute to the collective knowledge in the fabrication, characterization, magnetic and electrochemical properties of C/MFe₂O₄ composite nanofibers, where M are Ni²⁺, Co²⁺ and Cu²⁺. In overall, the major scientific and technical objectives of the thesis involve

1.2.1 To fabricate C/MFe₂O₄ composite nanofibers, where M are Ni²⁺, Co²⁺ and Cu²⁺.

1.2.2 To characterize the effect of MFe₂O₄ concentration on the structure and morphology of MFe₂O₄/carbon composite nanofibers.

1.2.3 To study the electrochemical properties of CNF, C/MFe₂O₄ and MFe₂O₄ electrode, where M are Ni²⁺, Co²⁺ and Cu²⁺.

1.2.4 To understand the effect of MFe₂O₄ nanoparticles in the CNFs matrix on the electrochemical properties.

1.3 Limitations of study

1.3.1 This study focuses on the fabrication of carbon nanofibers reinforced with three type magnetic ferrite nanoparticles of NiFe₂O₄, CoFe₂O₄, and CuFe₂O₄.

1.3.2 The carbonization is carried out only at 535 °C for 1 h, while the magnetic source concentration is varied as 0, 20, 40 and 60 wt.%, respectively.

1.3.3 The morphology, structure and magnetic properties of the C/MFe₂O₄ composite nanofibers are compared with those of the pure CNFs.

1.3.4 The electrochemical properties of the C/MFe₂O₄ electrode is compared with those of the pure CNFs and pure MFe₂O₄ (M = Ni, Co and Cu) electrodes.

1.4 Location of the research

Advanced Materials Physics (Amp.) Laboratory, School of Physics, Institute of Science, Suranaree University of Technology, Nakhon Ratchasima, Thailand.

1.5 Anticipated outcomes

1.5.1 Skill and expertise for fabrication and characterization techniques of the C/MFe₂O₄ composite nanofibers with improved properties for electrode material of electrochemical capacitors

1.5.2 Understanding of the magnetic and electrochemical properties of the carbon nanofibers (CNFs) and C/MFe₂O₄ composite nanofibers (M = Cu, Co and Ni).

1.5.3 International publications.

1.6 Outline of thesis

This thesis is divided into five chapters. The first chapter provides the introduction of the thesis. In the next chapter (chapter II), a brief review of information concerning with structure, synthesis method, and potential application of ferrite material, CNF, and CCNFs are given. Moreover, the theory approach concerning with magnetic and electrochemical properties are also detailed in this chapter. In chapter III, the preparation methodology and characterization method of CNF, C/MFe₂O₄ composite nanofibers and pure MFe₂O₄ nanoparticle are given. The information of all measurements techniques used in this work are also summarized in this chapter. Chapter IV presents the experimental results and discussion. Finally, the conclusions and suggestion of this thesis are addressed in chapter V.

CHAPTER II

LITERATURE REVIEWS

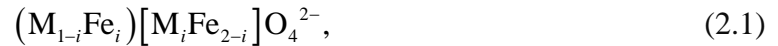
Chapter II reviews the literatures concerning with structural, growth, and potential applications of carbon nanofibers (CNFs), spinel ferrite material (MFe_2O_4) and the composite of them (C/MFe_2O_4). A simple description of the theoretical approach associated to magnetic and electrochemical properties are also detailed in this chapter.

2.1 The spinel ferrite (MFe_2O_4) material

2.1.1 Ferrite structure

Spinel ferrites are ferrimagnetic materials with mixtuer of metal and iron oxide. The molecular formula was described by MFe_2O_4 , where M and Fe are a divalent metal cation (e.g. Ni, Co, Cu, Fe, etc.) and trivalent iron cation, respectively. The ideal crystal lattice of spinel ferrite is cubic $Fd3m$. $CuFe_2O_4$ is only one of ferrite that presents tetragonal unit cell symmetry ($I41/amd$) (Jahn–Teller effect) if the sample is slowly cooled from high temperature (Evans and Hafner, 1968). Normally, cubic spinel structure contains two sites for metal cation occupancy: tetrahedral (A) and octahedral (B) sites (as seen in Figure 2.1). In the unit cell (with the lattice parameter value ~ 0.84 nm), eight molecules of MFe_2O_4 consists of 32 oxygen anions form a cubic close packing. There are ninety six possible positions for cations in the unit cell,

where twenty four cations (M^{2+} and Fe^{3+}) occupy eight of the sixty four available A sites and sixteen of the thirty two available B sites. According to the cations distribution, there are three types of spinel ferrite structure corresponding to the formula



where i is the degree of inversion. $i = 0$ for normal spinel structure (such as in zinc ferrites). $i = 1$ for inverse spinel structure such as magnetite Fe_3O_4 , ferrites $NiFe_2O_4$ and $CoFe_2O_4$. $0 < i < 1$ for case that the cation distribution possesses an intermediate degree of inversion. That is both sites contain a fraction of the M^{2+} and Fe^{3+} cations. $MnFe_2O_4$ represents this type of structure.

In this work, the prepared samples concerning with three types of ferrite: $CoFe_2O_4$, $CuFe_2O_4$ and $NiFe_2O_4$. These ferrites are typical ferrimagnetism materials with inverse spinel structure. The structure can be characterized in cubic ($Fd3m$) for $CoFe_2O_4$ and $NiFe_2O_4$. Except the $CuFe_2O_4$, either cubic ($Fd3m$) or tetragonal ($I41/amd$) structure can be characterized. Normally, the cubic structure of $CuFe_2O_4$ possesses a larger magnetic moment than that of the tetragonal due to larger cupric ions (Cu^{2+}) at tetrahedral sites. Normally, the magnetic behavior of spinel ferrite originates from magnetic moment of anti-parallel spins between $8Fe^{3+}$ ions at A sites and $8M^{2+}$, $8Fe^{3+}$ ions at B sites ($(Fe^{3+})_A[M^{2+}Fe^{3+}]_BO_4^{2-}$). The magnetic moments of Fe^{3+} ions from tetrahedral and octahedral sites cancel each other, while the net magnetization is due to the presence of M^{2+} in octahedral site. More information concerning with the spinel structure is shown in Table 2.1.

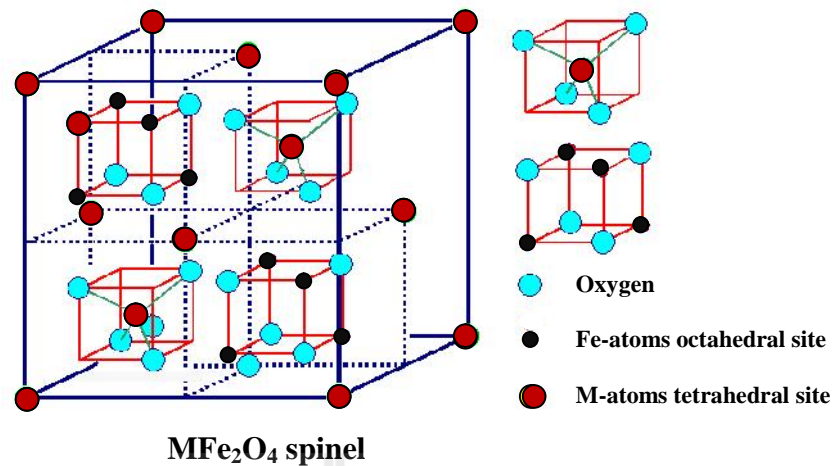


Figure 2.1 Schematic view of the MFe₂O₄ cubic structure (Adapted from Rabe, 2010).

Table 2.1 Details of site in spinel structure (Hench and West, 1990).

Site	Size (Å ^o)	Number available	Number occupied	Spinel Structure	
				Normal	Inverse
Tetrahedral (A-site)	0.3-0.6	64	8	8M ²⁺	8Fe ³⁺
Octahedral (B-site)	0.6-1.0	32	16	16Fe ³⁺	8Fe ³⁺ , 8M ²⁺

2.1.2 The synthesis methods

To date, the synthesis of magnetic materials on the nanoscale has been a field of intense study. This is due to the structure and properties of magnetic nanomaterials are different as they are at bulk size. Spinel ferrite (MFe₂O₄:M is a divalent metal ion) has been prepared by various methods such as sol-gel (Cheng *et al.*, 1998), coprecipitation (Roy and Ghose, 2006), electrodeposition (Dixit *et al.*, 2010; Kumbhar *et al.*, 2012), electrochemical method (Qi *et al.*, 2005), hydrothermal process (Rashad *et al.*, 2012), milling process (Liu *et al.*, 2005), electrospinning and thermal

decomposition (Ponhan *et al.*, 2009; Peng *et al.*, 2014) etc. It is important to note that, the synthesis of uniformly sized and shape is the key importance for applications. More details of the MFe_2O_4 ($M = Co, Cu, Ni$) synthesis studied in the past decade are listed in Table 2.2

Table 2.2 The synthesis of MFe_2O_4 in the past decade.

sample	methods	crystallite size (nm)	Magnetic properties	Electrochemical properties	Ref.
NiFe ₂ O ₄ CoFe ₂ O ₄ CuFe ₂ O ₄ (thin films)	Electrochemical	~50	-	460 mAh/g 460 mAh/g 452 mAh/g (10 μ A/cm ² : 0.01–3.0V)	NuLi and Qin., 2005.
CuFe ₂ O ₄ (nanowall)	Electrochemical	thickness of 10 nm	H _c 1.2-9.47 kOe M _s ~68 emu/g	-	Qi <i>et al.</i> , 2005
NiFe ₂ O ₄ (powder)	Hydrothermal	5-15	-	1314 mAh/g (0.2 mA/cm ² : 111.4 m ² g/)	Zhao <i>et al.</i> , 2007.
CuFe ₂ O ₄ nanofiber	Electrospinning	7.9 - 23.98	M _s 17.73- 23.98 emu/g	-	Ponhan <i>et al.</i> , 2009
NiFe ₂ O ₄ (thin film)	Pulsed laser deposition	47	M _s 45 emu/g (300K)	-	Dixit <i>et al.</i> , 2010
CuFe ₂ O ₄ (powder)	Co- precipitation	23±7	H _c 245.5 Oe (300 K)	-	Salavati- Niasari <i>et al.</i> , 2012
CuFe ₂ O ₄ (powder)	Hydrothermal	24.6-51.5	M _s 83.7 emu/g (200 °C; 24 h) H _c 138.7 Oe (100 °C; 12 h)	-	Rashad <i>et al.</i> , 2012

Table 2.2 (Continued) The synthesis of MFe_2O_4 in the past decade.

sample	methods	crystallite size (nm)	Magnetic properties	Electrochemical properties	Ref.
CoFe ₂ O ₄ (thin film)	Chemical deposition	34	-	366 F/g: ESR 1.1Ω (5 mV/s.)	(Kumbhar <i>et al.</i> , 2012)
CoFe ₂ O ₄ (powder)	Hydrothermal	44.7	H _c 4.2 kOe, M _s 67.0 emu/g	-	Ponce <i>et al.</i> , 2013
NiFe ₂ O ₄	Microwave assisted combustion	20	H _c 170 Oe	-	Mahmouda <i>et al.</i> , 2013
CoFe ₂ O ₄	Hydrothermal	-	-	733.5 mAh /g (200 mA/g)	Xiong <i>et al.</i> , 2014
CoFe ₂ O ₄	Co-precipitation	-	M _s 73 emu/g, H _c 717 Oe	-	Huixia <i>et al.</i> , 2014
CuFe ₂ O ₄ (powder)	Co-precipitation	14	M _s 9.3 emu/g H _c 41.07 Oe	-	Kanagaraj <i>et al.</i> , 2014
CuFe ₂ O ₄ (nanotube)	Electrospinnin g	-	-	816 mAh/g (200 mA/g)	Peng <i>et al.</i> , 2014

2.1.3 Applications of spinel ferrites

Spinel ferrites have been investigated in recent years for their low cost, high stability, easy to magnetize/demagnetize and useful electrical and magnetic properties. The applications of spinel ferrites were observed in various fields such as magnetic information storage device, magnetic bulk cores, magnetic fluids, and medical diagnostics (Caizer *et al.*, 2003). Recently, various studies have reported that spinel ferrites are possibly being able to store energy such as in lithium ion batteries and electrochemical capacitors (Nuli and Qin, 2005). The electrochemical characteristics of these materials are significantly affected by their particle size,

morphology and crystallinity (Do and Weng, 2006). However, the major drawback of these materials is the reversible capacity dropped rapidly with poor cycle ability. Moreover, spinel ferrite has very low electronic conductivity, which limits their electrochemical response for being used as an electrode material for Li-ion batteries. In addition, the structure of electrode material strongly influences on the electrochemical performance. The better electrochemical performance of MFe_2O_4 ($M = Cu, Ni, Co$) film electrodes comparing with their powder electrode counterpart was observed (Alcantara *et al.*, 2003). This is due to nanocrystalline film electrode can reduce the lithium ion diffusion distance and thus increase the volume effect on the reactivity of electrode material.

According to three types of ferrite in this study, $CoFe_2O_4$ is well known to have moderate saturation magnetization, tunable coercivity, high magnetocrystalline anisotropy, chemical stability and a mechanical hardness (Ayyappan *et al.*, 2010). These useful characteristics make it a good candidate for the recording media, memory ferrofluids, and sensors (Gopal Reddy *et al.*, 2000). Moreover $CoFe_2O_4$ is one of spinel ferrites that has been extensively studied as anode material for lithium ion batteries due to its low cost and its high theoretical capacity (916 mAh/g) (Guo *et al.*, 2010; Vidal Abarca *et al.*, 2011). However, poor electrical conductivity and huge volume changes of $CoFe_2O_4$ electrode during the charge/discharge processes lead to poor cycling stability. The making carbon-based composite is a way to enhance the electrical conductivity (Jin *et al.*, 2012). $CuFe_2O_4$ is an inverse spinel structure that has been extensively studied because it exhibits phase transitions, high electric conductivity, and chemical stability. In the last decade, it is used in a wide range of applications such as in catalytic (Kameoka *et al.*, 2010), Lithium ion batteries (Nuli

and Qin, 2005; Selvan *et al.*, 2006), gas sensing (Sun *et al.*, 2007), high density magneto-optic recording devices, magnetic refrigeration and ferrofluids (Roy and Ghose, 2006). NiFe_2O_4 is an inverse spinel structure that contains high electrical resistivity, very low magnetocrystalline anisotropy, wide band-gap, high saturation magnetization and moderate magnetostriction. This behavior makes it is a prime candidate for sensors, magnetoelectric composites, high density magnetic recording media, magnetic liquids and electronic devices. So far, the electrochemical properties of MFe_2O_4 have been studied and some of them are summarized in Table 2.2.

2.2 Carbon nanofibers

2.2.1 Carbon nanofibers structure

Carbon nanofiber (CNF) is one dimensional long thin carbon strand with nanometer-size diameter. The structure composed mostly of carbon atoms and distinguished from conventional carbon fibers (CF) in its smaller diameter. The CF diameters are in order of several micrometers, while CNFs have diameters of 50–200 nm (Feng *et al.*, 2014). The schematic comparison of CNF and CF is illustrated in Figure 2.2. The unique properties such as huge surface area (above $10^6 \text{ m}^2/\text{g}$), good electrical conductivity (106 S/m), high tensile strength (37 GPa), and high chemical stability (Teymourian *et al.*, 2013) of CNFs allow them to be used in our daily life. Moreover, CNFs have been widely applied in industry due to the ease in production processes compared to other forms of carbon.

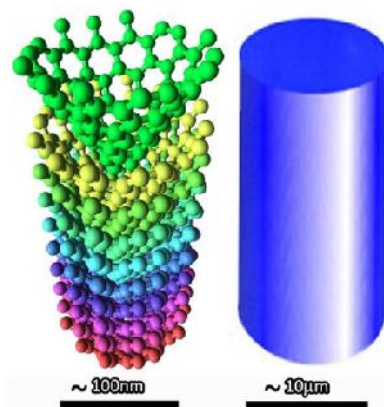


Figure 2.2 Schematic comparison of the carbon nanofiber (CNF) and carbon fiber (CF) (Adapted from Feng *et al.*, 2014).

2.2.2 The synthesis methods

Generally, CNFs can be synthesized via vapor growth method (Du *et al.*, 2000), chemical vapor depositing method (CVD) (Hsieh *et al.*, 2006), as well as the combination of electrospinning of polymer and carbonization method (Gu *et al.*, 2008). Among these methods, the carbonization process for convert material to be CNF under an inert gas atmosphere is the most preferred method due to not complicated and low cost. In fact, there are a number of processing techniques have been used for fabrication of CNF, such as drawing (Ondarcuhu *et al.*, 1998), phase separation (Ma *et al.*, 1999), template synthesis (Feng *et al.*, 2002), self assembly (Whitesides *et al.*, 2002) and electrospinning (Maensiri *et al.*, 2007). Among the above mentioned methods, electrospinning is the most attractive method due to its simplicity, low cost and efficient technique for producing uniform nano to micro scale fibers (Maensiri *et al.*, 2007; Gu *et al.*, 2008). Moreover, the web or mat structure of fibers is a good form to be used as electrode materials for energy storage devices due to largely counting on the transport on electrolyte ions.

There are several materials used for commercial carbon nanofibers including polymers (PAN, PVA), rayon, pitch and so on. Polyacrylonitrile (PAN) has been widely used because of its high carbon yield and thermal stability. The properties of the final CNF are decided by the types of material precursor. For example, CNF derived from pitch typically provides better electrical properties (Kinoshita *et al.*, 1988), but much lower modulus and strength were observed (Endo *et al.*, 2001). Normally, the synthesis of CNF by the combination of electrospinning and carbonization method involves three main stages; electrospinning, oxidative stabilization and carbonization, respectively. Stabilization is the heat treatment with temperature between 200 and 300 °C in air atmosphere to prevent fiber from melting during higher heat treatment. In this step, the ladder-polymer structure begins to form by reacting with oxygen. The cyclization of nitrile groups (C≡N) and crosslinking of the chain molecules (-C=N-C=N-) form of gases (H₂O, NH₃, CO, HCN, CO₂ or N₂) to give carbon fibers were also observed. Carbonization process is the heat treatment step up to 1000 °C to remove non carbon under inert gas atmosphere. Generally, the volume change and weight lose will occur during this step, in which decrease the CNF diameter. Additionally, the polymer type and the carbonization process play the most important roles in the quality of the prepared CNFs.

2.2.3 Applications of carbon nanofibers

The unique properties of CNFs as discussed earlier makes its numerous possible applications such as catalysts, reinforcing fillers in polymeric composites, supporting materials for metal nanoparticles, electrode materials for energy storage devices, etc. In this section, the review is focused on the literature of CNFs used as the electrode material for electrochemical capacitor. As known in the electrode materials applications that, the electrical conductivity and the surface area are always the first priority need to be considered (Wang *et al.*, 2014). CNF is a material has been used due to their large surface area and high electrical conductivity. The electrode material with higher specific surface area provided higher specific capacitance (Frackowiak *et al.*, 2001). However, the experimental specific capacitance observed in CNFs is lower than expected. Thus various activated carbons have been synthesized to create porosity, in which yield higher specific surface area of material. Moreover, the specific surface area is inversely proportional to the fiber diameter, thus the applications as material electrode require fibers with smaller diameters. The preparation and the electrochemical performance of CNFs in recent decades are listed in Table 2.3

Table 2.3 Typical values for electrochemical capacitance of carbon nanofibers.

Material electrode/ activating agent	Electrolyte	Capacitance/ surface area	Reference
ACNF(CO ₂ , 900 °C)	6M KOH	208 F/g (843 m ² /g)	Xu <i>et al.</i> , 2007
ACNF (steam/N ₂ , 900 °C)	6M KOH	143.5 F/g (1724.8 m ² /g)	Kim <i>et al.</i> , 2009
ACNF (KOH)	2M H ₂ SO ₄	255 F/g (1520 m ² /g)	Barranco <i>et al.</i> , 2010
CNF ACNF (CO ₂ , 850 °C)	1M H ₂ SO ₄ 1M H ₂ SO ₄	18 F/g 221 F/g (531 m ² /g)	Niu <i>et al.</i> , 2011
CNF	PEO-LiClO ₄ -EC-THF	3.81 F/g	Lekakou <i>et al.</i> , 2011
CNF	6M KOH	130.7 F/g	Kim <i>et al.</i> , 2011
CNF	6M KOH	46.5 F/g	Tai <i>et al.</i> , 2012
ACNF	0.1M Na ₂ SO ₄	47 F/g (250 m ² /g)	Natalia <i>et al.</i> , 2013
ACNF	1M H ₂ SO ₄	210 F/g (100 mV/s)	Tran <i>et al.</i> , 2013
CNF paper	6 MKOH 1 M (C ₂ H ₅) ₄ NBF ₄ /PC)	209 F/g (1317 m ² /g)	Ma <i>et al.</i> , 2014
CNF yarn	6M KOH	15.8 F/g (2 A/g)	Zhuang <i>et al.</i> , 2014

2.3 Carbon composite nanofibers

2.3.1 Structure of carbon composite nanofibers

Carbon composite nanofiber (CCNF) is carbon nanofiber containing different phase fillers. The structure of CNFC is decided by shape of CNF matrix. The diameter of the composite nanofiber is about hundreds of nanometers and their length can reach several micrometers.

2.3.2 The synthesis methods

As reported earlier that, the objective of carbon composite nanofibers is to improve its properties, and also favored over the cheaper price. To date, the synthesis methods of CCNF have been the subject of intense investigation, especially for application as the electrode materials. It is well known that, the materials for electrochemical capacitor electrode are divided in to three main types: carbon based (CNT, CNF, Graphene, etc.), metal oxides (RuO₂, MnO₂, Fe₃O₅ etc.) and conducting polymers (polyaniline (PANI), polypyrrole (PPy), etc.). The composite of these materials with CNF have been intensively investigated. The general preparation approaches of CNF matrix are a chemical vapor deposition growth and electrospinning as described in section 2.2.2. While, various methods for preparing the metal nanoparticles in which act as the composite material are similar as reported in section 2.1.2. The performance of composite fibers is strongly governed by the dispersion of nanoparticle in the CNF matrix. Thus, the dispersion is a key role in the synthesis of CCNF. It was found that CNF with large surface area can act as a support for the dispersion of metal nanoparticle, and thus improving the conductivity of electrode materials (Kim² *et al.*, 2012; Ren *et al.*, 2013). Moreover, surface treatment is a method to help the dispersion of metal oxide in the CNF matrix (Feng *et al.*, 2014).

2.3.3 Applications of carbon composite nanofibers

The carbon composite materials are able to be used in various field applications as reported in section 2.1.3. For the application as the electrode materials of energy storage devices, the combination of noble carbon with magnetic materials has been strongly conducted. Kuo and ko-worker (Kuo *et al.*, 2006) reported the preparation of

MnFe₂O₄/carbon black composite by co-precipitation method and found that the capacitance for the ferrite phase calcined at 350 °C is about 105 F/g. Wang and co-workers (Wang *et al.*, 2008) reported the excellent electrochemical properties after composite Co into CNF matrix (C/Co composite nanofibers). High capacity (>750 mAh/g) and rate capability (578 mAh/g at 1 C rate) were observed. Jin and co-workers (Jin *et al.*, 2012) synthesized the C/Fe₃O₄ and C/CoFe₂O₄ composite nanofibers by thermolysis of metal followed by carbon coating. They found the composites showed high specific capacity of 600 and 700 mAh/g, respectively, after 200 cycles at a rate of 0.2 C. High specific capacity value is arisen from high surface area by the ferrite nanoparticles and the efficient electron transport path through the surface conductive carbon from each active ferrite nanoparticles to a current collector. Peng and co-workers (Peng *et al.*, 2014) reported the properties of electrospun CuFe₂O₄ nanotubes by electrospinning method followed by thermal decomposition. The CuFe₂O₄ nanotubes delivered a high reversible capacity of 816 mAhg⁻¹ at 200 mA/g over 50 cycles due to its high specific surface areas as well as the unique hollow structure. Xia and co-workers (Xia *et al.*, 2012) synthesized CoFe₂O₄-graphene nanocomposite by hydrothermal for application as a high-capacity anode material of lithium-ion batteries. It was found that the prepared electrode with the 20 wt% graphene can deliver a high reversible specific capacity up to 1082 mAh/g as well as excellent cycling stability and rate capability.

For CNF/metal oxide composite prepared by electrospinning process, the preparation procedure can be either dispersion metal oxide nanoparticles in polymer-based carbon solution or mixed metal oxide and polymer source solution together before converting them to be nanofibers by electrospinning followed by carbonization

process to obtain CNF as the final product. So far, several carbon composite nanofibers with different preparation techniques for supercapacitors have been studied and lists of the works reported in literature are summarized in Table 2.4.

Table 2.4 List of carbon nanofibers composite (CNFC) for used as supercapacitor electrode.

Electrode materials	method	Electrolyte solution	capacitance (F/g)	Reference
CNF/Olygoaniline	CVD method	KOH	149	Kim <i>et al.</i> , 2004
CNF/Polypyrrole	Chemical deposition	6M KOH	300 (200 mV/s)	Kim <i>et al.</i> , 2006
CNF/Ag	Electrospinning and carbonization	0.5 M H ₂ SO ₄	231.91 (3% Ag)	Park <i>et al.</i> , 2008
CNF/ZnCl ₂	Electrospinning and carbonization	6M KOH	140 (5 wt.% ZnCl ₂)	Kim <i>et al.</i> , 2007
CNF/CoMnO ₂	VGCF	1M KOH	342 (100 mV/s)	Kim <i>et al.</i> , 2009
CNF/Polyaniline	Electrospinning and carbonization	1M H ₂ SO ₄	638	Yan <i>et al.</i> , 2011
CNF/MnO ₂	Electrospinning and carbonization	1M Na ₂ SO ₄	311	Zhi <i>et al.</i> , 2012
CNF/ V ₂ O ₅	Electrospinning and carbonization	6M KOH	150	Kim <i>et al.</i> , 2012
CNF/graphene	Electrospinning and carbonization	6M KOH	197	Tai <i>et al.</i> , 2012
CNF/B ₂ O ₃	Electrospinning and carbonization	6M KOH	184 (20 wt.% B ₂ O ₃)	Kim <i>et al.</i> , 2013

2.4 Theoretical Approach

In this section, a briefly concept of magnetic theory followed by the overview of electrochemical capacitor and their theoretical approach are presented.

2.4.1 Magnetic properties of materials

Magnetism is a property of matter in which results from either the moving around the nucleus or the spin motion of each electron. Each spinning electron causes a magnetic field to form around it. The magnetic field of one electron is cancelled by an opposite magnetic field produced by the other electron in the pair. The unpaired electron in iron, cobalt and nickel atoms cannot cancel the electron magnetic fields, and thus these elements act like a very small magnet. The magnetic moments (\sim) of atoms relate to the spins of electrons. The most common in the magnetic experiment is to apply a magnetic field (H) to a material and measure the magnetization (M) induced by the field. The magnetic field induction (B) in a sample is described by

$$B = H + 4\pi M \quad [cgs]. \quad (2.2)$$

The susceptibility ($\chi = M/H$) and the permeability ($\mu = B/H$) are two quantities related to M and B , where the susceptibility is a measure of the increase in magnetic moment caused by H and the permeability represents the relative increase in flux caused by the presence of the magnetic material.

The arrangement of the magnetic moment can be used to classify type of magnetic behavior. The diamagnetism is present when the magnetic moments are paired and overall cancel each other ($\mu_{net} = 0$). The diamagnetic materials have a negative susceptibility ($\chi < 0$), a very weak response in an applied magnetic field and do not retain magnetic moment when the magnetic field is removed. The paramagnetic behavior is present in uncoupled magnetic moment material. The incomplete

cancellation of electron spin which does not retain magnetic moment when the magnetic field is removed was observed. Ferrimagnetism is observed in the material that the magnetic moment in the neighboring sublattices incomplete cancellation due to their different magnitudes (Callister, 2003). Anti-ferromagnetism is the magnetic behavior that the neighboring different sublattices of materials having equal magnitude magnetic moments but align in the opposite directions ($\mu_{net} = 0$). The superparamagnetism is the magnetic behavior that the magnetic moments fluctuate around the easy axes of magnetization. If enough energy is supplied, magnetism can be reversed along this axis; therefore no hysteresis is observed. Ferromagnetism is permanent magnetic that the magnetic moments of the domains align along the direction of the applied magnetic field forming a large net magnetic moment. To describe the magnetization change with applied field of material, the hysteresis loop is used. Briefly, the magnetic moments in each domain of ferromagnetic material are aligned in one direction giving a net magnetization of each domain. With no applied field, the net magnetization is zero because the magnetic moments are randomly oriented in domains. When a field is applied, the rotation of domains was observed. Domain size increased until saturated if the rotation is in the field direction and vice versa. If the field direction is reversed, the magnetization does not follow the original path. The remanent magnetization (M_r) observed at applied field is zero, indicating to some domains still rotated in the former direction. To reduce M_r to zero, the field called coercivity (H_c) must be applied. The ferromagnetic nanoparticles may display a superparamagnetic behavior when either composed of a single magnetic domain or the temperature is above the blocking temperature. The schematic hysteresis loop and the corresponding rotation of magnetic moment are presented in Figure 2.3.

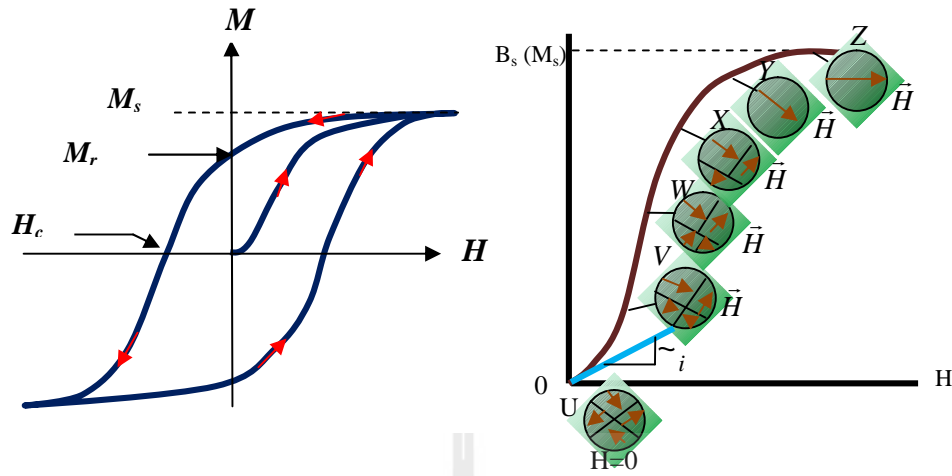


Figure 2.3 Hysteresis loop of a ferromagnetic behavior (Adapted from Coey, 2009).

2.4.2 Electrochemical properties of materials

2.4.2.1 Electrochemical capacitor

Electrochemical capacitor (EC) is an electrochemical device that has the ability to store or release charge over short periods of time. According to charge storage mechanism, there are two main types of ECs: the electric double layer capacitors (EDLCs) and pseudocapacitors. EDLC stores energy as a double layer at electrode/electrolyte interface via ion adsorption/desorption, while Pseudocapacitor stores energy via faradaic process when the oxidation state of the metal oxide is changed whereas the potential changes. The principle behind the capacitor is demonstrated in Figure 2.4.

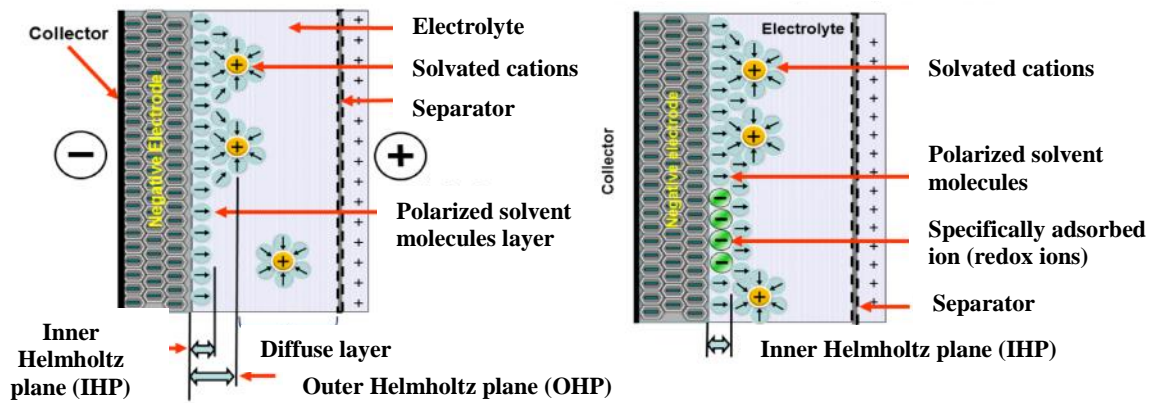


Figure 2.4 The principle charge storage mechanism of (a) EDLC (b) Pseudocapacitor (Adapted from <http://en.wikipedia.org/wiki/Supercapacitor>).

The capacitance (C : Farad) is the parameter to measure a capacitor's energy storage capability when the potential is applied. The capacitance equation of conventional capacitor is as follows

$$C = \frac{Q}{V} = \epsilon \frac{A}{d}, \quad (2.3)$$

where Q , V , ϵ , A and d are charge (Coulombs), electric potential (Volts), the dielectric constant of dielectric, conductor surface area, and dielectric thickness, respectively.

For EDLCs, the stored energy mechanism is similar to conventional capacitor but charge accumulates at the surface of electrode and electrolyte without dielectric. Experimentally, the complete cell (C_{cell}) can be considered as two symmetrical capacitors connected in series.

$$\frac{1}{C_{cell}} = \frac{1}{C_1} + \frac{1}{C_2} = \frac{2}{C_e}; C_1 = C_2 = C_e \quad (2.4)$$

The complete cell capacitance (C_{cell}) becomes half of the capacitance of each individual electrode (C_e)

$$C_{cell} = \frac{C_e}{2} \quad (2.5)$$

Literature values often quote the capacitance of a single carbon electrode in three electrode system (Qu and Shi, 1998). The value will be higher than the actual cell capacitance (a two electrode system). The specific capacitance of an electrode, C_e is given by

$$C_e (F / g) = \frac{2 \times C_{cell}}{m_e}, \quad (2.6)$$

where m_e is the weight of active material in a single electrode. According to the capacitance, the energy density and the power are given by

$$E = \frac{1}{2} CU^2 \quad (2.7)$$

$$P = \frac{U^2}{4R_s}, \quad (2.8)$$

where R_s is the equivalent series resistance (ESR) of the electrochemical cell.

For Pseudocapacitor, the energy is stored via Faradaic process, in which involving transfer of electron between the oxidant (Me^{n+}) and the reductant (Me) of a metal molecule substrate in contact with an electrolyte



The electrons enter the metal and the metal ions diffuse into the electrolyte for the forward reaction. The potential is given by the Nernst equation

$$E_p = E^0 + \frac{RT}{zF} \ln \frac{\frac{[Me^{n+}]}{[Me^{n+}] + [M]}}{1 - \frac{[Me^{n+}]}{[Me^{n+}] + [M]}}}, \quad (2.10)$$

where E^0 , zF , R , T , and F are the standard potential, amount of charge, gas constant, absolute temperature and Faraday constant, respectively. The square brackets denote species concentration.

2.4.2.1 Electrochemical cell configuration

In the electrochemical measurement, both of two-electrode and three-electrode configurations can be performed. Three-electrode system consists of a working electrode (WE), a counter electrode (CE), and a reference electrode (RE). WE is the electrode on which the reaction of interest is occurring. Its potential is varied linearly with time. RE is an electrode which potential maintains a constant (non-polarizable). The connection with this electrode is due to a potential of a single electrode that cannot be measured directly. CE is an electrode used to close the current circuit in the electrochemical cell. In the configuration system, the current flows through WE and CE, while the voltage is measured between the WE and RE.

Electrolyte is a solution that contains ions and act as charge carriers. This solution provides ions to the electrodes during oxidation and reduction. In the electrochemical cell, the ability to store charge depends on the accessibility of the ions to the surface-area, so ion size and pore size must be optimal. The energy density of cell can be limited by the electrolyte due to the cell voltage, and is strongly dependent on the electrolyte breakdown voltage, while the power density depends upon the cell's internal resistance (ESR) that is strongly dependent on electrolyte conductivity. There

are two types of electrolyte used in ECs: organic and aqueous. Aqueous solution provides higher capacitance and power compared to the organic electrolytes due to their higher ionic concentration, better conductivity (up to 1 S/cm) and smaller ionic size. However, the drawback of aqueous electrolyte is low breakdown voltage (~1.23 V determined by the electrochemical breakdown of water) (Bockris and Reddy, 1970). Most of commercial ECs recently have preferred to use organic electrolytes that provide large window voltages in the range of 2.5–2.7 V, and thus enhancing the energy density. However, the drawback of organic electrolyte is greater resistance and this limits the cell power density. The electrolytes often used are listed in Table 2.5.

Table 2.5 Electrolytes that are used often (Adapted from Inagaki *et al.*, 2010).

Electrolytes	Ion size (nm)		Electrolytes	Ion size (nm)	
	Cation	Anion		Cation	Anion
Organic			aqueous		
(C ₂ H ₅) ₄ N.BF ₄ (TEA ⁺ BF ₄ ⁻)	0.686	0.458	H ₂ SO ₄		0.533
(C ₂ H ₅) ₃ (CH ₃)N.BF ₄ (TEMA ⁺ BF ₄ ⁻)	0.654	0.458	KOH	0.26 ^a	0.533
(C ₂ H ₅) ₄ P.BF ₄ (TEP ⁺ BF ₄ ⁻)		0.458	Na ₂ SO ₄	0.36 ^a	
(C ₄ H ₉) ₄ N.BF ₄ (TBA ⁺ BF ₄ ⁻)	0.830	0.458	NaCl	0.36 ^a	0.508
(C ₆ H ₁₃) ₄ N.BF ₄ (TEA ⁺ BF ₄ ⁻)	0.96	0.458	Li-PF ₆	0.152 ^b	0.474
(C ₂ H ₅) ₄ N.CF ₃ SO ₃	0.686	0.540	Li-ClO ₄	0.152 ^b	

a is Stokes diameter of hydrated ions **b** is the diameter in PC, depending on the solvent used

CHAPTER III

RESEARCH METHODOLOGY

Chapter III describes the experimental procedure of the research, in which composed of two main sections. First, the background of materials fabrication is given. Secondly, the material characterization is explained.

3.1 Fabrication of C/MFe₂O₄ composite nanofibers

3.1.1 The precursor preparation

In this study, Polyacrylonitrile (C₃H₃N), N, N-dimethylformamide anhydrous (C₃H₇NO), Nickel (II) nitrate hexahydrate (Ni(NO₃)₂•6H₂O), Cobalt (II) nitrate hexahydrate (Co(NO₃)₂•6H₂O), Copper (II) nitrate (Cu(NO₃)₂•3H₂O)), and Iron (III) nitrate enneahydrate (Fe(NO₃)₂•9H₂O) were used as the starting materials. PAN was used as matrix for synthesis of magnetic nanoparticle due to it can prevent of agglomeration of the nanoparticles, control of the growth of the nanoparticles, and produce the uniform distribution of nanoparticles. The source and purity of all starting materials are listed in Table 3.1.

Electrospun PAN/MFe₂O₄ composite nanofibers (M are Ni, Co, and Cu) precursor were prepared by using mixed solution of polymer and metal sources. The polymer source was prepared by mixing of PAN in DMF solvent, whereas the metal source was obtained by mixing divalent metals nitrate with Iron nitrate in DMF solvent (the molar ratio of M:Fe was fixed as 1:2). The polymer source was stirred at

room temperature for 4 h followed by ultrasonication for 20 min, while the metal source was stirred at room temperature for 4 h. After that, both solutions were mixed together under magnetic stirring for at least 4 h in order to obtain homogeneously distributed solution. No other chemicals were added to the solution. In each composite material system, four samples with different weight ratio of polymer and magnetic source were set as 100/0, 80/20, 60/40, and 40/60, respectively. The details about the chemical compositions of the PAN/MFe₂O₄ composite solution were summarized in Table 3.1 - 3.2

Table 3.1 List of material used as starting materials for C/MFe₂O₄ composite nanofiber preparation, and their source and purity.

Materials	Source	Purity
Polyacrylonitrile (C ₃ H ₃ N)	Sigma-Aldrich	MW 150,000
<i>N,N</i> -dimethylformamide anhydrous (C ₃ H ₇ NO)	SIAL	99.8%
Iron (III) Nitrate Enneahydrate (Fe(NO ₃) ₂ •9H ₂ O)	Kento	99.95%
Nickel (II) Nitrate Hexahydrate (Ni(NO ₃) ₂ •6H ₂ O)	Kento	99.95%
Cobalt (II) Nitrate Hexahydrate (Co(NO ₃) ₂ •6H ₂ O)	Kento	99.95%
Copper (II) Nitrate (Cu(NO ₃) ₂ •3H ₂ O)	Carlo Erba	99.5%

Table 3.2 List of starting raw metallic materials for the preparation of C/MFe₂O₄ system (M = Cu, Co, Ni).

Material System	Polymer source		Metal source		
	PAN (g)	DMF (ml)	Ni(NO ₃) ₂ ·6H ₂ O (g)	Fe(NO ₃) ₂ ·9H ₂ O (g)	DMF (ml)
C/NiFe ₂ O ₄	3	30	-	-	-
	2.4	27	0.1594	0.4429	3
	1.8	27	0.3182	0.8841	3
	1.2	27	0.4770	1.3254	3
C/CoFe ₂ O ₄	3	30	-	-	-
	2.4	27	0.1595	0.4428	3
	1.8	27	0.3184	0.8840	3
	1.2	27	0.4773	1.3250	3
C/CuFe ₂ O ₄	3	30	-	-	-
	2.4	27	0.1386	0.4636	3
	1.8	27	0.2768	0.9256	3
	1.2	27	0.4141	1.3883	3

3.1.2 Fabrication of electrospun PAN/MFe₂O₄ composite nanofibers

Electrospinning (ES) is an excellent method for fiber fabrication with diameters of 20-1000 nm (Ramakrishna *et al.*, 2005). The electrostatic and mechanical forces are used to spin fiber from tip spinneret. The electrospinning system contains essential three components: high voltage power supply, syringe pump with needle tip and the ground target (Figure 3.3). To generate the fiber, a high voltage is applied between a droplet of a polymer solution and the ground target. With the increase of applied voltage, the solution becomes highly charged and then droplet at the needle tip. The Taylor's cone is generated. When the electrostatic repelling force overcomes the surface tension of the droplet, a charged jet of polymer solution is ejected, stretched, forms continuous filament and collected on the collector, respectively. The critical voltage was calculated by Taylor (Taylor, 1966) as

$$V_c^2 = 4 \frac{H^2}{L^2} \left(\ln \frac{2L}{R} - 1.5 \right) (0.117f R\chi), \quad (3.1)$$

where H , L , R and χ are the needle tip-ground target distance (cm), length of needle (cm), radius of needle tip (cm), and surface tension of spinning solution (dyn/cm), respectively.

There are more than 100 types of polymers that could be used as raw materials for electrospinning, such as PAN, PVP, PVA, PEO, protein, collagen, and so on. The parameters that affect morphologies and diameters of fibers are consisted of polymer solution parameter (concentration, surface tension), the process parameter (high voltage, feed rate and needle tip-ground target distance), and ambient parameter (humidity). Normally, the fiber diameter increases with solution viscosity (Jarusuwannapoom *et al.*, 2005). At low concentration solution, beads are formed

because of surface tension (Ramakrishna *et al.*, 2005). The higher voltage can lead to greater stretching of the solution due to the greater columb forces, and thus reducing the diameter of fibers (Megelski *et al.*, 2002). When the feeding rate is increased, there is a corresponding increase in the fiber diameter or bead size (Zhong *et al.*, 2002). The diameter of fiber can be increased by increasing the jet length. Decrease in electrostatic field strength results in less stretching of the fibers (Lee *et al.*, 2004). High humidity (water condenses on the surface fibers) was found to cause the formation of pores on the surface of the fibers (Bognitzki *et al.*, 2001). When the solution is electrospun at higher temperature, the fibers produced have more uniform diameter due to lower viscosity and greater solubility of the polymer in the solvent (Demir *et al.*, 2002).

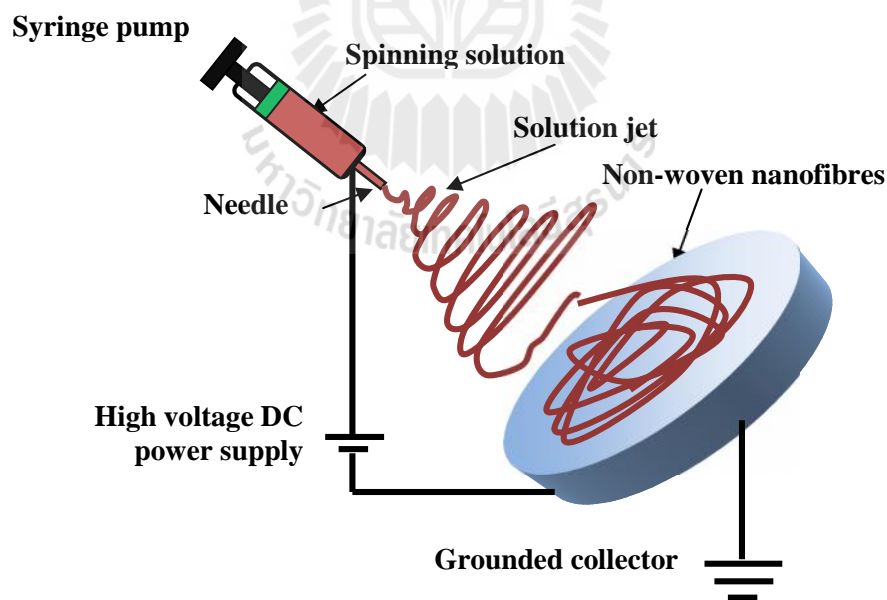


Figure 3.1 Schematic illustration of electrospinning set up.

3.1.3 Fabrication of C/MFe₂O₄ composite nanofibers

The obtained electrospun nanofibers were dried at 60 °C for 48 h before stabilization and carbonization, respectively. Stabilization is the process used to convert the linear polymer into a ladder structure and crosslink the chain molecules, thus can prevent the fibers from melting or fusing during higher temperature heat treatment. This step was carried out at 220 °C for 2 h in air atmosphere which breaks many of the hydrogen bonds and oxidizes the material. To obtain the C/MFe₂O₄ composite nanofibers, the stabilized samples were carbonized at 535 °C and holding them for 1 h under flowing of mixed air and argon atmosphere (with the flow rate ratio of 1:10). During carbonization, PAN is converted into carbon, while the binary metal precursors were decomposed to MFe₂O₄. Note that a slightly air adding due to the oxidation with air oxygen is needed to form those metal oxides. The final products are designated as C/CoFe₂O₄_0 (CNF), C/MFe₂O₄_0.2, C/MFe₂O₄_0.4, and C/MFe₂O₄_0.6, respectively. The condition parameters used in heat treatment process are lists in Table 3.3. The schematic illustration of the fabrication process and the formation of C/MFe₂O₄ composite nanofibers are presented in Figure 3.2. Moreover, the flowchart diagram showing the overview of experimental procedure performed in this work is illustrated in Figure 3.3.

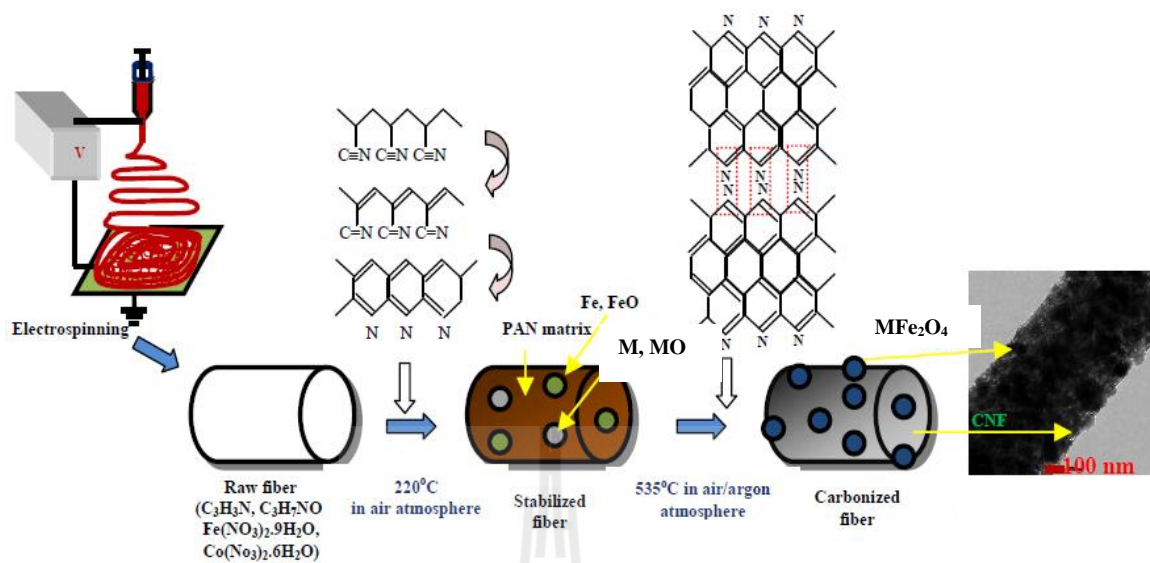


Figure 3.2 Schematic illustration of the fabrication process and the formation of C/MFe₂O₄ composite nanofibers.

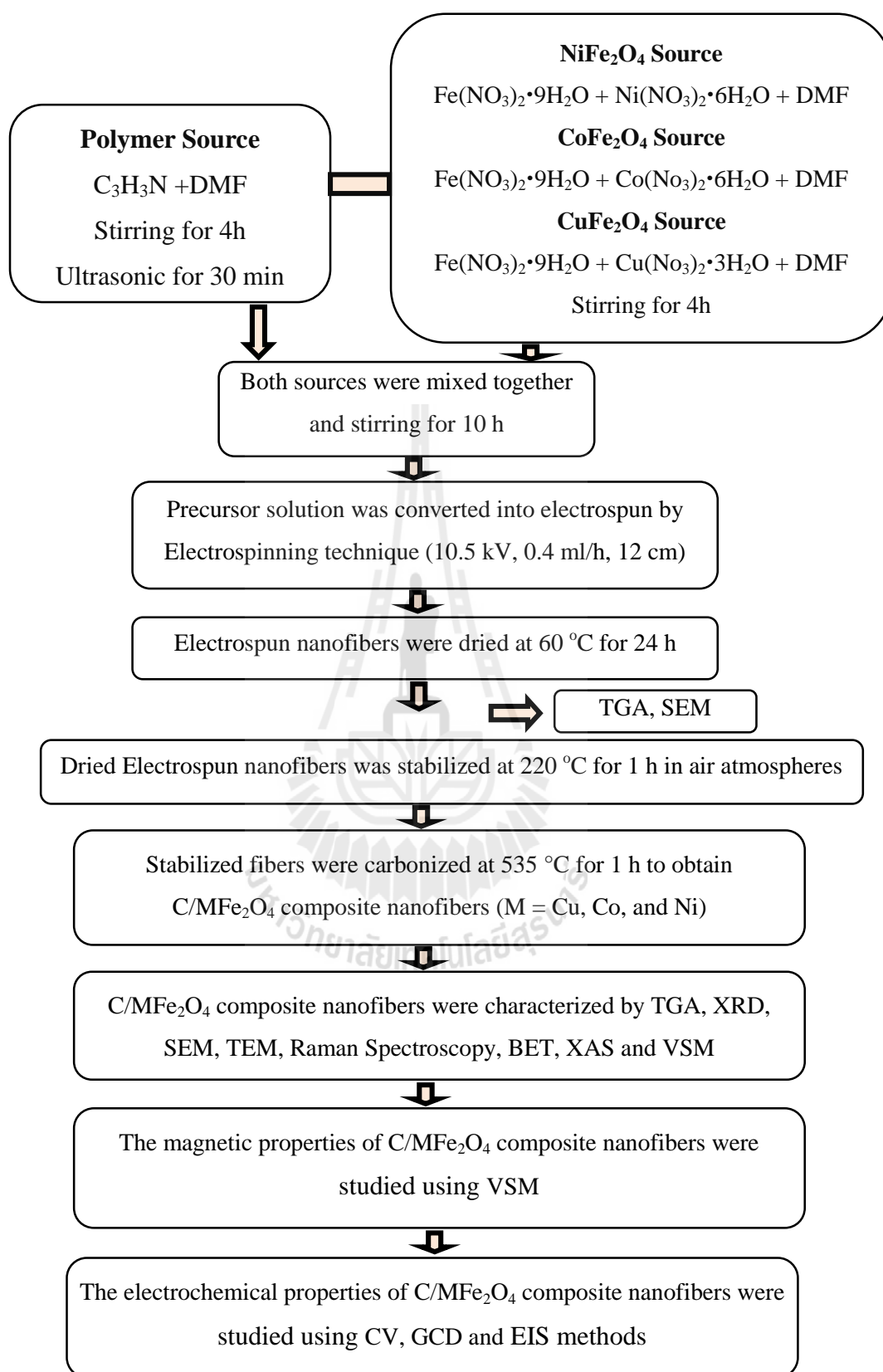


Figure 3.3 Diagram showing the preparation and characterization of C/MFe₂O₄ composite nanofibers (M = Cu, Co and Ni).

3.2 Material characterization

To understand the main features of the prepared samples, explaining their properties and determining areas for their potential applications, several characterization techniques were used and brief concepts are given as follows

3.2.1 Thermo gravimetric analyzer

Thermo gravimetric analysis (TGA) is a thermal technique used to determine the decomposition temperature of materials by monitoring the weight change as a function of temperature or time (<http://las.perkinelmer.com/Trainings/Courses.htm>). The prepared samples and the reference pan were subjected to thermo gravimetric and heated under flowing of gas (such as air, nitrogen, or argon) to prevent oxidation. The TGA curve is shown the weight loss (%) on the coordinate and time or temperature on the abscissa. Normally, the TGA performed simultaneously with DTA or DSC (Differential Thermal Analysis or Differential Scanning Calorimetry). The DTA signal shows the temperature difference between prepared samples and reference (Bhadeshia, 2002), and typically plotted versus temperature. The DSC signal very similar to DTA, while the advantage over DTA is the heat flow into or from the sample can be measured.

In this study, the TGA techniques was used to observe the weight loss as function of temperature for electrospun PAN and PAN composite with different magnetic sources content. The suitable temperature for stabilization and characterization were obtained from this technique. The sample weight for measurements was set at about 3 mg. The measurements were carried out both in air and nitrogen atmosphere from room temperature to 1200 °C with a heating rate of 10 °C/min by using TGA-DSC (METTLER TOLEDO STARe).

3.2.2 X-ray diffraction

The X-ray diffraction (XRD) is a technique used to evaluate the structure of a crystalline material (Cullity & Stock, 2001). The structural parameters such as the lattice constant (a), the crystallite size (D) and the atomic spacing (d) are obtained from this technique. The basic concept is based on the interferences phenomenon of two waves with the same wavelength and traveling in the same direction to the sample. The constructive and destructive interferences occur if a phase difference is $n\lambda$ (in phase) and $(n + 1/2)\lambda$ (out of phase), respectively. Schematic principle of XRD equipment is presented in Figure 3.4.

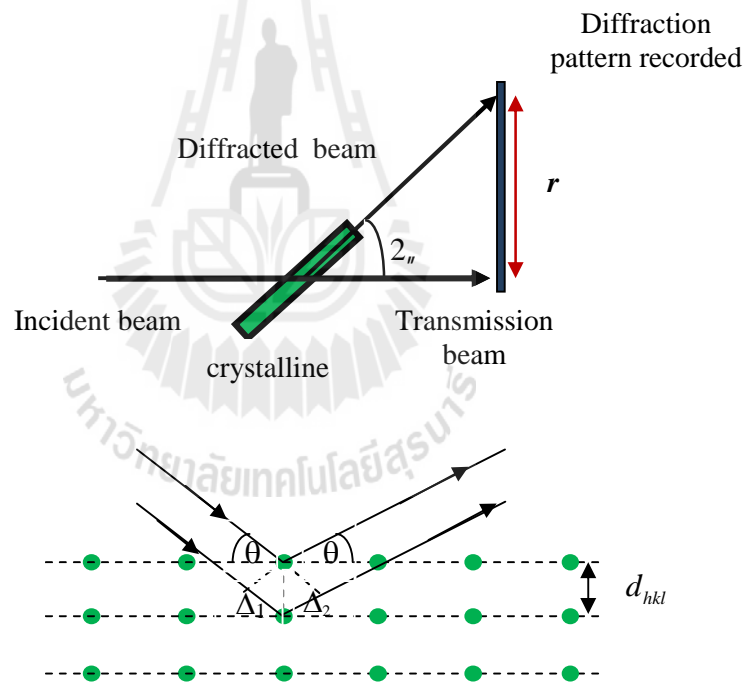


Figure 3.4 Schematic principle of XRD equipment (Adapted from <http://eserc.stonybrook.edu/ProjectJava/Bragg>).

When the constructive interference is detected, the information on the spacing between atomic planes of a crystal was obtained. But the deflected waves will not be in phase except when the Bragg equation is satisfied

$$2d \sin \theta = n\lambda \quad (3.2)$$

d is the spacing between atomic layers in a crystal, θ is the angle of incident beam, λ is the wavelength of the incident X-ray beam and n is an integer. The diffraction pattern can be used to identify the crystalline phases of the sample. According to the diffraction pattern, the crystallite size, lattice parameter and d-spacing can be estimated using the following equations, respectively. (Cullity and Stock, 2001)

$$D = \frac{k\lambda}{S \cos \theta} \quad (3.3)$$

$$a = \left(\lambda \sqrt{h^2 + k^2 + l^2} \right) / \sin \theta \quad (3.4)$$

$$d = \lambda / 2 \sin \theta \quad (3.5)$$

where λ is the wavelength of the radiation, k is the spherical shape factor (0.9), θ is the angle of the Bragg diffraction, and S is the full width at half maximum (FWHM) of the respective peaks.

In this work, the structure of CNF and C/MFe₂O₄ composite nanofibers were evaluated on X-ray diffractometer (Advance Bruker D8, Germany) with the Cu-K α radiation ($\lambda = 1.5406 \text{ \AA}$). The fiber samples were mashed as powder and placing them flat on a silicon glass. The XRD patterns were recorded in the 2θ of 10 to 80° with the time step of 0.5, and the step size of 0.02. The crystalline phase identification was carried out by comparison with the registered patterns of the Joint Committee for Powder Diffraction Standards (JCPDS).

3.2.3 Scanning electron microscopy

Scanning electron microscopy (SEM) is a characterization technique for observing the morphology of materials (Hafner, 2007). It is non-destructive technique, and it is possible to analyze the same materials repeatedly. In the measurement, the sample is scanned by electrons beam across the surface and collects scattered electron for imaging. Because the image is formed using backscattered signals, the sample does not require electronic transparency. As known that the electron beam is very narrow, thus the obtained SEM images have a large depth of three-dimensional appearance. This behavior is very useful for understanding the surface structure of a sample. Since the measurement sample must be conductivity to prevent charging, the coating sample with conducting material such as gold is necessary. In this work, the morphology and the particle size were investigated using scanning electron microscopy (SEM, JSM-6010LV). Although CNF matrix is found to be conductive materials, the coating with gold was also performed to increase the signal and resolution.

3.2.4 Transmission electron microscopy

Transmission electron microscopy or TEM is a microscopy technique to observe morphology and particle size distribution (Pennycook and Nellist, 1999). High resolution images can be recorded by transmission of electron beam through an ultra thin specimen, magnified and focused by an objective lens. The specimen needs to be thin enough to be transparent for electrons. In this work, all prepared samples were diluted in alcohol and dispersed on a 300 mesh copper grid following by dried in air and then measured under a 200 keV by using FEI TEM (TECNAI G²20, FEI,

USA). The corresponding selected-area electron diffraction (SAED) patterns were also recorded in this work. The MFe_2O_4 nanoparticle distribution in CNF matrix and their size were obtained by using the combination of TEM bright field image and the image j program.

3.2.5 Raman spectroscopy

Raman spectroscopy is a nondestructive sample technique for observing the structural fingerprints of carbon (Wang *et al.*, 2003). This technique provides understanding of the vibration properties, the microstructure of graphitic crystals and various disordered carbon materials (Samsonidze *et al.*, 2003). The basic principle is based on inelastic scattering of monochromatic light from a laser source. Photons of the laser light are absorbed by the sample and then reemitted, where the frequency of the reemitted photons is shifted up or down in comparison with original monochromatic frequency. This shift provides information about rotation and vibration molecular. The plotting of the shift light intensity with the frequency provides the Raman spectrum. Every band in the Raman spectrum corresponds to a specific vibrational frequency of a bond within the molecule.

In this work the Raman spectrum were recorded at room temperature using a triple spectrometer (JOBIN YVON HORIBA, T64000 triple monochromator, $\lambda = 532$ nm, FRANCE). All the spectra were obtained over a spectral range of $700 - 3250 \text{ cm}^{-1}$.

3.2.6 Brunauer-Emmett-Teller

The Brunauer Emmett Teller or BET is a characterization technique to observe the specific surface area of materials (Atkins, 1998). The principle measurement is based on the physical adsorption of gas on the surface of sample and by calculating the amount of adsorbate gas corresponding to a monomolecular layer on the surface. Normally, nitrogen gas and liquid nitrogen are used as the probe gas and the cold bath, respectively. The phenomenon of adsorption can be expressed with the following equation.

$$\frac{1}{W \left[\left(\frac{P_0}{P} \right) - 1 \right]} = \frac{1}{W_m C} + \frac{C-1}{W_m C} \left(\frac{P}{P_0} \right), \quad (3.6)$$

where W is the volume of gas adsorbed at standard temperature and STP pressure (273.15 K and 1.103×10^5 Pa) (ml). W_m is the volume of gas adsorbed at STP to produce an apparent monolayer on the sample surface (ml). P_0 is saturated pressure of adsorbate gas (Pa). P is partial vapour pressure of adsorbate gas in equilibrium with the surface at 77.4 K. C is dimensionless constant. At the relative pressures (P/P_0) lower than 0.05, N_2 is adsorbed in the form of single molecules. The multi-layered adsorption occurs in some small micropores with increasing in relative pressure. By decrease in relative pressure, desorption nitrogen was observed. When the shapes of the capillary pores are similar, the adsorption and desorption branches of the adsorption isotherm coincide with each other. The specific surface area can be calculated by

$$a_{BET} = \frac{W_m \dagger N_A}{mV_0} \quad (3.7)$$

Where W_m arise from the slop and the intercept of plot between the relative pressure and $1/W[(P_0/P)-1]$, \dagger is the area of the surface occupied by individual gas molecules, N_A is the Avogadro number, m is the sample mass and V_0 is the molar volume of gas ($22414 \text{ cm}^3/\text{molar}$ at atmospheric pressure). The six types of IUPAC standard adsorption isotherms are shown in Figure 3.5

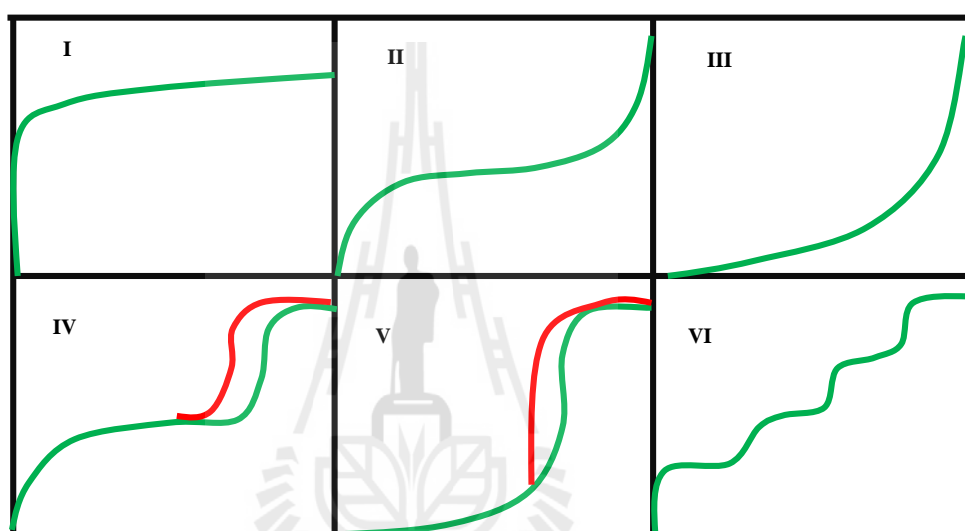


Figure 3.5 Categories of gas adsorption loops (IUPAC).

Type I is the typical isotherm of micro-porous ($< 2 \text{ nm}$) materials having relatively small external surface area. Type II or anti s-shaped adsorption isotherm is the normal forms for macroporous ($> 50 \text{ nm}$) and non porous adsorbents. Type III is characteristic of non-porous with low adsorbate-adsorbent interaction. A hysteresis loop feature in type IV related to the capillary condensation of the adsorbate in the mesopores ($2\text{-}50 \text{ nm}$) materials. Type V isotherm is related to weak adsorbate-adsorbent interaction at low P/P_0 , while the number of pore in the system is limited at middle and high relative pressure. Finally, type VI isotherm is characteristic of non-porous adsorbents with homogeneous surface.

In this study the Nitrogen adsorption/desorption was carried out on the Brunauer-Emmett-Teller analyzer (BET, BEL SORP MINI II, JAPAN) using the gas adsorption method. The prepared samples were degassed at 200 °C for 4 h at 10^{-5} Pa before measurement to ensure that the composite samples were clean and free of moisture. The specific surface area was calculated by BET method.

3.2.7 X-ray absorption spectroscopy

X-ray absorption spectroscopy (XAS) is a powerful technique for the structural study of material (Bunker, 2009). The measurement is performed by tuning the photon energy to a range where core electrons can be excited. The X-ray intensity (I) passing through an absorption layer with thickness x is expressed by the following equation

$$I = I_0 e^{-\mu x}, \quad (3.8)$$

where μ and I_0 are the probability that x-rays will be absorbed and the incoming X-ray intensity, respectively. The absorption X-ray increased dramatically when the energy matches well with the binding energy of electron. This causes a drop in the transmitted X-ray intensity. Normally, the absorption edge occurs when the incident photon energy is sufficient to cause excitation of a core electron of the absorbing atom to a continuum state. There are three main regions in the XAS spectra. First is the region at around 2-50 eV below the main adsorption edge. No significant adsorption phenomena occur. The pre-edge peak observed is related to the electronic transitions from the core level to empty state. Moreover, the strengths of such pre-edge peaks strongly depend on the coordination geometry around the absorbing atom such as number of neighbor atoms and valence state. Second region where the energy of

incoming X-ray is sufficient to transfer core electrons to higher unoccupied valence states is called the X-ray absorption near edge structure or XANES (2-50 eV above the adsorption edge). Analysis of this part gives the information on the oxidation state and the coordination number of the absorbing atom. The name of the edge depends upon the core electron which is excited. For instance, excitation of a 1s electron occurs at the K-edge, while excitation of a 2s or 2p electron occurs at an L-edge. Final region in the range of 50-1000 eV above the adsorption edge is called the extended X-ray absorption fine structure (EXAFS). In this region, the photo electrons have high kinetic energy enough to excited the core electron and the remaining energy cause the single scattering by the nearest neighbouring atoms. The analysis of this part gives information about the bond distance, coordination number, and kind of neighbors absorbing atom. Moreover, it is also a useful tool to determine the cation distribution in spinel ferrite structure. The EXAFS equation is given by

$$\chi(k) = \sum_j \frac{N_j S_0^2 f_j(k) e^{-2R_j/\lambda(k)} e^{-2k^2\sigma_j^2}}{kR_j^2} \sin[2kR_j + u_j(k)], \quad (3.9)$$

where S_0^2 is called amplitude reduction. $f(k)$ and $u(k)$ are scattering amplitude and phase shift, respectively. $\lambda(k)$ is the mean free path, R is the distance to neighboring atom, N is the coordination number of neighboring atom and σ^2 is mean square disorder of neighbor distance. The absorptions spectrum was transposed to k space using the formula $k = (2m(E - E_0) / \hbar)^{1/2}$, and Fourier transformed to the R space with a k^2 -weight.

In this work, to address the local environment around ions and the oxidation states of the Ni K-edge (8333 eV), Co K-edge (7709 eV), Cu K-edge (8979 eV), and Fe K-edge (7112 eV) in C/CuFe₂O₄, C/CoFe₂O₄ and C/NiFe₂O₄, XANES and EXAFS spectra were conducted at Beamline 8 (electron energy of 1.2 GeV; bending magnet; beam current 80-150 mA; 1.1 to 1.7×10^{11} photon s⁻¹) at the Synchrotron Light Research Institute (SLRI), Nakhon Ratchasima, Thailand. The samples were coated into the kapton tape during two frames sheet. All spectra were measured in the transmission mode with ionization chamber detectors. The normalized XAS data were processed after background subtraction in the pre-edge and post-edge region using the ATHENA software which is included in an IFEFFIT package (Ravel and Newville, 2005). Moreover, the cation distribution was obtained by fitting EXAFS data based on FEFF8.2 program (Ankudinov *et al.*, 2002).

3.2.8 Magnetic measurements

Vibrating sample magnetometer (VSM) is the instrument used for measures the magnetic properties of materials by the operation based on Faraday's Law of induction (Jiles, 1998). In the measurement process, the sample is placed in a uniform magnetic field and then is vibrated. If the material is magnetic, the uniform magnetic field will magnetize the sample by aligning the magnetic domains/spin with the magnetic field direction. The signal at the vibration frequency is proportional to the magnetic moment, the vibration amplitude and the vibration frequency. The output measurement provides the magnetization (M) as a function of a magnetic field (H). The behavior of M-H curve can be used to classify type of magnetic behavior as presented in section 2.4.1. Schematic diagram of the VSM is present in Figure 3.6

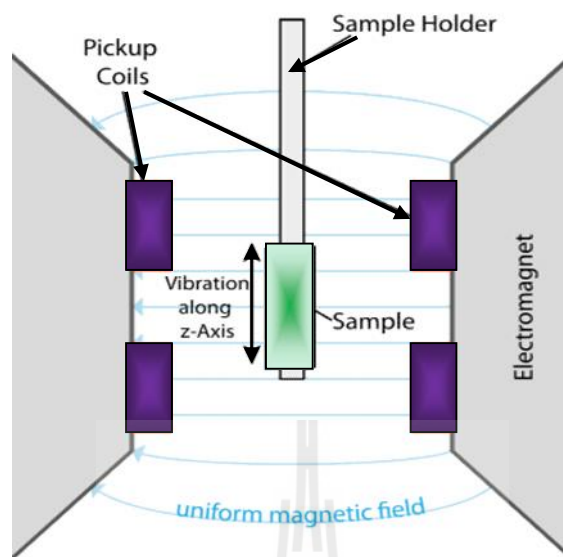


Figure 3.6 Schematic diagram of the VSM (Zhang *et al.*, 2009).

In this work, magnetic analysis was carried out on a vibrating sample magnetometer (VSM) (VersaLab™ PPMS®) at various measurement temperatures (50, 100, 200, 300 and 390 K). The sample with the weight of ~5 mg was put into the sample holder, and the magnetization was measured in a field range of ± 10 kOe. The parameters like saturation magnetization (M_s), remanent magnetization (M_r) and coercivity field (H_c) were obtained from the magnetization curve. The zero field-cooled and field-cooled (ZFC-FC) magnetizations were also studied in this work. The ZFC spectra were typically obtained by cooling in zero magnetic fields from a high temperature to a low temperature (390 to 50 K). The magnetization was measured at step wise increasing temperatures in a small field (500 Oe). The FC magnetization curve is obtained by measuring at stepwise decreasing temperatures in the same small applied field at each temperature.

3.2.9 Electrochemical measurements

The electrochemical measurement is the measuring of electrical quantities (current, potential, or charge) and their relationship to chemical parameters (Beguin and Frackowiak, 2001). Electrochemical behaviors of the prepared CNF, C/MFe₂O₄ and MFe₂O₄ (M=Cu, Co and Ni) were studied on a potentiostat galvanostat (PGSTAT 302N). Three electrodes system (WE, CE and RE) was used to evaluate the electrochemical performance via cyclic voltammetry (CV), electrochemical impedance spectroscopy (EIS), and galvanostatic charge/discharge (GCD) techniques. The working electrode was prepared by mixed C/MFe₂O₄ powder with acetylene black (conductive agent) and polyvinylidene difluoride (PVDF) (binder) with the weight ratio of 8:1:1. The *N, N*-dimethylformamide (DMF) was used as the solution solvent. The mixed precursor was making slurry by sonicating for 30 min and then dropping onto the 1 cm² glass diffusion layer (GDL). The active materials mass in each electrode was set at about 2 mg. The prepared electrode sheets were dried at 70 °C on a hot plate and then calcined at 200 °C in a vacuum oven for 1 h to remove the polymer binder. A platinum wire (Pt) and silver/silver chloride (Ag/AgCl: 3M NaCl) were used as the counter and reference electrode, respectively. The electrochemical cell systems (C/CuFe₂O₄, C/CoFe₂O₄ and C/NiFe₂O₄) were carried out using freshly prepared 1M KOH as the electrolyte. Moreover, the 0.5M Na₂SO₄ aqueous solution was also used for C/CuFe₂O₄ electrode.

3.2.9.1 Cyclic voltammetry

Cyclic Voltammetry (CV) is an electrochemical technique for measure the current flowing between working and counter electrodes in an electrochemical cell under the triangular potential waveform. The electron transfer mechanisms were also observed from this technique (Bard and Faulkner, 2001). In a cyclic voltammetry measurement, the potential of an electrode is cycled from a starting potential (E_1) to a final potential (E_2) and then back to the beginning. Normally, selected starting voltage is usually selected so that the chemical species under investigation are not initially oxidized or reduced, while the final potential is usually selected so that the potential interval (E_2-E_1) contains an oxidation or reduction process of interest. The current measured during this process is often normalized to the electrode surface area and referred to as the current density. The plot of current density against the applied potential is known as voltammogram. Figure 3.7 (b) shows three different schematic voltammograms of electrochemical capacitor: Ideal, resistive, and faradaic capacitor. An ideal capacitor display a rectangular shape (Figure 3.7 (b1)) due to the capacitance (C) would keep constant at a scan rate (Zhang *et al.*, 2011). When the resistances present, the rounding of the voltammogram corners was observed (Figure 3.7 (b2)). The redox peak will present with the cell that store energy via redox reaction (electron transfer) (Figure 3.7 (b3)). The sample with different oxidation states, the voltammogram with multiple peaks will observe.

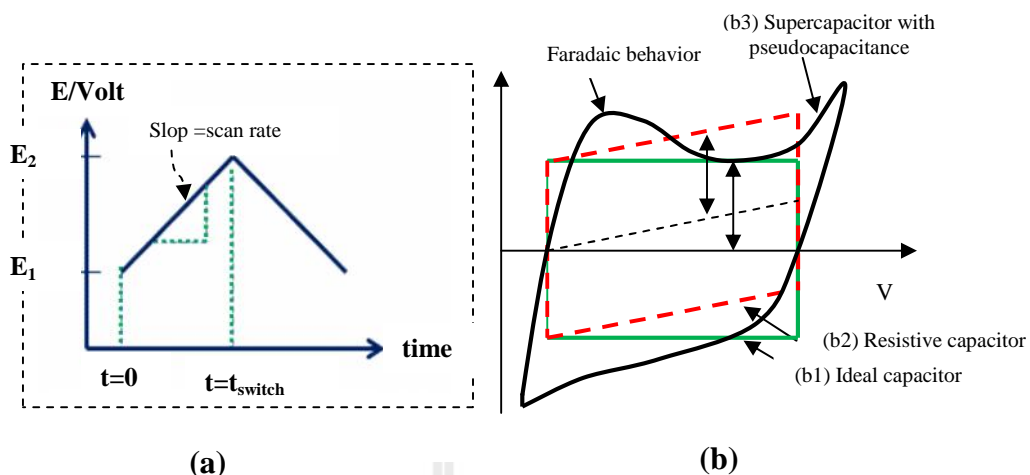


Figure 3.7 (a) The potential waveform applied to the working electrode in the cycle voltammetry experiment (b) Cyclic voltammogram of three different electrochemical capacitors: ideal, resistive, faradaic capacitors (Adapted from <http://en.wikipedia.org/wiki/Pseudocapacitance>).

There are three types of the electron transfer process including reversible, irreversible and quasi-reversible. In a reversible system, the electron transfers with rapidly rate in both forward and reverse scan. The magnitude of cathodic and anodic current is equal for all scan rates ($I_{p,c} / I_{p,a} = 1$) and proportional to the concentrations of the active species. The peak current at room temperature is given by the Randles-Sevcik quation

$$i_p = 2.69 \times 10^5 n^{3/2} A C D^{1/2} \nu^{1/2}, \quad (3.10)$$

where n, A, C, D and ν are the number of electron transferred/molecule, the electrode surface area (cm^2), the concentration (mol/cm^3), the diffusion coefficient (cm^2/s), and the potential scan rate (V/s), respectively. The anodic and cathodic peak potentials ($E_{p,a}, E_{p,c}$) are independent of the scan rate. The separation between them at all scan rates is given by

$$\Delta E_p = E_{p,a} - E_{p,c} = \frac{0.059}{n} V \quad (3.11)$$

In an irreversible process, the rate transfer of electron in the reverse scan is very slow.

The peak current and the peak potential, respectively are given by

$$i_p = 2.99 \times 10^5 n (\Gamma n_a)^{1/2} A C D^{1/2} \epsilon^{1/2} \quad (3.12)$$

$$E_p = E^0 - \frac{RT}{\Gamma n_a F} \left[0.78 - \ln \frac{k^0}{D^{1/2}} + \ln \left(\frac{\Gamma n_a F \epsilon}{RT} \right)^{1/2} \right], \quad (3.13)$$

where Γ and n_a are the transfer coefficient and the number of electrons involved in the charge transfer step, respectively. In irreversible process, the cathodic and anodic peak potentials are dependent of the scan rate.

In a quasi-reversible process, the current is controlled by the charge transfer and mass transport. The shape of the CV is a function of $k^0 / \sqrt{f a D}$, where $a = n F \epsilon / RT$. As $k^0 / \sqrt{f a D}$ increases, the process approaches the reversible case. For small values of $k^0 / \sqrt{f a D}$ (i.e. very fast ϵ), the system exhibits an irreversible behavior. The voltammograms of a quasi-reversible system exhibit a larger separation in peak potentials compared to a reversible system. One parameter related to the occurring of redox reaction of cell is called the standard potential. This parameter provides the information about direction of electron transfer in electrolyte solution.

According to the cyclic voltammogram, the capacitance for the variation of voltage with time is given by

$$\frac{dQ}{dt} = C \frac{dV}{dt} \quad (3.14)$$

$$C = \frac{i}{\epsilon}, \quad (3.15)$$

Where dQ/dt is the current (i) and dV/dt is the scan rate (ϵ). In the experimental, the average specific capacitance at different scan rates is defined as

$$C(F/g) = \frac{\int IdV}{m\epsilon\Delta U}, \quad (3.16)$$

where term $\int IdV$ refers to the area surround the CV curve, m is the weight of the active material within the electrode, ϵ is the scan rate and ΔU is the voltage window. According to the above equation, the specific capacitance of materials decreases with increasing of scan rate due to short time at high scan rate caused large internal resistance and hardly penetrated of electrolyte ions into inner pores during charge (Wang *et al.*, 2006; Yuan *et al.*, 2008).

In this work, the CV measurements were performed at room temperature over the scan rates of 2, 5, 10, 30, 50, 100, 150, and 200 mV/s in 1M KOH and at the scan rates of 10, 50, 75, 100, 150, and 200 mV/s in 0.5M Na₂SO₄. The potential window was set at various range of value to avoid the decomposition of aqueous electrolyte. For C/CuFe₂O₄ system, the potential windows of -0.3 to 2 V and -0.2 to 0.35 V were set for 0.5M Na₂SO₄ and 1M KOH, respectively. For C/CoFe₂O₄ and C/NiFe₂O₄ systems tested in 1M KOH, the potential windows of -0.2 to 0.35 and -0.3 to 0.4 V, respectively were set.

3.2.9.2 Galvanostatic charge/discharge

Galvanostatic charge discharge (GCD) technique is an electrochemical analysis to determine the kinetics and mechanism of electrode reactions. The basic principle is placing a constant current upon an electrode and measuring the variation of the resulting current through the solution. Normally, this technique is usually used

to investigate the charging and the discharging process of electrochemical capacitors (Conway, 1991; Conway *et al.*, 1997). The discharge capacitance (C) is estimated from the current (I) and slope ($\Delta V / \Delta t$) of the linear portion of the discharge curve via the expression.

$$C = \frac{I}{\Delta V / \Delta t} \quad (3.17)$$

The specific capacitance with mass m is thus given by

$$C_s = \frac{I \Delta t}{m \Delta V} \quad (3.18)$$

The coulomb efficiency ($\eta\%$) was observed by using the equation

$$\eta\% = \frac{t_d}{t_c} \times 100 \quad (3.19)$$

Where t_d and t_c are the total amount of discharge and charging times, respectively.

In this work, the GCD measurements for all the prepared electrodes were performed in 1 M KOH. The charge and discharge between the selected potential windows were measured with different current density of 0.1, 0.25, 0.5, 0.75, and 1 A/g, respectively.

3.2.9.3 Electrochemical impedance spectroscopy

Electrochemical impedance spectroscopy (EIS) is an impedance spectroscopy method that used a frequency response to evaluate the electrochemical behavior (kinetics, resistive, capacitive, etc.) of cell electrode. A brief concept is applying a sinusoidal potential of small amplitude to the cell electrodes and recorded the resulting current response. The apply sinusoidal potential and the responding current are given as

$$V(t) = V_0 \cos(\check{S}t) \text{ or } V(t) = V_0 \sin(\check{S}t) \quad (3.20)$$

$$I(t) = I_0 \cos(\check{S}t - w) \quad I = I_0 \sin(\check{S}t + w) \quad (3.21)$$

Where V_0 and I_0 are the signal and current amplitude, respectively. $\check{S} = 2\pi f$ is the angular frequency, and w is phase shift between current response and the potential.

According to Ohm's law, the complex impedance is then defined as

$$Z = \frac{V(t)}{I(t)} = |Z| \frac{\cos(\check{S}t)}{\cos(\check{S}t - w)} = |Z| e^{jw} = |Z| (\cos w - j \sin w) = Z' - jZ'' \quad (3.22)$$

$$Z = \frac{V(t)}{I(t)} = |Z| \frac{\sin(\check{S}t)}{\sin(\check{S}t + w)} = |Z| e^{jw} = |Z| (\cos w + j \sin w) = Z' + jZ'', \quad (3.23)$$

where Z' and Z'' are the real and imaginary parts of the complex impedance, respectively. The phase angle (w) and the modulus ($|Z|$) are as following equation

$$w = \tan^{-1} \left(\frac{Z''}{Z'} \right) \quad (3.24)$$

$$|Z| = \sqrt{(Z')^2 + (Z'')^2} \quad (3.25)$$

At $w = 0$, the impedance is real $Z(\check{S}) = Z'(\check{S})$ (purely resistive behavior). The capacitance in term of real (C') and imaginary (C'') part are as the following equation

$$C = \frac{1}{j\check{S}Z} = \frac{Z''}{\check{S}|Z|^2} - j \left(\frac{Z'}{\check{S}|Z|^2} \right) = C' - jC'' \quad (3.26)$$

The real part is the effective capacitance that the devices can delivery, while the imaginary part related to the irreversible resistivity loss in the device. According to the equation, the impedance decrease with increasing of capacitance and frequency. For electrochemical capacitor, high frequency and smaller time constant is a characteristic of high power density.

The EIS data was reported in two types plot: Nyquist and Bode plot. The Nyquist plot is the plot of the opposite imaginary part impedance ($-Z''$) versus the real part impedance (Z'), while the Bode plots is the logarithm plot of the impedance (Z) or phase angle (ϕ) versus the logarithm of the frequency. In the Nyquist plot, the intercept of curve at the real part axis (Z') is the equivalent series resistance (ESR) of the cell. The semicircle diameter at high frequency region corresponds to charge transfer resistance (R_{ct}) in which caused by faradic reaction. The slope of the linear curve at low frequency is called the Warburg resistance (W) and was used to describe the frequency dependent of ion diffusion into the bulk of the electrode surface. For not ideal cell or cell with lack of surface homogeneity, the constant phase element (CPE or Q) is used (Liu *et al.*, 2012; Sahoo *et al.*, 2011; Ren *et al.*, 2013). The parameter “ n ” obtained from CPE is used to observed the quality of the electrode material ($n=1, 0$ and $0.5 < n < 1$) indicates the ideal capacitors, the insulators, and the moderate capacitor behavior, respectively. To observe these parameters, the fitting EIS data with the equivalent circuit will be performed. The circuit elements used in the equivalent models are listed in Table 3.4.

Figures 3.8 (a) and 3.8 (b) show the example Nyquist plot with its equivalent Randles circuit for an electrochemical reaction under kinetic control (charge transfer) and an electrochemical system when both kinetics and diffusion are important, respectively. The Nyquist plot in Figure 3.8 (a) contains a semicircle at high frequency and the corresponding faradaic impedance can be written as

$$Z(\check{S}) = R_s + \underbrace{\left[\frac{R_{ct}}{1 + R_{ct}^2 C_{dl}^2 \check{S}^2} \right]}_{Z'(\check{S})} - j \underbrace{\left[\frac{R_{ct}^2 C_{dl} \check{S}}{1 + R_{ct}^2 C_{dl}^2 \check{S}^2} \right]}_{Z''(\check{S})} \quad (3.27)$$

This equation fit with the equation of a semicircle according to

$$\left[Z'(\check{S}) - \left(R_s + \frac{R_{ct}}{2} \right) \right]^2 + Z''(\check{S})^2 = \frac{R_{ct}^2}{4} \quad (3.28)$$

The frequency where the imaginary part of the impedance is maximum allow the determination of C_{dl} according to $\check{S}_{max} R_{ct} C_{dl} = 1$ where $\check{S}_{max} = 2\pi f_{max}$ and f_{max} being the frequency at the top of the semicircle. The Nyquist plot in Figure 3.8 (b) contains a semicircle at high frequency and a Warburg line at low frequency. The corresponding impedance is divided in to finite (Z_F) and infinite (Z_{IF}) diffusion layer as the following equation, respectively.

$$Z_F(\check{S}) = R_{ct} \left[1 + \frac{\check{\}}{(j\check{S})^{1/2}} \right] ; \check{\} = K_f / D_{ox}^{1/2} + K_b / D_{red}^{1/2} \quad (3.29)$$

$$Z_{IF}(\check{S}) = \left[R_s + R_{ct} \left(1 + \frac{1}{(2\check{S})^{1/2}} \right) - R_{ct}^2 \check{\}^2 C \right] - j \left(\frac{R_{ct} \check{\}}{(2\check{S})^{1/2}} \right) \quad (3.30)$$

Where $Z_F = R_{ct} \check{\} / (j\check{S})^{1/2}$ is called the Warburg impedance. K_b and K_f are the reaction kinetics rates of the electrochemical reactions. D_{red} and D_{ox} are the diffusion coefficients of the reduced and oxidized species, respectively (Conway, 1999).

In this work, the EIS measurements were performed after cyclic voltammetry test in order to study their resistive behavior. The measurements were carried out in the frequency range of 0.1 Hz to 10^5 Hz which is typically used for most electrochemical systems.

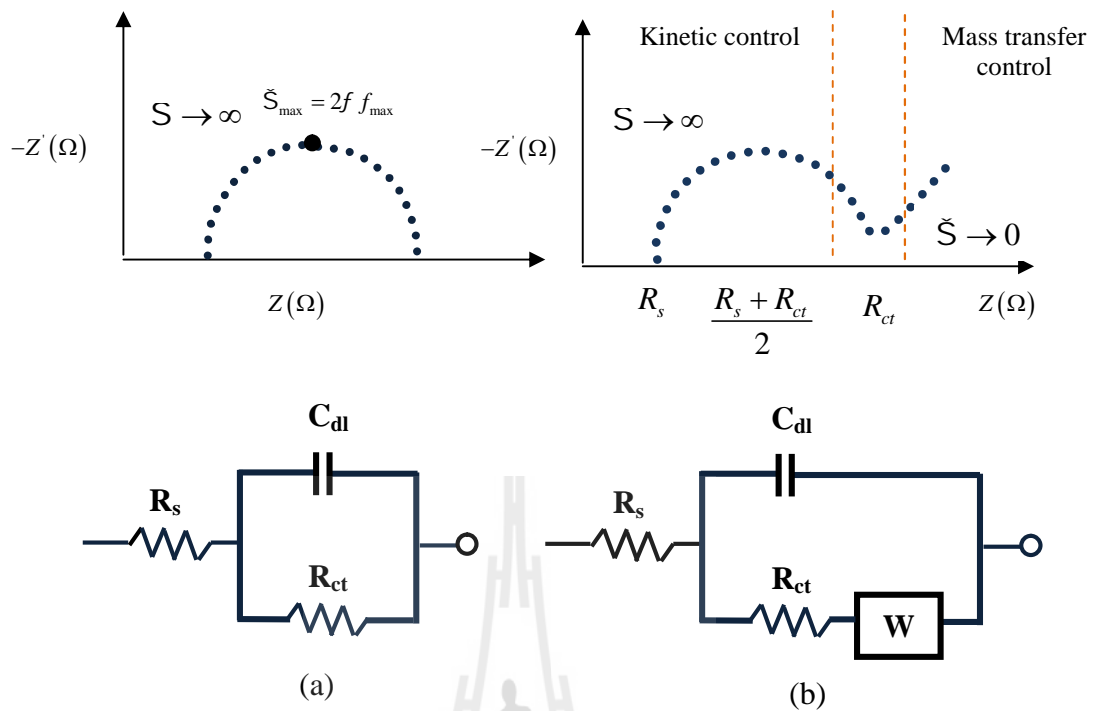


Figure 3.8 The Nyquist plot with its equivalent Randle circuit for (a) an electrochemical reaction under kinetic control (b) an electrochemical system under kinetics and diffusion (Adapted from <http://www.metrohm.co.th/Applications>).

Table 3.4 Circuit elements used in the equivalent models (Adapted from <http://www.metrohm.co.th/Applications>).

Equivalent element	Equivalent element	admittance	impedance	The parameter used
Resistor	R	$1/R$	R	R_p, R_Ω
Capacitor	C	$j\check{S}C$	$1/j\check{S}C$	C_{dl}, C_c
Inductor	L	$1/j\check{S}L$	$j\check{S}L$	
Warburg impedance	W	$Y_o\sqrt{j\check{S}}$	$1/Y_o\sqrt{j\check{S}}$	
Constant phase element	Q (CPE)	$Y_o(j\check{S})^n$	$1/Y_o(j\check{S})^n$	

R_p : Polarization resistance, R_Ω Ohmic resistance, C_{dl} : Double layer capacitance, C_c : Coating capacitance

CHAPTER IV

RESULTS AND DISCUSSION

Chapter IV deals with the results and their discussion. It is divided into three sections related to three different groups of prepared samples: C/CuFe₂O₄, C/CoFe₂O₄, and C/NiFe₂O₄, respectively. For each group of study, the thermogravimetric analysis (TGA) was used to observe weight loss as a function of temperature. The crystal structure was identified using X-ray diffraction (XRD), the structure fingerprints of carbon were determined by using Raman spectroscopy, and the electronic structure of spinel ferrite in the CNF matrix was evaluated by X-ray absorption spectroscopy (XAS). The specific surface area was evaluated by the Brunauer-Emmett-Teller (BET). The morphologies were investigated using high-resolution scanning electron microscopy (FE-SEM) and transmission electron microscopy (TEM). The magnetic measurements were carried out using a vibrating sample magnetometer (VSM). The effect of the magnetic source content on the magnetic properties is certainly interpreted. The electrochemical behaviors were studied via cyclic voltammetry (CV), galvanostatic charge/discharge (GCD) and electrochemical impedance spectroscopy (EIS) techniques, respectively. The influence of the magnetic concentration on the structure, morphology and magnetic structure is briefly discussed. The effect of different electrode materials (CNF, C/MFe₂O₄ and MFe₂O₄) on the electrochemical behavior is also described.

4.1 C/CuFe₂O₄ composite nanofibers

4.1.1 Structural and morphology characterization

4.1.1.1 Thermo gravimetric analysis (TGA) of the electrospun-based C/CuFe₂O₄ composite nanofibers.

Figure 4.1 shows TGA curves of the electrospun CNF and C/CuFe₂O₄ composite nanofibers with different magnetic source content. The measurements were performed by using a heating rate of 10 °C/min in the temperature range of 25 to 1200 °C under air and N₂ atmosphere. For the PAN fiber-based CNF and C/CuFe₂O₄_0.2, the TGA curves show three main steps of weight loss in the range of ~20-295, ~295-470 and ~620-1200 °C, respectively. For C/CuFe₂O₄_0.4 and C/CuFe₂O₄_0.6, the plateau was observed after 970 and 1000 °C, respectively. The results indicate that, the carbon nearly burn out for the sample with less amount of polymer sources. According to the spectra, PAN based CNF started to decompose at ~295 °C, while the starting weight loss at lower temperature was observed for the composite fibers. At stabilization temperature, the samples with higher magnetic source content exhibited higher weight loss (~7, ~16 and ~48% for C/CuFe₂O₄_0.2, C/CuFe₂O₄_0.4, and C/CuFe₂O₄_0.6, respectively). The weight loss at this temperature corresponds to the loss of chemically absorbed water molecular and all trapped solvents. The major weight loss at ~295 - 470 °C relate to the decomposition of metal nitrates along with the degradation of PAN polymer chain by dehydration. The common short plateau was observed between 471 and 620 °C, suggesting that at this region the crystalline CuFe₂O₄ could form as the decomposition of metal product (Maensiri and Nuansing, 2006). No plateau formed further up to 1200 °C was observed for C/CuFe₂O₄_0.2 and

C/CuFe₂O₄_0.4, indicating that the sample with large polymer source content was not almost burned away under inert gas atmosphere.

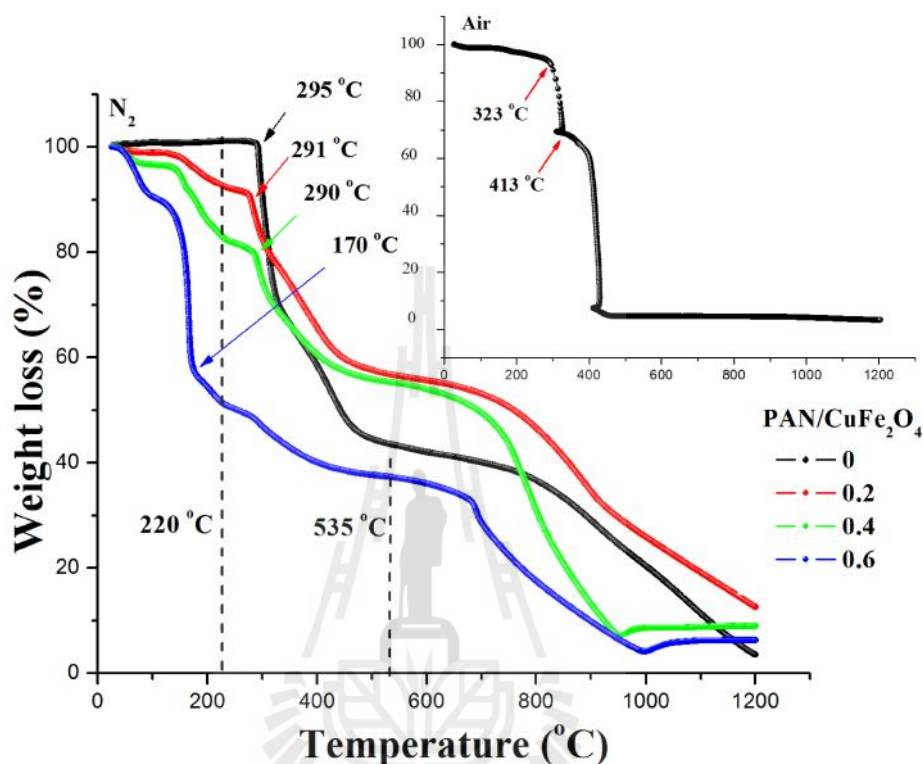


Figure 4.1 TGA curves of CNF and C/CuFe₂O₄ composite nanofibers under N₂ atmosphere and air atmosphere (in set).

4.1.1.2 X-ray diffraction (XRD) analysis of C/CuFe₂O₄ composite nanofibers.

Figure 4.2 shows XRD patterns of pure CNF and C/CuFe₂O₄ composite nanofibers with different magnetic source concentration after stabilized at 220 °C for 2 h in air atmosphere followed by carbonized at 535 °C for 1 h in argon atmosphere. The diffraction peaks at $2\theta = 18.4^\circ, 30.2^\circ, 35.6^\circ, 37.2^\circ, 43.2^\circ, 53.6^\circ, 57.2^\circ, 63.1^\circ$ and 75.1° match well with crystallite planes of (111), (220), (311), (222), (400),

(422), (511), (440), and (622), respectively for the cubic CuFe_2O_4 (JCPDS card no. 77-0010). The result implies that metallic Cu and Fe nitrate have been completely oxidized in the oxygen ambient, leading to the formation of CuFe_2O_4 . The diffraction peaks at around $2\theta = 26.0^\circ$ and 44.0° indicate the formation of graphite structure (Yang *et al.*, 2012) and can be indexed to (002) and (101) planes, respectively for the PDF card no. 75-1621. No other characteristic peaks were detected. The average crystallite size (D) of CuFe_2O_4 was calculated by using Scherrer's equation (Klug and Alexander, 1974) and the obtained values were 24.58, 36.29 and 45.73 nm for C/ $\text{CuFe}_2\text{O}_4_{0.2}$, C/ $\text{CuFe}_2\text{O}_4_{0.4}$ and C/ $\text{CuFe}_2\text{O}_4_{0.6}$, respectively. It is evident from the results that, the crystallite size increases with increasing of the magnetic source content possibly due to the effect of the particle agglomeration. The lowest crystallite size value of 24.6 nm for C/ $\text{CuFe}_2\text{O}_4_{0.2}$ implies less agglomeration. It could be speculated that, large amount of polymer source well supported the distribution of CuFe_2O_4 nanoparticle in CNF matrix. The average crystallite size of CNF was also calculated and the obtained value was 17.07 nm. The d-spacing value was calculated from peak (311) by using Bragg's law (Bragg, 1913). The obtained values of 2.498, 2.498 and 2.495 Å were obtained for C/ $\text{CuFe}_2\text{O}_4_{0.2}$, C/ $\text{CuFe}_2\text{O}_4_{0.4}$, and C/ $\text{CuFe}_2\text{O}_4_{0.6}$, respectively. The values are slightly lower than 2.524 Å of a cubic CuFe_2O_4 (JCPDS 77-0010) which is possibly resulted from the effect of CNF matrix. The obtained lattice constants of 8.526, 8.366 and 8.346 Å for C/ $\text{CuFe}_2\text{O}_4_{0.2}$, C/ $\text{CuFe}_2\text{O}_4_{0.4}$, and C/ $\text{CuFe}_2\text{O}_4_{0.6}$, respectively are close to that of bulk CuFe_2O_4 (8.37 Å⁰). For a C/ $\text{CuFe}_2\text{O}_4_{0.6}$, the crystallite size, the interplanar distance and the lattice parameter are very close to those previously reported for CuFe_2O_4 (Tangcharoen *et al.*, 2014).

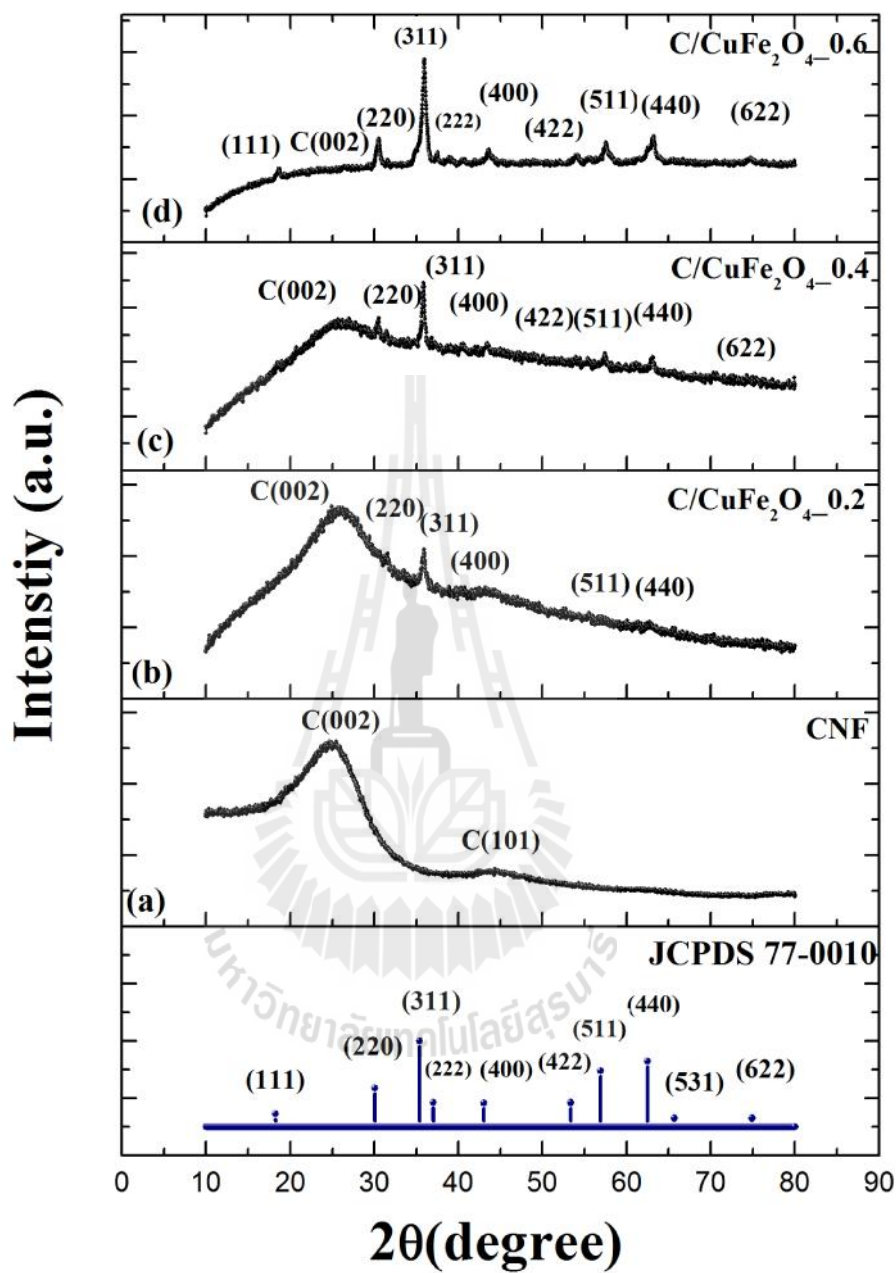


Figure 4.2 XRD patterns of (a) CNF, (b) C/CuFe₂O₄_0.2, (c) C/CuFe₂O₄_0.4 and (d) C/CuFe₂O₄_0.6 composite nanofibers.

4.1.1.3 Morphology of C/CuFe₂O₄ composite nanofibers by FE-SEM and TEM.

Figure 4.3 shows SEM and FE-SEM images of pure CNF, C/CuFe₂O₄_0.2, C/CuFe₂O₄_0.4, and C/CuFe₂O₄_0.6 composite nanofibers before and after carbonization at 535 °C for 1 h. The morphology of sample before heat treatment exhibited beige color, long straight, uniform in cross-section with the fibers diameters of 750-900 nm. The appearance of black color of fibers after carbonization is due to the formation of ladder ring structure (Friedlander *et al.*, 1968; Burlant and Parsons, 1956). The uniform fibers, long straight and minimum surface roughness with diameters range of 500-600 nm were obtained for CNF and C/CuFe₂O₄_0.2 (Figures. 4.3 (a), (b)), while the particle chain characteristic with diameters rang of 450-550 nm was observed for C/CuFe₂O₄_0.4 (Figure 4.3 (c)). The filmy fibers with porosity and worse uniformity were observed for C/CuFe₂O₄_0.6 (Figure 4.3 (d)).

Figure 4.4 shows TEM images with corresponding selected area electron diffraction pattern (SAED) of pure CNF and all C/CuFe₂O₄ composite nanofibers. TEM bright field images for the composite nanofibers show clearly the CuFe₂O₄ nanoparticles with the particle size of 5-50 nm embedded within the CNF matrix (Figures 4.4 (b), (c), and (d)). The corresponding SAED patterns of C/CuFe₂O₄ composite nanofibers show clearly diffraction spots of high crystallinity CuFe₂O₄, while arcs and diffuse rings represent to hexagonal graphite structure (002) (Figures 4.4 (b), (c), and (d)). Moreover, the corresponding SAED patterns of C/CuFe₂O₄ composite nanofibers match well to the crystal plane observed in the XRD patterns. No any spotty ring was observed in SAED pattern of CNF (Figure 4.4 (a)) suggesting a large amorphous characteristic of carbon.

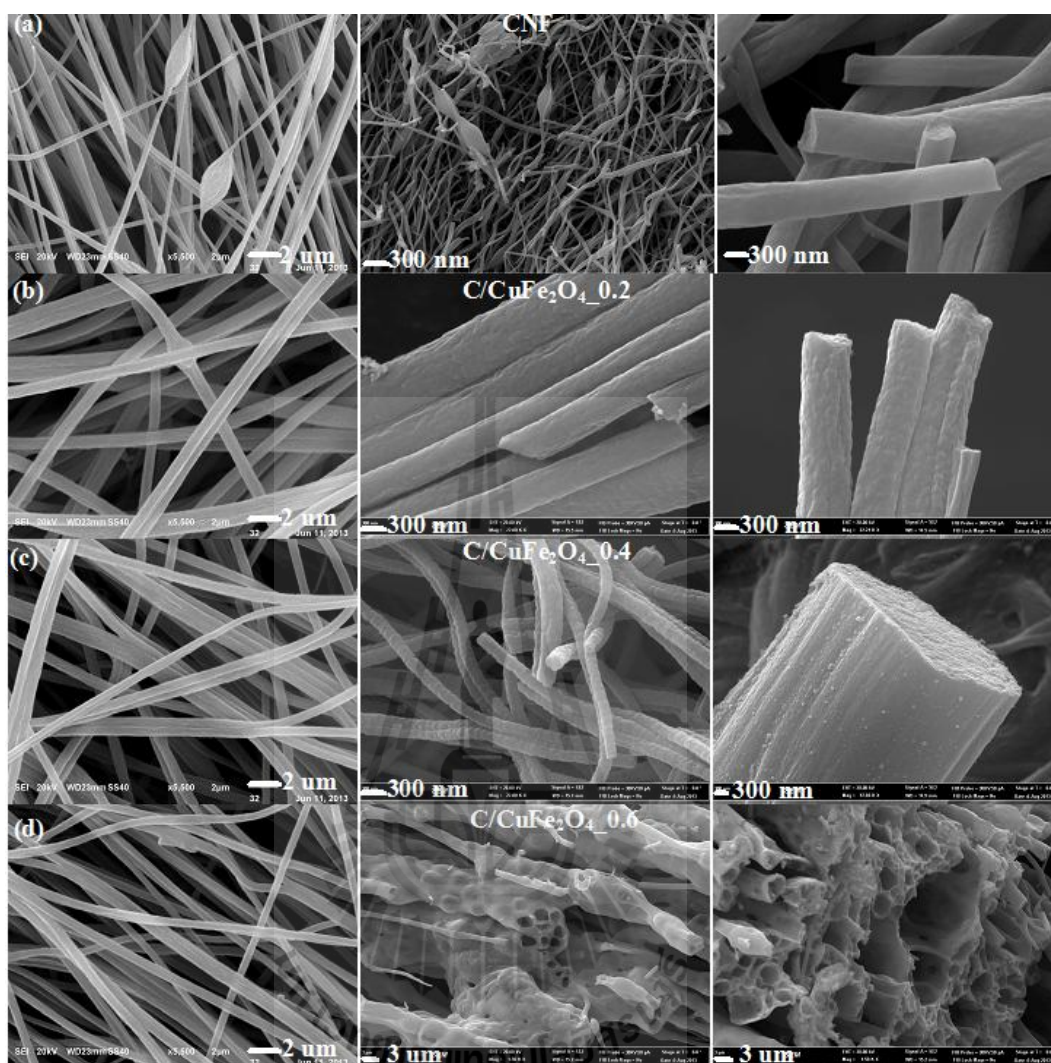


Figure 4.3 SEM micrographs of the electrospun $C/CuFe_2O_4$ composite nanofibers before carbonization (left), the fibers after carbonization (middle) and their FE-SEM images (right), respectively of (a) pure CNF, (b) $C/CuFe_2O_4_{0.2}$ (c), $C/CuFe_2O_4_{0.4}$, and (d) $C/CuFe_2O_4_{0.6}$ composite nanofibers.

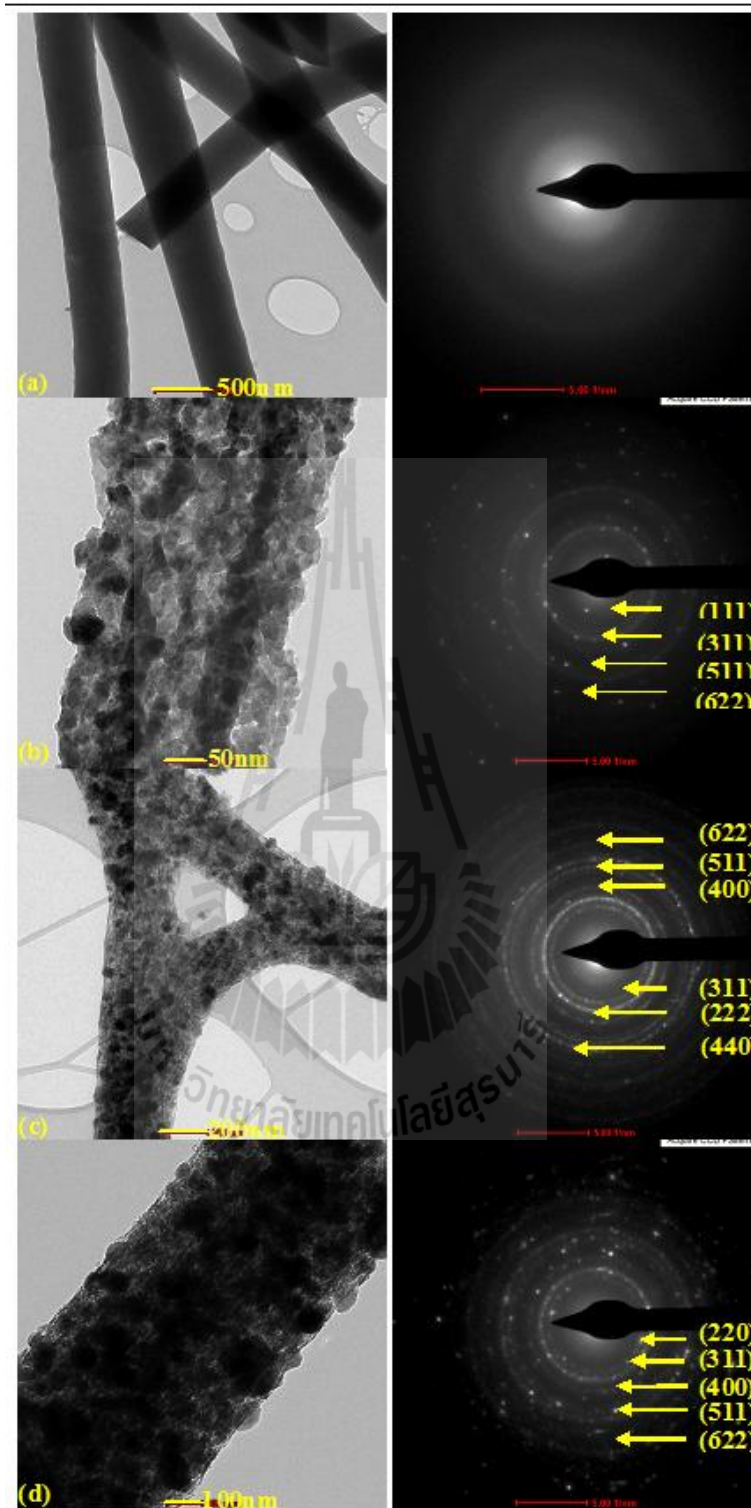


Figure 4.4 TEM bright field images (left) with the corresponding SAED pattern (right) of (a) pure CNF, (b) C/CuFe₂O₄_0.2, (c) C/CuFe₂O₄_0.4, and (d) C/CuFe₂O₄_0.6 composite nanofibers.

4.1.1.4 The structure fingerprints of C/CuFe₂O₄ composite nanofibers characterization by Raman spectroscopy.

Figure 4.5 shows Raman spectra of CNF and C/CuFe₂O₄ composite nanofibers with different metal source concentration. For all the prepared samples, two peaks centered at ~1580 (G band) and ~2700 cm⁻¹ (2D band) represent a characteristic of crystalline graphite (Vidano *et al.*, 1981). The G band is primary mode of graphite (E_{2g}) and attributed to the bond stretching of sp² atoms in both rings and chains (Ferrari and Robertson, 2000), while the G band is the result of two phonons lattice vibration process (Thomsen and Reich, 2000). Normally, a strong sharp peak of G band is subjected to graphene (Johannes *et al.*, 2011; Saito *et al.*, 2009), while a broad peak with the splitting is a result of interactions between the stacked graphene layer and corresponds to bulk graphite (Nemanich and Solin, 1979). An addition band at ~1340 cm⁻¹ is called D band, in which is attributed to breathing mode with A_{1g} symmetry (Tuinstra and Koenig, 1970). The generation of this peak implies the prepared samples represent a characteristic of graphite structure with disorder (or defect) (Nemanich and Solin, 1979), possibly due to extensive oxidation (Tuinstra and Koenig, 1970). To characterize the graphitization or defect quantities, the intensity ratio of the D and G band (I_D/I_G) was evaluated by using the Lorentzian fitting. The values of 1.69, 1.61 and 1.71 were obtained for C/CuFe₂O₄_0.2, C/CuFe₂O₄_0.4 and C/CuFe₂O₄_0.6, respectively. All the I_D/I_G values are slightly higher than 1.6 for pure CNF. The result implies that there is more disordered carbon structure of the composite nanofiber, possibly due to the intercalation of CuFe₂O₄ nanoparticle in to the graphite layers (Janes *et al.*, 2007). However, all the prepared samples show lower I_D/I_G value than those values observed in the disordered

structures ($I_D/I_G > 4$) (Ji and Zhang, 2009; Zou *et al.*, 2006). The in plane graphitic crystallite size (L_a) was also calculated from the data fitting using the equation: L_a (nm) = $C(\lambda)/(I_D/I_G)$, where $C(532 \text{ nm})$ is constant and is ~ 4 (Knight and White, 1989). The obtained value does not show any significant trend with the magnetic source content as listed in Table 4.1.

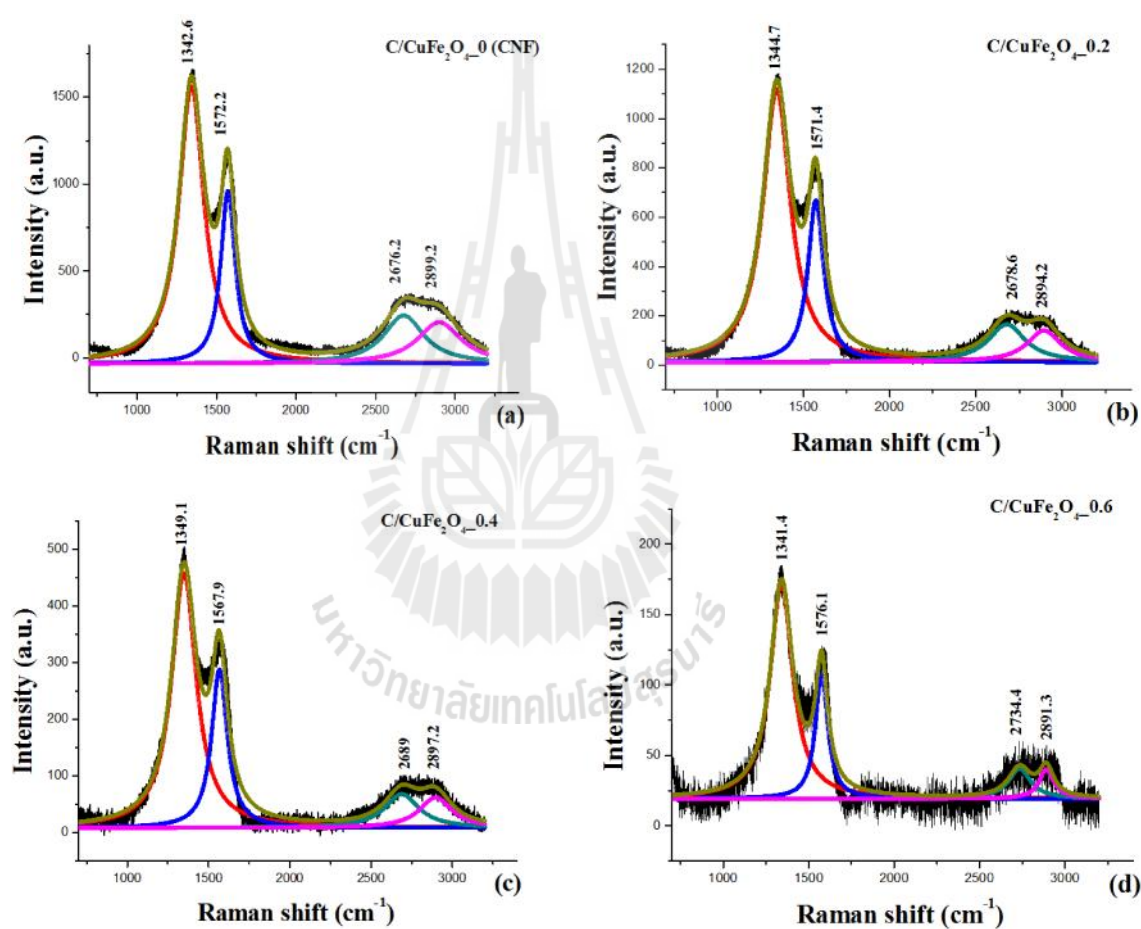


Figure 4.5 Raman spectra of (a) pure CNF, (b) C/CuFe₂O₄_0.2, (c) C/CuFe₂O₄_0.4, and (d) C/CuFe₂O₄_0.6 composite nanofiber.

Table 4.1 Lists of Raman peak height, Raman peak width, R value (I_D/I_G) and in plane graphite crystallite size (L_a) of CNF and C/CuFe₂O₄ composite nanofibers with different magnetic source concentration.

Sample	Peak height (cm ⁻¹)				Peak width (cm ⁻¹)				R	L_a (nm)
	D	G	2D ₁	2D ₂	D	G	2D ₁	2D ₂		
CNF	1981	1236.3	329.8	313.4	183.5	108.2	242.7	298.4	1.60	2.75
C/CuFe ₂ O ₄ 0.2	1386	820.4	191.4	160.3	192.4	111.7	259.3	236.9	1.69	2.61
C/CuFe ₂ O ₄ 0.4	563	350.0	74.7	67.4	183.4	117.3	256.6	241.0	1.61	2.73
C/CuFe ₂ O ₄ 0.6	192	112.2	26.7	26.0	158.2	87.2	157.9	105.2	1.71	2.57

4.1.1.5 Characterization of surface area of C/CuFe₂O₄ composite nanofiber by the Brunauer-Emmett-Teller method.

Figure 4.6 shows the N₂ adsorption/desorption isotherms of CNF and C/CuFe₂O₄ composite nanofibers with different magnetic source content. As known that, when N₂ gas comes into contact with material surface, the molecule gas will adsorb to the surface. The plot of amount of gas adsorbed/desorption over of partial pressures at constant temperature is called adsorption/desorption isotherm. It was found from the studied that, the isotherms of CNF, C/CuFe₂O₄_0.2 and C/CuFe₂O₄_0.4 belong to type I pattern according to the IUPAC classification. The results indicate that these three samples have microporous structure. For the pure CNF, a small adsorption quantity was observed at high relative pressure ($P/P_0 > 0.9$) suggesting the presence of small mesopores and macropores (Nan *et al.*, 2014). The C/CuFe₂O₄_0.6 composite nanofiber exhibited type IV with H3 hysteresis behavior at

high partial pressure. This is the typical isotherm of mesoporous carbon. The isotherms take place at very low relative pressure ($P/P_0 < 0.01$) and then jump between partial pressures of 0.45–0.99 (Wang *et al.*, 2012). The average pore diameters of 23.2, 4.0, 7.0 and 8.7 nm were obtained for CNF, C/CuFe₂O₄_0.2, C/CuFe₂O₄_0.4 and C/CuFe₂O₄_0.6, respectively. An increase of mean pore size with increasing of magnetic source content may be due to the difference in shrinkage between the metal and PAN polymer during the burn-off step (Guo *et al.*, 2009). All the mean pore size values of the composite nanofibers are significant low compared to pure CNF possibly due to the insertion of nanoparticles into the porosity. In the electrochemical studies, high mean pore size is considered as promising high power energy sources due to favor for charge accumulation in aqueous electrolytes (Raymundo-Pinero *et al.*, 2006). According to Brunauer–Emmett–Teller (BET) analysis, the specific surface areas of CNF, C/CuFe₂O₄_0.2, C/CuFe₂O₄_0.4 and C/CuFe₂O₄_0.6 were obtained to be 30, 190, 68 and 93 m²/g, respectively. The value does not show any significant trend. For the composite nanofibers, the lower value in surface area of C/CuFe₂O₄_0.4 and C/CuFe₂O₄_0.6 than C/CuFe₂O₄_0.2 is possibly due to larger crystallite size from the nanoparticle aggregation. The C/CuFe₂O₄_0.2 sample with largest CNF matrix can effectively reduce the aggregation of CuFe₂O₄ nanoparticles leading to higher specific surface area. The specific surface areas of all C/CuFe₂O₄ are very high compared to of CNF suggesting the formation of rough surface after the introduction of CuFe₂O₄. Thus, it is indicated that the uniform distribution of nanoparticles on the CNF matrix strongly depend on the polymer/magnetic ratio. In the electrochemical measurements, low surface area of CNF normally leads to long ions diffusion lengths and decreases active sites for ion

insertion/extraction reactions (Shi *et al.*, 2009). The BET specific surface area, mean pore diameter, and total pores volume of CNF the C/CuFe₂O₄ composite nanofibers are listed in Table 4.2.

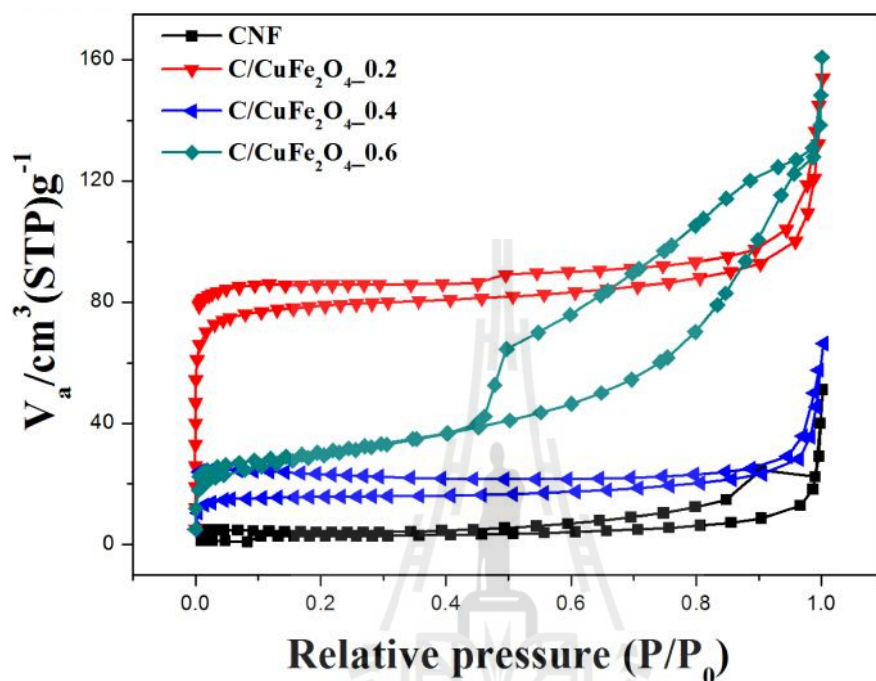


Figure 4.6 N₂ adsorption/desorption isotherms of (a) pure CNF, (b) C/CuFe₂O₄_0.2, (c) C/CuFe₂O₄_0.4, and (d) C/CuFe₂O₄_0.6 composite nanofibers.

Table 4.2 Summary of mean pore diameter, surface area and total pore volume of CNF and C/CuFe₂O₄ composite nanofibers with different metal source concentration.

Samples	Mean pore diameter (nm)	Surface area (m ² /g)	Total pore volume (cm ³ /g)
CNF	23.22	30.07	0.018
C/CuFe ₂ O ₄ _0.2	4.01	190.38	0.191
C/CuFe ₂ O ₄ _0.4	7.03	68.11	0.067
C/CuFe ₂ O ₄ _0.6	8.67	93.25	0.202

4.1.1.6 X-ray absorption spectroscopy study of the Fe and Cu K-edge in C/CuFe₂O₄ composite nanofibers.

Figure 4.7 shows the normalized XANES spectra and their corresponding first derivatives at Fe and Cu K-edge for C/CuFe₂O₄ composite nanofibers. The results were shown along with the standard samples of FeO, Fe₂O₃, Fe₃O₄, Cu foil, CuCl and CuO for Fe²⁺, Fe³⁺, Fe^{2+,3+}, Cu⁰⁺, Cu¹⁺ and Cu²⁺, respectively. The XANES spectra at Fe K-edge for all the prepared samples are very similar to that of Fe₂O₃ indicating Fe ion is in the +3 oxidation state (Saito *et al.*, 1999; Sakurai *et al.*, 2008). At Cu K-edge, the XANES spectra for all prepared samples are similar to CuO indicate to +2 oxidation state of Cu ions. These results at both edges were confirmed by the edge energies (Table 4.3) and their first derivative plots (Figures 4.7 (c), (f)). It was found at Fe K-edge that, the pre-edge peak was observed for all the prepared samples (Figure 4.7 (b)). This peak arises from the electric transition 1s to 3d quadrupole and relates to the quantity cation in tetrahedral site (Gomes *et al.*, 2011). At Cu K-edge, all the samples show weak and broadening pre-edge peak (Figure 4.7 (e)) indicating sparse of Cu cations are in octahedral sites. The pre-edge peak intensity of C/CuFe₂O₄_0.2 is close to that of C/CuFe₂O₄_0.6 and both values are higher than that of C/CuFe₂O₄_0.4 suggesting higher cations in tetrahedral site. The results are consistent with the EXAFs observation (Table 4.4-4.6). It has been also reported in the literature that, the intensity of pre-edge peak is proportional to the distortion of local structure around the absorbing metal ion from inversion symmetry (Park *et al.*, 2001). That is, if the lattice distortion increases, the intensity of pre-edge will be decreased (Croft *et al.*, 1997).

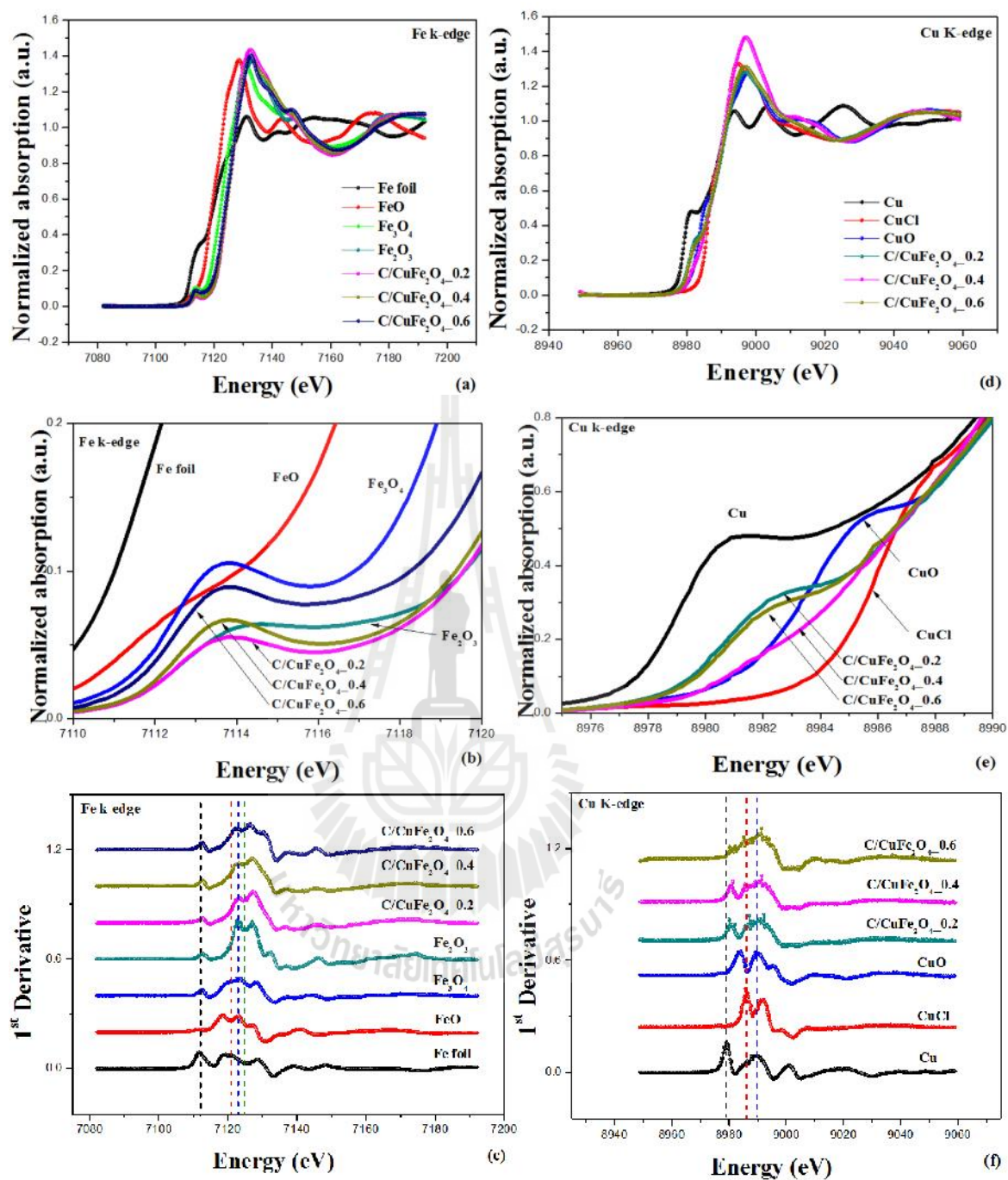


Figure 4.7 XANES spectra, pre-edge peak, and corresponding first derivatives plot, respectively of C/CuFe₂O₄ composite nanofibers at Fe K-edge (a, b, c) and at Cu K-edge (c, e, f).

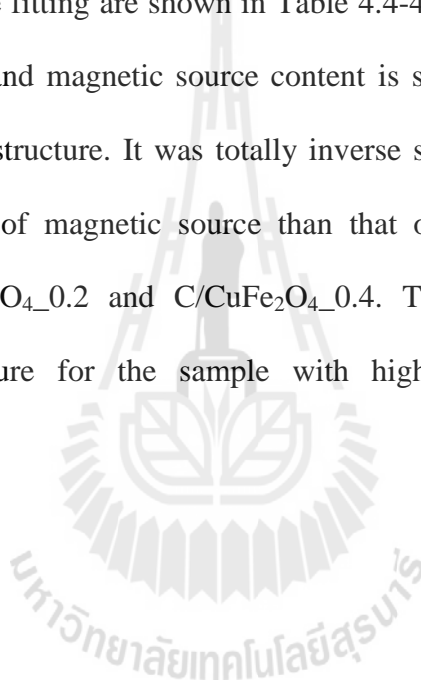
Table 4.3 Edge energies and oxidation state of all C/CuFe₂O₄ composite nanofibers along with the standard samples.

Sample/standard	Edge element	Oxidation state	Absorption edge (eV)
C/CuFe ₂ O ₄ _0.2	Fe	+3	7127.21
	Cu	+2	8990.41
C/CuFe ₂ O ₄ _0.4	Fe	+3	7127.21
	Cu	+2	8989.73
C/CuFe ₂ O ₄ _0.6	Fe	+3	7126.39
	Cu	+2	8990.7
Fe foil	Fe	0	7112
FeO	Fe	+2	7120.65
Fe ₃ O ₄	Fe	+2,+3	7123.40
Fe ₂ O ₃	Fe	+3	7124.85
Cu	Cu	0	8979
CuCl	Cu	+1	8986.22
CuO	Cu	+2,+3	8989.19

One of the most challenging in the study of spinel ferrite material is the distribution of cations over tetrahedral (A) and octahedral (B) site. The different distribution of cation over A and B site leads to different magnetic and electrical properties of materials (Liu *et al.*, 2000). Thus, determination of cation distribution between A and B site has been a subject of many studies (Wei *et al.*, 2001; Sakurai *et al.*, 2008; Carta *et al.*, 2009). In this section, EXAFS fitting was used to determine the cations distribution of CuFe₂O₄ in CNF matrix. Figure 4.8 shows the Fourier transform (FT) spectra in R space and EXAFS k² (k) weighted spectra in k space with the corresponding fitted spectra (dot line) at Fe and Cu k-edge for C/CuFe₂O₄

composite nanofibers. The Fourier transforming was performed in the range of 2.5-10 \AA^{-1} without phase shift corrections. It was found that, k^2 (k) values of C/CuFe₂O₄_0.2 and C/CuFe₂O₄_0.4 show significant difference from that of C/CuFe₂O₄_0.6 at both the Fe and Cu edge, indicating that their structural environment around Fe³⁺ and Cu²⁺ is different. According to the EXAFS fitting at Cu K-edge, the first shells at 1.905 \AA and 1.877 \AA for C/CuFe₂O₄_0.2 and C/CuFe₂O₄_0.4, respectively refer to B site cation which is surrounded by six nearest oxygen backscatterers (Cu_B-O). The second peak during 2.8-2.9 \AA for C/CuFe₂O₄_0.2 and 2.9-3.1 for C/CuFe₂O₄_0.4 with three backscatterers relates to the scattering of the second nearest neighbor cation located octahedral site (Cu_B-Fe_B and Cu_B-Cu_B) (Makovec *et al.*, 2011; Makovec *et al.*, 2009; Gomes *et al.*, 2006). The shift of peak position to lower R range of these two samples compared to C/CuFe₂O₄_0.6 relate to the different number of cations in each lattice site as confirmed by the data fitting (Table 4.4-4.6) and matched well to previous reported (Stewart *et al.*, 2007; Gomes *et al.*, 2006). At Fe edge, the first peak near 2 \AA is due to two Fe-O bond distances which are surrounded by four and six nearest oxygen backscatterers, respectively (Fe_A-O = 1.933 \AA and Fe_B-O = 2.099 \AA for C/CuFe₂O₄_0.2; Fe_A-O = 1.933 \AA and Fe_B-O = 2.118 \AA for C/CuFe₂O₄_0.4). For C/CuFe₂O₄_0.6, Cu and Fe ions are occupied in both A and B site with nearly portion (45.3 and 54.7% in A and B site, respectively). This reveals that the structure of C/CuFe₂O₄_0.6 is partial inverse spinel structure. The first shells at Cu k-edge originates from the Cu_A-O bond with four backscatterers at distance of 1.932 \AA and Cu_B-O bond with six backscatterers at distance of 2.106 \AA , respectively. At Fe k-edge, the first shells at 1.859 and 1.991 \AA originates from Fe_A-O bond with coordination number of four and Fe_B-O bond with coordination number of six,

respectively. The second shells during 2.5-2.9 Å with three surrounded backscatterers related to bond between cations in octahedral sites ($\text{Fe}_B\text{-Fe}_B$ and $\text{Fe}_B\text{-Cu}_B$), while the shell around 3.3-3.5 Å with six surrounded backscatterers corresponds to bond between cations at the tetrahedral ($\text{Fe}_A\text{-Fe}_A$, $\text{Fe}_A\text{-Cu}_A$). The occupation of Fe^{3+} cation in both A and B site was observed with nearly portion of 58.1 and 41.9%, respectively. The structural parameters of the EXAFS fitting obtained through the non-linear least square fitting are shown in Table 4.4-4.6. It is important to note that, the ratio of polymer and magnetic source content is strongly affected on the cation distribution and thus structure. It was totally inverse spinel structure for the sample with low percentage of magnetic source than that of polymer source content as observed in C/CuFe₂O₄_0.2 and C/CuFe₂O₄_0.4. The structure becomes partial inverse spinel structure for the sample with higher magnetic source content (C/CuFe₂O₄_0.6).



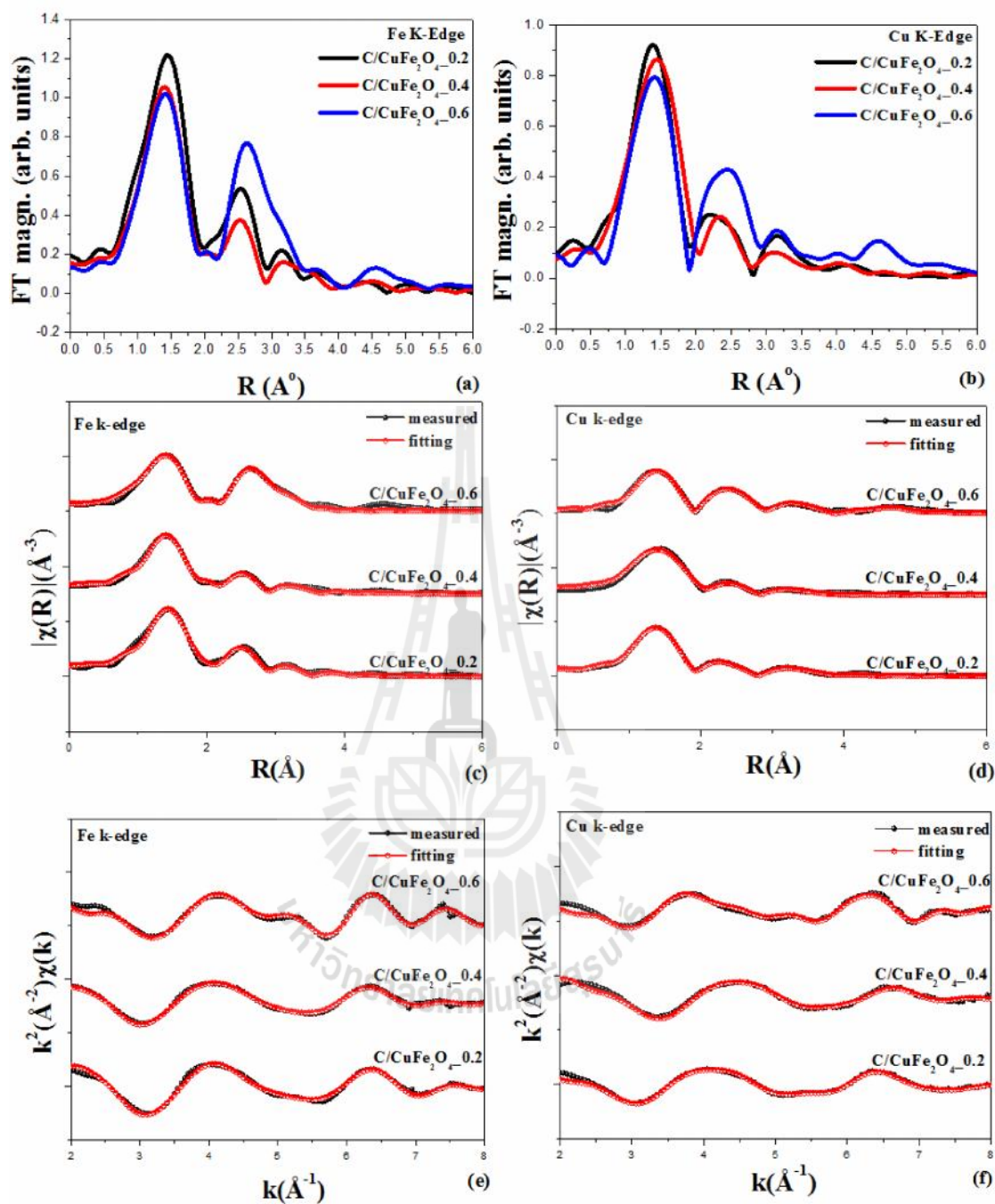


Figure 4.8 (a, b) Fourier transform in R-space of three different composite samples at Fe and Cu k-edge, respectively. (c, d) Fourier transform in R-space with the corresponding fitted spectra. (e, f) The $k^2(\chi(k))$ plots with the corresponding fitting spectra at Fe and Cu K-edge, respectively.

Table 4.4 Lists of coordinate number (N), amplitude reduction (S_0^2), Debye-Waller factor (σ^2), interatomic distances (R), and R-factor obtained by fitting the experimental EXAFS data at Fe and Cu K-edge for C/CuFe₂O₄_0.2.

Sample	Site	Shell	N	S_0^2	σ^2	R
Cu k-edge C/CuFe ₂ O ₄ _0.2	B	Cu-O	6	0.817	0.00594	1.90536
		Cu -Fe	3	0.817	0.03439	2.83214
		Cu -Cu	3	0.817	0.01372	2.91771
	R-factor 0.0020073	Cu -Fe	6	0.817	0.04031	3.32108
		Cu-O	12	0.817	0.01338	4.29197
Fe k-edge C/CuFe ₂ O ₄ _0.2	A	Fe-O	4	0.577	0.00300	1.93286
		Fe-Fe	6	0.577	0.01855	3.63419
		Fe-Cu	6	0.577	0.04075	3.63419
		Fe-Fe	4	0.577	0.01939	3.79579
		R-factor 0.0192816	Fe-O-O	12	0.577	0.00545
	B	Fe-O	6	0.235	0.00300	2.09985
		Fe-Cu	3	0.235	0.00928	2.99699
		Fe-Fe	3	0.235	0.00222	2.99699
		Fe-Fe	6	0.235	0.00260	3.51427
		Fe-O-O	24	0.235	0.00510	3.58468
		Fe-O	6	0.235	0.00526	3.68192

Table 4.5 Listes of coordinate number (N), amplitude reduction (S_0^2), Debye-Waller factor (σ^2), interatomic distances (R), and R-factor obtained by fitting the experimental EXAFS data at Fe and Cu K-edge for C/CuFe₂O₄_0.4.

Sample	Site	Shell	N	S_0^2	σ^2	R
Cu k-edge C/CuFe ₂ O ₄ _0.4 R-factor 0.0147114	B	Cu-O	6	0.931	0.01251	1.87718
		Cu -Fe	3	0.931	0.01442	3.12668
		Cu -Cu	3	0.931	0.01002	2.90524
	Cu-O	6	0.931	0.02414	3.75035	
		Cu-O	6	0.931	0.02194	3.29143
		Fe-O-O	36	0.931	0.02620	3.93222
Fe k-edge C/CuFe ₂ O ₄ _0.4 R-factor 0.0126495	A	Fe-O	4	0.551	0.00300	1.93340
		Fe-Fe	6	0.551	0.03004	3.63521
		Fe-Cu	6	0.551	0.80301	3.63521
		Fe-Fe	4	0.551	0.03137	3.79686
		Fe-O-O	12	0.551	0.00545	3.51194
		Fe-O-O	4	0.551	0.00600	3.86670
	B	Fe-O	6	0.167	0.00300	2.11766
		Fe-Cu	3	0.167	0.00886	3.02241
		Fe-Fe	3	0.167	0.00403	3.02241
		Fe-Fe	6	0.167	0.00473	3.54408
Fe-O-O	24	0.167	0.00512	3.61508		
Fe-O	6	0.167	0.00526	3.71314		

Table 4.6 Listes of coordinate number (N), amplitude reduction (S_0^2), Debye-Waller factor (σ^2), interatomic distances (R), and R-factor obtained by fitting the experimental EXAFS data at Fe and Cu K-edge for C/CuFe₂O₄_0.6.

Sample	Site	Shell	N	S_0^2	σ^2	R
Cu k-edge C/CuFe ₂ O ₄ _0.6 R-factor 0.0105175	A	Cu-O	4	0.453	0.00233	1.93249
		Cu-Fe	12	0.453	0.00720	3.46369
		Cu-O	12	0.453	0.00437	3.63955
		Cu-Cu	4	0.453	0.00300	3.67111
		Cu-O-O	48	0.453	0.00522	4.33572
	B	Cu-O	6	0.547	0.01487	2.10562
		Cu-Fe	3	0.547	0.00655	4.34245
		Cu-Cu	3	0.547	0.01364	2.47429
		Cu-Fe	6	0.547	0.00768	5.09117
		Cu-O	6	0.547	0.02609	3.69212
Fe k-edge C/CuFe ₂ O ₄ _0.6 R-factor 0.0144190	A	Fe-O	4	0.581	0.00300	1.85881
		Fe-Fe	6	0.581	0.00300	3.32857
		Fe-Cu	6	0.581	0.01500	3.50723
		Fe-O	12	0.581	0.00565	3.50101
		Fe-Fe	4	0.581	0.00313	3.47657
	B	Fe-O	6	0.419	0.00300	1.99111
		Fe-Cu	3	0.419	0.00439	2.99249
		Fe-Fe	3	0.419	0.02490	2.46277
		Fe-Fe	6	0.419	0.02919	2.88783
		Fe-O	6	0.419	0.00526	3.49129

4.1.2 Magnetic properties of C/CuFe₂O₄ composite nanofibers.

Figure 4.9 (a) shows room temperature magnetization of CNF and C/CuFe₂O₄ composite nanofibers after carbonization at 535 °C for 1 h. The magnetization was determined with applied fields of ± 10000 Oe at 50-390 K. It was found from Figure 4.9 (a) that, all composite samples show the ferrimagnetic behavior, while CNF exhibit diamagnetic behavior. In terms of electronic configuration of materials, diamagnetism is observed in materials with filled electronic subshells where the magnetic moments are paired and overall cancel each other. The saturation magnetization (M_s) of the C/CuFe₂O₄ composite nanofibers strongly depends on the magnetic source content and their crystallite size. The values of 0.32, 3.44 and 12.10 emu/g were obtained for C/CuFe₂O₄_0.2, C/CuFe₂O₄_0.4, and C/CuFe₂O₄_0.6, respectively. These values are quite low compared to the value of 33.4 emu/g of bulk CuFe₂O₄ (Goya *et al.*, 1998) and other reports on CuFe₂O₄ (Lv *et al.*, 2008; Salavati-Niasari *et al.*, 2011). The low M_s value observed in the prepared C/CuFe₂O₄ composite nanofibers is possibly due to either the existence of CNF extinguishing the surface magnetic moment with spin canting or the effect of crystallite size causing the disordered spins (Garcia-Otero *et al.*, 2000). The largest M_s value obtained for C/CuFe₂O₄_0.6 is possibly due to either its largest magnetic source concentration or the removal of the Cu²⁺ ions from B to A site (as seen in EXAFS analysis), which had previously compensated magnetically for some of the Cu²⁺ ions in the B site. Room temperature coercivity (H_c) and the squareness (M_r/M_s) show crystallite size independence behavior (Figure 4.9 (b)). The coercivity value of ~ 90 Oe was observed for the smallest particle size of 24 nm and reached a maximum value of ~ 178 Oe for the C/CuFe₂O₄_0.4 sample with particle size of 36.29 nm. The lowest

value of 54 Oe was observed in the C/CuFe₂O₄_0.6 sample with the largest particle size of 45.73 nm. This variation is not consistent with the results obtained on C/CoFe₂O₄ and C/NiFe₂O₄ composite nanofibers (sections 4.4.2 and 4.3.2) and also other reports (Goya et al., 1998, Krupicka and Novak, 1982). It is possible that, the largest H_c for C/CuFe₂O₄_0.4 may arise from the specific morphology like chain particle as seen in the Fe-SEM image (Figure 4.3 (c)). As known that, a system containing magnetic dipoles that are arranged into a linear chain will exhibit an increase in coercivity (Jacobs and Bean, 1955). It was also found from Figure 4.9 (b) that room temperature remanence ratios (M_r/M_s) for C/CuFe₂O₄_0.2, C/CuFe₂O₄_0.4 and C/CuFe₂O₄_0.6 were obtained to be 0.15, 0.31 and 0.13, respectively. All the values are lower than 0.5 implying the particles are predominantly not in the single domain state (Varma *et al.*, 2008). It is important to note that, the remanence ratio does not show any specific trend in respect to changing crystallite size. It is possible that the magnetic anisotropy (e.g. magnetocrystalline anisotropy, shape anisotropy or exchange anisotropy) plays an important role (An *et al.*, 2009; Nawale *et al.*, 2011).

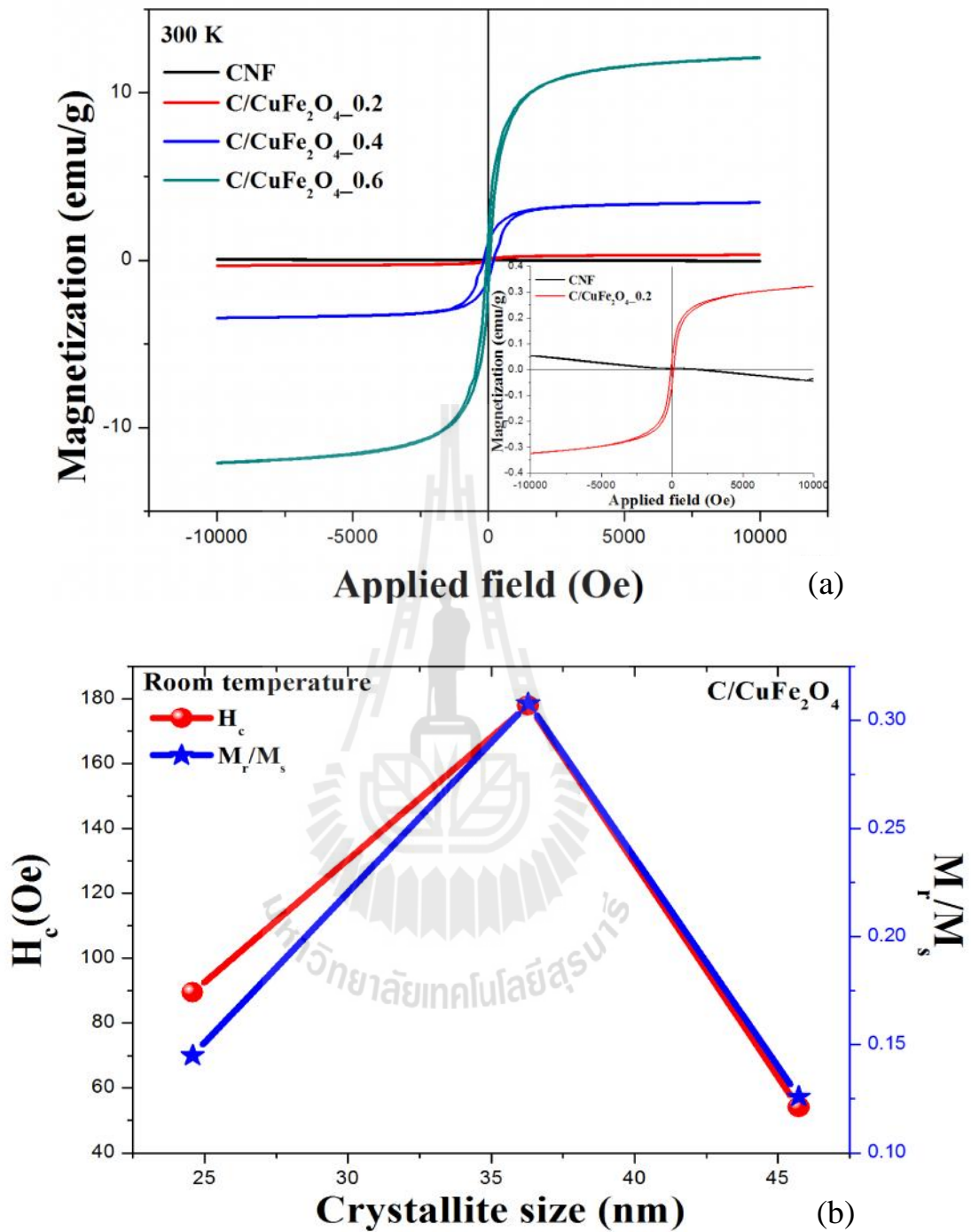


Figure 4.9 (a) Room temperature magnetization of CNF and three types of C/CuFe₂O₄ composite nanofibers carbonized at 535 °C for 1 h, (b) the variation of the coercivity (H_c) and the remanence ratio (M_r/M_s) with crystallite size at room temperature.

In this work, the magnetic properties were measured with varying temperature (50 – 390 K) and the results are shown in Figure 4.10. The magnetization hysteresis loops for all composite samples show close to s-shape curve with the existent remanent magnetization. This suggests ferrimagnetic behavior of materials (Laokul *et al.*, 2011). The hysteresis loops became wider with decreasing temperature suggesting the increase of M_s , M_r and H_c . Such behavior is possibly due to thermal fluctuations of the magnetic moments at high temperatures, while the magnetic moments were gradually induced and turned around in the direction of the applied field at low temperature (Caruntu *et al.*, 2007). For C/CuFe₂O₄_0.2 composite nanofiber, the magnetization is not saturated at ± 10 kOe even with measuring temperature of 50 K. This is possibly due to either a result of spin canting or the smallest particle size affect to small anisotropy that requires a larger field to be saturated together. Moreover, the non saturation aspect is postulated to arise from local defects, anisotropy and superparamagnetic grains (Dash *et al.*, 1999; Margulies *et al.*, 1996). For C/CuFe₂O₄_0.4 and C/CuFe₂O₄_0.6, the magnetizations increase with decreasing measurement temperature and all spectra tend to be saturated at 10 kOe, indicating the particles are already almost completely oriented for a field of around 10 kOe. This behavior may be due to much larger magnetocrystalline anisotropy characteristic from their large crystallite size. The variation of the squareness with the measurement temperature is shown in Figure 4.11. The values are decrease with increasing of temperature for all the prepared samples.

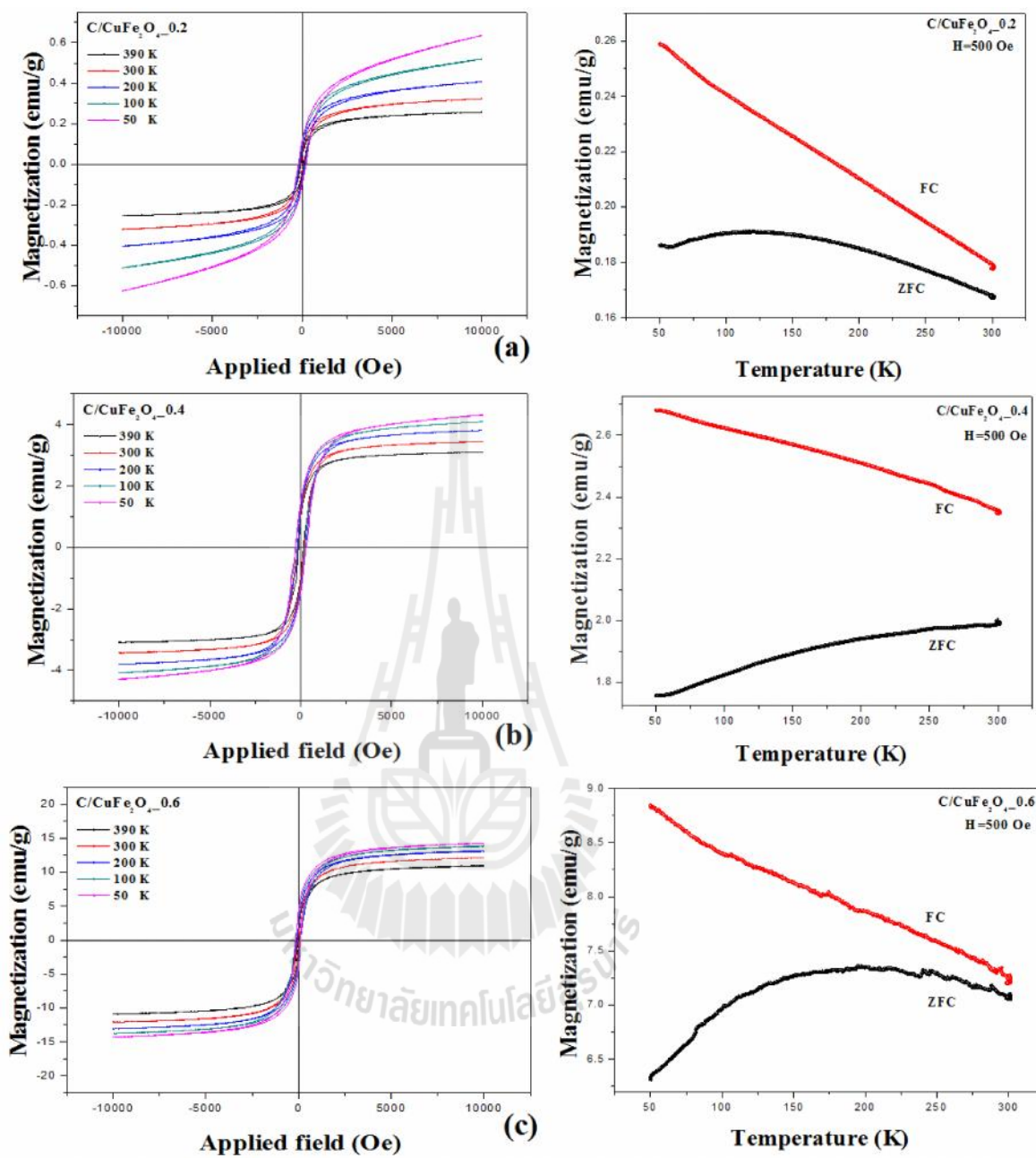


Figure 4.10 The measuring temperature dependence of magnetization and their corresponding zero field-cooled and field-cooled (ZFC-FC) for (a) C/CuFe₂O₄_0.2 (b) C/CuFe₂O₄_0.4 (c) C/CuFe₂O₄_0.6 composite nanofibers.

The zero-field-cooled (ZFC) and field-cooled (FC) of the prepared samples were also measured at the temperature between 50 and 300 K. The results for each sample are shown in the right hand side of Figure 4.10. It was found from ZFC that a broad maximum centered at approximately 121 and 196 K for C/CuFe₂O₄_0.2 and C/CuFe₂O₄_0.6, respectively. This maximum can be assigned to the blocking temperature (T_B) of the CuFe₂O₄ material. No end raise of ZFC was observed for C/CuFe₂O₄_0.4 indicating T_B of this sample is being higher than room temperature. The FC magnetization curves for all samples are slightly decreases with increasing temperature. Lists of the magnetic parameters is presented in Table 4.7

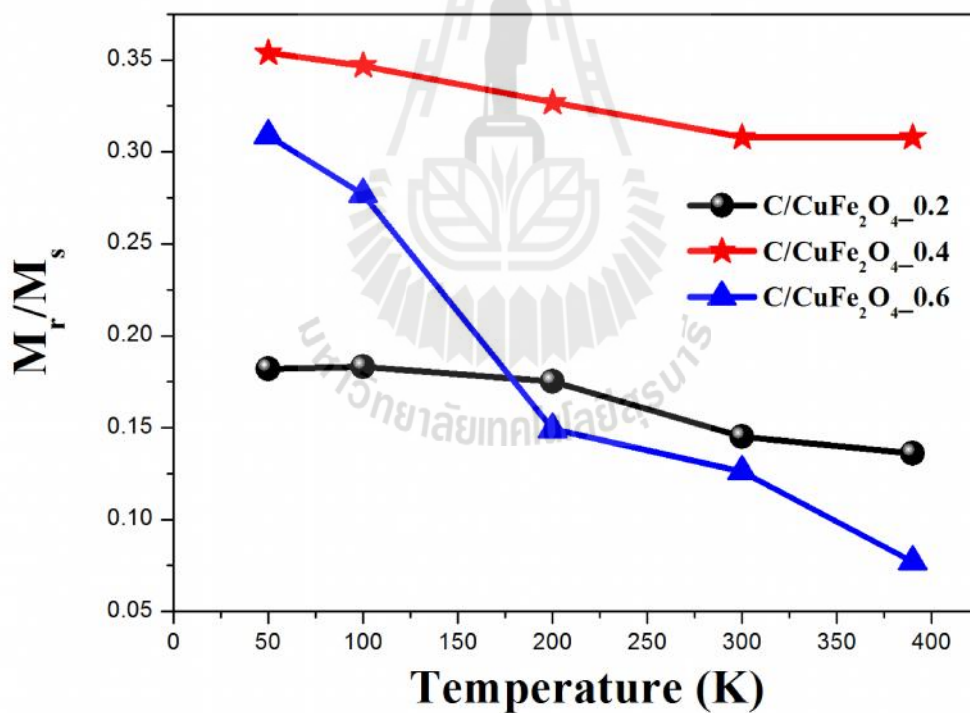


Figure 4.11 The dependence of M_r/M_s on the measurement temperature for C/CuFe₂O₄_0.2, C/CuFe₂O₄_0.4, and C/CuFe₂O₄_0.6 composite nanofibers.

Table 4.7 Lists of the magnetic parameters: coercivity (H_c), saturation magnetization (M_s), squareness ratio (M_r/M_s) and blocking temperature (T_B) of C/CuFe₂O₄ composite nanofibers with different magnetic source concentration.

Sample	Crystallite size (nm)	T (K)	H_c (Oe)	M_s (emg/g)	M_r/M_s	T_B (K)
C/CuFe ₂ O ₄ _0.2	24.58	50	218.0	0.636	0.182	121
		100	167.0	0.519	0.183	
		200	124.0	0.406	0.175	
		300	89.5	0.324	0.145	
		390	63.5	0.257	0.136	
C/CuFe ₂ O ₄ _0.4	36.29	50	291.5	4.303	0.354	>300
		100	270.0	4.090	0.347	
		200	173.0	3.805	0.327	
		300	178.0	3.442	0.308	
		390	127.0	3.097	0.308	
C/CuFe ₂ O ₄ _0.6	45.73	50	133.0	14.259	0.309	196
		100	172.0	13.789	0.277	
		200	81.0	13.157	0.149	
		300	54.1	12.105	0.126	
		390	27.5	10.968	0.077	

4.1.3 Electrochemical properties of C/CuFe₂O₄ composite nanofibers

To identify the electrochemical properties of CNF, C/CuFe₂O₄, and CuFe₂O₄ electrodes, the cyclic voltammetry (CV), galvanostatic charge/discharge (GCD), and electrochemical impedance spectroscopy (EIS) were performed. The measurements were carried out in three electrodes system using 0.5 M Na₂SO₄ and 1 M KOH of aqueous electrolyte. The GCD was measured at a variety of current densities (0.1 to 1 A/g). The impedance behavior of electrodes was tested in a frequency range of 0.1-10⁵ Hz. The effect of different electrode type on the electrochemical properties is investigated.

4.1.3.1 Cyclic Voltammetry measurement

Figure 4.12 shows the voltammogram (CV) of CNF, C/CuFe₂O₄ and CuFe₂O₄ electrodes, in which was recorded over the potential window of -0.3 to 2 V in 0.5 M Na₂SO₄. It was found that, the area surrounded by CV curves for the C/CuFe₂O₄ composite electrode is larger than that of other two electrodes suggesting the largest induced current and thus supporting the high cell capacitance. No any redox peak was observed for pure CNF revealing to typical double layer behavior (Wen *et al.*, 2009; Qu *et al.*, 2008). For pure CuFe₂O₄ and C/CuFe₂O₄ electrode, the redox peak was observed suggesting the charge storage mechanism via the reduction/oxidation transition of CuFe₂O₄. During oxidation reaction, ions are transferred from electrolyte to the electrode (generated positive current), while the ions are released back into the electrolyte during reduction reaction (generated negative current). The large anodic peak appears at around 0.85 and 0.60 V for C/CuFe₂O₄ and CuFe₂O₄, respectively. Such behavior could be attributed to the oxidation reactions of both metallic Fe and Cu (Rongier *et al.*, 1998). In the reverse

scan, the cathodic peak appears at around 0.25 and 0.1 V for C/CuFe₂O₄ and CuFe₂O₄, respectively. By the variation of CV curve with the scan rate of 10-200 mV/s, the current density increases with increasing of the scan rate because flux towards the electrode is large at faster scan. For CNF and CuFe₂O₄ electrodes, the enlarging voltages from -0.3 to 2.0 V generate the oxygen evolution from the water electrolysis. This behavior could be avoided due to the oxygen evolution causing large pseudocapacitance of electrochemical cell. The redox peaks of CuFe₂O₄ and C/CuFe₂O₄ electrodes still exhibit (at different potential) with the varying scan rate, indicating a good rate capability of electrode (Yang *et al.*, 2011). For C/CuFe₂O₄ electrode (Figure 4.12 (b)), the anodic and cathodic peaks are in the range of 0.4 - 0.85 V and 0.01 - 0.25 V, respectively. The peaks in forward scan could be assigned to the stepwise oxidation of Fe⁰/Fe³⁺ (~0.7 V), and the cathodic peak in the reverse scan corresponds to the reaction of Cu¹⁺/Cu²⁺ (0.1 - 0.25 V), respectively (Xing *et al.*, 2013). For pure CuFe₂O₄ electrode (Figure 4.12 (c)), the anodic peak is clearly seen in the range of 0.3 - 0.75 V, while the cathodic peak was observed in the range of 0.17 - 0.29 V. It is important to note from the voltammogram of C/CuFe₂O₄ electrode that, the potential separation between two peaks (ΔE_{pp}) depends on the scan rate, where ΔE_{pp} is a parameter used for classified major difference between a reversible and an irreversible voltammogram. The ΔE_{pp} values increase with increasing of scan rate as seen in Table 4.8 indicating the C/CuFe₂O₄ electrode exhibited the irreversible behavior. The increase of peak separation with increasing scan rate may be due to the effect of resistance or the increase of over potentials (Tang *et al.*, 2012).

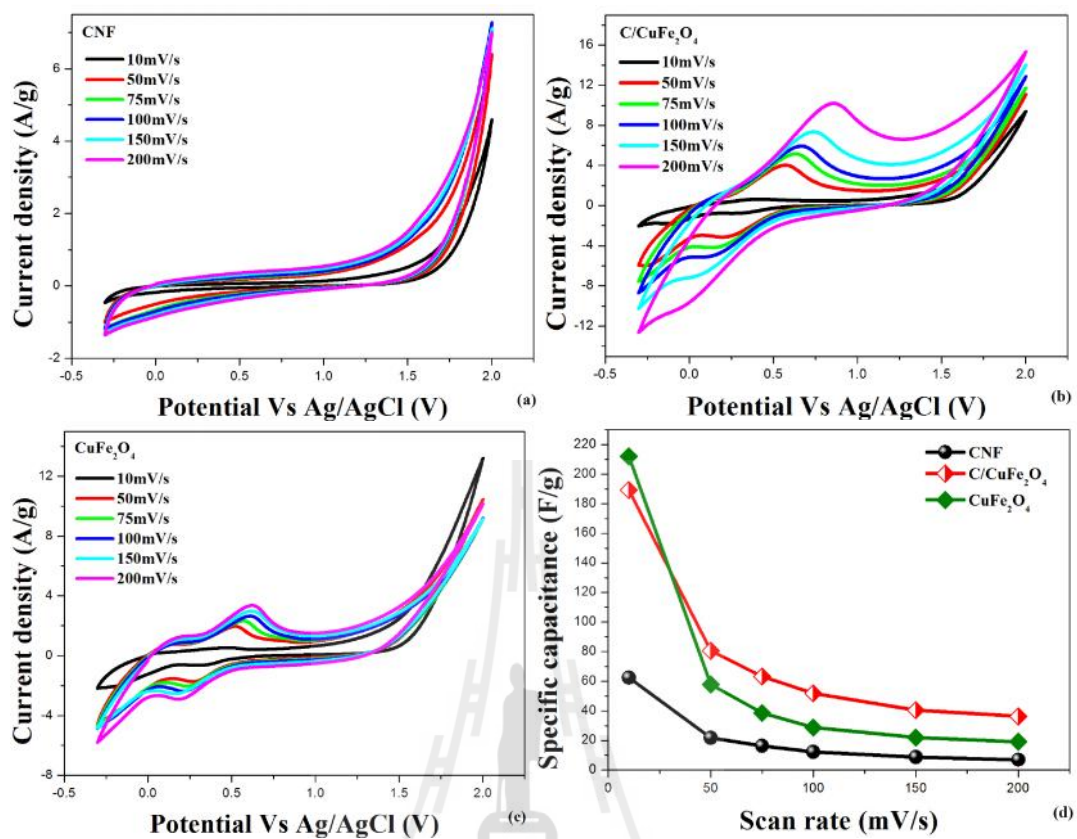


Figure 4.12 Cyclic voltammograms (CV) in 0.5 M Na₂SO₄ at different scan rates of (a) CNF, (b) C/CuFe₂O₄, and (c) CuFe₂O₄, respectively. (d) The corresponding specific capacitance at different scan rates of CNF, C/CuFe₂O₄ and pure CuFe₂O₄.

Table 4.8 Lists of anodic and cathodic potential of C/CuFe₂O₄.

Scan rate (mV/s)	E _{anodic} (V)	E _{cathodic} (V)	ΔE
10	0.418	0.256	0.162
50	0.571	0.198	0.373
75	0.627	0.133	0.494
100	0.667	0.0615	0.606
150	0.736	0.0972	0.639
200	0.857	0.0189	0.876

Figure 4.12 (d) shows the specific capacitance as a function of scan rate for CNF, C/CuFe₂O₄ and CuFe₂O₄ electrodes, where the specific capacitance was obtained from integrating the CV curve as Eq. 3.16. It was found that, the specific capacitance of materials decreases with increasing of scan rate. This is because short time at high scan rate caused large internal resistance and retarded the penetration of electrolyte ions into inner pores during charge (Wang *et al.*, 2006; Yuan *et al.*, 2008). At the scan rate higher than 30 mV/s, the specific capacitance of C/CuFe₂O₄ is higher than those of pure CuFe₂O₄ and CNF electrodes, respectively. This is possibly because large surface area of C/CuFe₂O₄ yields higher density supporting the electrolyte ions penetration and thus high capacitance. It is also possible that, the copper ferrite nanoparticles in the CNF matrix support the faster ions transport by reducing the distance to the inside electrode (Patil *et al.*, 2012; Li *et al.*, 2010). At scan rate of 10 mV/s, the specific capacitance was obtained to be 191 F/g for C/CuFe₂O₄ electrode. This value is close to those values previously reported on spinel ferrite electrodes such as RGO/CoFe₂O₄ (123.2 F/g) and GO/CoFe₂O₄ (21.1 F/g) (He *et al.*, 2012).

Figure 4.13 shows the voltammograms of CNF, C/CuFe₂O₄ and CuFe₂O₄ recorded in 1 M KOH electrolyte over the potential windows of -0.2 to 0.35 V. It was found that, the trend of area surrounded by CV curves is similar to that tested in 0.5 M Na₂SO₄ electrolyte. The area curve of C/CuFe₂O₄ composite electrode is larger than that of CuFe₂O₄ and CNF electrodes, respectively, implying that C/CuFe₂O₄ electrode has higher electrochemical performance than that of CuFe₂O₄ and CNF, respectively. The operating windows of -0.2 to 0.35 V are lower than those of 0.5M Na₂SO₄ electrolyte (-0.3 to 2 V) due to the problem of hydrogen-oxygen evolution. No any

redox peak was observed for pure CNF, confirming the typical double layer behavior of electrode (Wen *et al.*, 2009; Qu *et al.*, 2008). For C/CuFe₂O₄ and CuFe₂O₄ electrodes, the cathodic peak was observed at nearly 0.25 V. By varying the scan rates between 2 and 200 mV/s, the current density increases with increasing the scan rate. The CV of CNF exhibited rectangular shape at low scan rates (< 50 mV/s). While at increased scan rate, the shape deviates from rectangular possibly due to relatively slow diffusion of electrolyte ions within the electrode material (Sharma *et al.*, 2008; Peng *et al.*, 2011). The cathodic peak potential of pure CuFe₂O₄ is almost stable with the variation of scan rate, while small variation in the range of 0.21- 0.23 V was observed for C/CuFe₂O₄ electrode suggesting the reaction of Cu¹⁺/Cu²⁺ (0.1-0.25 V). The corresponding specific capacitances as a function of scan rate are shown in Figure 4.13 (d). The specific capacitance of all values for all the prepared electrodes are lower than that reported in 0.5 M Na₂SO₄ solution due to the narrower potential window used. However, C/CuFe₂O₄ electrode still shows larger value than that of other two electrodes confirming the better electrochemical performance after making composite of a CNF with CuFe₂O₄. This superior electrochemical capacitive performance can be attributed to the combined contribution of the redox pseudocapacitance of CuFe₂O₄ and the electric double layer capacitance of CNF.

The cycle stability of CNF, C/CuFe₂O₄ and CuFe₂O₄ electrode was observed by repeating the cyclic voltametry for 1000 cycles. The plots of the specific capacitance retention against the cycle number are shown in Figure 4.13 (e). It was found after 1000 cycles that, high capacitance retention with the values of 97, 86 and 79% was observed for CNF, C/CuFe₂O₄ and CuFe₂O₄ electrodes, respectively. The best cycle life of CNF electrode compared to the other two samples may be because

either fast ion response or large CNF network structure restricts the change of electrode during charge/discharge process. The cycle ability drops significantly for C/CuFe₂O₄ and CuFe₂O₄ electrodes, respectively, mainly attributed to pseudo capacitance arising from CuFe₂O₄ nanoparticles. The better rate capability of C/CuFe₂O₄ than CuFe₂O₄ electrode is possibly due to its charge carriers that could be effectively and rapidly conducted back and forth from the CuFe₂O₄ nanoparticles to the current collector through the highly conductive CNF. Moreover, with the free space between the CuFe₂O₄ nanoparticles in CNF matrix working as an elastic buffer, this electrode could accommodate larger volume expansion/contraction compared to that of the pure CuFe₂O₄ electrode. For CuFe₂O₄ electrode, the large particle size from the agglomeration of CuFe₂O₄ nanoparticles could be pulverized due to large volume changes during charge/discharge processes, and thus leading to fast capacity fading. Other factors such as the dissolution of active material in electrolyte and the instability of electrode also have strongly affected on the fade in capacitance (Yu *et al.*, 2011)

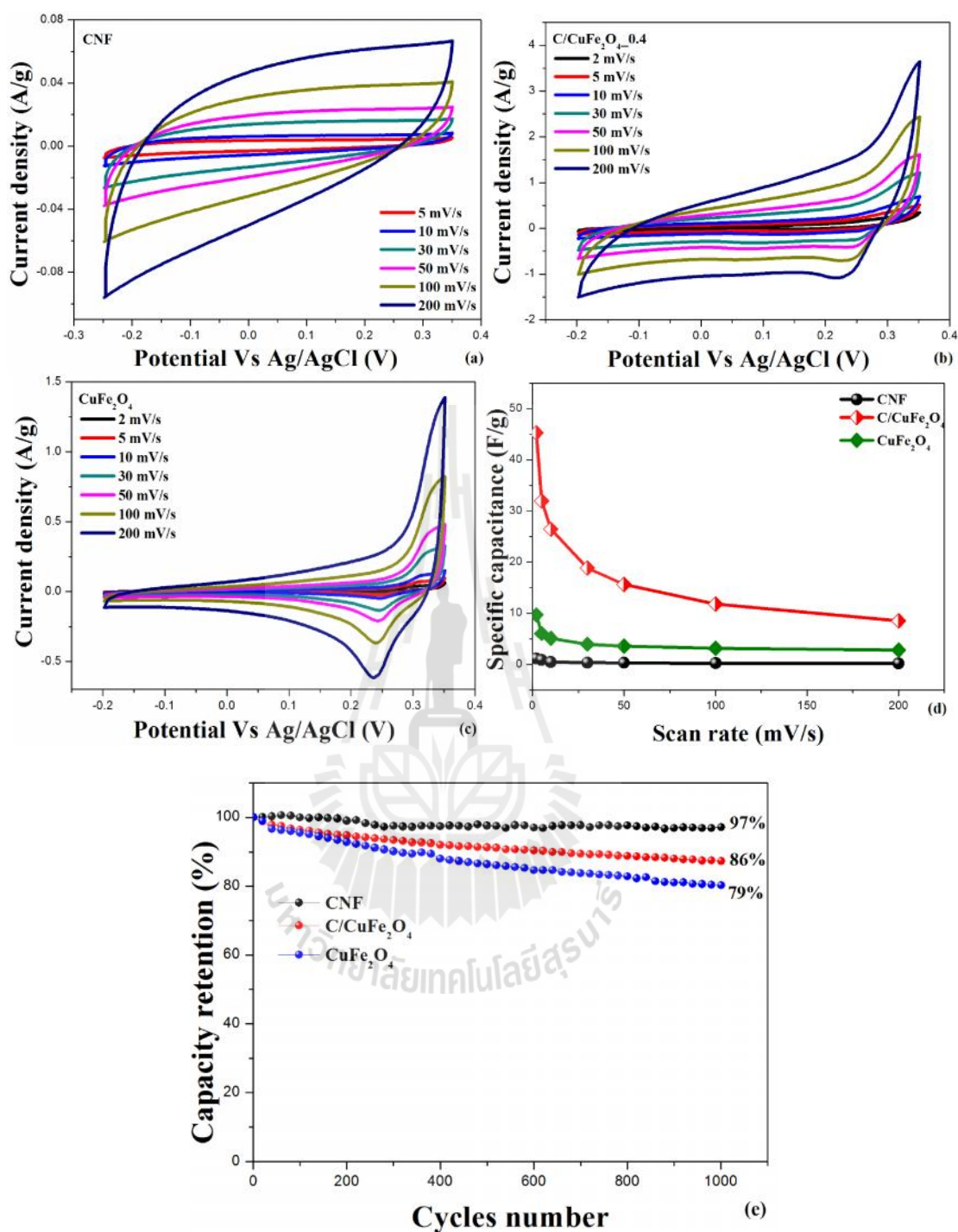


Figure 4.13 Cyclic voltammograms (CV) at different scan rates of (a) CNF, (b) C/CuFe₂O₄, and (c) CuFe₂O₄ electrodes in 1.0 M KOH electrolyte. (d) The corresponding specific capacitance at different scan rates. (e) The specific capacity retention of CNF, C/CuFe₂O₄ and CuFe₂O₄ electrodes at 1000 cycles.

4.1.3.2 Galvanostatic charge/discharge measurements

Figures 4.14 (a), (b), and (c) show the representative charge/discharge curves of CNF, C/CuFe₂O₄ and CuFe₂O₄ electrodes, respectively, at different current densities of 0.1, 0.25, 0.5, 0.75, and 1.0 A/g. It was found that, the shape of charge/discharge curves for all the prepared electrodes is not ideal. The distortion shape of curve is strongly observed in CuFe₂O₄ and C/CuFe₂O₄ electrode. Note that, their discharging curve is nonlinear due to the redox reaction during the discharge process (Yang *et al.*, 2010). The charging process is longer than the discharging process for all spectra indicating a slow entrance of electrolyte ions into micropores (Ma *et al.*, 2014). The coulomb efficiency ($\eta\%$) was also calculated at current density of 1 A/g. The values of 73.5, 72.7 and 79 were obtained for the CNF, C/CuFe₂O₄, and CuFe₂O₄ electrodes, respectively. All the values are less than 99% for very symmetric triangular shape. Figure 4.14 (d) shows the corresponding Ragone plot of CNF, C/CuFe₂O₄ and CuFe₂O₄ electrodes. It was found that, the energy density for all the prepared electrode are very low compared to that of carbon-based EDLCs electrode (~5Wh/kg) (Bao *et al.*, 2008), but the value is in the range of electrochemical capacitor electrode (Simon *et al.*, 2008). At current density of 1 A/g, the energy densities of about 0.17, 0.172 and 0.10 Wh/kg with corresponding power densities of 244.8, 310.4, and 380.2 W/kg were obtained for the CNF, C/CuFe₂O₄ and CuFe₂O₄ electrodes, respectively. At each current density, the power density of CuFe₂O₄ electrode is higher than those of the other two samples. In contrast, the C/CuFe₂O₄ and pure CNF show higher energy density compared to pure CuFe₂O₄. It is speculated that, their fibrous morphology with optimized pore size of the C/CuFe₂O₄ and pure CNF allow them to achieve high energy density. The energy density and power

density of C/CuFe₂O₄ show slightly higher than that of pure CNF at the same current density. This is possibly due to the conductivity enhancement of material electrode after making a composite of CNF with CuFe₂O₄ nanoparticles.

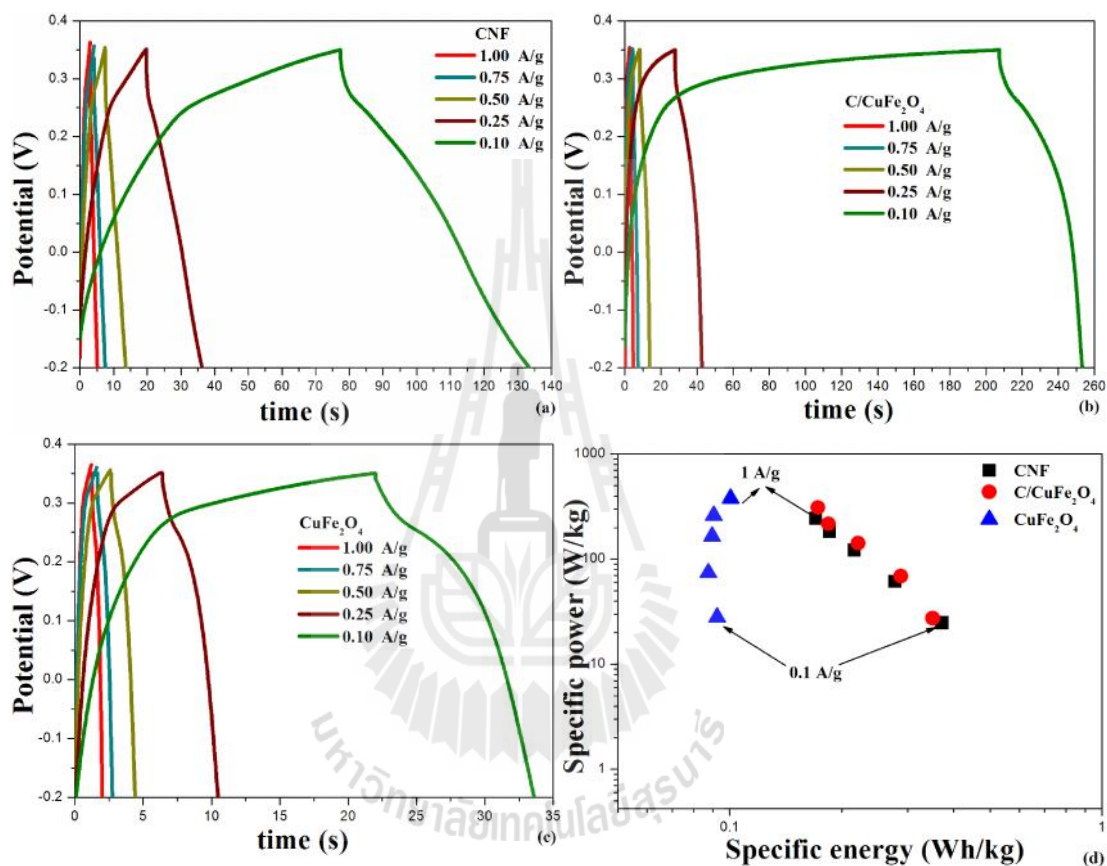


Figure 4.14 Galvanostatic charge/discharge curves of (a) CNF, (b) C/CuFe₂O₄, and (c) CuFe₂O₄ electrodes at current densities of 0.1, 0.25, 0.5, 0.75 and 1.0 A/g in 1 M KOH electrolyte solution. (d) The corresponding Regone plot.

4.1.3.3 Electrochemical Impedance Spectroscopy (EIS) measurements

The electrochemical behavior was further study by EIS experiment. EIS is an electrochemical technique for evaluating the charge transport behavior and probing the resistance at electrode/electrolyte interface. In this work, the measurement were performed after cyclic voltammetry technique and carried out in the frequency range of 0.1 Hz – 10^5 Hz in 1 M KOH. The results were presented either in the Nyquist plot, the plot of the opposite imaginary part impedance ($-Z''$) versus the real part impedance (Z') or the Bode plot: the frequency dependence of phase angle (ω Vs f) and the frequency dependence of impedance (Z Vs f) plots.

Figure 4.15 shows the Nyquist plots of three prepared electrodes (CNF, C/CuFe₂O₄ and CuFe₂O₄). The Nyquist plot of the CNF electrode shows almost a straight line at low frequency without semicircle arc at high frequency region implying no charge transfer resistance (R_{ct}) and good electrical conductivity (Laforgue, 2011). For C/CuFe₂O₄ and pure CuFe₂O₄ electrodes, a single semicircle at high frequency was observed attributed to the charge transfer resistance (R_{ct}). The sloping line at low frequency region is called the Warburg resistance (W), representing the frequency dependence of ion diffusion into the bulk of the electrode surface (Cheng *et al.*, 2011). The Warburg impedance is small if the diffusing reactants don't have to move very far (at high frequency). The deviation of straight line from the vertical axis is attributed to large diffusion resistance for electrolyte ions (Wang *et al.*, 2006). A steepest slope indicates good capacitive behavior and corresponds to electrodes that efficiently allow ions to penetrate pores.

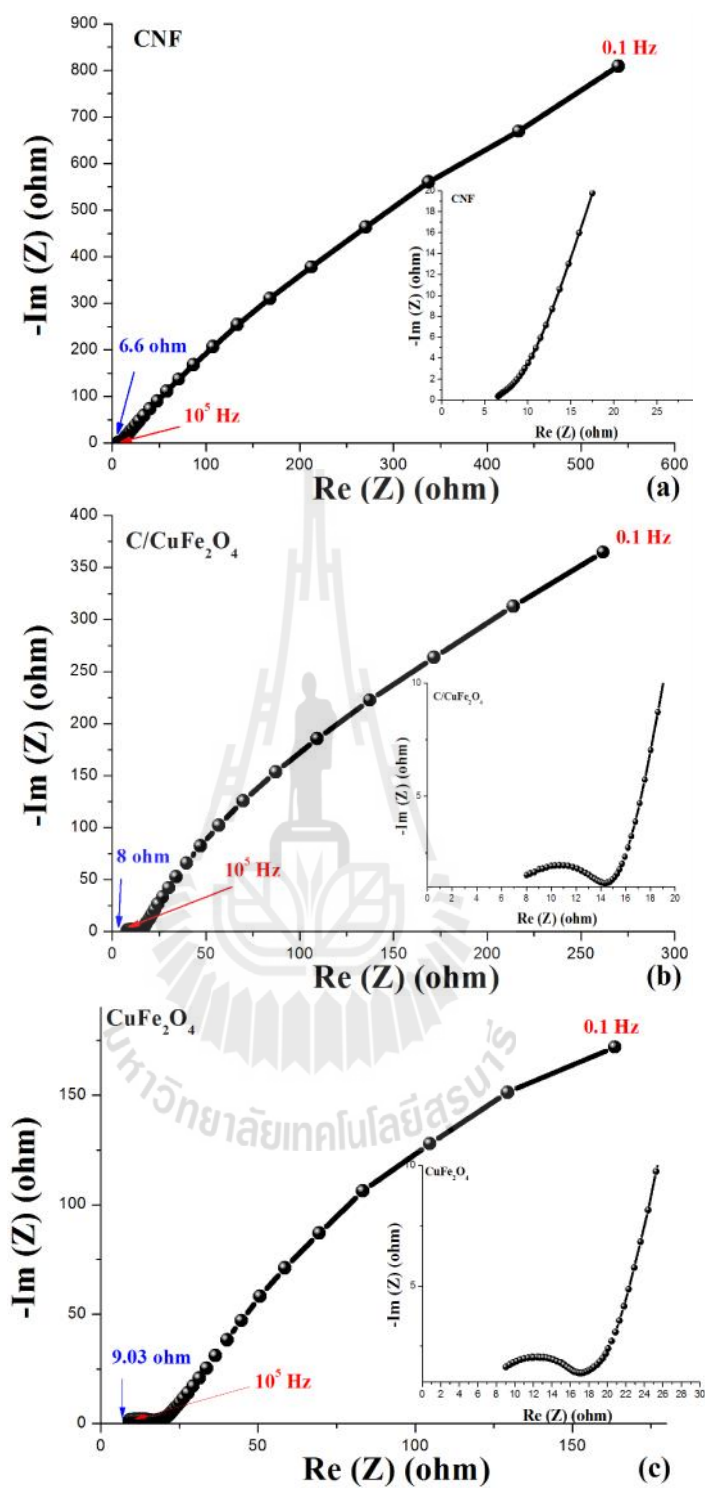


Figure 4.15 Nyquist impedance plots at a frequency range of 0.1 Hz-100 kHz in 1 M KOH electrolyte solution for (a) CNF, (b) C/CuFe₂O₄, and (c) CuFe₂O₄ electrodes.

According to the Nyquist plot, the x-intercept on real axis (Z) at high frequency represents a combined resistance (R_s) including intrinsic resistance of electrode materials, ionic resistance of electrolyte and contact resistance between electrode and current collector (Khomeenko *et al.*, 2006; Wang² *et al.*, 2012). The values of 6.6, 8 and 9.03 Ω were obtained for CNF, C/CuFe₂O₄ and CuFe₂O₄ electrodes, respectively. The charge transfer resistance can be estimated from the semicircle diameter and was obtained to be 0, 6.3 and 7.27 Ω for CNF, C/CuFe₂O₄ and CuFe₂O₄, respectively. The lowest value for the CNF electrode suggests that the well-aligned structure of CNF provides commendable channels for the electrolyte ion and current transport, and thus supporting better electrolyte ions pore accessibility (Wang *et al.*, 2010). High charge transfer resistance for C/CuFe₂O₄ and CuFe₂O₄ electrodes is possibly due to roughness surface from CuFe₂O₄ causing the enlarged contact area and aggregation of the nanoparticles that may block the penetration of electrolyte ions. However, the introduction of CuFe₂O₄ in CNF matrix is caused shortened electrolyte ion diffusion paths. Therefore, it is speculated that, the electron and ions can be more easily transferred, resulting in better electrolyte pore accessibility, and this thus enhances electrical conductivity (Snook *et al.*, 2011). Moreover, the composite of CuFe₂O₄ with CNF matrix can effectively suppress the aggregation of CuFe₂O₄ nanoparticles, and thus resulting in high surface area. The large interface area not only provides more electron ions insertion/extraction sites, but also facilitates fast ion transfer between electrode and electrolyte, thus leading to a large reversible specific capacity of the nanocomposite electrode (Zhu *et al.*, 2011). This behavior was confirmed by lower charge transfer resistance of C/CuFe₂O₄ than CuFe₂O₄ electrode. In addition, the slope line at low frequency increases and tends to become more purely capacitive for

the pure CNF, C/CuFe₂O₄, and CuFe₂O₄ electrodes, respectively. The results suggest that, the electrolyte greatly penetrates into the interior of bulk CNF than that of C/CuFe₂O₄ and CuFe₂O₄, respectively. The shortest length for CuFe₂O₄ cell indicating that the electrolyte ion just surface being accessed.

Figure 4.16 shows the Bode plots for CNF, C/CuFe₂O₄ and CuFe₂O₄ electrodes in 1M KOH electrolyte solution. Figure 4.16 (a) shows the frequency dependence of phase angle during 0.1 to 10⁵ Hz. It was found from the plots that, the phase angle decreases and is closed to zero with the increase of frequency. At frequency of 0.1 Hz, the phase angles of -56.3°, -54.3°, and -46.4°, respectively were obtained for the CNF, C/CuFe₂O₄ and CuFe₂O₄ electrodes, respectively. All the values are not even close to -90° for ideal capacitors (Conway, 1991). The value decreased from -54.3°, for C/CuFe₂O₄ to -46.4° for CuFe₂O₄, indicating further transition to more pseudocapacitive properties (Krishnamoorthy *et al.*, 2014). Normally, the Warburg impedance exhibits a phase shift of 45°. The values of capacitor response frequency (f_0) at the phase angle of -45° were about 21.2, 4.5 and 0.88 Hz, for CNF, C/CuFe₂O₄ and CuFe₂O₄ electrodes, respectively. The corresponding relaxation time constant τ_0 was calculated by using the equation $\tau_0 = 1/f_0$ and was obtained to be about 0.047, 0.22 and 1.14 s. The lowest time constant of CNF electrode supported high power delivery or fast charge-discharge process (Girija and Sangaranarayanan, 2006; Burke, 2000). Figure 4.16 (b) shows the frequency dependence of impedance for CNF, C/CuFe₂O₄ and CuFe₂O₄ electrodes at 0.2 V. At the frequency less than 20 Hz, the CNF electrode showed largest impedance and became lowest at the frequency over 30 Hz. The C/CuFe₂O₄ electrode showed

lower impedance value than CuFe_2O_4 electrode at all frequency over 7 Hz implying its better capacitance.

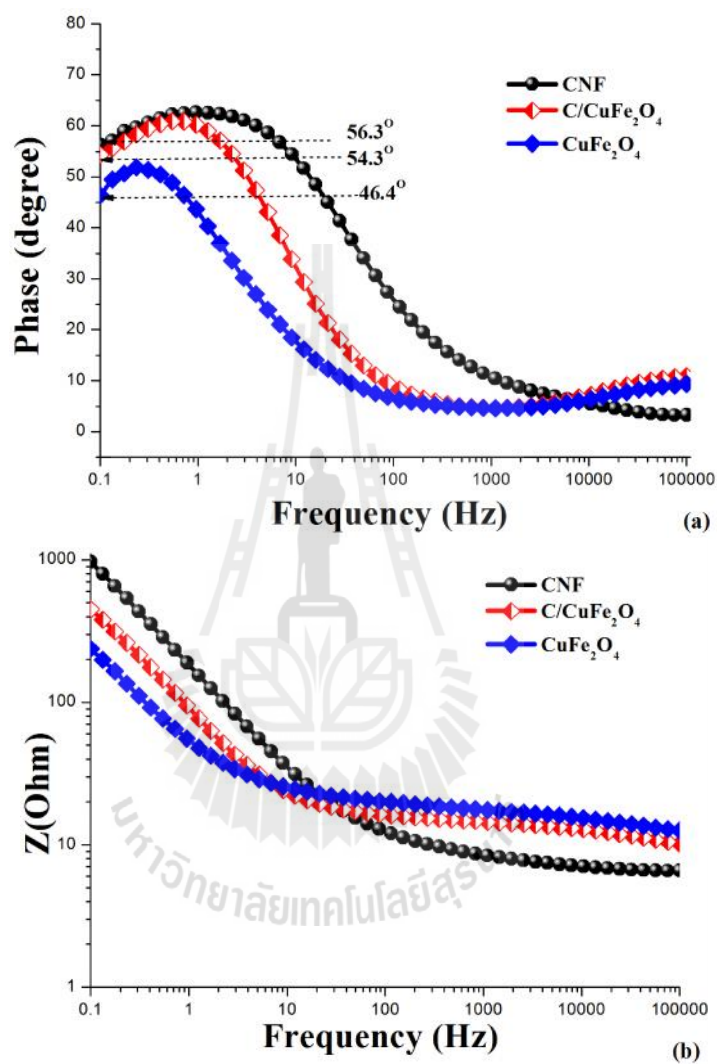


Figure 4.16 Bode plots of (a) frequency dependence of phase angle (b) impedance dependence on frequency of CNF, C/ CuFe_2O_4 and CuFe_2O_4 electrodes.

4.2 C/CoFe₂O₄ composite nanofibers

4.2.1 Structural and morphology characterization

4.2.1.1 Thermo gravimetric analysis (TGA) of the electrospun-based C//CoFe₂O₄ composite nanofibers.

To determine the suitable heat treatment condition to form the composite phase of carbon and CoFe₂O₄, the as spun PAN and PAN composite with different magnetic source content were analyzed by using TGA. The measurements were performed by using the heating rate of 10 °C/min in the temperature range of 25 to 1200 °C under air and N₂ atmosphere. The weight loss spectra as function of temperature are presented in Figure 4.17. It was found that, the TGA spectra of pure CNF, C/CoFe₂O₄_0.2, and C/CoFe₂O₄_0.4 show three main steps of weight loss in the range of ~20 -295, ~295- 470 and ~ 620-1200 °C. While for C/CoFe₂O₄_0.6, the plateau after 1100 °C was also observed. Pure CNF starts to decompose at about 295 °C, while the starting weight loss at lower temperature was observed for the composite nanofibers. The remaining weight percentage at 295 °C with the value of ~44, ~56, and ~82 and ~92 %, were obtained for C/CoFe₂O₄_0.6, C/CoFe₂O₄_0.4, C/CoFe₂O₄_0.2, and pure CNF, respectively. The results suggest that, higher weight loss was observed for the samples with higher magnetic source content. The major weight loss at ~295 - 470 °C relate to the decomposition of metal nitrates along with the degradation of some PAN polymer chain. The selected stabilization temperature could be lower than this range of temperature to obtain a large amount of final products. After major weight loss, the common short plateau between 471 and 620 °C was observed. The crystalline CoFe₂O₄ could form as the decomposition of metal product at this range of temperature (Maensiri and Nuansing, 2006). The plateau after

1100 °C for C/CoFe₂O₄_0.6 indicating the carbon for this material almost burned away under inert gas atmosphere. The inset figure shows weight loss of electrospun under air atmosphere. Two weight loss steps (at ~300 and ~400 °C) and the flat of curve in the range of 400 up to 1200 were observed.

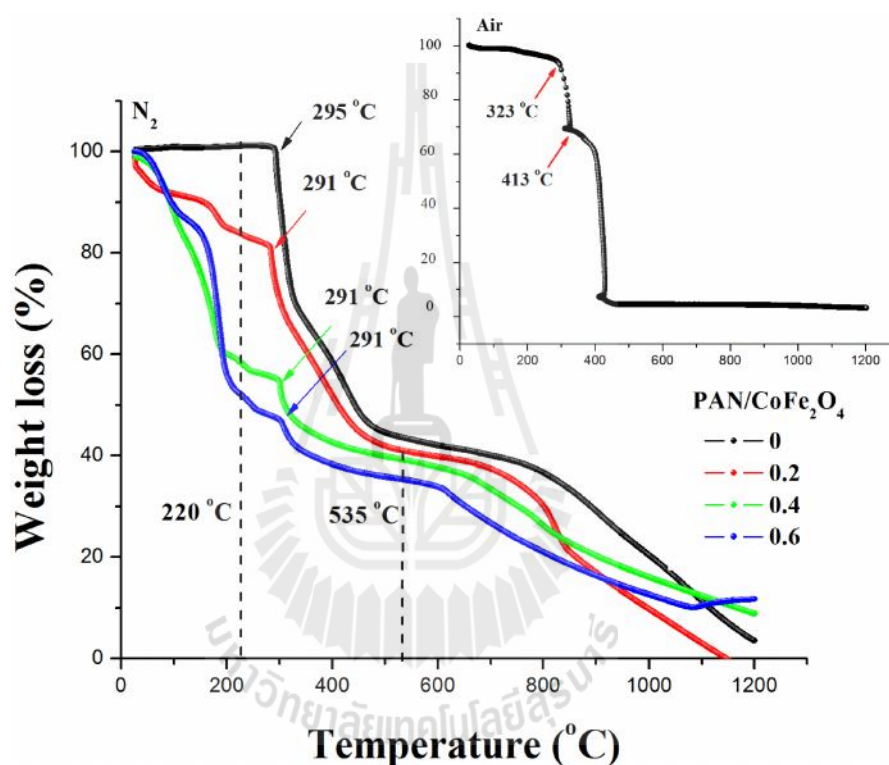


Figure 4.17 TGA curves of CNF and C/CoFe₂O₄ composite nanofibers under N₂ atmosphere and air atmosphere (in set).

4.2.1.2 X-ray diffraction (XRD) analysis of C/CoFe₂O₄ composite nanofibers

Figure 4.18 shows XRD patterns of the CNF and C/CoFe₂O₄ composite nanofibers with different magnetic source content after being stabilized at 220 °C for 1 h in air atmosphere followed by carbonized at 535 °C for 1 h under mixed of air and argon atmosphere. The diffraction peaks at 18.6, 30.4, 35.8, 37.4, 43.4, 53.9, 57.4, 63.1 and 75.5° relate to crystallite planes of (111), (220), (311), (222), (400), (422), (511), (440), and (622), respectively, of cubic spinel structure (Fd3m) CoFe₂O₄ (PDF card no. 22-1086) (Thang *et al.*, 2005). The XRD pattern exhibits considerable line broadening consistent with the fine-particle nature of the cobalt ferrite. The broad diffraction peak at around $2\theta = 26.0^\circ$ and weak peak at 44.0° indicate the formation of graphite structure (Yang *et al.*, 2012) and can be indexed to (002) and (101) planes of the PDF card no. 75-1621, respectively. The weak diffraction peak (002) of graphite with increasing magnetic source content may be due to the crystal growth of CoFe₂O₄ between the interlayer of graphite destroyed the regular layer stacking (Fu *et al.*, 2012). The average particle size (D) of CoFe₂O₄ was calculated by using Scherrer's equation (Klug and Alexander, 1974). The obtained values were 21.54, 54.36 and 44.92 nm for C/CoFe₂O₄_0.2, C/CoFe₂O₄_0.4 and C/CoFe₂O₄_0.6, respectively. The larger particle size of C/CoFe₂O₄_0.4 than that of C/CoFe₂O₄_0.6 is possibly due to larger agglomeration of particles. The d-spacing values of peak (311) was calculated by using Bragg's law and the obtained values of 2.511, 2.517 and 2.506 Å were obtained for C/CoFe₂O₄_0.2, C/CoFe₂O₄_0.4, and C/CoFe₂O₄_0.6 respectively. All the d-spacing values are slightly lower than 2.53 Å for a cubic CoFe₂O₄ (JCPDS 22-1086) possibly due to the effect of CNF matrix. The d-spacing value of 3.33 nm for

pure CNF is close to the typical structure of well graphitized carbonaceous materials (3.38 nm). The lattice constants of 8.372, 8.391 and 8.353 Å for C/CoFe₂O₄_0.2, C/CoFe₂O₄_0.4, and C/CoFe₂O₄_0.6, respectively are close to 0.8391 ± 0.005 Å of the bulk CoFe₂O₄ (Mendelson, 1969).

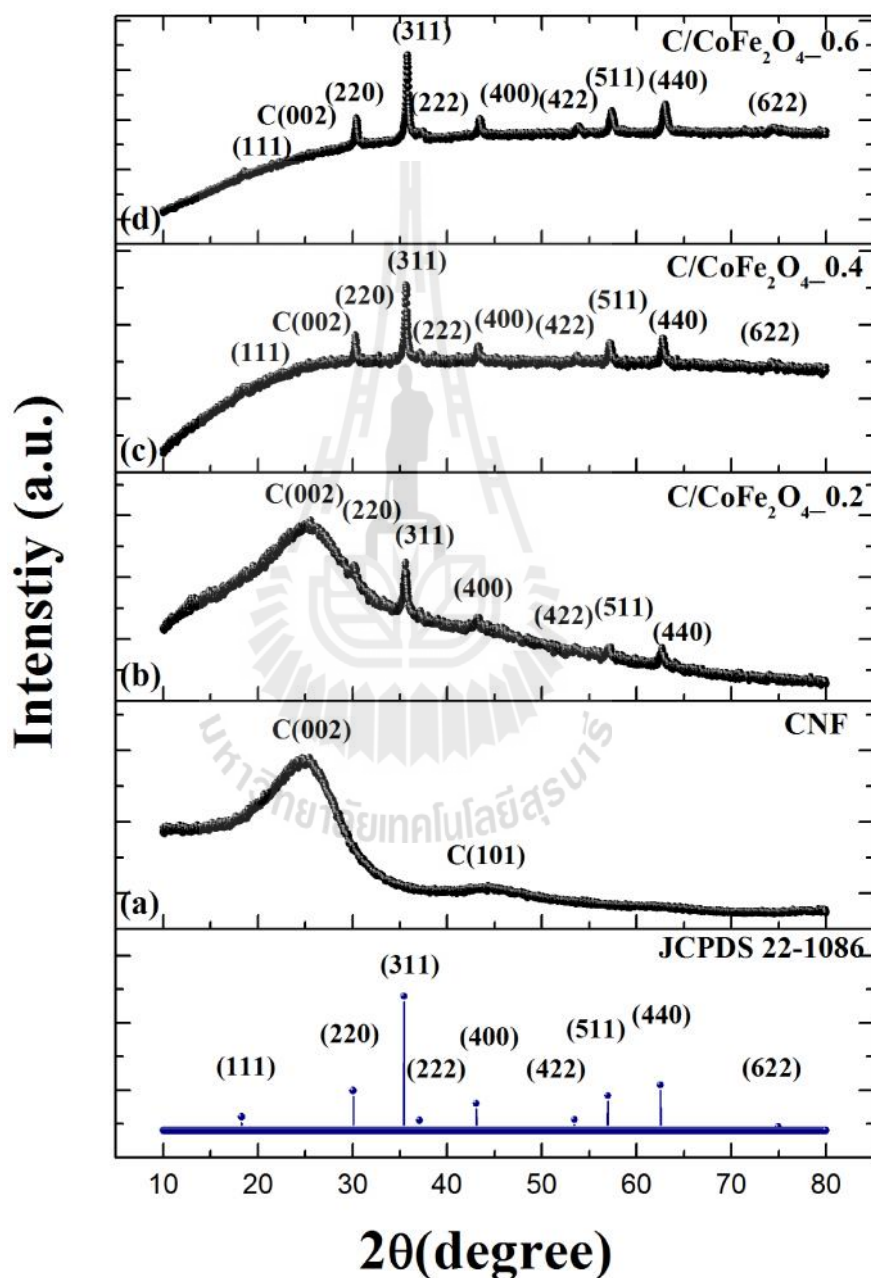


Figure 4.18 XRD patterns of (a) CNF, (b) C/CoFe₂O₄_0.2, (c) C/CoFe₂O₄_0.4 and (d) C/CoFe₂O₄_0.6 composite nanofibers.

4.2.1.3 Morphology of C/CoFe₂O₄ composite nanofibers by FE-SEM and TEM

The morphology of CNF and C/CoFe₂O₄ composite nanofibers before and after carbonization was investigated by Fe-SEM images. The results are revealed in Figure 4.19. It is evident from SEM micrograph that, each individual of as-spun nanofibers before heat treatment appeared long straight and uniform in cross-section with the diameters range from 530-790 nm. The presence of beads in as spun pure PAN is possibly due to low concentration of the solution without magnetic source (Zhang² *et al.*, 2009), The presence of beads is a common problem as they can decreased specific surface area of fibers (Li and Xia, 2004; Demir *et al.*, 2002). No any beads were observed for all electrospun composite nanofibers. After carbonization at 535 °C, the fibers diameters shrinkage of about 11.8, 24.3, 24.6 and 22.3% were obtained for CNF, C/CoFe₂O₄_0.2, C/CoFe₂O₄_0.4 and C/CoFe₂O₄_0.6, respectively. The shrinkage was due to the combustion of PAN resulting in weight loss as presented in TGA curve. Moreover, the fibers started to filmy, attached to other fibers and the uniformity got worse were observed in C/CoFe₂O₄_0.6 (Figure 4.19 (d)).

Figure 4.20 shows the TEM images with corresponding selected-area electron diffraction pattern (SAED) of pure CNF and C/CoFe₂O₄ composite nanofibers. The TEM bright field images of the composite nanofiber show clearly the CoFe₂O₄ nanoparticles with the average particle size of 10-50 nm embedded within the CNF matrix. The corresponding SAED patterns of C/CoFe₂O₄ composite nanofiber correspond to the crystal plane observed in the XRD patterns. The presence of several continue rings diffraction spots, denotes the nanocrystalline CoFe₂O₄. No

any spotty rings were observed in SAED of pure CNF due to its amorphous characteristic.

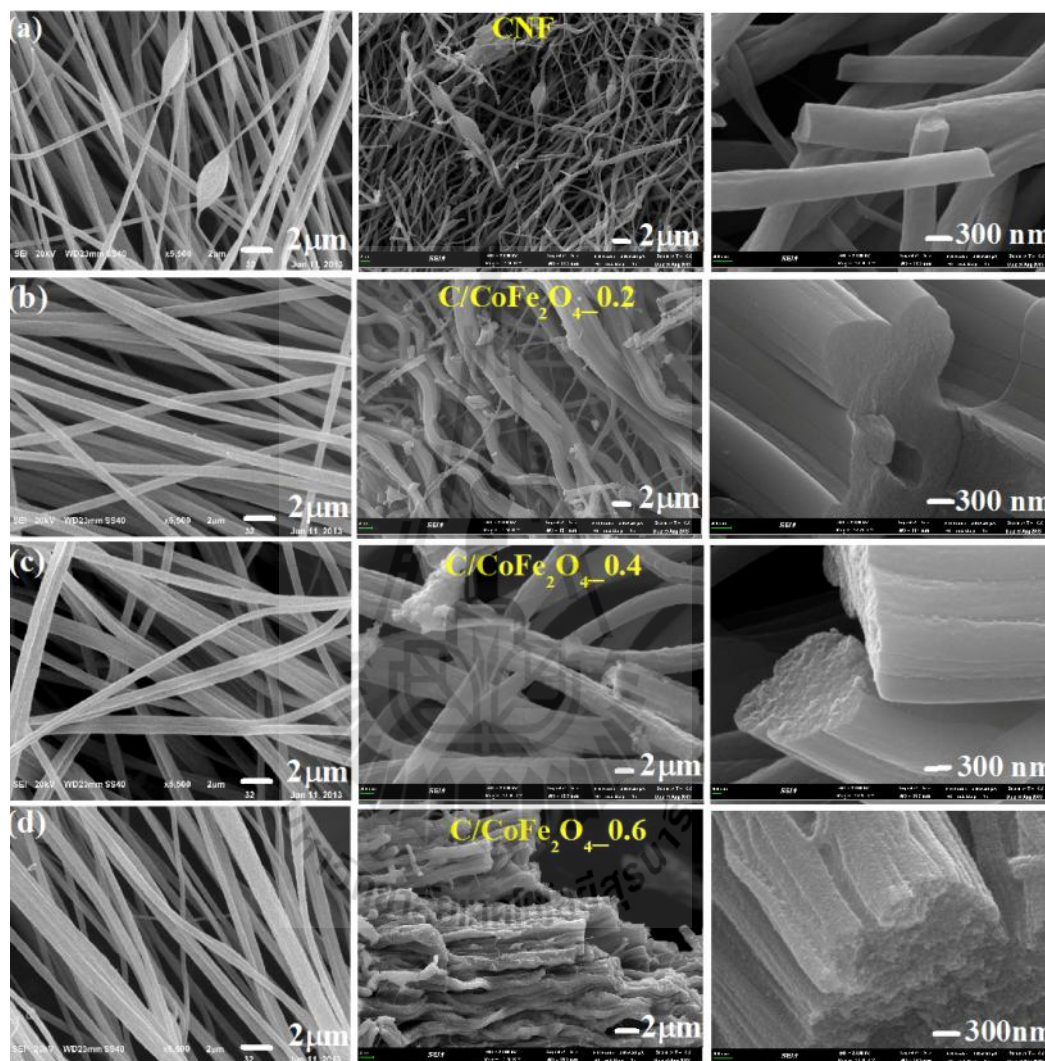


Figure 4.19 SEM micrographs of the electrospun C/CoFe₂O₄ composite nanofibers before carbonization (left), the fibers after carbonization (middle) and their Fe-SEM images (right), respectively of (a) pure CNF, (b) C/CoFe₂O_{4_0.2} (c), C/CoFe₂O_{4_0.4}, and (d) C/CoFe₂O_{4_0.6}.

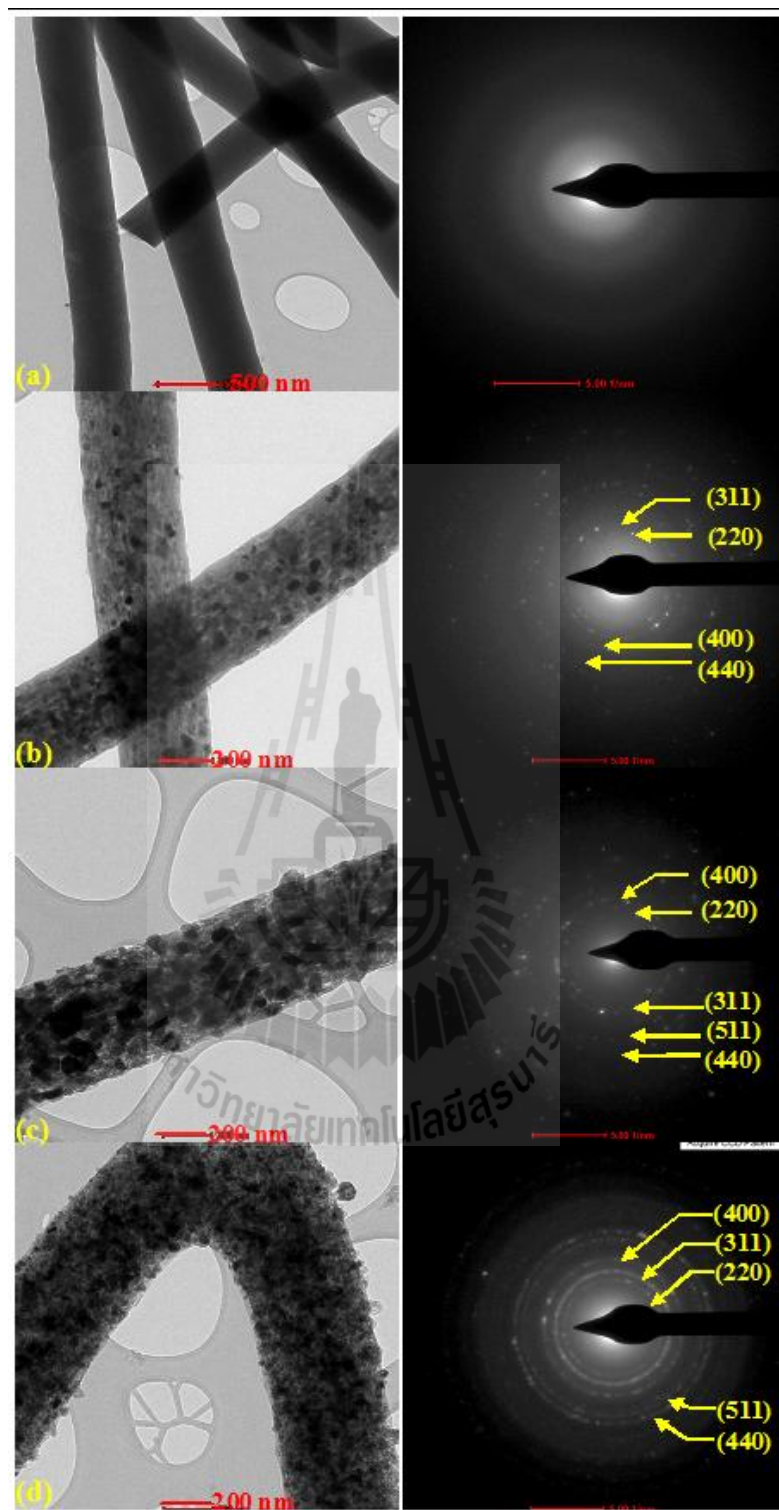


Figure 4.20 TEM bright field images (left) with the corresponding SAED pattern (right) of (a) pure CNF, (b) C/CoFe₂O₄_0.2, (c) C/CoFe₂O₄_0.4, and (d) C/CoFe₂O₄_0.6 composite nanofibers.

4.2.1.4 The structure fingerprints of C/CoFe₂O₄ composite nanofibers characterization by Raman spectroscopy.

The structure of pure CNF and C/CoFe₂O₄ composite nanofibers were further study by Raman spectroscopy. In this work, the Raman spectra of CNF and C/CoFe₂O₄ composite nanofibers are shown in Figure 4.21. The Graphite-like carbon materials usually exhibit G and D band at around 1580 cm⁻¹ and a peak at 1350 cm⁻¹, respectively (Ferrari, 2007). To characterize the graphitization or defect quantities, the intensity ratio of the D and G band ($R = I_D/I_G$) was evaluated by using the Lorentzian fitting. High intensity ratio was observed for the carbonaceous materials with high degree of defects, while the value tend to zero refer to the material that composed entirely of sp³ bonded carbon. In this work, the values of 1.60, 1.57, 1.83 and 1.42 were obtained for CNF, C/CoFe₂O₄_0.2, C/CoFe₂O₄_0.4 and C/CoFe₂O₄_0.6, respectively. The lowest value of 1.42 for C/CoFe₂O₄_0.6 suggests the greatest degree of graphite cluster in the sample (Ji and Zhang, 2009). It is possible that high concentration of magnetic source acts as graphitization catalyst. All prepared samples show lower R value than those values observed in the disordered structures ($I_D/I_G > 4$) (Ji and Zhang, 2009). In this work, the in-plane graphitic crystallite size (L_a) was also calculated from the data fitting using the equation: L_a (nm) = $C(\lambda) / (I_D/I_G)$, where C (532 nm) is constant and is ~ 4.4 (Knight and White, 1989). According to the equation, high defects high the D peak intensity and thus the smaller L_a . The L_a values of 2.75, 2.80, 2.41 and 3.10 were obtained for CNF, C/CoFe₂O₄_0.2, C/CoFe₂O₄_0.4 and C/CoFe₂O₄_0.6, respectively. The result is in good agreement with observed in C/CuFe₂O₄ group. Lists of Raman parameters are presented in Table 4.9

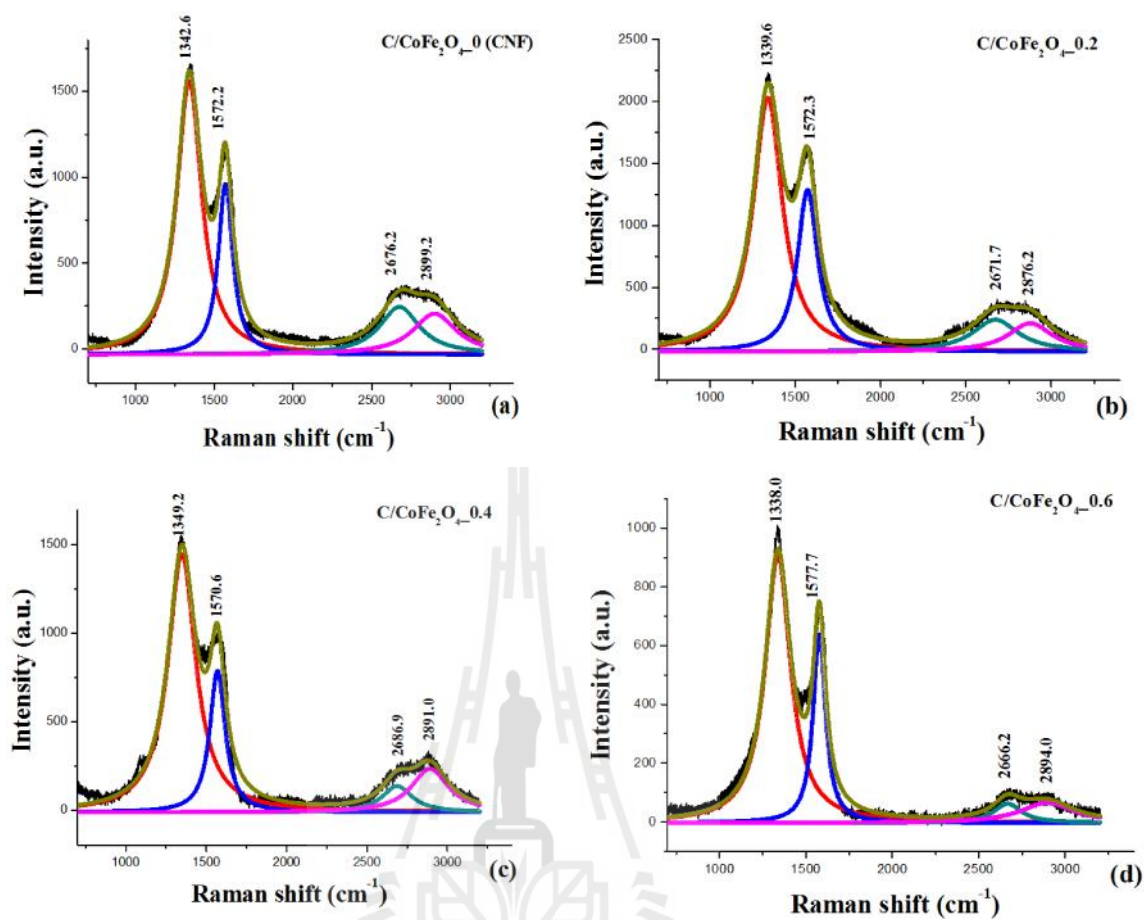


Figure 4.21 Raman spectra of (a) pure CNF, (b) C/CoFe₂O₄_0.2, (c) C/CoFe₂O₄_0.4, and (d) C/CoFe₂O₄_0.6 composite nanofiber.

Table 4.9 Lists of Raman peak height, Raman peak width, R value (I_D/I_G) and in plane graphite crystallite size (L_a) of CNF and C/CoFe₂O₄ composite nanofibers with different magnetic source concentration.

Sample	Peak height (cm ⁻¹)				Peak width (cm ⁻¹)				R	L_a (nm)
	D	G	2D ₁	2D ₂	D	G	2D ₁	2D ₂		
CNF	1981	1236.3	329.8	313.4	183.5	108.2	242.7	298.4	1.60	2.75
C/CoFe ₂ O ₄ 0.2	2568	1636.9	323.8	288.4	206.8	143.4	326.5	314.1	1.57	2.80
C/CoFe ₂ O ₄ 0.4	1832	1003.3	186.2	311.3	208.1	116.4	229.5	278.1	1.83	2.41
C/CoFe ₂ O ₄ 0.6	1142	804.6	82.5	86.0	177.2	87.40	195.1	373.5	1.42	3.10

4.2.1.5 Characterization of surface area of C/CoFe₂O₄ composite nanofiber by the Brunauer-Emmett-Teller.

Figure 4.22 shows the N₂ adsorption/desorption isotherms of CNF and C/CoFe₂O₄ samples with different CoFe₂O₄ source content. According to IUPAC classification (section 3.2.6), the isotherm of pure CNF is type I with a small loop at high relative pressure ($P/P_0 > 0.8$) suggesting micro pore structure with the presentation of small meso and macro-pores. C/CoFe₂O₄_0.2 and C/CoFe₂O₄_0.4 exhibited type I without a small loop at high relative pressure suggest the micropore structure. The isotherms of C/CuFe₂O₄_0.6 exhibit a typical IV with H3 hysteresis loop characterizing the appearance of mesopores (Inagaki *et al.*, 2010). The adsorption jump was observed between partial pressures of 0.45–0.95, followed by a linear increase up to 0.99. The average pore size values of 23.2, 4.35, 8.29 and 4.26 nm were obtained for CNF, C/CoFe₂O₄_0.2, C/CoFe₂O₄_0.4 and C/CoFe₂O₄_0.6

respectively. The composite nanofibers show significant low value compared to pure CNF. In electrochemical studies, the ability to store charge of cell is dependent on the accessibility of the ions to the porous surface-area, so electrolyte ion size and electrode material pore size must be optimal. The BET surface area was found to be about 30, 121, 60 and 151m²/g for CNF, C/CoFe₂O₄_0.2, C/CoFe₂O₄_0.4 and C/CoFe₂O₄_0.6, respectively. It is speculated from the result that, the composite of CNF with CoFe₂O₄ may effectively reduce the aggregation of CoFe₂O₄ nanoparticles and thus leading to larger specific surface area compared to pure CNF. The BET specific surface area, the mean pore diameter and the total pore volume of the CNF and C/CoFe₂O₄ composite nanofiber with different metal source concentration are listed in Table 4.10.

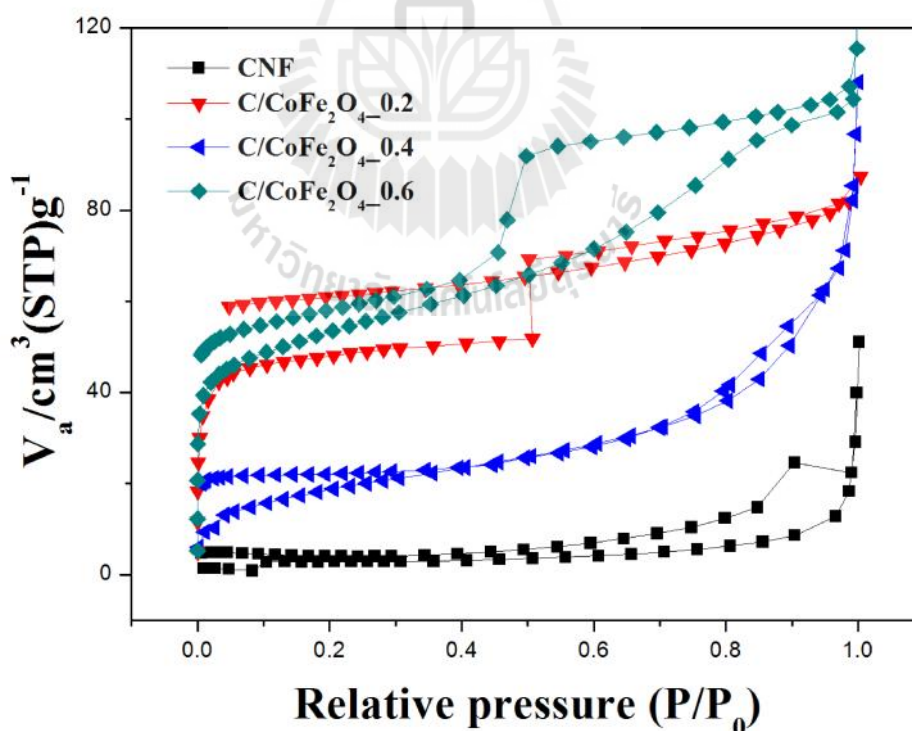


Figure 4.22 N₂ adsorption/desorption isotherms of (a) pure CNF, (b) C/CoFe₂O₄_0.2, (c) C/CoFe₂O₄_0.4, and (d) C/CoFe₂O₄_0.6 composite nanofibers.

Table 4.10 Summary of mean pore diameter, surface area and total pore volume of CNF and C/ CoFe₂O₄ composite nanofibers with different metal source concentration.

Samples	Mean pore diameter (nm)	Surface area (m ² /g)	Total pore volume (cm ³ /g)
CNF	23.22	30.07	0.0178
C/CoFe ₂ O ₄ _0.2	4.36	120.54	0.1313
C/CoFe ₂ O ₄ _0.4	8.30	59.82	0.1240
C/CoFe ₂ O ₄ _0.6	4.26	151.15	0.1609

4.2.1.6 X-ray absorption spectroscopy study of the Fe and Co K- edge in C/CoFe₂O₄ composite nanofibers.

In order to determine the oxidation states of Co and Fe ions in CoFe₂O₄, XANES spectra at room temperature were measured at Fe and Co K-absorption edges. Figure 4.23 shows the normalized XANES spectra at the Fe and Co K-edge and their corresponding first derivatives spectra for the C/CoFe₂O₄ composite nanofibers. The oxidation states of Fe and Co in CoFe₂O₄ nanoparticle are shown along with the standard samples of Fe foil, FeO, Fe₂O₃, Fe₃O₄, Co foil, CoO and Co₃O₄ for Fe⁰, Fe²⁺, Fe³⁺, Fe^{2+,3+}, Co⁰⁺, Co²⁺ and Co³⁺, respectively. XANES spectra at Fe K-edge show similar to Fe₂O₃ for all the prepared samples indicating Fe³⁺ oxidation state. The results were confirmed by their first derivatives plot as shown in Figure 4.23 (c). The pre-edge peak at Fe K-edge (1s to 3d transitions with 3d-4p mixing) (Grunes, 1983) was observed for all the prepared samples. Strong intensity peak is typical for Fe atom in tetrahedral site and the results are consistent with the EXAFS observation which will be discussed later. At Co K-edge, the spectra of

C/CoFe₂O₄_0.2 and C/CoFe₂O₄_0.4 look very similar to CoO, and it could be concluded from the first derivatives plot (Figure 4.23 (f)) that the oxidation state of cobalt are +2. The XANES spectra for C/CoFe₂O₄_0.6 show distinct features and it seems to arise from a combination of CoO and Co₃O₄ (as inset of Figure 4.23 (d)). The result was confirmed by edge energies (Table 4.11) and its first derivatives plot that, Co ions in C/CoFe₂O₄_0.6 were mixed oxidation state of Co⁺² and Co⁺³ although these phases were not found in the XRD patterns. The pre-edge peak at Co K-edge for the C/CoFe₂O₄_0.6 is largest suggesting huge occupation of Co²⁺ in A site. Low Co²⁺ ions in B site may be attributed to two possible reasons. First, it is possibly due to the transition of Co²⁺ ions to A site. Second, it is the effect from the combination of second phases of CoO and Co₃O₄, as known that Co₃O₄ is the normal spinel structure where Co²⁺ and Co³⁺ ions occupy A sites, respectively. Lower intensity pre-edge peak of C/CoFe₂O₄_0.2 and C/CoFe₂O₄_0.4 samples at Co K-edge indicates the fraction of Co²⁺ is mostly located at B site confirming the inverse spinel structure of material. The results are compatibility with the EXAFs study, in which presented in the next part. The edge energies and oxidation states at Fe and Co K-edge for all the prepared samples are listed in Table 4.11.

Table 4.11 Edge energies and oxidation states of all C/CoFe₂O₄ composite nanofibers along with the standard samples.

Sample/standard	Edge element	Oxidation state	Absorption edge (eV)
C/CoFe ₂ O ₄ _0.2	Fe	+3	7125.03
	Co	+2	7720.42
C/CoFe ₂ O ₄ _0.4	Fe	+3	7125.17
	Co	+2	7720.79
C/CoFe ₂ O ₄ _0.6	Fe	+3	7125.09
	Co	+2,+3	7722.17
Fe	Fe	0	7112
FeO	Fe	+2	7120.65
Fe ₃ O ₄	Fe	+2,+3	7123.40
Fe ₂ O ₃	Fe	+3	7124.85
Co	Co	0	7708.96
CoO	Co	+2	7720.79
Co ₃ O ₄	Co	+2,+3	7724.4

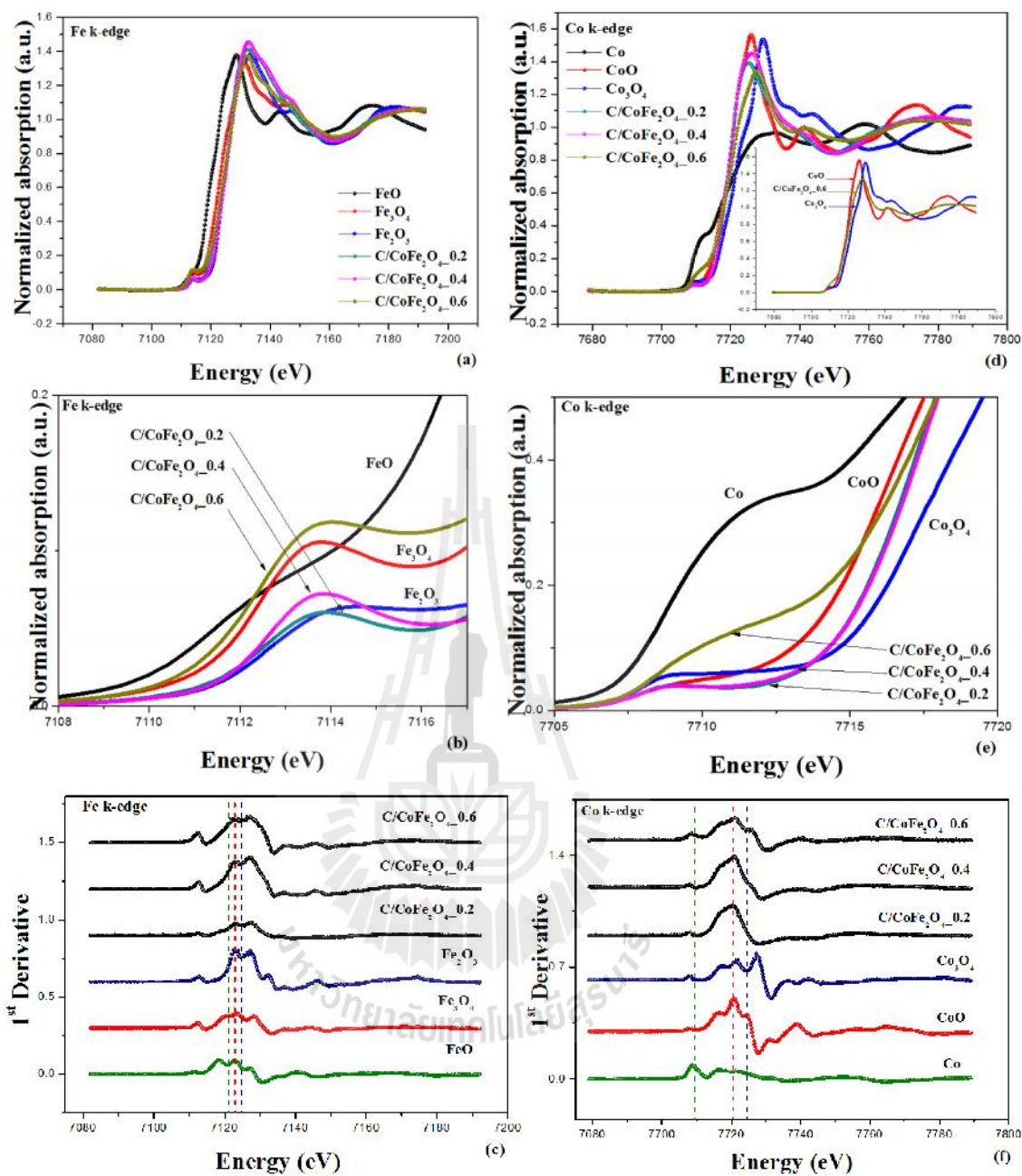


Figure 4.23 XANES spectra, pre-edge peak, and corresponding first derivatives plot, respectively of C/CoFe₂O₄ composite nanofibers at Fe K-edge (a, b, c) and at Co K-edge (d, e, f).

To further understand the environment of Co and Fe atom in CoFe_2O_4 structure, the EXAFS data at Fe and Co K-edge for all composite nanofibers were studied. As known that, the distribution of cations over A and B sites of spinel ferrite materials strongly influence on their magnetic and electrical properties. In this section the distribution of cations (Co^{2+} and Fe^{3+}) in CoFe_2O_4 was studied. Normally, bulk CoFe_2O_4 is inverse spinel structure. The divalent cations (Co^{2+}) occupy B sites, while the trivalent cations (Fe^{3+}) occupied in both A and B sites. In EXAFS analysis, the Fourier transforming was performed in the range of 2.5-10 \AA^{-1} . The $k^2\chi(k)$ weighted in k space and the corresponding Fourier transform (FT) in R space from experiment and fitting results without phase correction of some prepared samples are shown in Figure 4.24. It was found from the study that, the profiles at Co and Fe K-edges of C/ $\text{CoFe}_2\text{O}_4_{0.2}$ are similar to those of C/ $\text{CoFe}_2\text{O}_4_{0.4}$ apart from a slightly reduction in the amplitude of the peaks (Figures 4.24 (a), (b)). The result indicates their similarity of the local environment around the absorber Fe^{3+} or Co^{2+} . The EXAFs profile of C/ $\text{CoFe}_2\text{O}_4_{0.6}$ shows significant difference, indicating its structural environment around Fe^{3+} and Co^{2+} is different.

At Fe K-edge of C/ $\text{CoFe}_2\text{O}_4_{0.2}$, the first shells fitted indicate that A site cation is surrounded by four nearest oxygen backscatterers at a distance 1.933 \AA ($\text{Fe}_A\text{-O}$). Meanwhile, the B site cations have six backscatterers ($\text{Fe}_B\text{-O}$) at distance of ~ 2.14 \AA . The results were also observed in C/ $\text{CoFe}_2\text{O}_4_{0.4}$ but the interatomic distances are slightly lower (1.930 \AA for $\text{Fe}_A\text{-O}$; 2.071 \AA for $\text{Fe}_B\text{-O}$). The second shell fitted at the distance of ~ 3 \AA (3.049 and 2.951 \AA for C/ $\text{CoFe}_2\text{O}_4_{0.2}$ and C/ $\text{CoFe}_2\text{O}_4_{0.4}$, respectively) with three metal backscatterers is typical for cations occupied B sites ($\text{Fe}_B\text{-Co}_B$, $\text{Fe}_B\text{-Fe}_B$). Meanwhile, at ~ 3.6 \AA surrounded by six metal backscatterers, it

is typical of the cations occupying in either A or B site ($\text{Fe}_A\text{-Fe}_A = 3.635 \text{ \AA}$; $\text{Fe}_A\text{-Co}_A = 3.635 \text{ \AA}$ and $\text{Fe}_B\text{-Fe}_B = 3.575 \text{ \AA}$ for C/CoFe₂O₄_0.2; $\text{Fe}_A\text{-Fe}_A = 3.628 \text{ \AA}$; $\text{Fe}_A\text{-Co}_A = 3.628 \text{ \AA}$, and $\text{Fe}_B\text{-Fe}_B = 3.466 \text{ \AA}$ for C/CoFe₂O₄_0.4). Moreover, the cations occupying A site with four metal backscatters were observed at the distance $\sim 3.8 \text{ \AA}$ ($\text{Fe}_A\text{-Fe}_A = 3.796$ and 3.789 \AA for C/CoFe₂O₄_0.2 and 0.4, respectively). At Co K-edge of C/CoFe₂O₄_0.2, the spectra show two significant nearest shell. The first shells at $\sim 2.04 \text{ \AA}$ originated from Co_B-O bond with coordination number of six, while the second shells was found at $\sim 2.53 \text{ \AA}$ corresponds to Co_B-Co_B neighbors located at B site. For C/CoFe₂O₄_0.4, the absorber environment does not change significantly from that of the C/CoFe₂O₄_0.2 (2.02 \AA for Co_B-O and 2.94 \AA for Co_B-Co_B). It should be noted for Fe and Co K-edges that, the shorter interatomic distance of Fe-O than Co-O in C/CoFe₂O₄ and C/CoFe₂O₄_0.4 is due to smaller atomic radius of Fe³⁺ compared to Co²⁺ (Kravtsov *et al.*, 2006). The third shells at distance of $\sim 3.5 \text{ \AA}$ is relating to the distribution of cations in A site. Then, the intense feature of second shells when compared to the third shells reveals the major portion of Co ions located in B site. This result confirmed the inverse spinel structure of the samples. However, it should be noted for C/CoFe₂O₄_0.2 and C/CoFe₂O₄_0.4 that their structures are not a perfect inverse spinel. It could be included the tetrahedral environment for Co similar to that used for Fe in the fitting. However, the quality of the fits (R-factor) is satisfactory. Very low R factor indicates a good quality of the fitting and confirmed totally inverse spinel structure. Good obtained result is possibly due to less number of Co atoms in A site and could be neglected as our assumption. For fitting spectra of C/CoFe₂O₄_0.6 shown that, the first shells at 1.935 and 2.097 \AA originates from Co_A-O bond with coordination number of four and Co_B-O bond with coordination number

of six, respectively, while the second shells at 3.479 Å and 2.412 Å corresponds to $\text{Co}_A\text{-Fe}$ and $\text{Co}_B\text{-Co}_B$, respectively. Higher feature of the second shells compared to the first shells is due to the large number of the surrounded Co ions in A site with the coordination number of twelve. According to EXAFs fitting data, it was found the occupation of Co^{2+} cation in both A and B site with nearly portion (58.9 and 41.1% in A and B site, respectively). The result reveals that the structure of $\text{C/CoFe}_2\text{O}_4_{-0.6}$ is partial inverse spinel structure. At Fe k-edge, the first shells at 1.819 and 1.955 Å originates from $\text{Fe}_A\text{-O}$ bond with coordination number of four and $\text{Fe}_B\text{-O}$ bond with coordination number of six, respectively. The second shells were found at 3.183 Å and 2.834 Å corresponds to $\text{Fe}_A\text{-Co}$ and $\text{Fe}_B\text{-Co}$, respectively. It was also found from the EXAFS fitting that, Fe^{3+} ions occupied in both A and B site with the portion of 38.5 and 61.5%, respectively. The structural parameters of the EXAFS fitting are listed in Table 4.12-4.14.



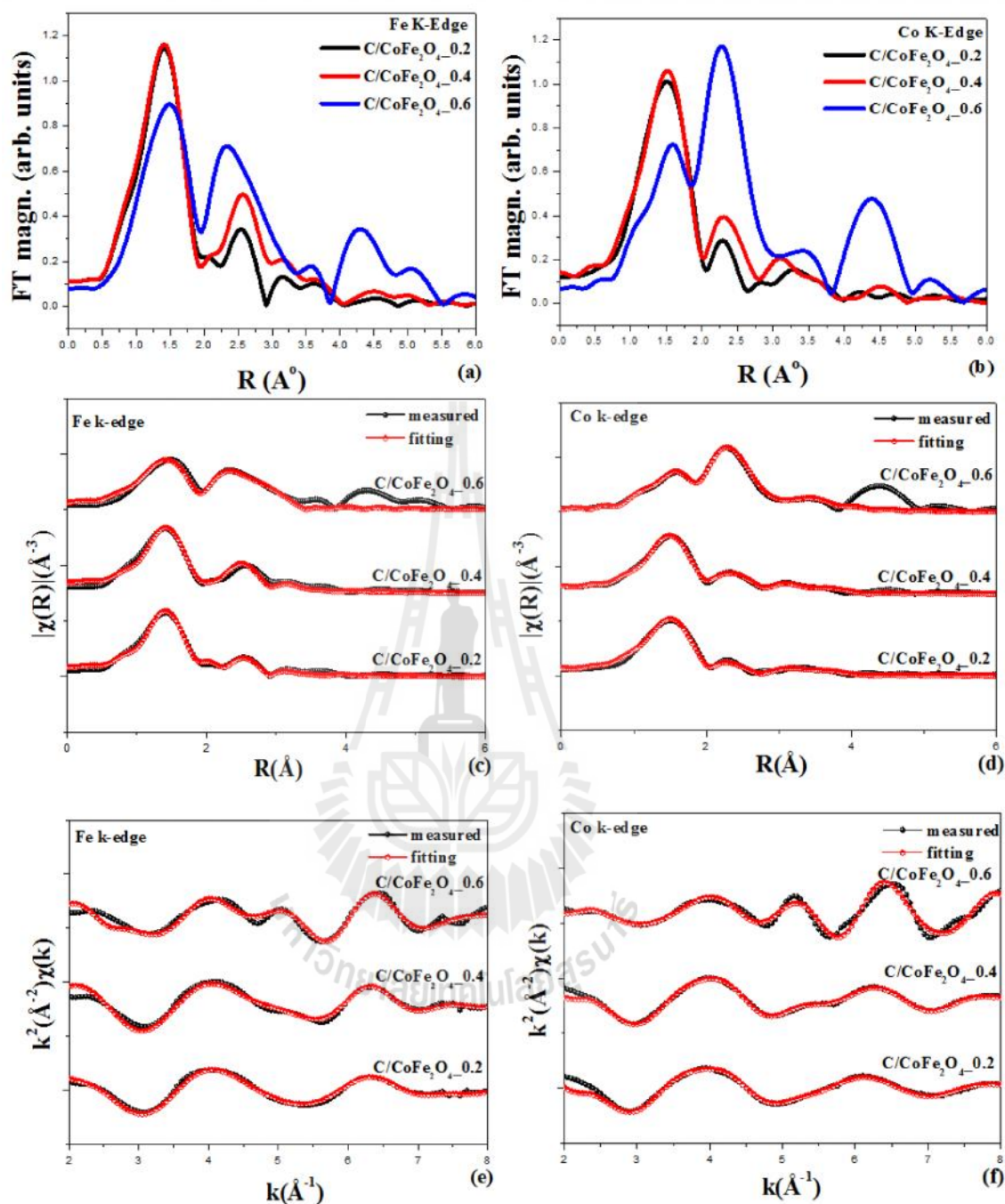


Figure 4.24 (a, b) Fourier transform in R-space of three different composite samples at Fe and Co k-edge, respectively. (c, d) Fourier transform in R-space with the corresponding fitted spectra. (e, f) The $k^2(\chi(k))$ plots with the corresponding fitting spectra at Fe and Co K-edge, respectively.

Table 4.12 Lists of coordinate number (N), amplitude reduction (S_0^2), Debye-Waller Factor (σ^2), interatomic distances (R), and R-factor obtained by fitting the experimental EXAFS data at Fe and Co K-edge for C/CoFe₂O₄_0.2.

Sample	Site	Shell	N	S_0^2	σ^2	R	
Co k-edge C/CoFe ₂ O ₄ _0.2	B	Co-O	6	0.880	0.01400	2.03979	
		Co-Fe	3	0.880	0.02801	3.25449	
		Co-Co	3	0.880	0.02768	2.52536	
		R-factor	Co-Fe	6	0.880	0.03277	3.41464
		0.0079902	Co-O	6	0.880	0.02451	3.44513
			Co-O	12	0.880	0.03151	4.53261
			Co-O-O	36	0.880	0.02941	4.29592
Fe-O	4		0.614	0.00300	1.93308		
Fe k-edge C/CoFe ₂ O ₄ _0.2	A	Fe-Fe	6	0.614	0.02357	3.63460	
		Fe-Co	6	0.614	0.73657	3.63460	
		Fe-Fe	4	0.614	0.02357	3.79623	
		R-factor	Fe-O-O	4	0.614	0.00600	3.86605
		0.0098747	Fe-O	6	0.134	0.00300	2.13597
			Fe-Fe	3	0.134	0.00987	3.04855
			B	Fe-Co	3	0.134	0.00417
Fe-Fe	6			0.134	0.00987	3.57473	
Fe-O-O	24			0.134	0.00336	3.64635	

Table 4.13 Lists of coordinate number (N), amplitude reduction (S_0^2), Debye-Waller Factor (σ^2), interatomic distances (R), and R-factor obtained by fitting the experimental EXAFS data at Fe and Co K-edge for C/CoFe₂O₄_0.4.

Sample	Site	Shell	N	S_0^2	σ^2	R	
Co k-edge C/CoFe ₂ O ₄ _0.4	B	Co-O	6	0.670	0.01012	2.01627	
		Co-Fe	3	0.670	0.01627	3.19223	
		Co-Co	3	0.670	0.01414	2.94488	
	R-factor 0.0055208	Co-Fe	6	0.670	0.01903	3.40560	
		Co-O	6	0.670	0.01774	3.46210	
		Co-O	12	0.670	0.02278	4.53656	
Fe k-edge C/CoFe ₂ O ₄ _0.4	A	Fe-O	4	0.630	0.00300	1.92951	
		Fe-Fe	6	0.630	0.06502	3.62790	
		Fe-Co	6	0.630	0.01954	3.62790	
		R-factor 0.0193022	Fe-Fe	4	0.630	0.06762	3.78923
		Fe-O-O	12	0.630	0.00543	3.50488	
		Fe-O-Fe	12	0.630	0.00300	3.86263	
	B	Fe-O	6	0.277	0.00300	2.07113	
		Fe-Fe	3	0.277	0.00300	2.95601	
		Fe-Co	3	0.277	0.04265	2.95601	
		Fe-Fe	6	0.277	0.00351	3.46622	
		Fe-O	6	0.277	0.00525	3.63156	
Fe-O-O	24	0.277	0.00510	3.53566			

Table 4.14 Lists of coordinate number (N), amplitude reduction (S_0^2), Debye-Waller Factor (σ^2), interatomic distances (R), and R-factor obtained by fitting the experimental EXAFS data at Fe and Co K-edge for C/CoFe₂O₄_0.6.

Sample	Site	Shell	N	S_0^2	σ^2	R
Co k-edge C/CoFe ₂ O ₄ _0.6 R-factor 0.0740676	A	Co-O	4	0.589	0.00180	1.93536
		Co-Fe	12	0.589	0.00300	3.47963
		Co-O	12	0.589	0.00339	3.64493
		Co-Co	4	0.589	0.00275	3.64238
		Co-O-Fe	24	0.589	0.00480	3.79399
	B	Co-O	6	0.411	0.00300	2.09718
		Co-Fe	3	0.411	0.00300	2.78802
		Co-Co	3	0.411	0.00164	2.41184
		Co-Fe	6	0.411	0.00352	3.26938
		Co-O-O	24	0.411	0.00512	3.58009
Fe k-edge C/CoFe ₂ O ₄ _0.6 R-factor 0.0485138	A	Fe-O	4	0.385	0.00300	1.81936
		Fe-Fe	6	0.385	0.00400	3.40233
		Fe-Co	6	0.385	0.02869	3.18331
		Fe-O	12	0.385	0.00565	3.42670
		Fe-Fe	4	0.385	0.00786	3.44184
	B	Fe-O-O	48	0.385	0.00673	4.08175
		Fe-O	6	0.615	0.00300	1.95489
		Fe-Co	3	0.615	0.00125	2.83394
		Fe-Fe	3	0.615	0.00300	3.01270
		Fe-Fe	6	0.615	0.00352	3.53270
		Fe-O	6	0.615	0.00526	3.42779

4.2.2 Magnetic properties of C/CoFe₂O₄ composite nanofibers.

The magnetic properties of CNF and three types of C/CoFe₂O₄ composite nanofibers with applied fields of ± 10 kOe are shown in Figure 4.25. The magnetization was measured and normalized to the whole mass measurement sample. It was found from the M-H curve at room temperature (Figure 4.25 (a)) that, CNF shows diamagnetic behavior, while all composite samples exhibit the ferrimagnetic behavior with the saturation magnetization (M_s) increased linearly with increasing of magnetic source content (0.22, 2.55 and 42.8 emu/g for C/CoFe₂O₄_0.2, C/CoFe₂O₄_0.4, and C/CoFe₂O₄_0.6, respectively). The largest value of C/CoFe₂O₄_0.6 was higher than those of other carbon based composite such as MWCNT/CoFe₂O₄ (23 emu/g) (Gonzalez-Sandoval *et al.*, 2004), CNT/CoFe₂O₄ (29.6 emu/g) (Jiang *et al.*, 2010). However, all M_s obtained in our study are lower than that of 74.08 emu/g for bulk CoFe₂O₄ (Okuno *et al.*, 1992). The reasons for such behavior are possibly due to the existence of CNF extinguishing the surface magnetic moment with spin canting (Garcia-Otero *et al.*, 2000). It is worth nothing that the saturation magnetization is not linear dependent on their particle size (Table 4.15). This result is not consistent with results obtained on CoFe₂O₄ nanoparticles reported in literature (Zhao, *et al.*, 2008; Chen *et al.*, 2010). The M_s of C/CoFe₂O₄_0.4 (2.55 emu/g) is much lower than that of C/CoFe₂O₄_0.6 (42.76 emu/g), even though the average particle size is not much different (54 and 45 nm for C/CoFe₂O₄_0.4 and C/CoFe₂O₄_0.6, respectively). It is possible that the content of CoFe₂O₄ also influences on the magnetic properties. Higher content is much dominated. On the other hand, C/CoFe₂O₄_0.6 with smaller crystalline size has a higher M_s than C/CoFe₂O₄_0.4 possibly due to the stronger influence of surface effect from nano

particle. As known that the nanoparticle caused increased volume fraction of surface atoms within the particles and thus contributes to increase of the saturation magnetization value. The coercivity (H_c) shows crystallite size dependent behavior. Higher particle size leads to increase of coercivity. The relationship between the coercive field and crystallite size can be attributed to the change of the effective anisotropy constant of the particles (Jiang *et al.*, 1999). The coercivity values of 612, 1245 and 825 Oe were obtained for C/CoFe₂O₄_0.2, C/CoFe₂O₄_0.4 and C/CoFe₂O₄_0.6, respectively. All H_c values are close to bulk value of CoFe₂O₄ (750-1000 Oe) (Craik, 1975). The enhanced coercivity of the particle dispersion in the CNF matrix is due to the decreased interparticle dipolar interaction, in which arises from the increased nanoparticle spacer distance for the single-domain nanoparticles (Gao *et al.*, 2007; Gao *et al.*, 2008; Klabunde, 2001). The remanence ratio (M_r/M_s) of 0.28, 0.502 and 0.38 were obtained for C/CoFe₂O₄_0.2, C/CoFe₂O₄_0.4 and C/CoFe₂O₄_0.6, respectively. The remanence ratio of 0.502 for C/CoFe₂O₄_0.4 very closed to 0.5 for a system of non-interacting single domain particles with uniaxial anisotropy. It is expected for randomly oriented and completely blocked nanoparticle (Maaz *et al.*, 2007). Other values are lower than 0.5 implying that the particles are in the multiple domain states (Varma *et al.*, 2008). The variation of H_c and M_r/M_s with crystallite size of the prepared samples at room temperature was presented in Figure 4.25 (b). Both of H_c and M_r/M_s values are increased with increasing of crystallite size, this is well agree with the other reported on the CoFe₂O₄/PVAc composite fiber (Ju *et al.*, 2008).

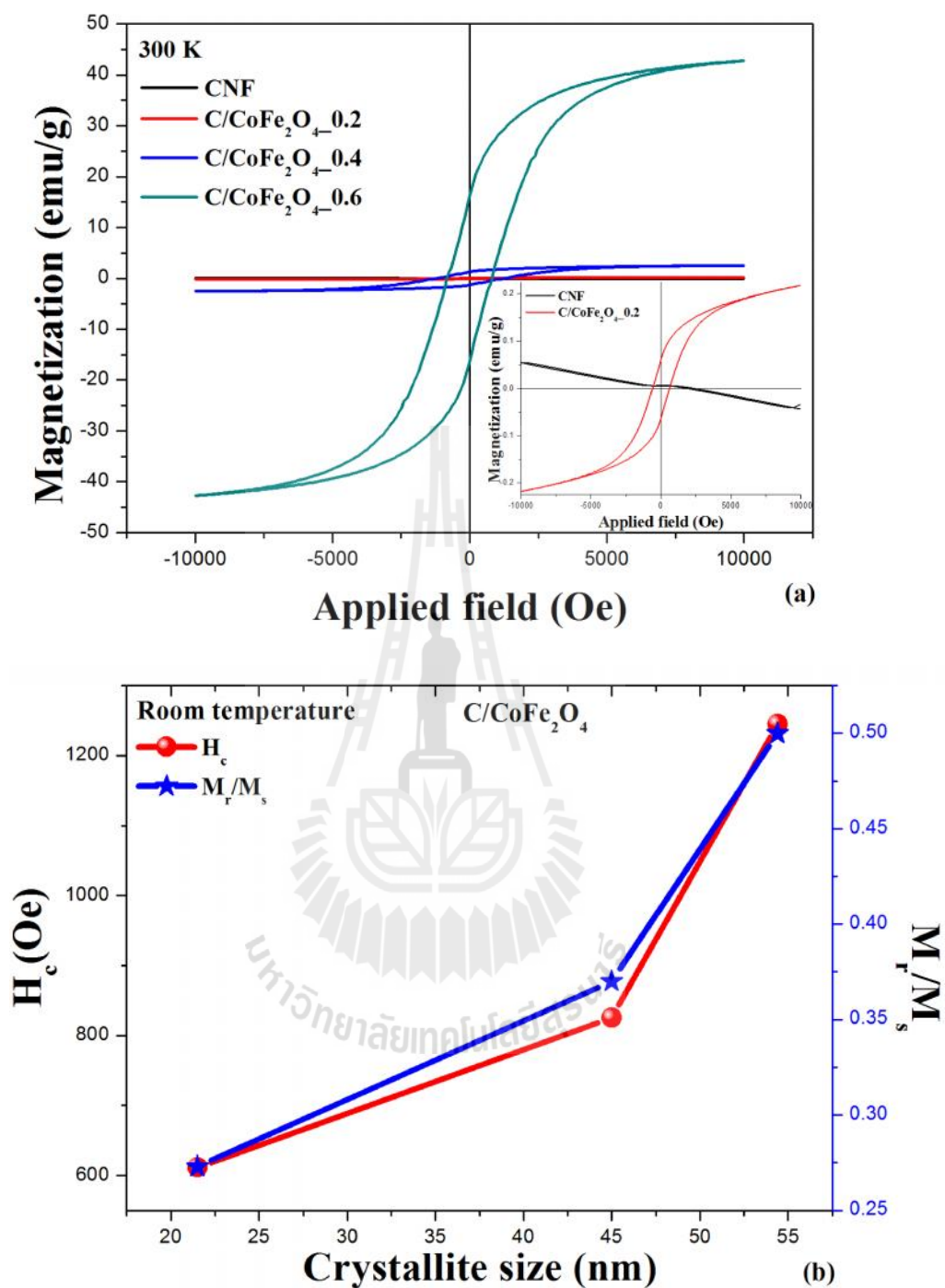


Figure 4.25 (a) Room temperature magnetization of CNF and three types of C/CoFe₂O₄ composite nanofibers carbonized at 535 °C for 1 h, (b) the variation of the coercivity (H_c) and the remanence ratio (M_r/M_s) with crystallite size at room temperature.

The ferrimagnetic behavior for all composite nanofibers was also measured by varying measuring temperature (200 - 390 K). One observes differences in shape of the normalised hysteresis loops depending on temperatures as seen in Figure 4.26. The hysteresis loop for all the prepared samples became wider with decrease measuring temperature. The result suggests increasing of M_s , M_r and H_c due to the suppression of thermal agitation. The squareness value decreased with increasing of temperature as shown in Figure 4.27. The largest squareness value of 0.725 for C/CoFe₂O₄_0.4 was observed at 200 K suggesting randomly oriented equiaxial particles with cubic magnetocrystalline anisotropy at this temperature (Charles *et al.*, 1988). At higher temperature the squareness value is less than 0.5 refer to the particle interact by magnetostatic interaction. The right hand side of the magnetization curve in Figure 4.26 show zero-field-cooled (ZFC) and field-cooled (FC) spectra of the prepared samples measured at the temperature between 50 and 300 K. It was found from ZFC that the magnetic moment increases continuously up to 300 K. No end of raise was observed, indicating the blocking temperature (T_B) being higher than room temperature. The result is consistent with result obtained on CoFe₂O₄/carbon nanofibers prepared by coprecipitation method (Liu *et al.*, 2000; Chen *et al.*, 2010). Large T_B for all the prepared samples is possibly due to large particle size with large volume, thus increasing anisotropy energy. This means the probability to cross over the anisotropy barrier is decreased (Maaz *et al.*, 2007). The corresponding values of the coercivity (H_c), the saturation magnetization (M_s), the remnant magnetization (M_r), and the squareness ratio (M_r/M_s) of CNF and C/CoFe₂O₄ composite nanofibers with different magnetic source concentration are summarized in Table 4.15.

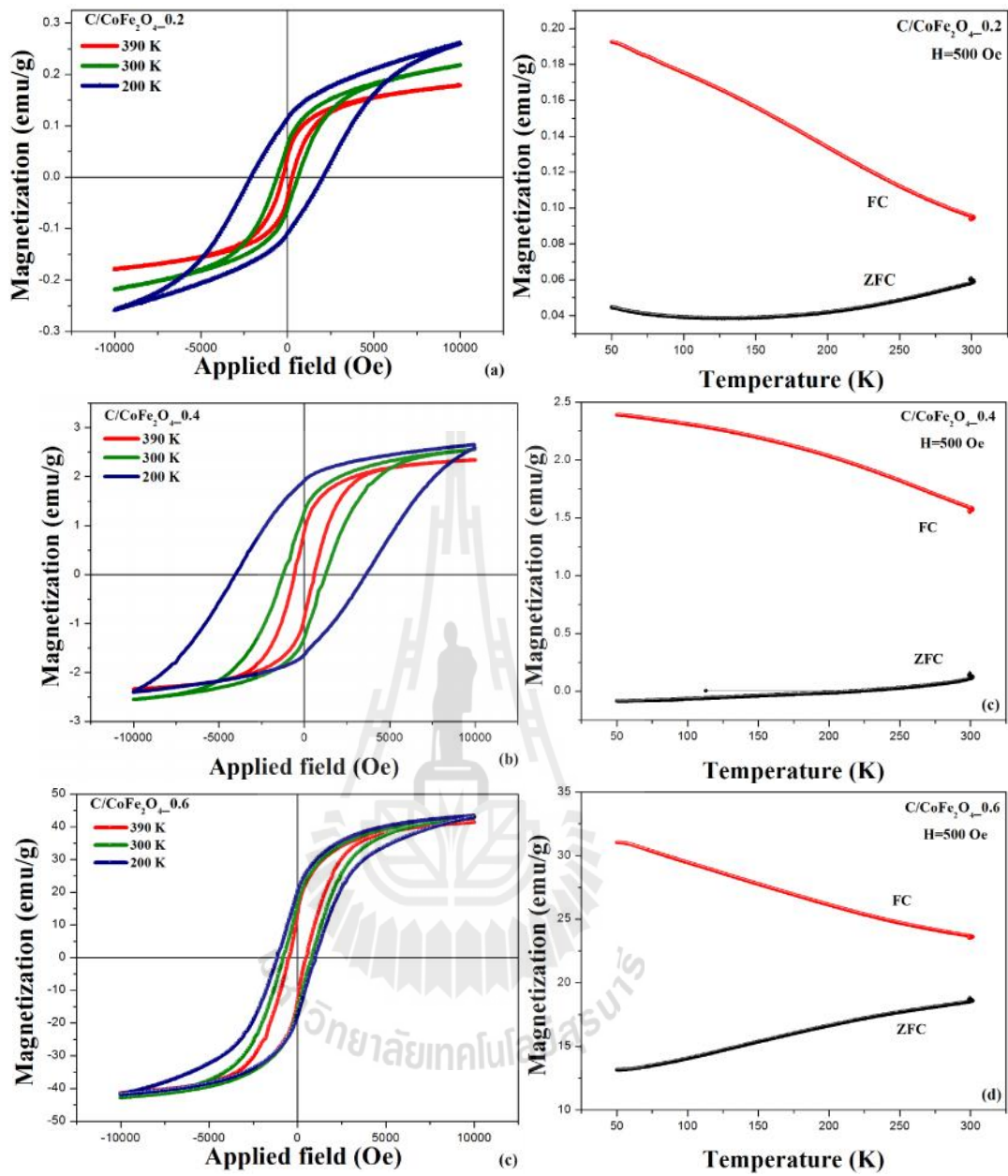


Figure 4.26 The measuring temperature dependence of magnetization and their corresponding zero field-cooled and field-cooled (ZFC-FC) for (a) C/CoFe₂O₄_0.2 (b) C/CoFe₂O₄_0.4 (c) C/CoFe₂O₄_0.6 composite nanofibers.

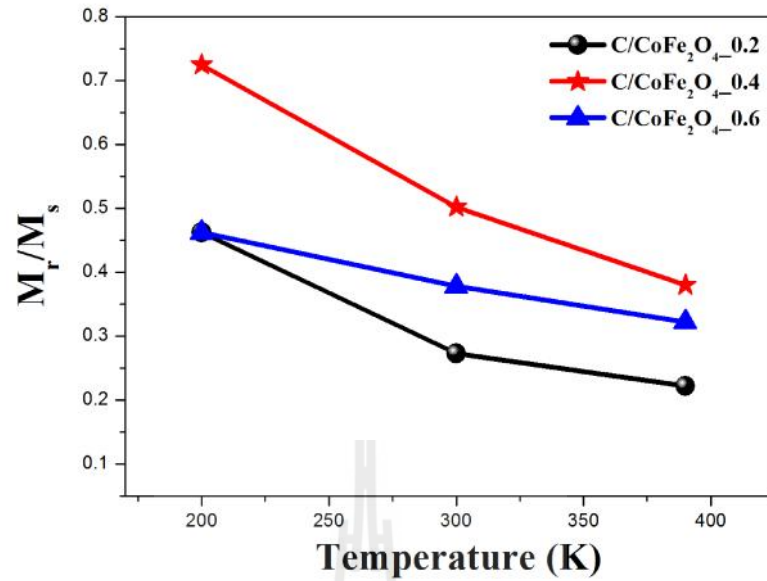


Figure 4.27 The dependence of M_r/M_s on the measurement temperature for C/CoFe₂O₄_0.2, C/CoFe₂O₄_0.4, and C/CoFe₂O₄_0.6 composite nanofibers.

Table 4.15 Lists of the magnetic parameters: coercivity (H_c), saturation magnetization (M_s), squareness ratio (M_r/M_s) and blocking temperature (T_B) of C/CoFe₂O₄ composite nanofibers with different magnetic source concentration.

Sample	Crystallite size (nm)	T (K)	H_c (Oe)	M_s (emg/g)	M_r/M_s	T_B (K)
C/CoFe ₂ O ₄ _0.2	21.54	200	2118	0.26	0.462	>300
		300	612	0.22	0.273	
		390	56	0.18	0.222	
C/CoFe ₂ O ₄ _0.4	54.36	200	4025	2.65	0.725	>300
		300	1245	2.55	0.502	
		390	580	2.34	0.380	
C/CoFe ₂ O ₄ _0.6	44.92	200	1151	43.37	0.462	>300
		300	825	42.76	0.378	
		390	505	41.43	0.322	

4.2.3 Electrochemical properties study of C/CoFe₂O₄ composite nanofibers

In this section, the capacitive performance of C/CoFe₂O₄ electrode were evaluated using cyclic voltammetry (CV), galvanostatic charge/discharge (GCD) and the electrochemical impedance spectroscopy (EIS) techniques in 1 M KOH electrolyte solution. The CV measurement was performed in the potential range of -0.2 - 0.35 V. The galvanostatic charge/discharge test was run at the current density of 0.1, 0.25, 0.5, 0.75 and 1 A/g. The impedance behavior was tested in a frequency range of 0.1 - 10⁵ Hz.

4.2.3.1 Cyclic Voltammetry measurement

Figure 4.28 show cyclic voltammograms of CNF, C/CoFe₂O₄ and CoFe₂O₄ electrodes in 1.0 M KOH electrolyte. The operating voltage potential was set from -0.2 to 0.35 to avoid the oxygen evolution. The measured currents were normalized with the electrode mass. It was found that, C/CoFe₂O₄ shows the largest area surrounded CV curve, while CNF electrode shows the smallest area. No significant current peak was observed in CV curve of CNF suggesting typical double layer behavior of electrode (Wen *et al.*, 2009; Qu *et al.*, 2008). The characteristics of redox peaks were observed in the CV curve of CoFe₂O₄ and C/CoFe₂O₄ electrodes relates to electron reduction/oxidation transition. It can speculate that CoFe₂O₄ nanoparticles generate the pseudo capacitance. No anodic peak was observed during the selected potential window, while the negative current peak in which arises from the cathodic reduction was clearly observed at around 0.21 and 0.23 V for C/CoFe₂O₄ and CoFe₂O₄, respectively. This cathodic peak is probably associated with the reduction of Fe³⁺ and Co²⁺ of the CoFe₂O₄ (Chu *et al.*, 2004). According to the varying scan rate up from 2 to 200 mV/s, the current density for all the prepared cells

increase with increasing of the scan rate due to flux towards the electrode is larger at faster scan. CNF electrode shows CV curves as box-like shape at lower scan rate than 50mV/s suggesting the typical for ideal capacitor behavior. The rectangular shape distortion was observed at higher scan rate, possibly due to the electrode resistance (Patil *et al.*, 2013). Each CV curve of C/CoFe₂O₄ and CoFe₂O₄ electrodes still exhibit a cathodic peak at around 0.20-0.25 V and 0.22-0.24 V, respectively, for all scan rates. The values are lower than Fe³⁺/Fe²⁺ (0.77 V) and Co³⁺/Co²⁺ (1.84V) possibly due to the individual reduction processes of Fe³⁺ and Co²⁺ emerging into one peak. The cathodic peak of C/CoFe₂O₄ shifted to lower potential with increasing of scan rate compared to CoFe₂O₄ electrode may be due to CNF matrix effect. Figure 4.28 (d) show the specific capacitance as a function of scan rate for CNF, C/CoFe₂O₄ and pure CoFe₂O₄ in 1M KOH electrolyte solution. At scan rate of 5 mV/s, the specific capacitance of 42 F/g for C/CoFe₂O₄ is higher than that of 21.1 F/g for GO/CoFe₂O₄ composite. However, the values quite low compared to 123 F/g for Graphene/CoFe₂O₄ composite (He *et al.*, 2012). The result is possibly due lower surface area of CNF than graphene yields lower current density. High value of capacitance at low scan rate was observed for all the prepared electrodes possibly due to the electrolyte ions have more time for penetrate to the pore. The specific capacitance of C/CoFe₂O₄ is higher than that of pure CNF and pure CoFe₂O₄ at all scan rates may be attributed to large channels between CNF and CoFe₂O₄ speed up the ionic transportation into pores and supporting the specific capacitance (Ning *et al.*, 2011). Moreover, the combination of the pseudocapacitance behavior of CoFe₂O₄ and the electric double layer capacitance of CNF well supported the enhancement of specific capacitance.

Typically, good cycle ability is one of the most important demands for observed the electrochemical performance of electrochemical capacitor. In this work, the specific capacitance retention is used for study long term stability of CNF, C/CoFe₂O₄ and CoFe₂O₄ electrodes. The specific capacitance retention after 1000 cycles as a function of cycle numbers for all the prepared electrodes is presented in Figure 4.28 (e). It was found from the spectra that, the specific capacitance retention for all samples decreased with increasing of charge/discharge cycles. The remaining specific capacitances about 98, 84, and 67% were obtained for CNF, C/CoFe₂O₄ and CoFe₂O₄, respectively. The trend is matches well with reported in C/CuFe₂O₄ and C/NiFe₂O₄ group. CNF electrode showed the best cycle stability possibly due to large CNF network structure restricts the change of electrode during charge/discharge process. The lower retention of C/CoFe₂O₄ and pure CoFe₂O, respectively is mainly attributed to pseudocapacitor charge/discharge mechanism arising from cobalt ferrite nanoparticle. It is considered that during the charge/discharge, the electrolyte may penetrate the layer through pores, cracks, inter-crystalline gap, etc., thus leading to large volume changes caused poor cycling stability, respectively.

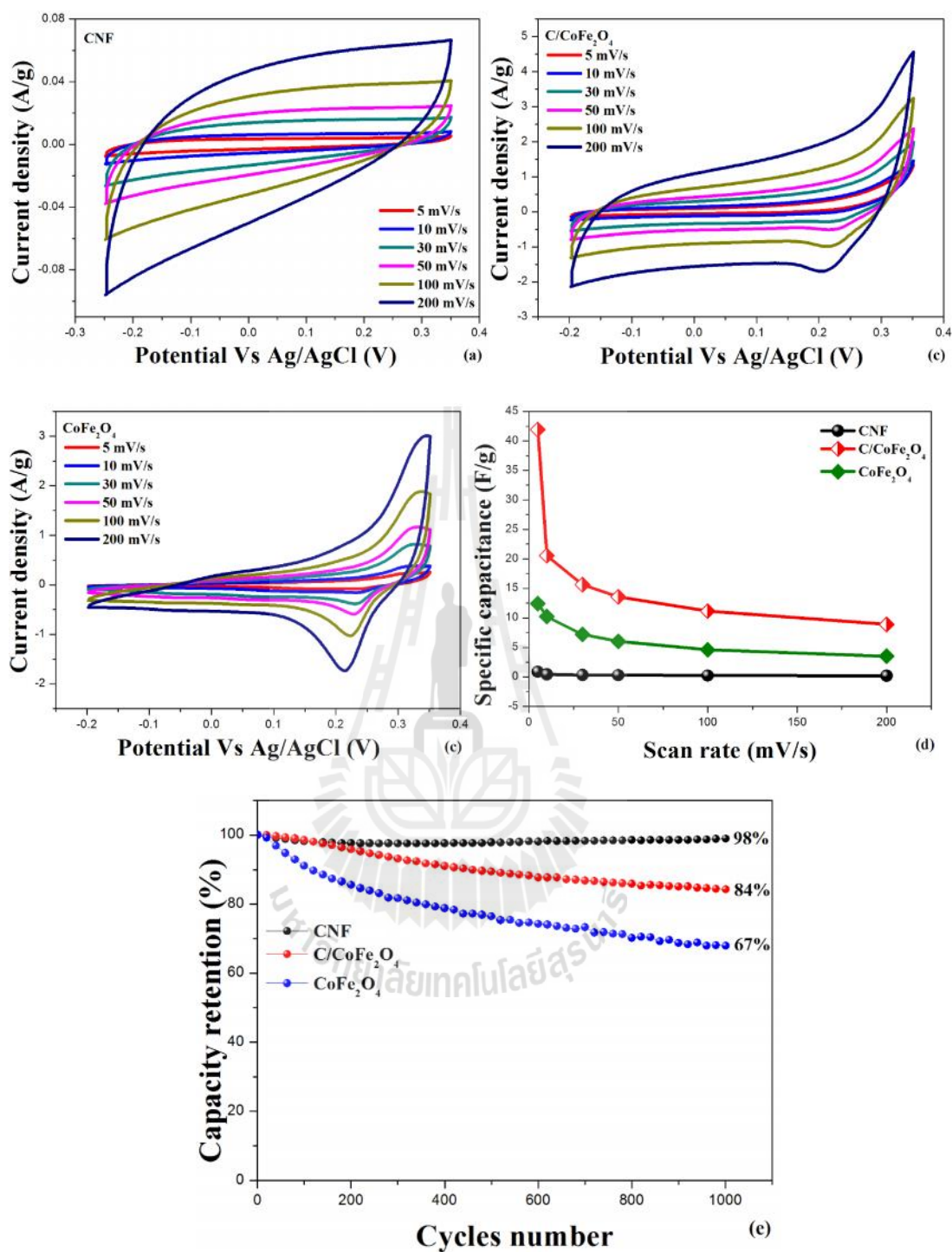


Figure 4.28 Cyclic voltammograms (CV) at different scan rates of (a) CNF, (b) C/CoFe₂O₄, and (c) CoFe₂O₄ electrodes in 1.0 M KOH electrolyte. (d) The corresponding specific capacitance at different scan rates. (e) The specific capacity retention of CNF, C/CoFe₂O₄ and CoFe₂O₄ electrodes at 1000 cycles.

4.2.3.2 Galvanostatic charge/discharge measurements

Figure 4.29 shows the galvanostatic charge/discharge curves of CNF, C/CoFe₂O₄ and CoFe₂O₄ electrodes in 1 M KOH aqueous solution. The cut-off voltage of charging/discharging was -0.2 - 0.35 V. The measurement was performed at different current density of 0.1, 0.25, 0.5, 0.75, and 1 A/g in a three-electrode system. It was found that the shape of charge/discharge curve for all electrodes is not linear and symmetric, which is a characteristic of non ideal capacitive behavior for electrochemical capacitors (Ye *et al.*, 2005). At a current density, the discharging time of CNF is very close to of C/CoFe₂O₄ electrode and longer than that of CoFe₂O₄ electrode. The results indicate the slower released electrolyte ions from the porosity of CNF and C/CoFe₂O₄ (Ma *et al.*, 2014). The energy deliverable efficiency ($\eta\%$) was observed at current density of 1 A/g and using Eq. 2.16. The values of 79.1, 88.4, and 85.3 were obtained for CNF, C/CoFe₂O₄, and CoFe₂O₄ electrodes, respectively. Figure 4.29 (d) shows the energy and power densities of CNF, C/CoFe₂O₄, and CoFe₂O₄ electrodes were calculated based on the galvanostatic charge/discharge. Among three different electrodes, C/CoFe₂O₄ shows almost highest energy density at all current densities, while the highest power density was observed in CoFe₂O₄ electrode. At current density of 1 A/g, the energy density of about 0.27, 0.29 and 0.11 Wh/kg with a corresponding power density of about 268.7, 231.6, and 278.4 W/kg was obtained for the CNF, C/CuFe₂O₄ and CuFe₂O₄ electrodes, respectively. The highest energy density of C/CoFe₂O₄ electrode is possibly due to the fibrous morphology of CNF with the free space between the CoFe₂O₄ nanoparticle caused optimized pore size, and thus allow them to achieve high energy density.

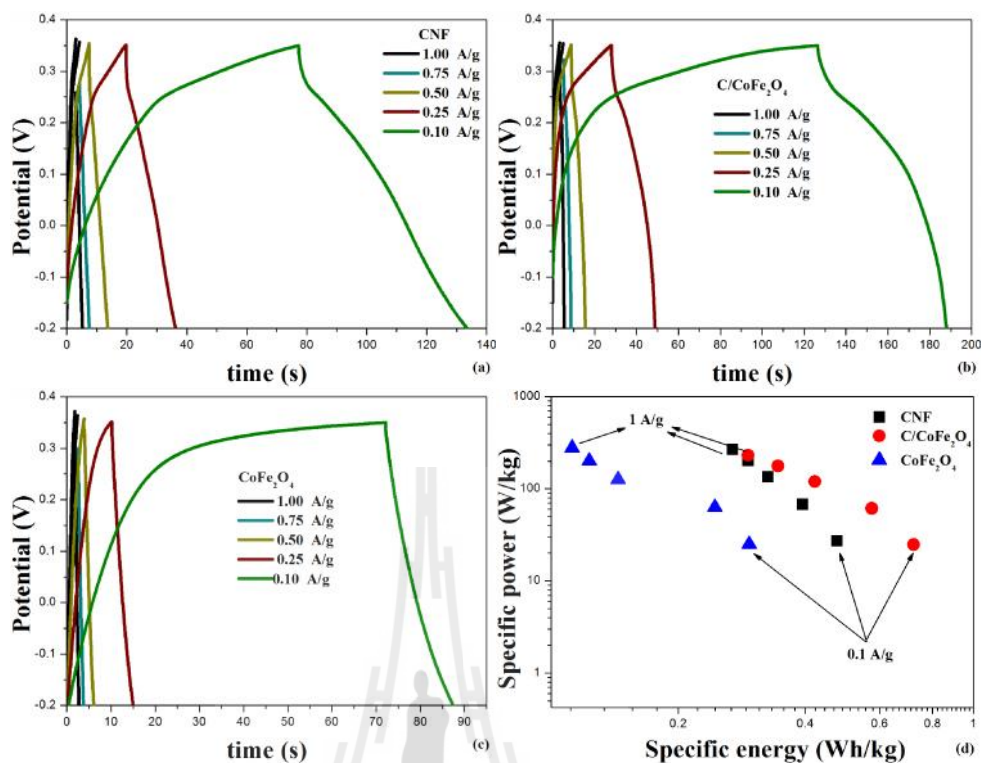


Figure 4.29 Galvanostatic charge/discharge curves of (a) CNF, (b) C/CoFe₂O₄, and (c) CoFe₂O₄ electrodes at current densities of 0.1, 0.25, 0.5, 0.75 and 1.0 A/g in 1 M KOH electrolyte solution. (d) The corresponding Ragone plot.

4.2.3.3 Electrochemical Impedance spectroscopy measurements

Figure 4.30 shows the Nyquist plots of CNF, C/CoFe₂O₄ and CoFe₂O₄ electrodes in 1 M KOH. Similar to the results reported for the C/CuFe₂O₄ system, the Nyquist plot of CNF electrode showed almost a straight line at lower frequency without semicircle arc at higher frequency region. This implies the EDLC behavior, and no interfacial resistance of CNF electrode could provide commendable channels for the electrolyte ion and current transport (Laforgue, 2011). C/CoFe₂O₄ and CoFe₂O₄ electrodes show a charge transfer resistance (R_{ct}), which relate to semicircle arc at high frequency. It was found from the spectra that, the R_s values of 9.3, 7.78

and 7.5Ω were obtained for the CNF, C/CoFe₂O₄ and CoFe₂O₄ electrodes, respectively. This resistance was estimated from the real axis intercept at high frequency (Lu *et al.*, 2010; Li *et al.*, 2010). The R_{ct} values of 0, 0.85 and 1.9Ω were obtained for CNF, C/CoFe₂O₄ and CoFe₂O₄ electrodes, respectively. Lower value of 0.85Ω for the C/CoFe₂O₄ electrode than that of 1.9Ω for the CoFe₂O₄ electrode suggests the advantage of the composite between fibrous and CoFe₂O₄ nanoparticles. The C/CoFe₂O₄ structure may provide the channels for the electrolyte ion and current transport, and thus supporting better electrolyte ions pore accessibility (Wang *et al.*, 2010). The result was confirmed by the steepest slope of the straight line at low frequency for the C/CoFe₂O₄ electrode (Snook *et al.*, 2011). It was found that, the slope increases and tends to become more purely capacitive for the pure CNF, C/CoFe₂O₄, and CoFe₂O₄ electrodes, respectively. The longest straight line for CNF electrode indicates that the penetration of electrolyte ions into the interior bulk would be greatest. The shortest length for CoFe₂O₄ cell indicates that the electrolyte ion just surface is being accessed. It is speculated that, the composite of CoFe₂O₄ with CNF matrix can effectively suppress the aggregation of CoFe₂O₄ nanoparticles, and thus resulting to high surface area, in which supports either electrolyte accessibility or the charge transfer rate toward the electrode in the electrolyte solution (Zhu *et al.*, 2011).

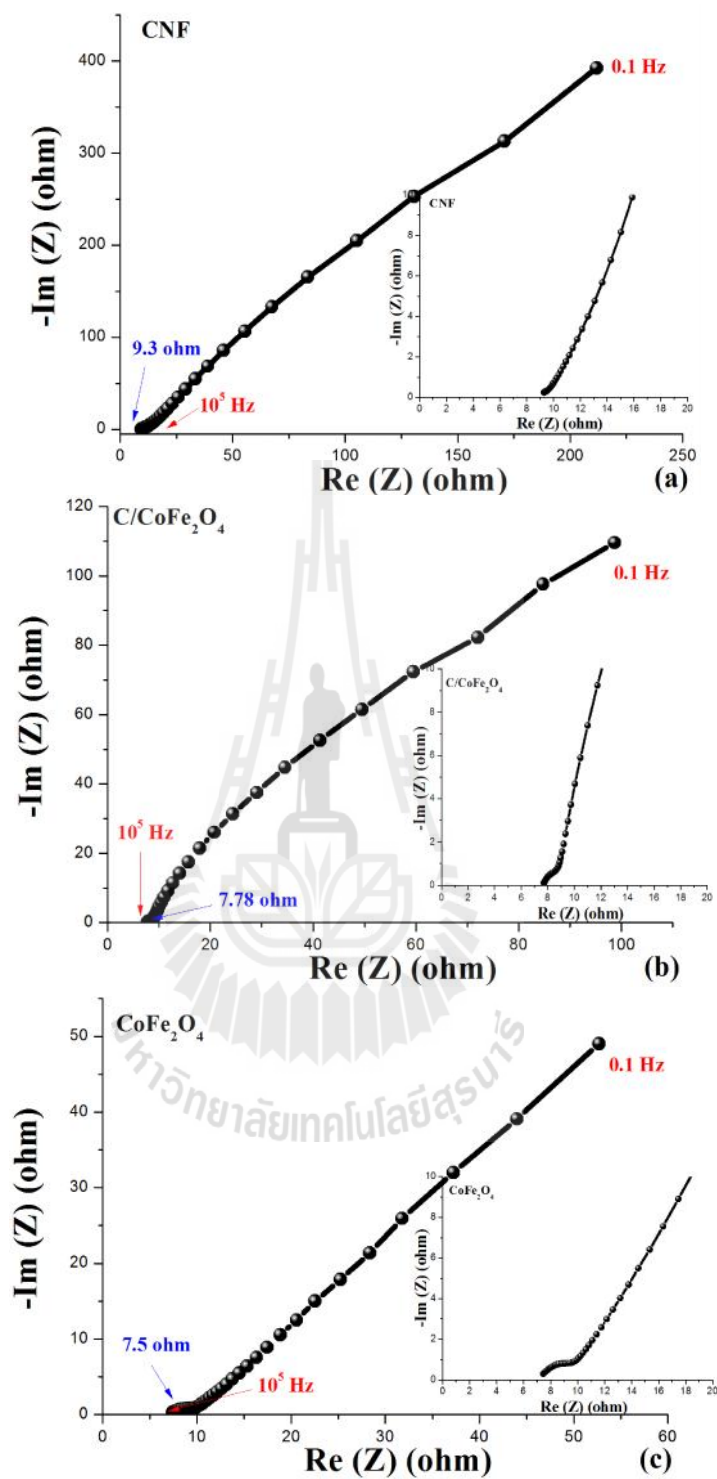


Figure 4.30 Nyquist impedance plots at a frequency range of 0.1 Hz-100 kHz in 1 M KOH electrolyte solution for (a) CNF, (b) C/CoFe₂O₄ and (c) CoFe₂O₄ electrodes.

Bode plot is another form to present the EIS data. For ideal capacitors, the Nyquist plot should be vertical and the phase angle in the Bode plot at low frequencies should be -90° (Conway, 1999). Figure 4.31 (a) shows the frequency dependence the phase angle for CNF, C/CoFe₂O₄ and CoFe₂O₄ electrodes. The values of -61° , -48° , and -43° were obtained at 0.1 Hz for CNF, C/CoFe₂O₄ and CoFe₂O₄, respectively. All the phase angle values are lower than the value for ideal capacitors. The values of capacitor response frequency (f_0) at the phase angle of -45° were 5.1, 3.2 and less than 0.1 Hz were obtained for the CNF, C/CoFe₂O₄ and CoFe₂O₄ electrodes, respectively. Thus, the relaxation time constant ($\tau_0 = 1/f_0$) was calculated to be about 0.196, 0.313 and larger than 10 s, for the CNF, C/CoFe₂O₄ and CoFe₂O₄ electrodes, respectively. It can be seen that the low time constant of CNF and C/CoFe₂O₄ electrodes supported high power delivery or fast charge-discharge process when compared to CoFe₂O₄ electrode (Girija and Sangaranarayanan, 2006; Burke, 2000). The frequency dependence of impedance at 0.2 V for CNF, C/CoFe₂O₄ and CoFe₂O₄ electrodes are presented in Figure 4.31 (b). It was found that, the variation of impedance strongly depends on the frequency. The value slightly decreases at higher frequency for all the prepared electrodes. At frequency lower than 10 Hz, the CNF exhibited largest impedance compared to C/CoFe₂O₄ and CoFe₂O₄ electrodes. At frequency over 10 Hz, the C/CoFe₂O₄ electrode showed lowest impedance indicating better capacitance.

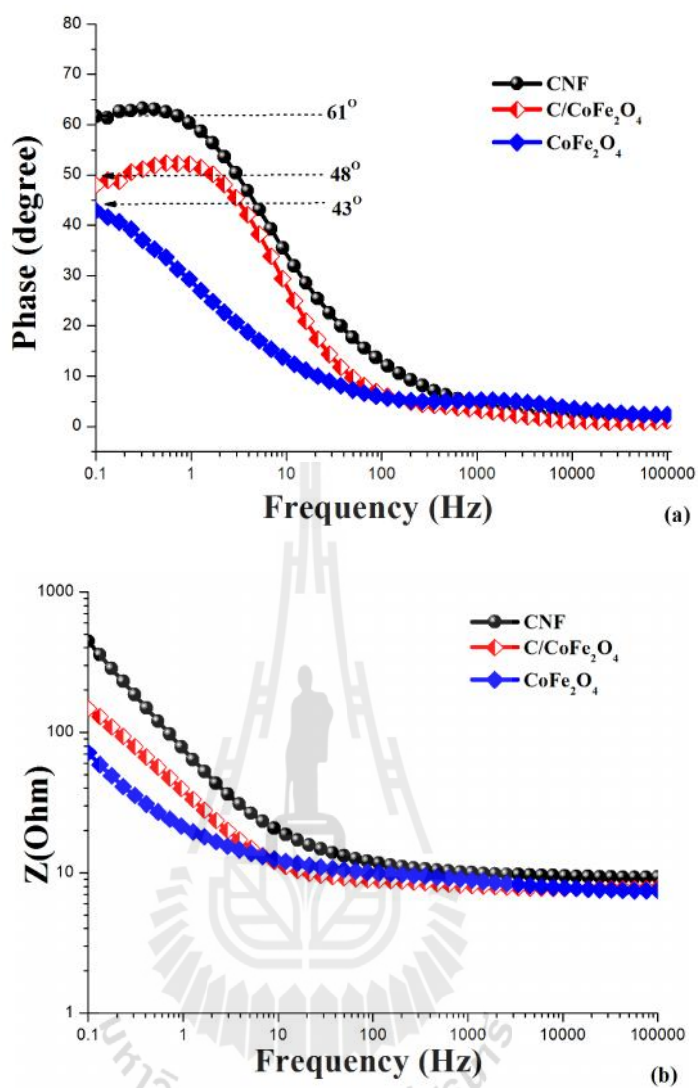


Figure 4.31 Bode plots of (a) frequency dependence of phase angle (b) impedance dependence on frequency of CNF, C/CoFe₂O₄ and CoFe₂O₄ electrodes.

4.3 C/NiFe₂O₄ composite nanofibers

4.3.1 Structural and morphology characterization

4.3.1.1 Thermo gravimetric analysis (TGA) of the electrospun-based C/NiFe₂O₄ composite nanofibers.

Figure 4.32 shows TGA curves of the electrospun based CNF and C/NiFe₂O₄ composite nanofibers with different magnetic source content. The test was performed by using a heating rate of 10 °C/min in the temperature range from 25 - 1200 °C under N₂ atmosphere. It is evident from the spectra that, all prepared nanofibers were degraded through three steps in the range of ~20 - 295, ~295 - 480 and ~ 580-1200 °C. Consider at stabilization temperature (220 °C), the percentage of weight lost almost constant for pure CNF, while the value of about 13, 18 and 31% were obtained for C/NiFe₂O₄_0.2, C/NiFe₂O₄_0.4, and C/NiFe₂O₄_0.6, respectively. The results suggest that, higher weight loss was observed for the samples with higher magnetic source content. The weight loss became more than 50% in the second step due to the degradation of PAN side chain along with the decomposition of metal nitrates precursor. The major weight loss at the third step associated to the decomposition of PAN main chain. Moreover, the common short plateau between 480 and 670 °C was observed for all samples. It is speculated at this range of temperature that, the crystalline NiFe₂O₄ could form as the decomposition of metal product (Maensiri and Nuansing, 2006). No any plateau after 670 °C was observed suggesting the remaining carbon in the materials.

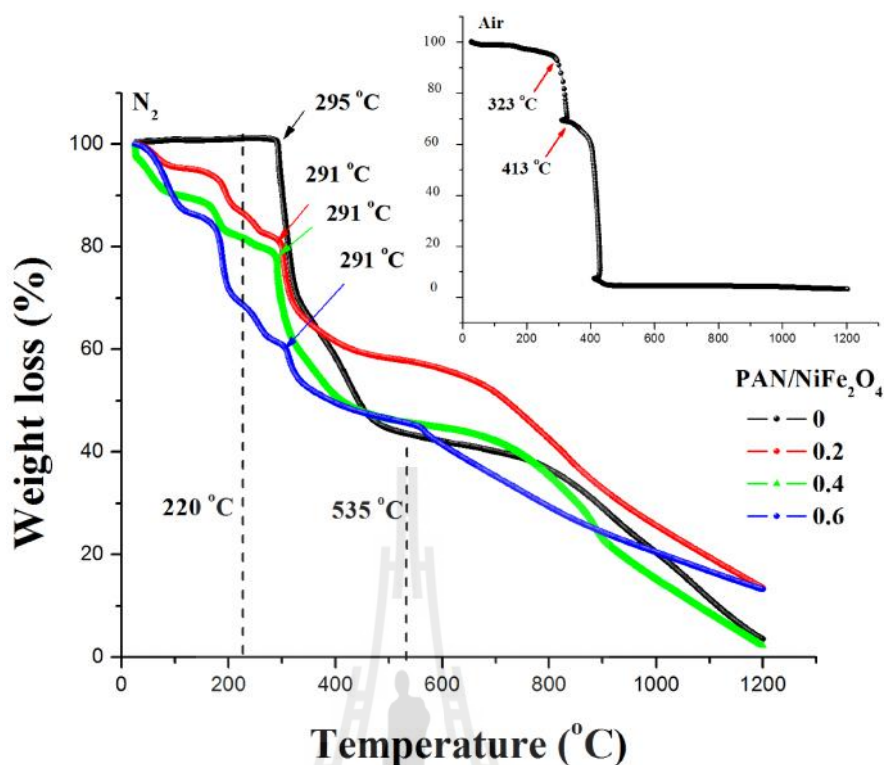


Figure 4.32 TGA curves of CNF and C/NiFe₂O₄ composite nanofibers under N₂ atmosphere and air atmosphere (in set).

4.3.1.2 X-ray diffraction (XRD) analysis of C/NiFe₂O₄ composite nanofibers

Figure 4.33 shows XRD patterns of pure CNF and C/NiFe₂O₄ composite nanofibers with different magnetic source content after stabilized at 220 °C for 2 h in air atmosphere followed by carbonized at 535 °C for 1 h in argon atmosphere. It was found that, the XRD patterns of composite nanofibers show mixed phase structures of graphite and nickel ferrite. No other foreign phase was detected, ensuring the phase purity. A broad diffraction peak around $2\theta = 26.0^\circ$ and 44.0° , corresponding to the diffraction of the (002) plane and (101) of the graphite structure, respectively (JCPD 75-1621). The diffraction peak at 30.62, 36.00, 37.62, 43.72, 54.18, 57.81, 63.36 and

75.21 ° relates to crystallite planes of (220), (311), (222), (400), (422), (511), (440), and (622), respectively. The results are matches well with the reported value cubic spinel structure (JCPDS 86-2267). The peak broadening for low magnetic source content samples suggest a poor development of the ferrite structure and the most sharp peaks of the ferrite structure were observed for the composite content of 60 wt.%. The average crystallite size was estimated, using the Scherrer's equation. The obtained values were 17.07, 30.34, 34.87 and 41.53 nm for CNF, C/NiFe₂O₄_0.2, C/NiFe₂O₄_0.4 and C/NiFe₂O₄_0.6, respectively. It is found from the calculation that, the crystallite size values of all composite nanofibers are higher than that of pure CNFs. Moreover the value increases with increasing of magnetic source concentration. The smallest crystallite size of C/NiFe₂O₄_0.2 relates to the broadening XRD peak and may arises from large concentration of CNF matrix acts as inhibition template of NiFe₂O₄ nanoparticles prevent the aggregation of nanoparticle. The d-spacing values of peak (311) are 2.496, 2.489 and 2.492 Å for C/NiFe₂O₄_0.2, C/NiFe₂O₄_0.4, and C/NiFe₂O₄_0.6 respectively. The values are slightly lower than 2.514 Å of a cubic NiFe₂O₄ (JCPDS 86-2267). The lattice constants of 8.385, 8.337 and 8.334Å were obtained for C/NiFe₂O₄_0.2, C/NiFe₂O₄_0.4, and C/NiFe₂O₄_0.6, respectively. The value is in good agreement with the bulk value of NiFe₂O₄ (8.337 Å° JCPDS 86-2267).

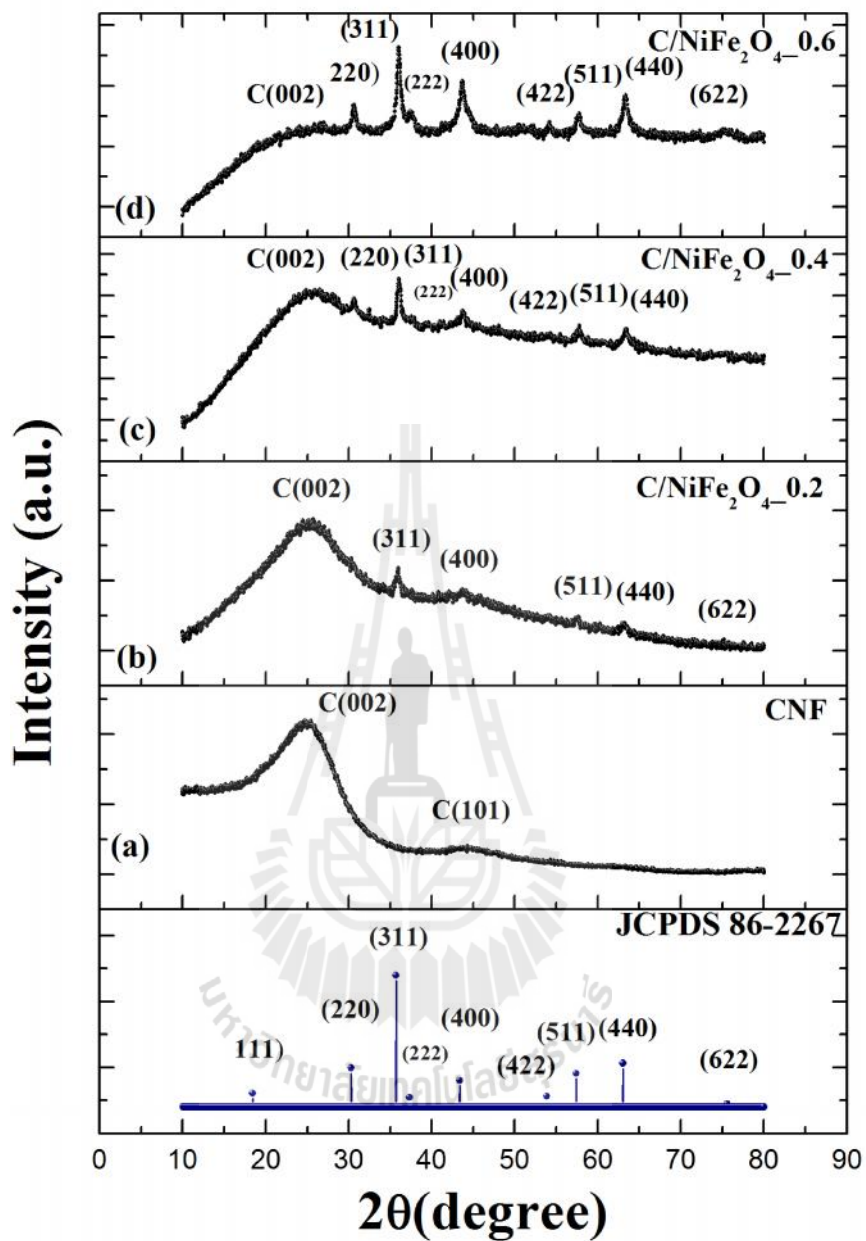


Figure 4.33 XRD patterns of (a) CNF, (b) C/NiFe₂O₄_0.2, (c) C/NiFe₂O₄_0.4 and (d) C/NiFe₂O₄_0.6 composite nanofibers.

4.3.1.3 Morphology of C/NiFe₂O₄ composite nanofibers by FE-SEM and TEM.

The surface morphology of CNF and C/NiFe₂O₄ composite nanofibers were investigated by SEM and the results are presented in Figure 4.34. It was found from the spectra that, as-spun nanofibers before heat treatment shows clearly smooth fibers and uniform in cross-section with the average diameters of 445-850 nm. After carbonization at 535 °C, the shrinkage of fibers diameters was observed with the values of about 11.8, 25.7, 29.6 and 32.3% for CNF, C/NiFe₂O₄_0.2, C/NiFe₂O₄_0.4 and C/NiFe₂O₄_0.6, respectively due to the removal of PAN polymer and the decomposition of metal precursors in the carbonization process. The fibers with lower polymer source concentration compared to metal source content generated larger shrinkage fibers diameter. The shrinkage with broken fibers was found for C/NiFe₂O₄_0.4, while the fibers almost completely merged together was observed with C/NiFe₂O₄_0.6. The filmy fibers of C/NiFe₂O₄_0.6 well agree as observed in C/CuFe₂O₄_0.6 and C/CoFe₂O₄_0.6 composite nanofibers. This behavior is possibly due to a very high viscosity of magnetic source concentration compared to polymer source content.

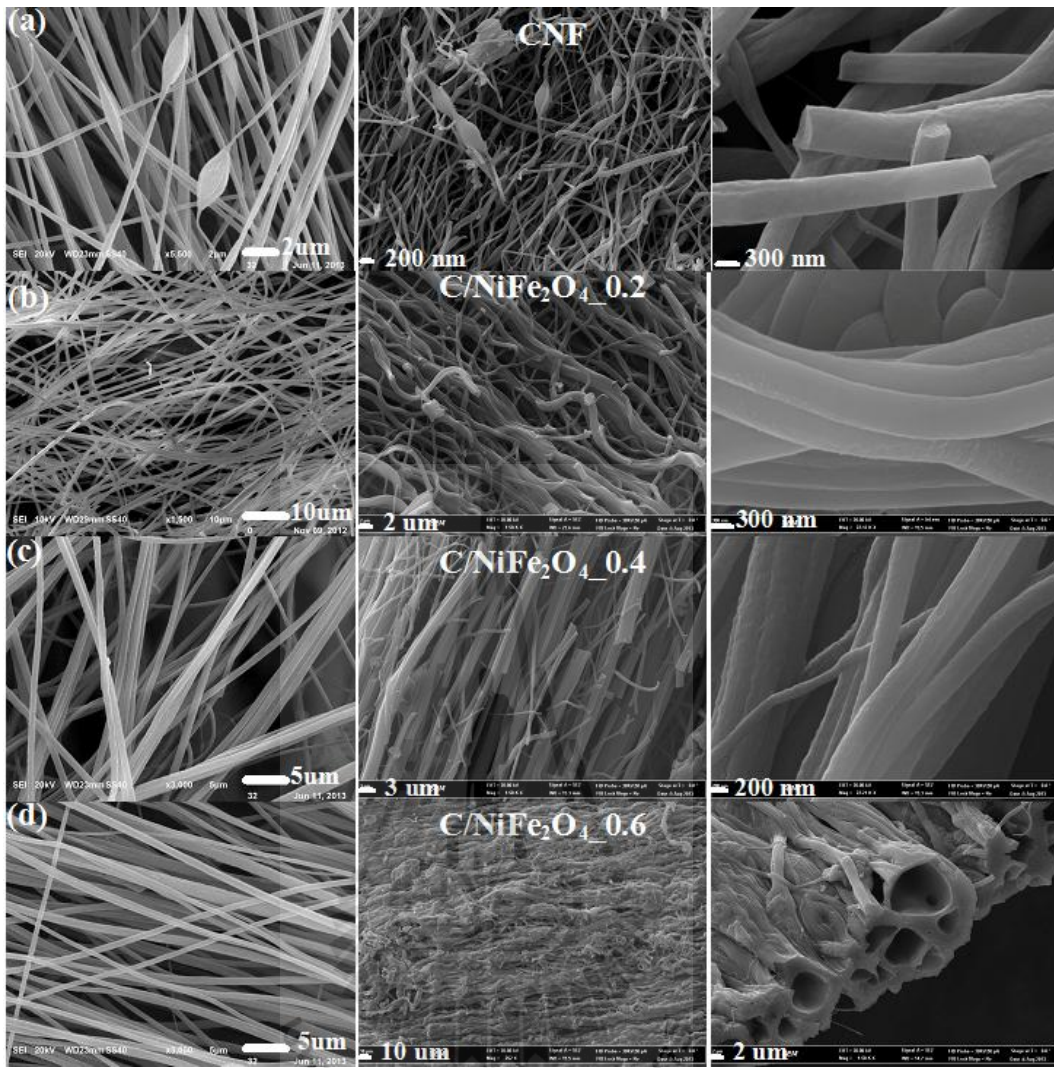


Figure 4.34 SEM micrographs of the electrospun C/NiFe₂O₄ composite nanofibers before carbonization (left), the fibers after carbonization (middle) and their FE-SEM images (right), respectively of (a) pure CNF, (b) C/NiFe₂O₄_0.2 (c), C/NiFe₂O₄_0.4, and (d) C/NiFe₂O₄_0.6.

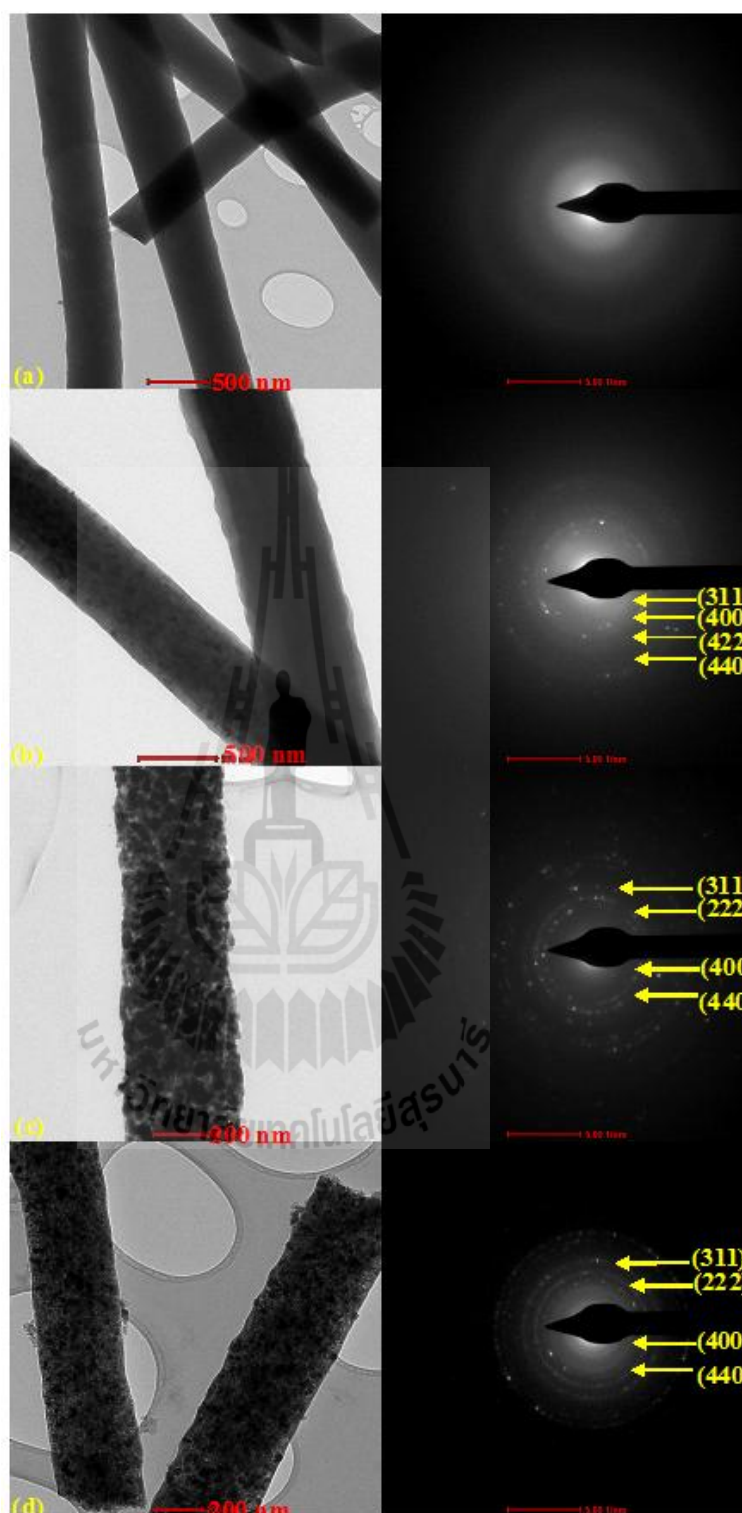


Figure 4.35 TEM bright field images (left) with the corresponding SAED pattern (right) of (a) pure CNF, (b) C/NiFe₂O₄_0.2, (c) C/NiFe₂O₄_0.4, and (d) C/NiFe₂O₄_0.6 composite nanofibers.

Figure 4.35 shows TEM image with corresponding selected area electron diffraction pattern (SAED) of pure CNF and C/NiFe₂O₄ composite nanofibers. It can be seen that, TEM bright field images show clearly the NiFe₂O₄ nanoparticles are uniformly grown within the CNF matrix for the composite nanofibers. Meanwhile, there is plenty of space between nanofibers, which is beneficial for electrolyte diffusion in electrochemical test. The average size of NiFe₂O₄ nanoparticles is in the range of 10-70 nm. The corresponding SAED patterns of C/NiFe₂O₄ composite nanofiber show clearly diffraction spots, in which indexed to high crystallinity of NiFe₂O₄. Arcs and diffuse rings represent to hexagonal graphite structure (002). No any spotty ring was observed in SAED pattern of CNF suggests to the large characteristic of amorphous carbon. The smooth surface without any particles was observed in the TEM bright field image.

4.3.1.4 The structure fingerprints of C/NiFe₂O₄ composite nanofibers characterization by Raman spectroscopy.

Figure 4.36 shows Raman spectra of CNF, C/NiFe₂O₄_0.2, C/NiFe₂O₄_0.4 and C/NiFe₂O₄_0.6 composite nanofibers. Three peak centered at ~1345 cm⁻¹ (D band), ~1570 (G band) and ~2700 cm⁻¹ (2D band) were observed for all the prepared samples. G and 2D band are corresponds to Raman active E_{2g2} mode of graphite lattice vibration and the second order of the D-band, respectively. These two peaks represent a characteristic of crystalline graphite (Thomsen and Reich, 2000; Ferrari and Robertson, 2000). D band at ~1343 cm⁻¹ is attributed to breathing mode with A_{1g} symmetry. This peak becomes active in the presence of disorder in the graphitic structure (Tuinstra and Koenig, 1970; Nemanich and Solin, 1979; Ferrari

and Robertson, 2000). The intensity ratio of the D peak to the G peak, denoted by $R = I_D/I_G$, represents the amount of ordered graphite crystallites in the CNFs (Zhou *et al.*, 2009). In this work, R value for the composite nanofibers increased with increasing of magnetic source content (1.71, 1.74 and 1.78 for C/NiFe₂O₄_0.2, C/NiFe₂O₄_0.4 and C/NiFe₂O₄_0.6, respectively). All the R values are higher than that of pure CNF (1.6), implies more disordered carbon structure was observed due to the intercalation of NiFe₂O₄ nanoparticle in to graphite layers. The in plane graphitic crystallite size (L_a) was also calculated from the data fitting using the equation: L_a (nm) = $C(\lambda)/(I_D/I_G)$, where $C(532$ nm) is constant and is ~ 4 (Knight and White, 1989). The obtained results of L_a are listed in Table 4.16. It was found that, the highest value was observed in CNF. For C/NiFe₂O₄ composite nanofibers, the value decreased with increasing the magnetic source concentration and crystallite size.

Table 4.16 Lists of Raman peak height, Raman peak width, R value (I_D/I_G) and in plane graphite crystallite size (L_a) of CNF and C/NiFe₂O₄ composite nanofibers with different magnetic source concentration.

Sample	Peak height (cm ⁻¹)				Peak width (cm ⁻¹)				R	L_a (nm)
	D	G	2D ₁	2D ₂	D	G	2D ₁	2D ₂		
CNF	1981	1236.3	329.8	313.4	183.5	108.2	242.7	298.4	1.60	2.75
C/NiFe ₂ O ₄ 0.2	2434	1427.1	354.2	291.4	201.8	110.1	256.3	274.5	1.71	2.58
C/NiFe ₂ O ₄ 0.4	1515	870.4	206.1	155.8	184.8	107.5	248.8	221.6	1.74	2.53
C/NiFe ₂ O ₄ 0.6	308	173.2	29.1	37.4	144.5	82.0	109.2	120.8	1.78	2.47

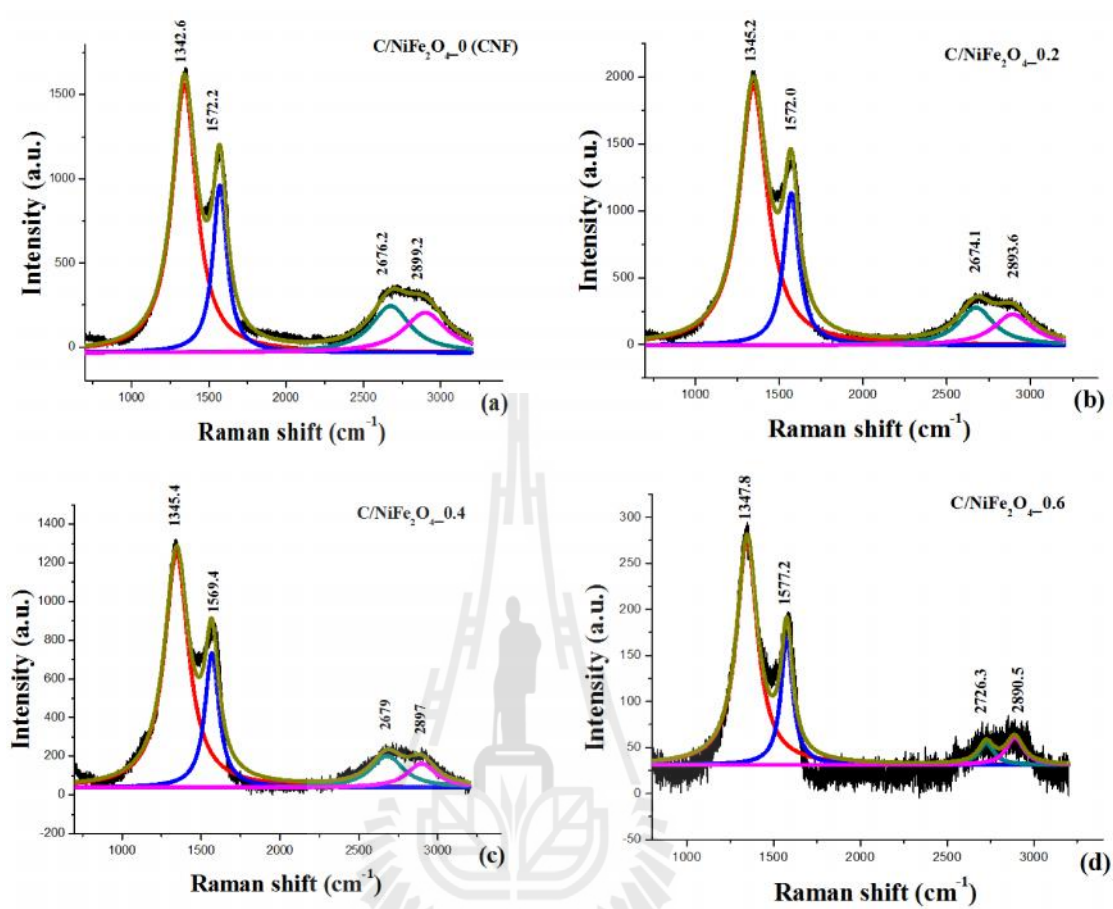


Figure 4.36 Raman spectra of (a) pure CNF, (b) C/NiFe₂O₄_0.2, (c) C/NiFe₂O₄_0.4, and (d) C/NiFe₂O₄_0.6 composite nanofiber.

4.3.1.5 Characterization of surface area of C/NiFe₂O₄ composite nanofibers by the Brunauer-Emmett-Teller.

Figure 4.37 shows the N₂ adsorption/desorption isotherms of CNF and C/NiFe₂O₄ with different magnetic source concentration. The isotherms of each sample show similar shape as previous reported in C/CuFe₂O₄ and C/CoFe₂O₄ groups. i.e., CNF, C/NiFe₂O₄_0.2 and C/NiFe₂O₄_0.4 samples show type I behavior indicates that these membranes have relatively micro-porous. An additional small adsorption quantity appears at P/P₀ > 0.8 for CNF indicating small amount of meso/macro -pores in the sample (Nan *et al.*, 2014). The C/NiFe₂O₄_0.6 exhibited type IV isotherms with H3 hysteresis loop suggesting a characteristic of large amounts of mesopores (Inagaki *et al.*, 2010). The BET surface area was found to be about 30, 209, 120 and 90 m²/g for CNF, C/NiFe₂O₄_0.2, C/NiFe₂O₄_0.4, and C/NiFe₂O₄_0.6, respectively. The values of the composite nanofibers decreased with increasing the NiFe₂O₄ concentration and crystallite size. Low value for CNF may lead to long ions diffusion lengths and decreased active sites for ions insertion/extraction reaction. Much larger value of the composite nanofibers than that of pure CNF suggests the composite of CNF with NiFe₂O₄ can effectively reduce the aggregation of NiFe₂O₄ nanoparticles leading to a large specific surface area of the composite nanofibers. However, the mean pore diameter of the composite nanofibers is significant low compared to pure CNF possibly arise from the occupation of NiFe₂O₄ nanoparticles inside the pores. The BET specific surface area, mean pore diameter and total pore volume of the C/NiFe₂O₄ composite nanofibers are listed in Table 4.17.

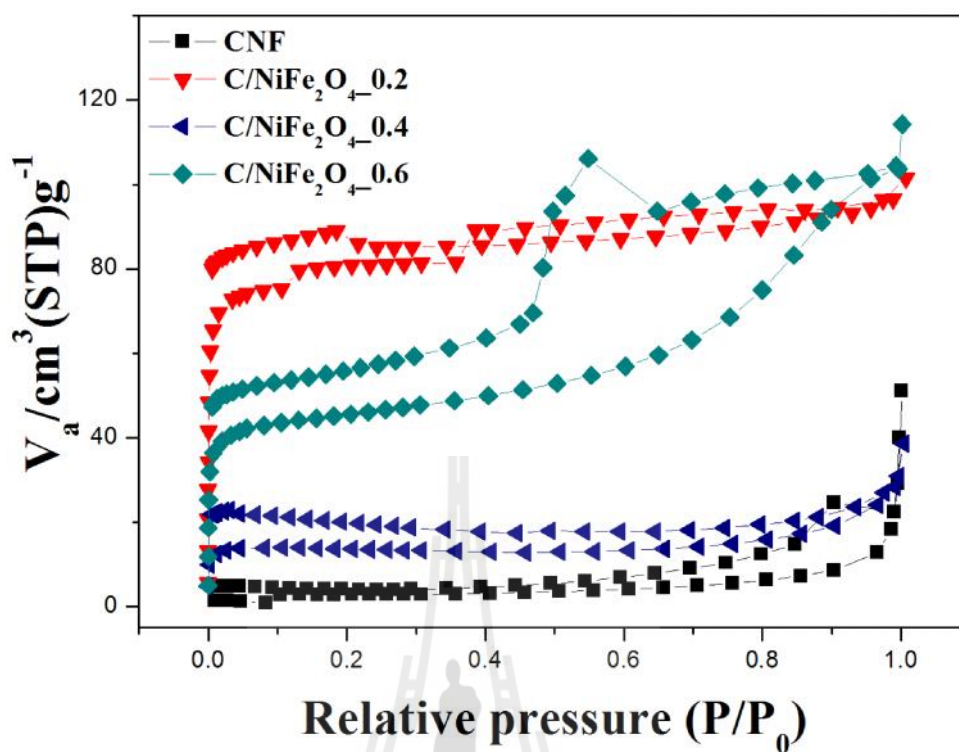


Figure 4.37 N₂ adsorption/desorption isotherms of (a) pure CNF, (b) C/NiFe₂O_{4_0.2}, (c) C/NiFe₂O_{4_0.4}, and (d) C/NiFe₂O_{4_0.6} composite nanofibers.

Table 4.17 Summary of mean pore diameter, surface area, and total pore volume of CNF and C/ NiFe₂O₄ composite nanofibers with different metal source concentration.

Samples	Mean pore diameter (nm)	Surface area (m ² /g)	Total pore volume (cm ³ /g)
CNF	23.217	30.0711	0.0178
C/NiFe ₂ O _{4_0.2}	2.9150	209.67	0.1528
C/NiFe ₂ O _{4_0.4}	5.2971	120.60	0.1597
C/NiFe ₂ O _{4_0.6}	5.8070	89.81	0.0433

4.3.1.6 X-ray absorption spectroscopy study of the Fe and Ni K- edge in C/NiFe₂O₄ composite nanofibers.

Figure 4.38 shows normalized XANES spectra at the Fe and Ni K-edge for the C/NiFe₂O₄ composite nanofibers and their corresponding first derivatives spectra. In this section, the oxidation states of Fe and Ni in NiFe₂O₄ structure are shown along with the standard samples of FeO, Fe₂O₃, Fe₃O₄, Ni foil, NiO and NiCl₂ for Fe²⁺, Fe³⁺, Fe^{2+,3+}, Ni⁰⁺, Ni²⁺ and Ni²⁺, respectively. It was found from the study that, the position of the absorption edge at Fe K-edge is similar to Fe₂O₃ which is typical for Fe in the oxidation state of +3. While at Ni K-edge, the edge energies and the feature are similar to that of NiO sample reference, indicating +2 oxidation state of Nickel. It was found at Fe K-edge that, all prepared samples exhibited strong intensity pre edge peak which is a typical for Fe atom in tetrahedral coordinate. The C/NiFe₂O₄_0.6 composite nanofibers shows larger pre-edge peak than those of C/NiFe₂O₄_0.4 and C/NiFe₂O₄_0.2 composite nanofibers, respectively, suggesting the Fe atom in tetrahedral is larger than observed in other two samples. The results are consistent with the EXAFS observation which will be discussed later. Moreover, the pre-edge peak at Ni K-edge allows us to confirm the oxidation state of nickel ion as Ni²⁺ and their partial location in tetrahedral sites. Very low intensity of Ni pre-edge peak indicates that the fraction of Ni²⁺ is mostly located at B site, i.e., high degree of inversion confirming the inverse spinel structure. The edge energies and oxidation states at Fe and Co K-edge for all the prepared samples and the standard material are listed in Table 4.18.

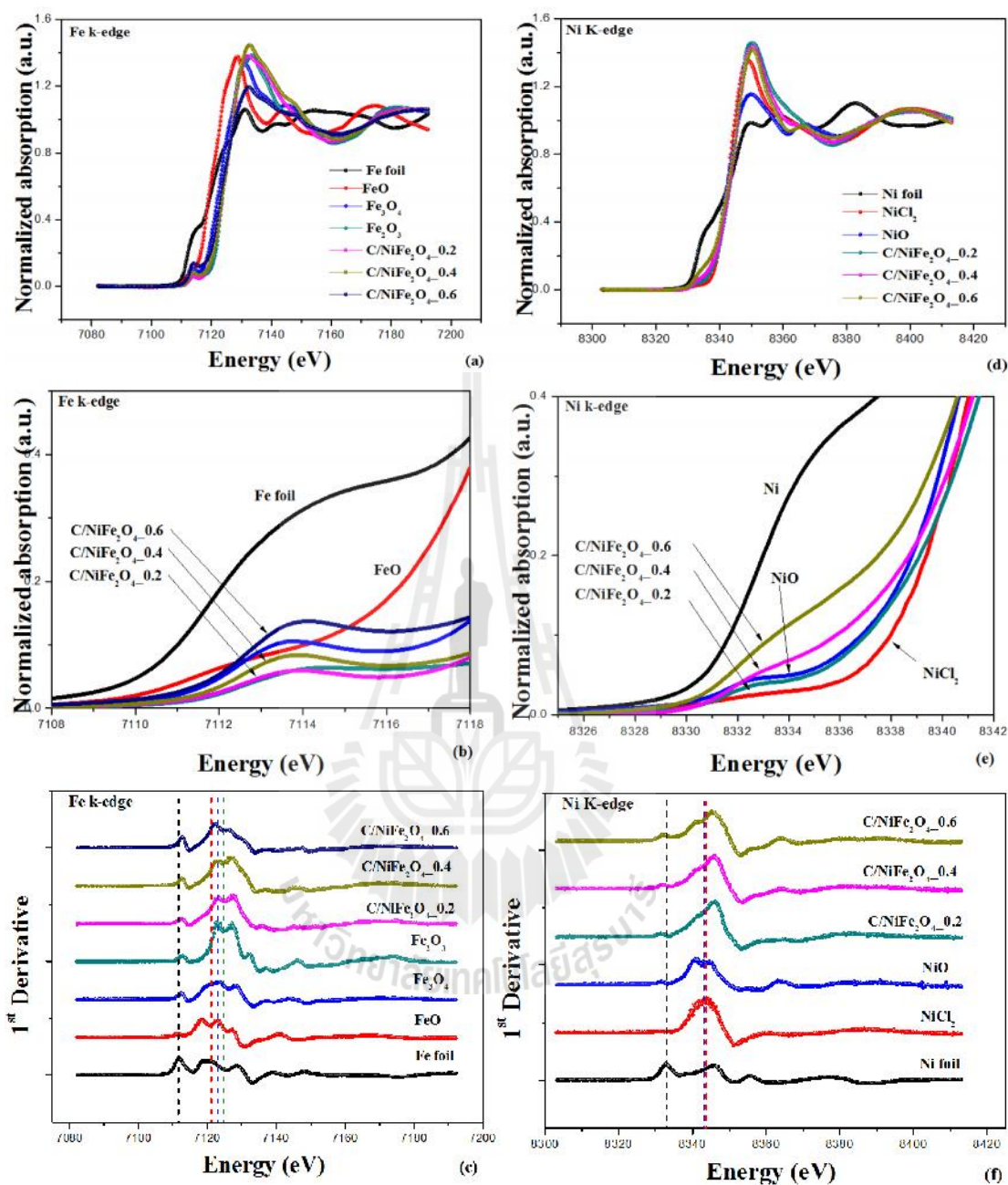


Figure 4.38 XANES spectra, the corresponding first derivatives plot and the pre-edge peak, respectively of C/NiFe₂O₄ composite nanofibers at Fe K-edge (a, b, e) and at Ni K-edge (c, d, f).

Table 4.18 Edge energies and oxidation states of all C/NiFe₂O₄ composite nanofibers along with the standard samples.

Sample/standard	Edge element	Oxidation state	Absorption edge (eV)
C/NiFe ₂ O ₄ _0.2	Fe	+3	7125.3
	Ni	+2	8345.8
C/NiFe ₂ O ₄ _0.4	Fe	+3	7125.48
	Ni	+2	8346
C/NiFe ₂ O ₄ _0.6	Fe	+3	7124.6
	Ni	+2	8345.2
Fe foil	Fe	0	7112
FeO	Fe	+2	7120.65
Fe ₃ O ₄	Fe	+2,+3	7123.40
Fe ₂ O ₃	Fe	+3	7124.85
Ni foil	Ni	0	8333
NiO	Ni	+2	8342.97
NiCl ₂	Ni	+2	8343.54

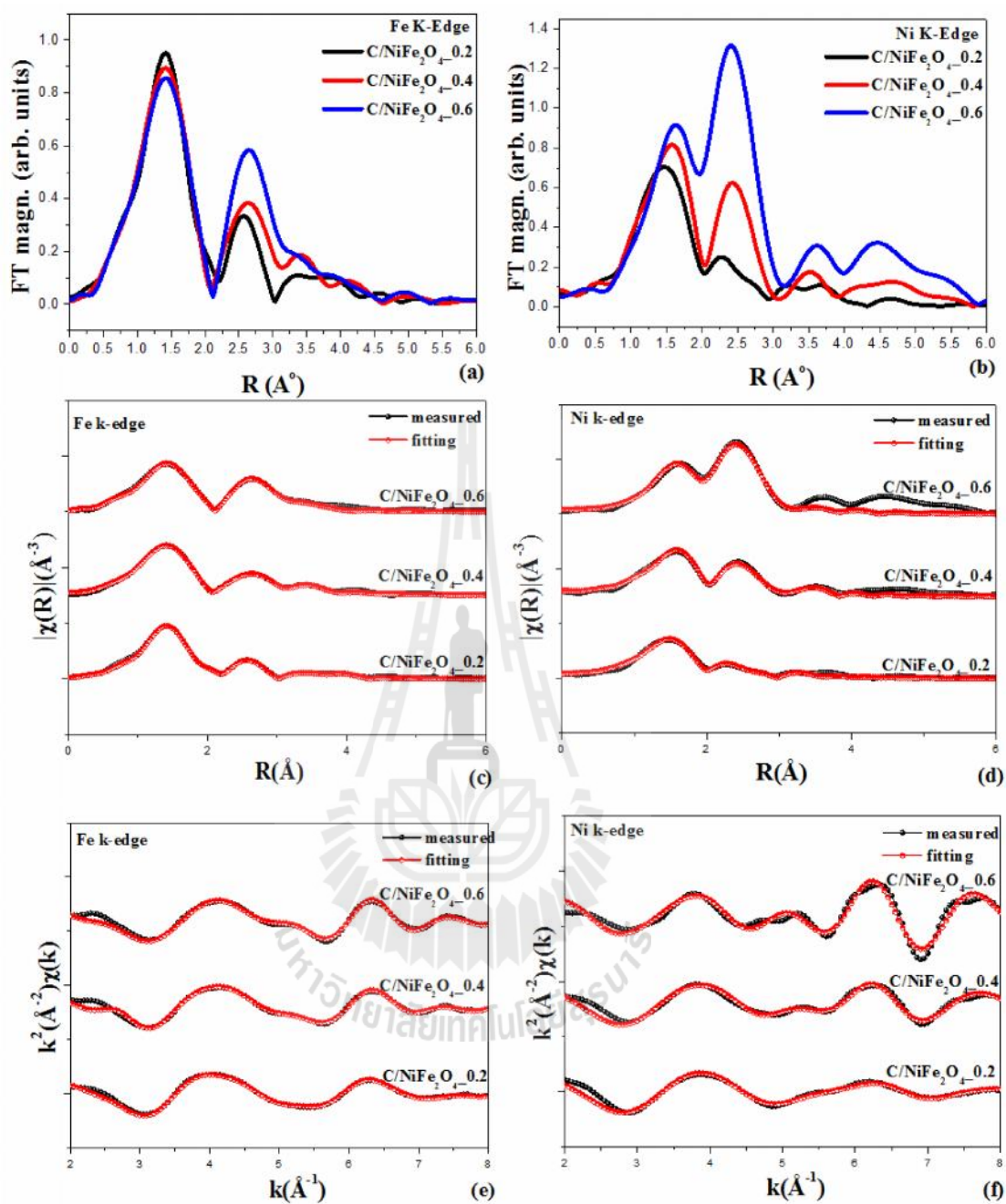


Figure 4.39 (a, b) Fourier transform in R-space of three different composite samples at Fe and Ni k-edge, respectively. (c, d) Fourier transform in R-space with the corresponding fitted spectra. (e, f) The $k^2(\chi(k))$ plots with the corresponding fitting spectra at Fe and Ni K-edge, respectively.

To further understand the environment of Ni and Fe atom of NiFe₂O₄ inverse spinel structure, the EXAFS data at Fe and Ni K-edge of the prepared samples were fitted.

Bulk NiFe₂O₄ particles have an inverse spinel structure in which all Ni²⁺ ions occupy octahedral site (B site). Half of the Fe³⁺ ions preferentially occupy tetrahedral sites (A site) and the rest fill B sites. In this section, the cation distribution between A and B site of spinel structure was obtained from the fitting. Figure 4.39 shows the $k^2\chi(k)$ weighted in k space and the corresponding Fourier transform (FT) in R space in both experiment (-) and fitting (·) spectra without phase shift correction. It is important to note that the Fourier transforms without phase shift corrections resulting in the peak position shift to lower distance with respect to the actual interatomic distance. The structure parameters arise from the EXAFS fitting are tabulated in Table 4.19-21. It was suggest from the EXAFS fitting that, the structure of C/NiFe₂O₄_0.2 and C/NiFe₂O₄_0.4 composite nanofibers were totally inverse spinel structure. The majority of Ni ions occupy B sites, while Fe ions are both in A and B sites. The $k^2(k)$ values at both Fe K-edges are similar for all tree prepared samples, indicating similarity of the local environment around the absorber Fe ions. In contrast, the $k^2(k)$ plot in C/NiFe₂O₄_0.6 sample at Ni K-edge show significant difference, indicating that the structural environment around Ni²⁺ is different. The Fourier transform spectra at Fe K-edge of C/NiFe₂O₄_0.2, C/NiFe₂O₄_0.4, and C/NiFe₂O₄_0.6 show similarity. The first shells indicates the tetrahedral site cation is surrounded by four nearest oxygen backscatterers (Fe_A-O), and the octahedral site cations with six surrounded backscatterers (Fe_B-O). The Fe_A-O (Fe_B-O) distance with the value of 1.868 (1.999), 2.013 (1.812) and 1.800 (1.948) Å were obtained for

C/NiFe₂O_{4_0.2}, C/NiFe₂O_{4_0.4}, and C/NiFe₂O_{4_0.6}, respectively. The second shells fitted at the distance of 3.005, 2.980 and 2.893 Å with three metal backscatterers in octahedral site were obtained for C/NiFe₂O_{4_0.2}, C/NiFe₂O_{4_0.4} and C/NiFe₂O_{4_0.6}, respectively. These distances relate to Fe_B-Fe_B and Fe_B-Ni_B (as seen in Table 4.19-4.21). Meanwhile, the third shells at ~3.5 Å surrounded by six metal backscatterers is a typical for cations occupying in either A or B site (Fe_A-Fe_A = 3.400 Å for C/NiFe₂O_{4_0.2}; Fe_A-Fe_A = 3.509 Å and Fe_B-Fe_B=3.494 Å for C/NiFe₂O_{4_0.4} Å). The cations occupying A site with four metal backscatters were also observed at the distance ~3.6 Å (Fe_A-Fe_A = 3.552, 3.665 and 3.400 Å for C/NiFe₂O_{4_0.2}, C/NiFe₂O_{4_0.4} and C/NiFe₂O_{4_0.6}, respectively).

At Ni K-edge, the Fourier transform spectra for all the prepared samples look different from each other, especially the second shells. C/CoFe₂O_{4_0.2} shows two significant nearest shell. The first shells at ~2.00 Å originated from Ni_B-O bond with coordination number of six, while the second shells centered at 2.8-3 Å corresponds to Ni_B-Fe_B or Ni_B-Ni_B neighbors with three backscatters. For C/NiFe₂O_{4_0.4}, the absorber environment of the first shells does not change significantly from that of the C/NiFe₂O_{4_0.2} (2.05 Å for Ni_B-O). Meanwhile, the significant change was observed in the second shells. The third shells at distance of 3.388 Å is relating to the distribution of cations in octahedral site (either Ni_B-Fe_B or Ni_B-Ni_B). For C/CoFe₂O_{4_0.6}, the EXAFs fitting shown that, the Ni ions are distributed in both A and B sites, in which a characteristic of partial inverse spinel structure. The first shells at 2.00 and 2.078 Å with four and six nearest backscatters, correspond to Ni_A-O and Ni_B-O bond, respectively. The second shells was found at ~2.9 Å corresponds to Ni_B-Fe_B or Ni_B-Ni_B distance with three backscatters. It was also found that, the occupation

of Ni^{2+} cation in both A and B site are nearly portions (50.5 and 49.5% in A and B site, respectively). The result confirmed the partial inverse spinel structure of $\text{C/NiFe}_2\text{O}_4_{0.6}$. It is important to note for $\text{C/NiFe}_2\text{O}_4_{0.6}$ composite nanofibers that, the higher amplitude of the second peak than that of the first peak depends somewhat on the site of the absorber-ion incorporation. May be the incorporation at tetrahedral sites ($\text{CN} = 12$) will produce higher amplitude of the first peak compared to the incorporation at tetrahedral sites ($\text{CN} = 4$). The degree of inversion is the parameter used to explain the structural changes and was evaluated from the values of S^2 between cation tetrahedral and octahedral sites. It was found from the EXAFS fitting that, the octahedral occupation of Ni^{2+} ions with the value of 74.3, 76.9 and 50.5% were obtained for $\text{C/NiFe}_2\text{O}_4_{0.2}$, $\text{C/NiFe}_2\text{O}_4_{0.4}$ and $\text{C/NiFe}_2\text{O}_4_{0.6}$, respectively. The occupation of Fe^{3+} at tetrahedral and octahedral, respectively are 34.5 and 65.5% for $\text{C/NiFe}_2\text{O}_4_{0.2}$, 37.7 and 62.3% for $\text{C/NiFe}_2\text{O}_4_{0.4}$, and 37.7 and 62.3% for $\text{C/NiFe}_2\text{O}_4_{0.6}$. For $\text{C/NiFe}_2\text{O}_4_{0.2}$ and $\text{C/NiFe}_2\text{O}_4_{0.4}$, large portion of Ni ions occupied B site, while Fe ion occupied both in A and B site with nearly portion confirmed the totally inverse spinel structure of samples. Meanwhile, for $\text{C/NiFe}_2\text{O}_4_{0.6}$, the occupied of Ni ions in both A and B site with nearly portion suggests it partially inverse spinel structure. The local structure and distribution of the metal ions on tetrahedral and octahedral sites in the oxygen lattice are of importance for the magnetic properties of ferrites (Henderson *et al.*, 2007).

Table 4.19 Lists of coordinate number (N), amplitude reduction (S_0^2), Debye-Waller factor (σ^2), interatomic distances (R), and R-factor obtained by fitting the experimental EXAFS data at Fe and Ni K-edge for C/NiFe₂O₄_0.2.

Sample	Site	Shell	N	S_0^2	σ^2	R
Ni k-edge C/NiFe ₂ O ₄ _0.2 R-factor 0.0157265	B	Ni-O	6	0.743	0.01382	2.00870
		Ni-Fe	3	0.743	0.01269	2.89309
		Ni-Ni	3	0.743	0.00996	3.08680
		Ni-Fe	6	0.743	0.02221	3.32771
Fe k-edge C/NiFe ₂ O ₄ _0.2 R-factor 0.0012125	A	Fe-O	4	0.345	0.00014	1.86825
		Fe-Fe	6	0.345	0.02162	3.40089
		Fe-Ni	6	0.345	0.00517	3.36551
		Fe-O	12	0.345	0.00027	3.51880
		Fe-Fe	4	0.345	0.02254	3.55234
	B	Fe-O	6	0.655	0.00546	1.99933
		Fe-Ni	3	0.655	0.01728	3.00560
		Fe-Fe	3	0.655	0.01934	3.82274
		Fe-Fe	6	0.655	0.02268	4.48254
		Fe-O	6	0.655	0.00959	3.50538
		Fe-O-O	24	0.655	0.00951	3.48822

Table 4.20 Lists of coordinate number (N), amplitude reduction (S_0^2), Debye-Waller factor (σ^2), interatomic distances (R), and R-factor obtained by fitting the experimental EXAFS data at Fe and Ni K-edge for C/NiFe₂O₄_0.4.

Sample	Site	Shell	N	S_0^2	σ^2	R	
Ni k-edge C/NiFe ₂ O ₄ _0.4	B	Ni-O	6	0.769	0.01288	2.04776	
		Ni-Fe	3	0.769	0.00331	3.57655	
		Ni-Ni	3	0.769	0.01142	2.50724	
	R-factor 0.0110659	Ni-Fe	6	0.769	0.00830	3.38771	
		Ni-O	6	0.769	0.02263	3.59038	
	Fe k-edge C/NiFe ₂ O ₄ _0.4	A	Fe-O	4	0.377	0.00300	2.01251
Fe-Fe			6	0.377	0.00400	3.50910	
Fe-Ni			6	0.377	0.00942	3.66943	
R-factor 0.0028691			Fe-O	12	0.377	0.00565	3.79050
			Fe-Fe	4	0.377	0.00418	3.66514
Fe-O-O			48	0.377	0.00473	4.44615	
B		Fe-O	6	0.623	0.01654	1.81177	
		Fe-Ni	3	0.623	0.00747	3.22413	
		Fe-Fe	3	0.623	0.02700	2.97987	
		Fe-Fe	6	0.623	0.03166	3.49420	
		Fe-O	6	0.623	0.02900	3.17679	

Table 4.21 Lists of coordinate number (N), amplitude reduction (S_0^2), Debye-Waller factor (σ^2), interatomic distances (R), and R-factor obtained by fitting the experimental EXAFS data at Fe and Ni K-edge for C/NiFe₂O₄_0.6.

Sample	Site	Shell	N	S_0^2	σ^2	R
Ni k-edge C/NiFe ₂ O ₄ _0.6	A	Ni-O	4	0.505	0.00100	2.00637
		Ni-Fe	12	0.505	0.04011	3.41621
		Ni-O	12	0.505	0.04015	3.42221
		Ni-Ni	4	0.505	0.00300	3.28780
		Ni-O-Fe	24	0.505	0.04111	3.77638
	B	Ni-O	6	0.495	0.00100	2.07825
		Ni-Fe	3	0.495	0.00238	2.92917
		Ni-Ni	3	0.495	0.00238	2.91402
		Ni-Fe	6	0.495	0.00262	3.44026
		Ni-O	6	0.495	0.00300	2.90387
Fe k-edge C/NiFe ₂ O ₄ _0.6	A	Fe-O	4	0.429	0.00300	1.80078
		Fe-Fe	6	0.429	0.00400	3.25532
		Fe-Ni	6	0.429	0.00450	3.10457
		Fe-O	12	0.429	0.00565	3.39171
		Fe-Fe	4	0.429	0.00418	3.40007
	B	Fe-O-O	4	0.429	0.00673	4.04007
		Fe-O	6	0.571	0.00300	1.94764
		Fe-Ni	3	0.571	0.00338	2.89341
		Fe-Fe	3	0.571	0.01286	3.29453
		Fe-Fe	6	0.571	0.01507	3.86317
		Fe-O	6	0.571	0.00526	3.41504

4.3.2 Magnetic properties of C/NiFe₂O₄ composite nanofibers

Figure 4.40 shows the magnetic behavior studied of the CNF and C/NiFe₂O₄ composite nanofibers after carbonized at 535 °C for 1 h. Room temperature magnetization for all the prepared samples was presented in Figure 4.40 (a). It was found that, CNF exhibits diamagnetic behavior, while all composite samples show the ferrimagnetic behavior. The saturation magnetizations (M_s) values of 0.182, 2.812 and 25.83 emu/g were obtained for C/NiFe₂O₄_0.2, C/NiFe₂O₄_0.4 and C/NiFe₂O₄_0.6, respectively. The M_s value increased with increasing of the crystallite size suggests the obtained nanoparticles caused increased volume fraction of surface atoms within the particles and thus contributes to increase of M_s . The result is matched well to the previous reported (Nathani and Misra, 2004; Nawale *et al.*, 2011). However, all obtained values are lower than bulk NiFe₂O₄ particles (54.5 emu/g) (Maaz *et al.*, 2009) may be due to the existence of CNFs, the surface defect of NiFe₂O₄ nanoparticles, and the stress between the NiFe₂O₄ crystallites and the surfaces of CNFs. Moreover, the configuration of Ni²⁺ and Fe³⁺ ions in both A and B sites may tends to increase the net magnetization (Pradeep *et al.*, 2008). Figure 4.40 (b) shows the variation of the coercivity (H_c) and the squareness (M_r/M_s) with crystallite size at room temperature. It was found that, both types of value increased with increasing of crystallite size. Low coercivity was observed for all the prepared samples (47, 65 and 158 Oe for C/NiFe₂O₄_0.2, C/NiFe₂O₄_0.4 and C/NiFe₂O₄_0.6, respectively) compared to bulk value of NiFe₂O₄ (750-1000 Oe) (Huang and Chen, 2004). The result may be due to low shape anisotropy and multiple domains of NiFe₂O₄ octahedral allow them to magnetize in directions along their easy magnetic axes without hysteresis losses. The squareness with the values of 0.088, 0.133 and 0.264

were obtained for C/NiFe₂O₄_0.2, C/NiFe₂O₄_0.4 and C/NiFe₂O₄_0.6, respectively. All values are lower than 0.5 indicates not in single domain state of NiFe₂O₄ nanoparticle (Varma *et al.*, 2008).

Figure 4.41 show the typical hysteresis loops at different measurement temperature (50 - 390K) and their corresponding zero field cooled-field cooled curve (ZFC-FC) for C/NiFe₂O₄_0.2, C/NiFe₂O₄_0.4 and C/NiFe₂O₄_0.6. It was found from the results that, the magnetization for C/NiFe₂O₄_0.2 is very weak and its hysteresis loop is not reach complete saturation even at 10 kOe (Figure 4.41 (a)). This phenomenon is often observed in nanosized materials and may be due to the presence of a spin disordered surface layer which requires a larger field to be saturated. For C/NiFe₂O₄_0.4 and C/NiFe₂O₄_0.6, the complete saturation was observed indicates the particles are already almost completely oriented for a field of around 10 kOe. The observed results may be due to their large particle size caused much larger magnetocrystalline anisotropy characteristic. It was found that, all prepared samples exhibited wider hysteresis loop with decreasing the measurement temperature, suggesting the enhancement of M_s , M_r and H_c values. The remanence ratio (M_r/M_s) decrease with increasing measurement temperature for all samples (Figure 4.42). C/NiFe₂O₄_0.2 has lowest remnant magnetization at all measurement temperature. The result associated to the suggestion that the lack of saturation of the magnetization curve can strongly contribute to the decrease of the remnant magnetization.

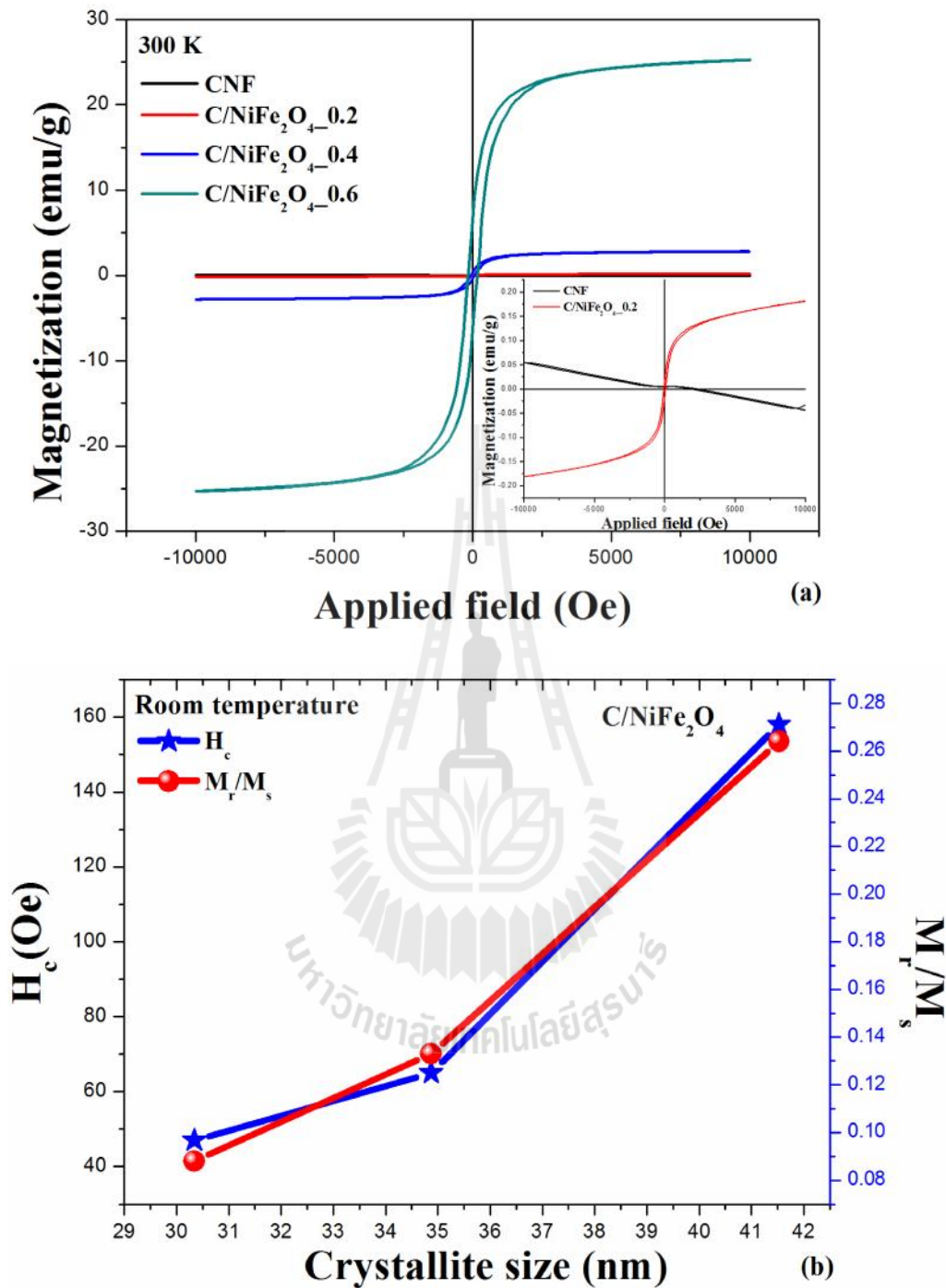


Figure 4.40 (a) Room temperature magnetization of CNF and three types of C/NiFe₂O₄ composite nanofibers carbonized at 535 °C for 1 h, (b) the variation of the coercivity (H_c) and the remanence ratio (M_r/M_s) with crystallite size at room temperature.

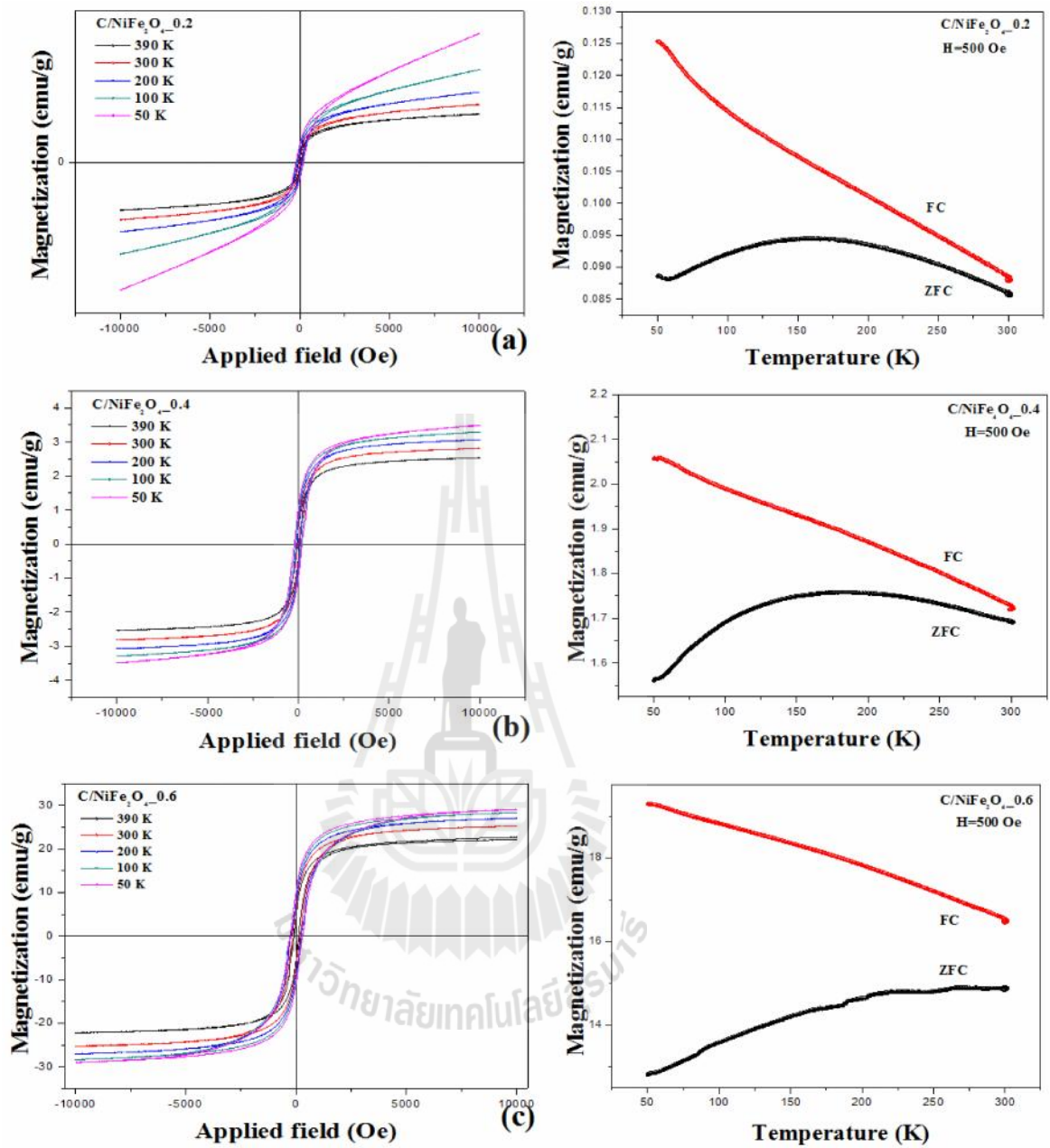


Figure 4.41 The measuring temperature dependence of Magnetization and their corresponding zero field-cooled and field-cooled (ZFC-FC) for (a) C/NiFe₂O₄_0.2 (b) C/NiFe₂O₄_0.4 (c) C/NiFe₂O₄_0.6 composite nanofibers.

Field-cooled and Zero-field-cooled (FC-ZFC) technique is used for observed the characteristic blocking-unblocking process of the particle magnetic moment when thermal energy is changed. The measurements were recorded at the temperature between 50 and 390 K, and the results are shown in Figure 4.41 (right hand side). It is found from ZFC that, the magnetic moment increases continuously up to 161 and 184 K for C/NiFe₂O₄_0.2, and C/NiFe₂O₄_0.4, respectively and then decreased. No end of raise was observed in this range of temperature for C/NiFe₂O₄_0.6, indicating the blocking temperature (T_B) being higher than room temperature. High blocking temperature for C/NiFe₂O₄_0.6, possibly due to large particle size caused large volume and thus large anisotropy energy. So for this sample the probability to cross over the anisotropy barrier is decreased (Maaz *et al.*, 2007). It is importance to note that, the obtained blocking temperature exhibited increased with increasing particle size. The result corresponds to the previous reported (Liu *et al.*, 2000). In FC spectra, the magnetization for all samples decreased with increasing the measurement temperature. Lists of the magnetic parameters are summarized in Table 4.22.

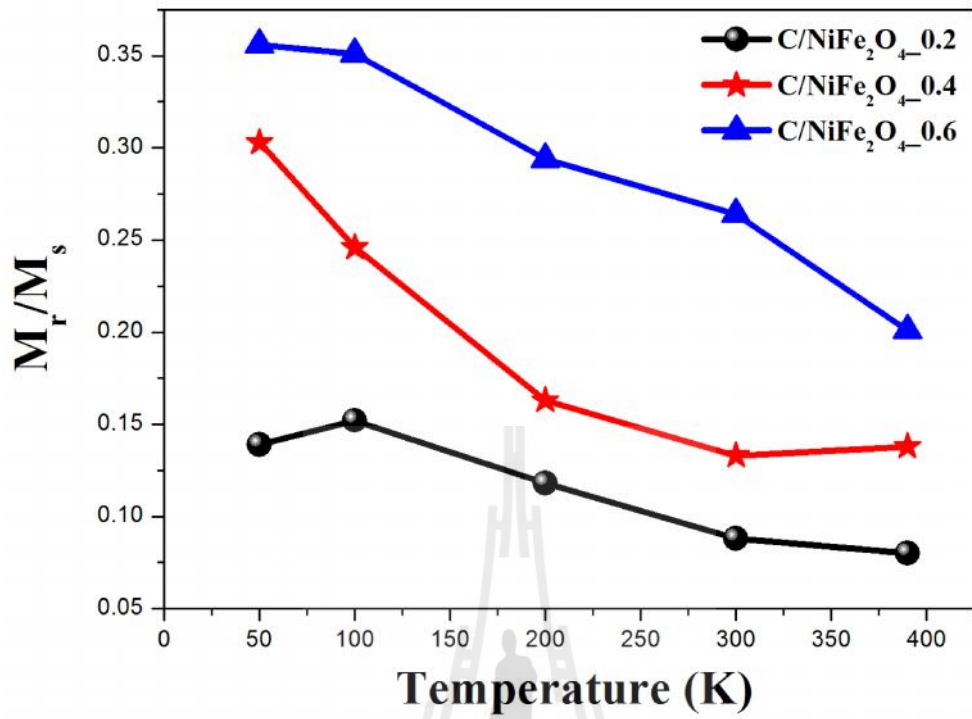


Figure 4.42 The dependence of M_r/M_s on the measurement temperature for C/NiFe₂O₄_0.2, C/NiFe₂O₄_0.4, and C/NiFe₂O₄_0.6 composite nanofibers.

Table 4.22 Lists of the magnetic parameters: coercivity (H_c), saturation magnetization (M_s), squareness ratio (M_r/M_s) and blocking temperature (T_B) of C/NiFe₂O₄ composite nanofibers with different magnetic source concentration.

Sample	Crystallite size (nm)	T (K)	H_c (Oe)	M_s (emg/g)	M_r/M_s	T_B (K)
C/NiFe ₂ O ₄ _0.2	30.34	50	210	0.403	0.139	161
		100	152.5	0.290	0.152	
		200	84	0.220	0.118	
		300	47	0.182	0.088	
		390	34	0.150	0.080	
C/ NiFe ₂ O ₄ _0.4	34.87	50	219	3.495	0.303	183
		100	155	3.292	0.246	
		200	91	3.068	0.163	
		300	65	2.812	0.133	
		390	57	2.540	0.138	
C/NiFe ₂ O ₄ _0.6	41.53	50	274	29.05	0.356	>300
		100	269	28.37	0.351	
		200	240	27.06	0.294	
		300	158	25.23	0.264	
		390	92	22.70	0.201	

4.3.3 Electrochemical properties of C/NiFe₂O₄ composite nanofibers

In this section, the capacitive performance of CNF, C/NiFe₂O₄ and NiFe₂O₄ were evaluated using cyclic voltammetry (CV), Galvanostatic charge/discharge (GCD), and Electrochemical impedance spectroscopy (EIS) techniques. The electrolyte used in this study was 1M KOH. The CV measurement was performed in potential range of -0.2-0.45V. The galvanostatic charge/discharge test was performed at the current density of 0.05, 0.1, 0.25, 0.5, 0.75 and 1A/g. The impedance behavior of all prepared electrodes was tested in a frequency range of 0.1-10⁵Hz.

4.3.3.1 Cyclic Voltammetry measurement

Figure 4.43 show cyclic voltammetry (CV) of CNF, C/NiFe₂O₄ composite nanofibers and pure NiFe₂O₄ electrode, in which was tested in 1 M KOH electrolyte over the potential range of -0.3 to 0.45 V. The potential rang used in this work is narrower than 0-0.65 V for pure NiFe₂O₄ electrode in 1M KOH reported by Al-Hoshan and co-work (Al-Hoshan *et al.*, 2012) possibly due to the polymer-based preparation of material and the problem of oxygen evolution. It was found that, the voltammogram for CNF electrode was different, regardless of the influence of electrodes material. CNF electrode did not give any redox peak in this selected potential region revealing to typical double layer behavior (Wen *et al.*, 2009; Qu *et al.*, 2008). The C/NiFe₂O₄ and NiFe₂O₄ voltammogram show a cathodic reduction peak at about 0.3V. No any oxidation peak was observed in the selected potential range. A slight hump around 0.45 V was observed. This indicates some irreversible reactions happen when potential window is higher than 0.45 V. Thus, the optimum working potential window is from -0.30 to 0.4 V. By varying the scan rate of 2, 5, 10, 30, 50, 100 and 200 mV/s, the surrounded CV curve gradually increase. CV curve of

CNF electrode was kept as quasi-rectangular at low scan rate (< 50 mV/s) indicates the predominant EDL capacitive behavior (Stankovich *et al.*, 2006; Stoller *et al.*, 2008; Inagaki *et al.*, 2010), while the deviation of curve was observed at higher scan rate. C/NiFe₂O₄ and NiFe₂O₄ electrodes show both of rectangular and redox peak in CV curve, suggesting the combination of EDLC and pseudo capacitance mechanism in charge storage. The shape of all curves are almost the same at difference scan rate, indicating electrodes were charged and discharge at a pseudo constant rate over the entire potential range. This unique feature implies that the capacitive behavior of electrode is close to the ideal capacitive behavior (Yang *et al.*, 2011). Figure 4.43 (d) shows the specific capacitance as function of scan rate for CNF, C/NiFe₂O₄ and pure NiFe₂O₄ electrodes. The specific capacitance of all electrodes decreases with increase of sweep rate possible due to short time cause hardly penetrated of ions into inner pores during charge (Wang *et al.*, 2006; Yuan *et al.*, 2008). It was found from the spectra that, the specific capacitance of C/NiFe₂O₄ electrode is highest with the value of 50.8 F/g at lowest scan rate (2mV/s) and then drops rapidly to lower than CNF in the range 5-50 mV/s sweep rate. An interesting finding is that, for a potential scan rate higher than of 50mV/s, the specific capacitance of the C/NiFe₂O₄ electrode was higher than that of CNF in which continuous decreased. This behavior illustrates the influence of NiFe₂O₄ nanoparticle when composite to pure CNF. The larger capacitance of C/NiFe₂O₄ electrode compared to CNF electrode is possibly due to either the synergistic effect between CNF and NiFe₂O₄ or larger surface area supporting the insertion of electrolyte ions. Large channels between CNF matrix and NiFe₂O₄ nanoparticules may speed up the ionic transportation inside the pores even under high sweep rate (Ning *et al.*, 2011). Thus, it is easy to understand the

enhancement of the capacity of the fiber with the addition of NiFe_2O_4 nanoparticles. This behavior makes $\text{C/NiFe}_2\text{O}_4$ very promising for capacitor application. Finally, it was found that, the NiFe_2O_4 electrode shows lowest specific capacitance at all scan rates. The result is possibly due to either the electrolyte solution is not suitable for this electrode material or pure NiFe_2O_4 without CNF matrix caused lower penetration of electrolyte ions.

The retention as a function of cycle numbers for CNF, $\text{C/NiFe}_2\text{O}_4$ and NiFe_2O_4 electrodes are shown in Figure 4.43 (e). It was found that, the decreasing of retention after 1000 cycles was observed with increasing of magnetic source content (98, 88, and 84% for CNF, $\text{C/NiFe}_2\text{O}_4$ and NiFe_2O_4 , respectively). The charge/discharge behavior of CNF is almost steady at 1000 cycles indicates good cycle stability. This is due to large CNF network structure restricts the change of electrode during charge/discharge process. Low capacity retention of $\text{C/NiFe}_2\text{O}_4$ and pure NiFe_2O_4 , respectively is mainly attributed to pseudo capacitance arising from NiFe_2O_4 nanoparticle. The electrode pulverization of these material induced by huge volume changes during the charge/discharge processes, thus leading to poor cycling stability and rate capability. However, the specific capacitance retention of 88% after 1000 cycles for $\text{C/NiFe}_2\text{O}_4$ also presents good operation stability. Due to its stable electrochemical properties, excellent reversibility and long cycle life, $\text{C/NiFe}_2\text{O}_4$ composite has effective potential for used as the electrode material of electrochemical capacitor.

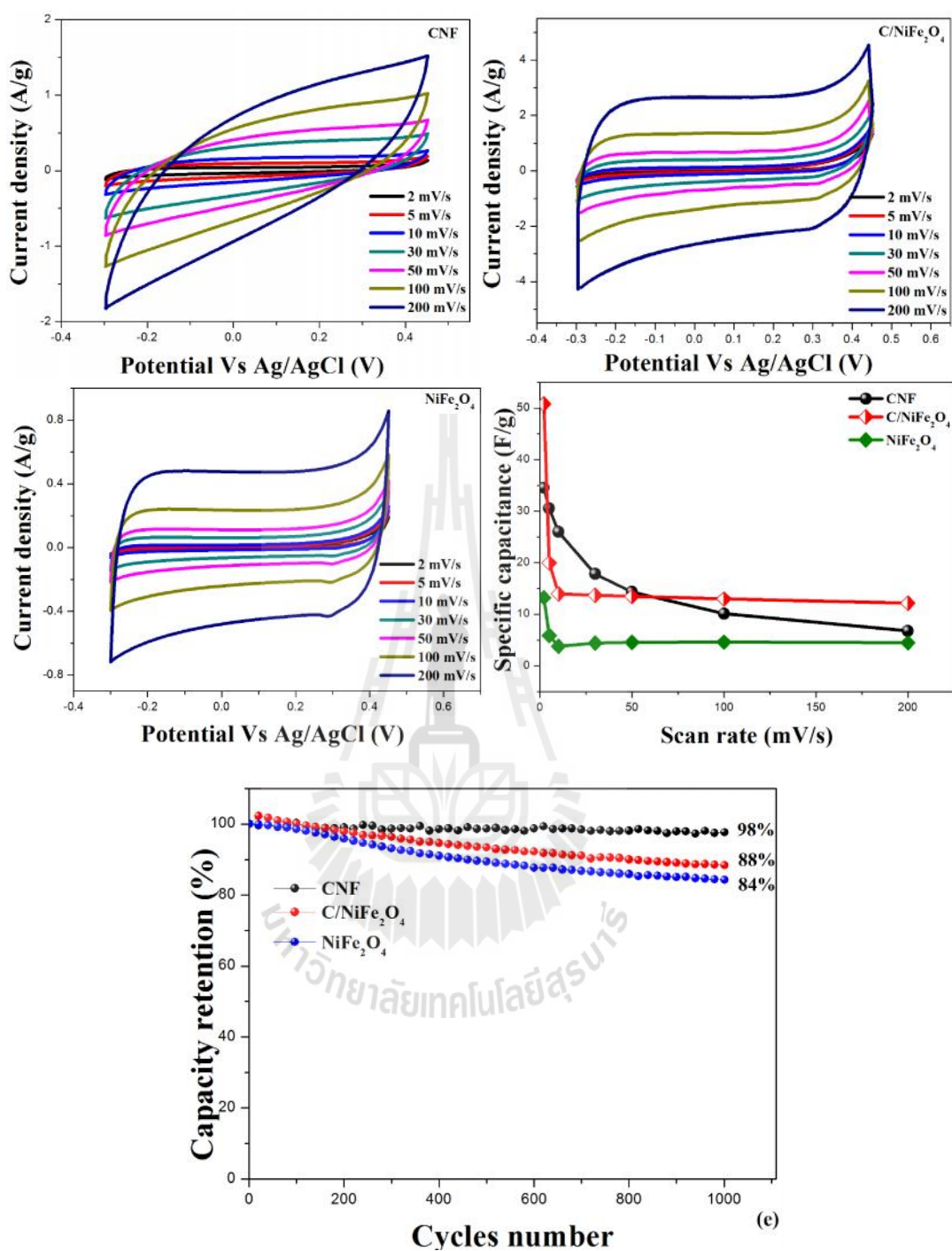


Figure 4.43 Cyclic voltammograms (CV) at different scan rates of (a) CNF, (b) C/NiFe₂O₄, and (c) NiFe₂O₄ electrodes in 1.0 M KOH electrolyte. (d) The corresponding specific capacitance at different scan rates. (e) The specific capacity retention of CNF, C/NiFe₂O₄ and NiFe₂O₄ electrodes at 1000 cycles.

4.3.3.2 Galvanostatic charge/discharge measurements

The electrochemical properties of the prepared electrode are investigated further by means of galvanostatic charge/discharge. The measurement was performed by charging/discharging between -0.25 to 0.25 V and the current densities of 0.05, 0.1, 0.25, 0.5, 0.75 and 1 A/g in 1 M KOH electrolyte solution. At these current densities, the shape of all charge/discharge curves is nearly linear and symmetric, which is characteristic of a good capacitance behavior (Ye *et al.*, 2005).

Figure 4.44 displays the galvanostatic charge/discharge (GCD) curves at different current density for CNF, C/NiFe₂O₄ and NiFe₂O₄ electrodes. It was found that, all electrodes showed nearly linear discharge curves without hump, suggesting a typical linear relationship with time. This is a characteristic of an electric double layer capacitance. In fact, the spectra of C/NiFe₂O₄ and NiFe₂O₄ should not show ideal shape due to their pseudocapacitance behavior arises from the Faradaic process of NiFe₂O₄ nanoparticle. However the selected potential window for GCD (-0.25 to 0.25 V) is not cover the redox peak (~0.3V). There fore nearly ideal GCD shape was observed. The coulomb efficiency (η) of the electrode during charge/discharge of 89, 74 and 86% were obtained for CNF, C/NiFe₂O₄ and NiFe₂O₄ electrodes, respectively. The value is less than 99%, meaning loss in coulombic efficiency during charge/discharge. The energy and power densities of the CNF, C/NiFe₂O₄ and NiFe₂O₄ electrodes were calculated and the result was presented in the Ragone plot as shown in Figure 4.44 (d). Among these electrodes C/NiFe₂O₄ showed highest energy density at all current density compared to other two electrodes. While, the CNF electrode shows slightly larger power densities than C/NiFe₂O₄ at all current densities. C/NiFe₂O₄ electrode exhibits an energy density of 0.29 Wh/kg at a power density of

12.4 W/kg and still maintains 0.073 Wh/kg at a power of 218 W/kg. The value very low compared to other metal oxide reported such as MnO_2 cell (7 Wh/kg at 5 kW/kg) (Wu *et al.*, 2010) and NiO cells (15-20 Wh/kg) (Wang¹ *et al.*, 2008; Inoue *et al.*, 2010). However, the obtained values still is in the range of electrochemical capacitor (Simon *et al.*, 2008). It is note that, the energy and power densities can be further improved by forming composites with activated CNF.

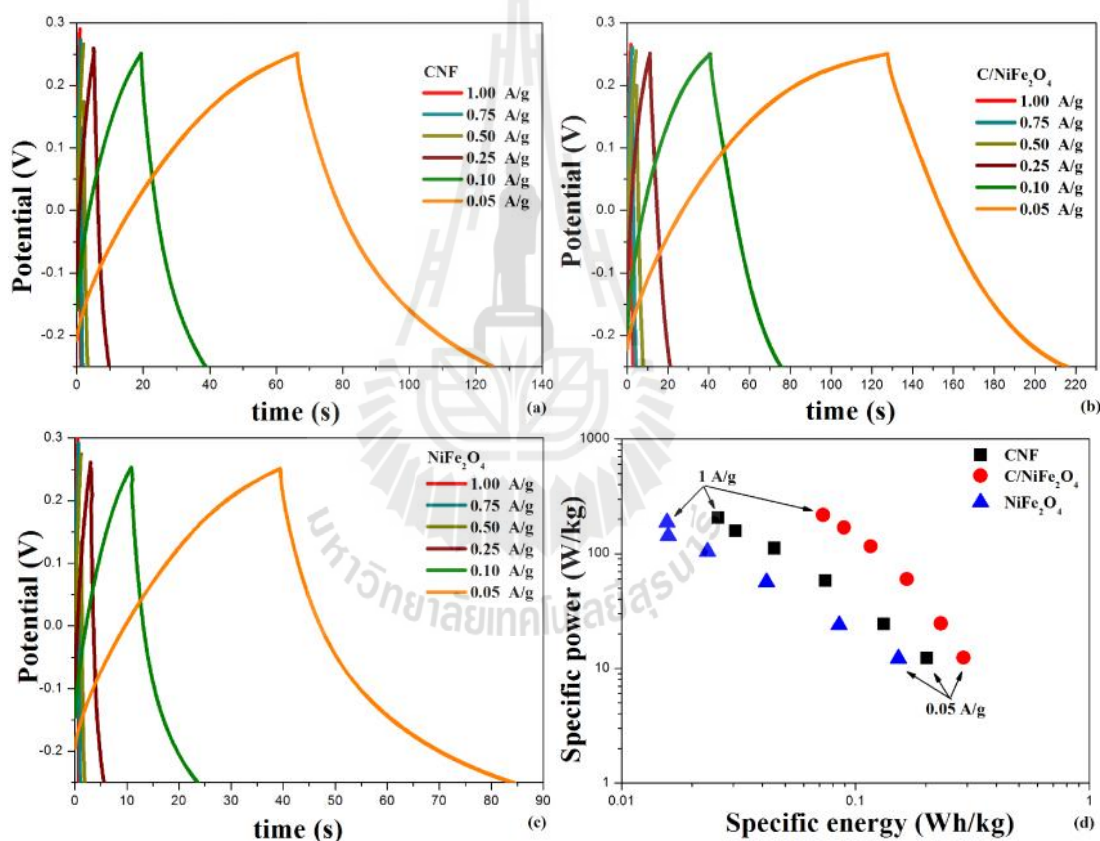


Figure 4.44 Galvanostatic charge/discharge curves of (a) CNF, (b) C/NiFe₂O₄, and (c) NiFe₂O₄ electrodes at current densities of 0.05, 0.1, 0.25, 0.5, 0.75 and 1.0 A/g in 1 M KOH electrolyte solution. (d) The corresponding Ragone plot.

4.3.3.3 Electrochemical Impedance Spectroscopy (EIS) measurements

Figure 4.45 shows Nyquist plots of CNF, C/NiFe₂O₄ and NiFe₂O₄ electrodes, where the measurements were carried out in the frequency range of 0.1 Hz – 10⁵ Hz in 1M KOH. A straight line at lower frequency without semicircle was observed for CNF electrode. The results suggest an EDLC behavior and negligible charge transfer resistance of CNF (Laforgue, 2011). For C/NiFe₂O₄ and pure NiFe₂O₄ electrodes, a single semicircle at high frequency with a straight line at lower frequency was observed. This indicates the charge storage mechanism of these cells is based on both electrical double layer and Faradaic process (Hu and Chu, 2001). The values of the combined resistance (R_s) values of 9.3, 7.8 and 7.4 Ω were obtained for CNF, C/NiFe₂O₄ and NiFe₂O₄ electrodes, respectively. The charge transfer resistances of 0.5 and 2.15 Ω were obtained for C/NiFe₂O₄ and NiFe₂O₄ electrodes, respectively. The lower value of charge transfer resistance obtained in C/NiFe₂O₄ electrode than that of NiFe₂O₄ electrode is possibly due to the carbon acting as conductive matrix for nanoparticle dispersion, and provides a large interface area between electrode and electrolyte. Moreover, the composite of these materials caused shortened electrolyte ion diffusion paths, and thus electron and ions can be more easily transferred resulting in an enhancement electrical conductivity (Snook *et al.*, 2011). The largest charge transfer resistance value for NiFe₂O₄ is possibly due to roughness surface from NiFe₂O₄ causing the enlarged contact area. No charge transfer was observed for CNF electrode indicating no interfacial resistance (Laforgue, 2011). This behavior is similar to an ideal electrical double layer capacitor (Heli *et al.*, 2012; Sharma and Zhai, 2009). The electrolyte ion diffusion into pore is characterized by the linear part of sloped line at low frequency. A pure capacitor should exhibit a vertical line and the

deviation from the vertical line is attributed to the inner-pore diffusion resistance for electrolyte ions, which strongly depends on the detailed porous structure of the different samples. In this study, the slope increases and tends to become more purely capacitive for the pure CNF, C/NiFe₂O₄, and NiFe₂O₄ electrodes, respectively. The longest straight line for CNF electrode indicating the penetration of electrolyte ions into the interior bulk would be greatest. The shortest length for NiFe₂O₄ cell indicates that the electrolyte ion just surface is being accessed.

Figure 4.46 shows the Bode plots of CNF, C/NiFe₂O₄, and NiFe₂O₄ electrodes in 1M KOH solution. The frequency dependence of the phase angle for these three electrodes is shown in Figure 4.46 (a). It was found at lowest frequency (0.1 Hz) that, the phase angle values of -52°, -49°, and -36° were obtained for CNF, C/NiFe₂O₄ and NiFe₂O₄ electrodes, respectively. All obtained values is far from -90°, indicating that the response is not purely capacitive. The values of capacitor response frequency (f_0) at the negative value of phase angle equal to -45 were about 4, 0.45, and less than 0.1 Hz for the CNF, C/NiFe₂O₄ and NiFe₂O₄ electrodes, respectively. These values are found to be in the lower frequency range, which is an indicative of good capacitive behaviour of an electrode material (Zhang *et al.*, 2006). The values of the corresponding relaxation time constant calculated by the equation $\tau_0 = 1/f_0$ were obtained to be 0.25, 2.22 and larger than 10 s, respectively. The lowest time constant of CNF indicates the highest high power delivery of the cell (Girija and Sangaranarayanan, 2006; Burke, 2000). The frequency dependence of impedance for CNF, C/NiFe₂O₄ and NiFe₂O₄ at 0.2 V was presented in Figure 4.46 (b). The impedance value increases with decrease in frequency for all the prepared electrodes. The C/NiFe₂O₄ electrode shows the lowest impedance at all frequency impling the

better conductivity compared to other two electrodes. This observed behavior is possibly due to the nature of both CNF and NiFe_2O_4 .

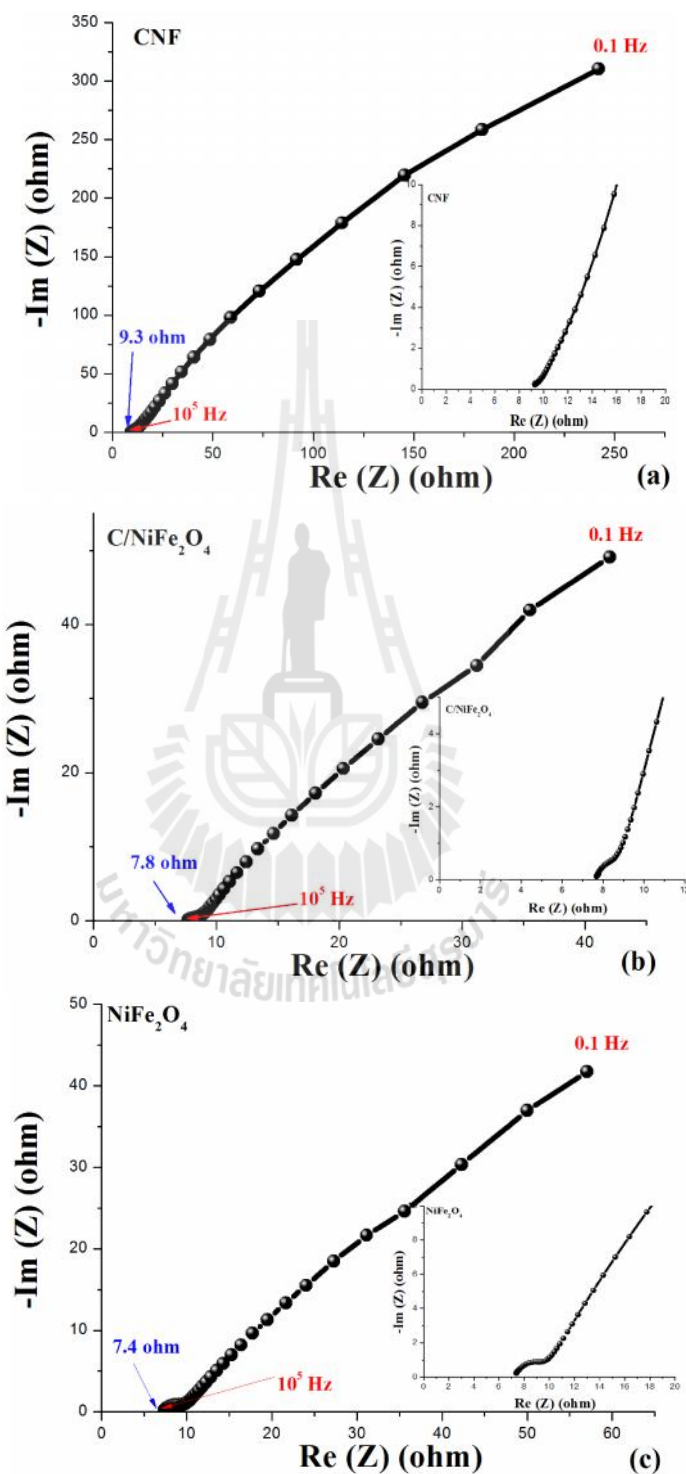


Figure 4.45 Nyquist impedance plots at a frequency range of 0.1 Hz-100 kHz in 1 M KOH electrolyte solution for (a) CNF, (b) C/ NiFe_2O_4 and (c) NiFe_2O_4 electrodes.

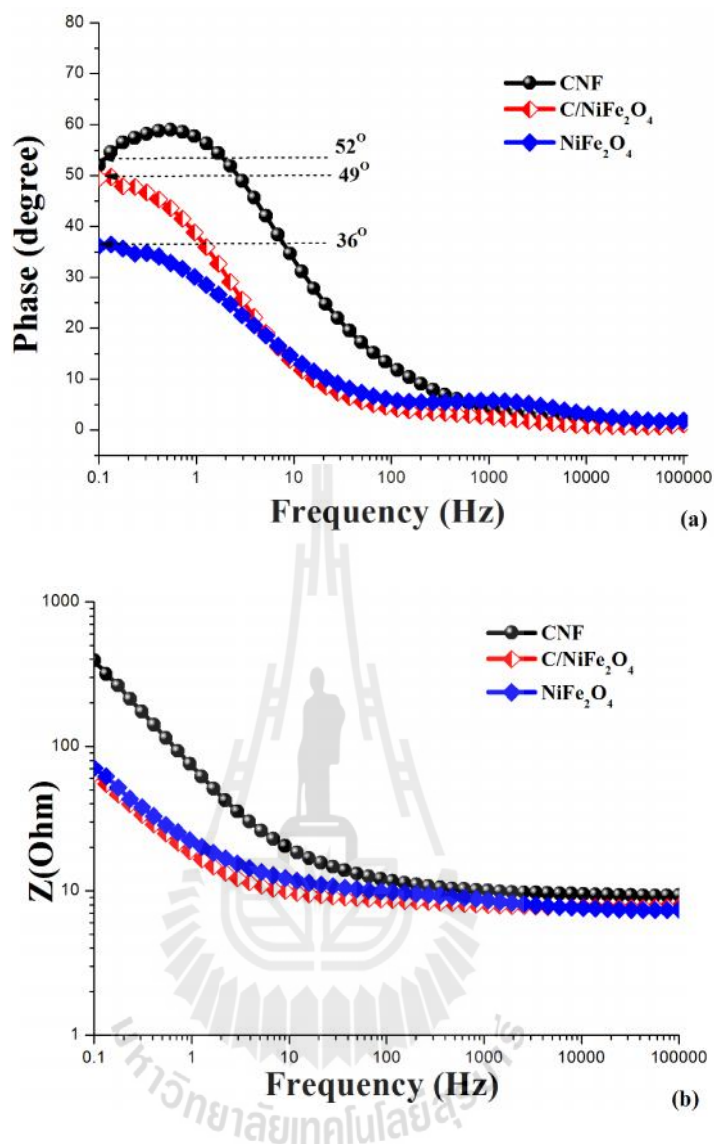


Figure 4.46 Bode plots of (a) frequency dependence of phase angle (b) impedance dependence on frequency of CNF, C/NiFe₂O₄ and NiFe₂O₄ electrodes.

CHAPTER V

CONCLUSIONS

In this study, carbon/spinel ferrite composite nanofibers (C/MFe₂O₄; M is Cu, Co, and Ni) have been successfully fabricated by using electrospinning technique followed by carbonization under mixture of air and argon atmosphere. In each composite system, four samples with different weight ratio of polymer and magnetic source were set as 100/0, 80/20, 60/40, and 40/60, respectively and the final products are designated as C/MFe₂O₄_0, C/MFe₂O₄_0.2, C/MFe₂O₄_0.4, and C/MFe₂O₄_0.6, respectively. The surface morphology, crystal structure, and local structure of the prepared samples were characterized by TGA, XRD, SEM, TEM, BET, Raman spectroscopy, and XAS techniques. The magnetic properties were observed by VSM, while the electrochemical properties were studied by CV, GCD and EIS techniques. In the electrochemical measurements, bulk MFe₂O₄ has been also studied for comparison. Conclusions based on the carbon nanofibers reinforced with different types of spinel ferrite nanoparticles are summarized as follows

5.1 The structure and morphology characterization

The C/MFe₂O₄ (M = Cu, Co and Ni) composite nanofibers show composite structure of cubic MFe₂O₄ and amorphous carbon. The average crystallite size of CuFe₂O₄ and NiFe₂O₄ nanoparticles increased with increasing the magnetic source content (~25-46 and ~30-42 nm for C/CuFe₂O₄ and C/NiFe₂O₄, respectively), but not

for CoFe_2O_4 (~ 22 , ~ 54 , and ~ 45 for $\text{C}/\text{CoFe}_2\text{O}_4_{0.2}$, $\text{C}/\text{CoFe}_2\text{O}_4_{0.4}$, and $\text{C}/\text{CoFe}_2\text{O}_4_{0.6}$, respectively). It could be seen that the samples with large amount of polymer source concentration better supported the distribution of MFe_2O_4 nanoparticles in CNF matrix, and reduced the particle agglomeration. This resulted in smaller crystallite size of the MFe_2O_4 nanoparticles. The d-spacing values for all $\text{C}/\text{MFe}_2\text{O}_4$ system are slightly lower than bulk cubic MFe_2O_4 (i.e., 2.524 \AA , 2.530 \AA and 2.514 \AA for cubic CuFe_2O_4 (JCPDS 77-0010), CoFe_2O_4 (JCPDS 22-1086) and NiFe_2O_4 JCPDS 86-2267, respectively), possibly due to the effect of CNF matrix. The lattice constant values for all $\text{C}/\text{MFe}_2\text{O}_4$ systems are in good agreement with those of bulk values (8.370 , 0.839 and 0.8337 \AA for cubic CuFe_2O_4 , CoFe_2O_4 and NiFe_2O_4 , respectively). The oxidation states of Fe and M ions in MFe_2O_4 structure are +3 and +2, respectively except for $\text{C}/\text{CoFe}_2\text{O}_4_{0.6}$, which shows a mixed oxidation state of Co (+2 and +3). The percentage of magnetic source content strongly influences the spinel structure. It was totally inverse spinel structure for the samples with magnetic source content lower than 50 wt.% ($\text{C}/\text{MFe}_2\text{O}_4_{0.2}$ and $\text{C}/\text{MFe}_2\text{O}_4_{0.4}$), while the structure becomes partially inverse spinel for the sample containing magnetic source content higher than 50 wt.% ($\text{C}/\text{MFe}_2\text{O}_4_{0.6}$). In the latter structure, the M^{2+} occupied in both A and B sites with the different portion (45.3 and 54.7%, respectively for $\text{C}/\text{CuFe}_2\text{O}_4_{0.6}$; 58.9 and 41.1%, respectively for $\text{C}/\text{CoFe}_2\text{O}_4_{0.6}$; 50.5 and 49.5%, respectively for $\text{C}/\text{NiFe}_2\text{O}_4_{0.6}$).

According to the morphology observation, the as spun nanofibers with diameters in the range of 455-900 nm were observed before heat treatment process. The shrinkage of about 20-35% was observed after carbonization due to the combustion of PAN and the decomposition of magnetic source (i.e., 450-550, 430-

570, and 400-600 for C/CuFe₂O₄, C/CoFe₂O₄, and C/NiFe₂O₄ systems, respectively). It is important to note that, the filmy fiber, attached to other fibers and the worse uniformity were observed for all C/MFe₂O₄_0.6 samples. The values of specific surface area of the composite nanofibers were obtained to be in the range of 68.11 - 190.38 m²/g for C/CuFe₂O₄, 60 - 151 m²/g for C/CoFe₂O₄, and 89.8 - 209.67 m²/g for C/NiFe₂O₄. There is no any significant trend with the variation of magnetic source concentration. However, all the surface area values are higher than that of pure CNF (30.07 m²/g). This behavior suggests the advantage of the existence of MFe₂O₄ nanoparticles in CNF matrix.

5.2 The Magnetic properties

According to the magnetic properties study, CNFs exhibited diamagnetic, while all C/MFe₂O₄ composite samples showed ferrimagnetic behavior. The obtained values of room temperature saturation magnetization (M_s) for all C/MFe₂O₄ composite nanofibers were about ~0.3-12, ~0.2-43, and ~0.2-25 emu/g for C/CuFe₂O₄, C/CoFe₂O₄, and C/NiFe₂O₄ system, respectively. For the C/CuFe₂O₄ and C/NiFe₂O₄ systems, the M_s increased with increasing the crystallite size possibly due to large particle size causing an increase in volume fraction of surface atoms within the particles. The independence of M_s on crystallite size for C/CoFe₂O₄ system might be due to the other different parameters which influence the value of M_s in the ferrite system. Moreover, all M_s values are lower than those of bulk MFe₂O₄ (i.e., 33.4, 74.08, and 54.5 emu/g for CuFe₂O₄, CoFe₂O₄ and NiFe₂O₄, respectively). This is possibly due to either the existence of CNF matrix extinguishing the surface magnetic moment with spin canting or the disorder spins from the different crystallite size. The

obtained values of coercivity (H_c) are 89.5, 178.0, and 54.1 nm for C/CuFe₂O₄ samples with particle sizes of 24.58, 36.29 and 45.73 nm, 612, 825 and 1245 Oe for C/CoFe₂O₄ samples with particle sizes of 21.5, 44.9 and 54.4 nm, and 47, 65 and 158 Oe for C/NiFe₂O₄ samples with particle sizes of 30.34, 34.87 and 41.53 nm, respectively. It can be seen that the coercivity for C/CoFe₂O₄ and C/NiFe₂O₄ systems exhibited crystallite size dependent, and larger particle size leads to increase of coercivity. The squareness (M_r/M_s) values for all samples are lower than 0.5 implying that the particles are predominantly not in the single domain state. Except for C/CoFe₂O_{4_0.4}, the M_r/M_s value of 0.502 is closed to 0.5 for a system of non-interacting single domain particles with uniaxial anisotropy. This behavior is possibly due to its largest crystallite size compared to those of the C/CoFe₂O_{4_0.2} and C/CoFe₂O_{4_0.6}. By varying the measuring temperature (50-390 K), it was found that the M_s and H_c increased with decreasing temperature. This behavior is possibly due to the magnetic moment that was induced and turned around in the direction of applied field at low temperature. Thus, the magnetization increased, while at high temperature the thermal fluctuations of the magnetic moments presented. On the other hand, the random orientation of spins at high temperature causes the coercivity to be low at high temperature. It was found for C/CuFe₂O_{4_0.2} and C/NiFe₂O_{4_0.2} that the magnetization was not saturated at ± 10 kOe even at low temperature of 50 K suggesting that their particles were not completely oriented for a field of around ± 10 kOe. This behavior is possibly due to either a result of spin canting or the smallest particle size that affects small anisotropy and requires a larger field to be saturated together. In C/CoFe₂O₄ system, the blocking temperature (T_B) for all the prepared samples is larger than room temperature, while a variety of values was observed in the

other two systems. The T_B values were obtained to be 121, >300, 196 K for C/CuFe₂O₄_0.2, 0.4, 0.6, respectively, and 161, 183, >300 for C/NiFe₂O₄_0.2, 0.4, 0.6, respectively.

5.3 The Electrochemical properties

According to the electrochemical properties study, the effect of electrode material on the electrochemical properties was investigated in the CNF, C/MFe₂O₄ and MFe₂O₄ electrodes (M = Cu, Co and Ni). In this section, the summarized relate to the charge storage mechanism, the specific capacitance and the energy density. Firstly, the charge storage mechanism strongly depends on type of the electrode material. It was found that, the CNF electrode stored energy via the accumulation of charge at electrode/electrolyte interface (EDLC), while the pseudocapacitor charge/discharge mechanism was observed in the C/MFe₂O₄ and MFe₂O₄ electrodes. It is seen from the experimental results that, the latter behavior arises from the MFe₂O₄ metal oxide as seen from the redox peaks in CV curve. In 0.5 M Na₂SO₄, the anodic and cathodic peaks at around 0.85 and 0.25 V, respectively were observed for the C/CuFe₂O₄ electrode, while the peaks at ~0.6 and 0.1 V, respectively were observed for the CuFe₂O₄ electrode. The anodic peak could be assigned to the stepwise oxidation of Fe⁰/Fe³⁺ (~0.7 V), while the cathodic peak relate to the stepwise reduction of either Cu²⁺/Cu⁺ or Cu²⁺/Cu (0.16, 0.335 V), respectively. In 1M KOH electrolyte solution, the narrower potential window was observed due to the problem of hydrogen-oxygen evolution (-0.2 to 0.35 V for C/CuFe₂O₄ and C/CoFe₂O₄, and -0.3 to 0.45 V for C/NiFe₂O₄ system). A cathodic peak potential was observed for all the C/MFe₂O₄ and MFe₂O₄ samples (at 0.21-0.23 V, ~0.28-0.3 V, and ~0.3 V for

C/CuFe₂O₄, C/CoFe₂O₄, and C/NiFe₂O₄ system, respectively). These redox processes are believed to be associated with reduction of Cu²⁺ to Cu¹⁺/Cu, Co²⁺ to Co, and Ni²⁺ to Ni.

Secondly, the specific capacitance calculated from CV curves showed different value dependence on the electrolyte solution and potential window used as clearly seen in C/CuFe₂O₄ system. At the same scan rate of 50 mV/s, the specific capacitance values of 22, 70 and 58 F/g for CNF, C/CuFe₂O₄, and CuFe₂O₄, respectively were observed in 0.5M Na₂SO₄ with the potential windows of -0.3 to 2V, while the values of 0.3, 16 and 3.6 F/g were obtained in 1M KOH with the potential windows of -0.2 to 0.35V. It was found that the C/CuFe₂O₄ exhibited the highest value in both electrolyte solutions suggesting the advantage of composite material and confirming the better electrochemical performance after making a composite of CNF with CuFe₂O₄. For the other two systems, the superior electrochemical capacitive performance for C/MFe₂O₄ compared to CNF and MFe₂O₄ electrodes was also observed. The results indicate that the capacitive behavior of CNF is remarkably improved when composited with MFe₂O₄ nanoparticles. This behavior can be attributed to the combined contribution of the main redox pseudocapacitance of MFe₂O₄ and partly from the electric double layer capacitance of CNF. Moreover, the synergistic effect between CNF and MFe₂O₄ may also play a crucial role. Larger surface area with free space between MFe₂O₄ and CNF may well support the insertion of electrolyte ions and speed up rate transportation inside the pores. Among three electrodes in each system, the capacitance retention of CNF is better than those of C/MFe₂O₄ and MFe₂O₄ electrodes, respectively (i.e., 97, 86, 79% for C/CuFe₂O₄ system; 98, 84 and 67% for C/CoFe₂O₄ system; 98, 88, 84% for C/NiFe₂O₄ system).

This may be because the CNF network structure restricts the change of electrode volume during charge/discharge process. Moreover, its EDLC charge storage mechanism also supports the stability due to the accumulation of ions at the electrode/electrolyte during charging/discharging process. The better rate capability of C/MFe₂O₄ than that of MFe₂O₄ electrode is possibly due to the free space between the MFe₂O₄ nanoparticles in CNF matrix working as an elastic buffer that could accommodate larger volume expansion/contraction compared with the pure MFe₂O₄ electrode. As a result, less volume change during charge/discharge processes was observed. While, for pure MFe₂O₄ electrodes, the stronger pseudocapacitor behavior during charge/discharge process may result in huge volume changes, thus leading to poor cycling stability.

Finally, the energy density for all the prepared electrodes were found to be quite low but was still in the range observed in electrochemical capacitor of 0.02-20 Wh/kg (Simon *et al.*, 2008). Among the three different electrodes in each system, C/MFe₂O₄ showed almost highest energy density compared to CNF and MFe₂O₄ electrodes at all current densities. By consider at a current density of 1 A/g, the energy density for C/MFe₂O₄ was improved about 2, 9, and 64% after adding the CuFe₂O₄, CoFe₂O₄ and NiFe₂O₄, respectively into CNF matrix. Moreover, the improvements of ~42, 62, and 79% in comparison with the pure MFe₂O₄ electrodes were also observed. Except for the synergistic effect between the CNF matrix and MFe₂O₄ nanoparticles as reported earlier, the existence of CNF improved the conductivity and caused the high charge transfer kinetics of C/MFe₂O₄ that supported the enhancement of specific capacitance and thus energy density. The conductivity improvement of C/MFe₂O₄ electrodes can be observed from their lower charge transfer resistance than that of

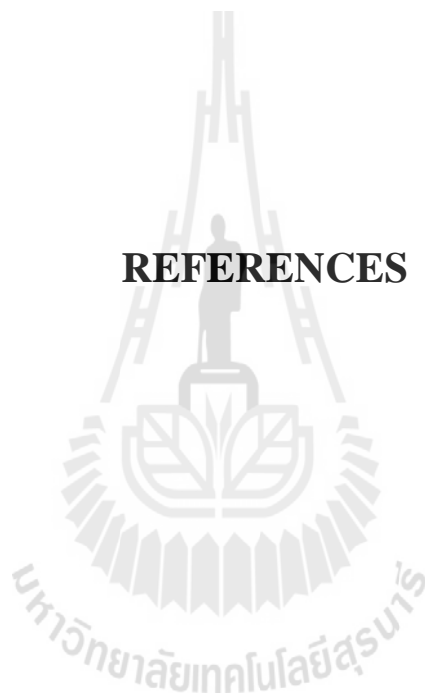
MFe₂O₄ (6.3 and 7 Ω for C/CuFe₂O₄ and CuFe₂O₄, respectively; 0.85 and 1.9 Ω for C/CoFe₂O₄ and CoFe₂O₄, respectively; 0.5 and 2.15 Ω for C/NiFe₂O₄ and NiFe₂O₄, respectively).

5.4 Suggestion for future work on C/MFe₂O₄

From the results obtained in this study, several investigations from the experiments still cannot be clearly explained. Therefore, it is interesting to conduct the following studies,

- (1) Investigation of the stoichiometry of MFe₂O₄ (M=Cu, Co, Ni) using the energy dispersive spectroscopy (EDS) is required to confirm the fraction of constituent element of Fe, Cu, Co, Ni, and O ions in the prepared samples.
- (2) Investigation of oxygen vacancies in the sub lattice tetrahedral and octahedral sites of inverse spinel structure using the X-ray Photoelectron spectroscopy (XPS) is essential to have a better understanding of the formation of ferrimagnetic behavior.
- (3) Investigation of the electric conductivity values of CNF and C/MFe₂O₄ composite nanofibers is required to confirm the improvement of the electrochemical performance after making composite of a CNF with MFe₂O₄.
- (4) More investigation of the EIS spectra should be fitted to the equivalent circuit to obtain the Warburg impedance, double layer capacitance, and pseudocapacitance.

REFERENCES



REFERENCES

- Atkins, P.W. (1998). **Physical Chemistry** (6th ed). San Francisco: W.H. Free-man and Company.
- Ankudiov, A.L., Bouldin, C.E., Rehr, J.J., Sims, J., and Hung, H. (2002). Parallel calculation of electron multiple scattering using Lanczos algorithms. **Physical Review B**. 65: 104107.
- Alcantara, R., Jaraba, M., Lavela, P., Tirado, J.L., and Jumas, J.C. (2003). Changes in oxidation state and magnetic order of iron atoms during the electrochemical reaction of lithium with NiFe₂O₄. J. Olivier-Fourcade. **Electrochemistry Communications**. 5: 16.
- An, Z.G., Pan, S.L., and Zhang, J.J. (2009). Synthesis, tunable assembly of spear-like nickel nanocrystallites: from urchin-like particles to prickly chains. **The Journal of Physical Chemistry C**. 113: 1346.
- Ayyappan, S., Mahadevan, S., Chandramohan, P., Srinivasan, M.P., Philip, J., and Rai, B. (2010). Influence of Co²⁺ ion concentration on the size, magnetic properties, and purity of CoFe₂O₄ spinel ferrite nanoparticles. **The Journal of Physical Chemistry C**. 114: 6334.
- Al-Hoshan, M.S., Singh, J.P., Al-Mayouf, A.M., Al-Suhybani, A.A., and Shaddad, M.N. (2012). Synthesis, physicochemical and electrochemical properties of nickel ferrite spinels obtained by hydrothermal method for the oxygen evolution reaction (OER). **International Journal of Electrochemical Science**. 7: 4959-4973.

- Bragg, W.L. (1913). The diffraction of short electromagnetic waves by a crystal. **Proceedings of the Cambridge Philosophical Society**. 17: 43-57.
- Burlant, W.J., and Parsons, J.L. (1956). Pyrolysis of polyacrylonitrile. **Journal of Polymer Science**. 22 (101): 249-256.
- Bockris, J.M., and Reddy, A.K. (1970). **Modern Electrochemistry (Chapter 1)**. Plenum. 720.
- Burke, A. (2000). Ultracapacitors: why, how, and where is the technology. **Journal of Power Sources**. 91: 37.
- Bard, A.J., and Faulkner, L.R. (2001). **Electrochemical methods: Fundamentals and Applications** (2nd ed). New York: John Wiley & Sons.
- Bao, S.J., Li, C.M., and Guo, C.X. (2008). Biomolecule-assisted synthesis of cobalt sulfide nanowires for application in supercapacitors. **Journal of Power Sources**. 180: 676-681.
- Barranco, V., Lillo-Rodenas, M.A., Linares-Solano, A., Pico, F., Ibanez, J., Agulloruedar, F., Oya, A., Amarilla, J.M., and Rojo, J.M. (2010). Amorphous carbon nanofibers and their activated carbon nanofibers as supercapacitor electrodes. **Journal of Physical Chemistry C**. 114: 10302-07.
- Craik, D.J. (1975). **Journal Magnetic Oxides**. New York: John Wiley & Sons.
- Charles, S.W., Chandrasekhar, R., O'Grady, K., and Walker, M. (1988). Remanence curves of cobalt ferrite powders obtained by fractionation of a suspension through a silica gel column. **Journal of Applied Physics**. 64: 5840.
- Conway, B.E. (1991). Transition from supercapacitor to battery behavior in electrochemical energy storage. **Journal of the Electrochemical Society**. 138: 1539.

- Croft, M., Sills, D., Greenblatt, M., Lee, C., Cheong, S.W., and Ramanujachary, K.V. (1997). Systematic Mn d-configuration change in the $\text{La}_{1-x}\text{Ca}_x\text{MnO}_3$ system: A Mn K-edge XAS study. **Physical Review B**. 55 (14): 8726-8732.
- Cheng, F., Peng, Z., Liao, C., Xu, Z., Gao, S., Yan, C., Wang, D., and Wang, J. (1998). Chemical synthesis and magnetic study of nanocrystalline thin films of cobalt spinel ferrites. **Solid State Communications**. 107: 471-476.
- Conway B.E. (1999). **Electrochemical supercapacitors: Scientific fundamental and technological applications**. New York: Kluwer Academic/Plenum Publisher.
- Cullity, B. D., and Stock, S.R. (2001). **Elements of X-ray diffraction**. Prentice-Hall, Englewood Cliffs.
- Caizer, C., Popovici, M., and Savii, C. (2003). Spherical $(\text{Zn Ni}_{1-x}\text{Fe}_2\text{O}_4)$ nanoparticles in an amorphous $(\text{SiO}_2)_{1-x}$ matrix, prepared with the sol-gel method. **Acta Materialia**. 51: 3607-3616.
- Callister, W. (2003). **Materials science and engineering an introduction** (6th ed). New York: John Wiley & Sons.
- Chu, Y.Q., Fu, Z.F., and Qin, Q.Z. (2004). Cobalt ferrite thin films as anode material for lithium ion batteries. **Electrochimica Acta**. 49: 4915-4921.
- Chen, Q.L., Xue, K.H., Shen, W., Tao, F.F., Yin, S.Y., and Xu, W. (2004). Fabrication and electrochemical properties of CNT array electrode for supercapacitor. **Electrochimica Acta**. 49: 4157-4161.
- Caruntu, D., Caruntu, G., and O'Connor, C.J. (2007). Magnetic properties of variable sized Fe_3O_4 nanoparticles synthesized from non-aqueous homogeneous solutions of polyols. **Journal of Physics D: Applied Physics** 40: 5801-5809.

- Coey, J.M.D. (2009). **Magnetism and magnetic materials**. New York: Cambridge University Press.
- Carta, D., Casula, M.F., Falqui, A., Loche, D., Mountjoy, G., Sangregorio, C., and Corrias, A. (2009). A structural and magnetic investigation of the inversion degree in ferrite nanocrystals MFe_2O_4 (M=Mn, Co, Ni). **Journal of Physical Chemistry B**. 113: 8606-8615.
- Chen, I.H., Wang, C.C., and Chen, C.Y. (2010). Fabrication and characterization of magnetic cobalt ferrite/polyacrylonitrile and cobalt ferrite/carbon nanofibers by electrospinning. **Carbon**. 48: 604.
- Cheng, Q., Tang, J., Ma, J., Zhang, H., Shiya, N., and Qin, L.C. (2011). Graphene and nanostructured MnO_2 composite electrodes for supercapacitors. **Carbon**. 49: 2917-25.
- Dash, J., Prasad, S., Venkataramani, N., Krishnan, R., Kishan, P., Kumar, N., Kulkarni, S.D., and Date, S.K. (1999). Study of magnetization and crystallization in sputter deposited LiZn ferrite thin films. **Journal of Applied Physics**. 86: 3303.
- Du, J.H., Su, G., and Bai, S. (2000). Electroless nickel deposition on the surface of vapor grown carbon nanofibers. **New Carbon Materials**. 15: 49-53.
- Demir, M.M., Yilgor, I., Yilgor, E., and Erman, B. (2002). Electrospinning of polyurethane fibers. **Polymer**. 43: 3303-3309.
- Do, J.S., and Weng, C.H. (2006). Electrochemical and charge/discharge properties of the synthesized cobalt oxide as anode material in Li ion batteries. **Journal of Power Sources**. 159: 323.

- Dixit, G, Singh, J.P., Srivastava, R.C., Agrawal, H.M., Choudhary, R.J., and Gupta, A.J. (2010). Structural and magnetic behavior of NiFe₂O₄ thin film grown by pulsed laser deposition. **Indian Journal of Pure&Applied Physics**. 48: 287.
- Evans, B.J., and Hafner, S. (1968). Mössbauer resonance of Fe₅₇ in oxide spinels containing Cu and Fe. **Journal of Physics and Chemistry of Solids**. 29: 1573.
- Endo, M., Kim, Y.A., Hayashi, T., Nishimura, K., Matushita, T., Miyashita, K., and Dresselhaus, M.S. (2001). Vaporgrown carbon fibers (VGCFs): Basic properties and battery application, **Carbon**. 39: 1287-1297.
- Friedlander, H.F., Peebles Jr, L.H., Brandrup, J., and Kirby, J.R. (1968). On the chromophore of polyacrylonitrile VI. Mechanism of color formation in polyacrylonitrile. **Macromolecules**. 1(1): 79-86.
- Ferrari, A.C. and Robertson, J. (2000). Resonant Raman spectroscopy of disordered, amorphous, and diamondlike carbon. **Physical Review B**. 61: 14095.
- Frackowiak, E., and Beguin, F. (2001). Carbon materials for electrochemical storage of energy in capacitors. **Carbon**. 39(6): 937-50.
- Feng, L., Li, S., Li, H., Zhai, J., Song, Y., Jiang, L., and Zhu, D. (2002). Superhydrophobic surface of aligned polyacrylonitrile nanofibers. **Angewandte Chemie International Edition**. 41(7): 1221-1223.
- Ferrari, A.C. (2007). Raman spectroscopy of graphene and graphite: Disorder, electron-phonon coupling, doping and nonadiabatic effects. **Solid State Communications**. 143: 47.

- Fan, Z., Chen, J., Cui, K., Sun, F., Xu, Y., and Kuang, Y. (2007). Preparation and capacitive properties of cobalt-nickel oxides/carbon nanotube composite. **Electrochimica Acta**. 52: 2959-2965.
- Fu, Y.S., Chen, H.Q., Sun, X.Q., and Wang, X. (2012). Combination of cobalt ferrite and graphene: High-performance and recyclable visible-light photocatalysis. **Applied Catalysis B**. 280: 111-112.
- Feng, L., Xie, N., and Zhong, J. (2014). Carbon nanofibers and their composite: A review of synthesizing, properties and applications. **Materials**. 7: 3919.
- Grunes, L.A. (1983). Study of the K edges of 3d transition metals in pure and oxide form by x-ray-absorption spectroscopy. **Physical Review B**. 27: 2111.
- Goya, G.F., Rechenberg, H.R. and Jiang, J.Z. (1998). Structural and magnetic properties of ball milled copper ferrite. **Journal of Applied Physics**. 84: 1101.
- Garcia-Otero, J., Porto, M., Rivas, J., and Bunde, A. (2000). Influence of dipolar interaction on magnetic properties of ultrafine ferromagnetic particles. **Physical Review Letters**. 167: 99.
- Gopal Reddy, C.V., Manorama, S.V., and Rao, V.J. (2000). Preparation and characterization of ferrite as gas sensor materials, **Journal of Materials Science Letters**. 19: 775-778.
- Gonzalez-Sandoval, M.P., Beesley, A.M., Miki-Yoshida, M., Fuentes-Cobas, L., and Matutes-Aquino, J.A. (2004). Comparative study of the microstructural and magnetic properties of spinel ferrites obtained by co-precipitation. **Journal of Alloys and Compounds**. 369(1-2): 190.

- Gomes, J.A., Sousa, M.H., da Silva, G.J., Tourinho, F.A., Filho, J.M., Azevedo, G.M., Itri, R., Azevedo, G.M., and Depeyrot, J. (2006). Cation distribution in copper ferrite nanoparticles of ferrofluids: A synchrotron XRD and EXAFS investigation. **Journal of Magnetism and Magnetic Materials**. 300: 213.
- Girija, T.C., and Sangaranarayanan, M.V. (2006). Analysis of polyaniline based nickel electrodes for electrochemical capacitors. **Journal of Power Sources**. 156: 705.
- Gu, S.Y., Wu, Q.L., and Ren, J. (2008). Preparation and surface structures of carbon nanofibers produced from electrospun PAN precursors. **New Carbon Materials**. 23(2): 171-176.
- Guo, Q.H., Zhou, X.P., Li, X.Y., Chen, S.L., Seema, A., Greiner, A., and Hou, H.Q. (2009). Supercapacitors based on hybrid carbon nanofibers containing multiwalled carbon nanotubes. **Journal of Materials Chemistry**. 19: 2810.
- Guo, X.W., Lu, X., Fang, X.P., Mao, Y., Wang, Z.X., Chen, L.Q., Xu, X.X., Yang, H., and Liu, Y.N. (2010). Lithium storage in hollow spherical ZnFe_2O_4 as anode materials for lithium ion batteries. **Electrochemistry communications**. 12: 847.
- Gomes, J.A., Azevedo, G.M., Depeyrot, J., Mestnik-Filho, J., da Silva, G.J., Tourinho, A., and Perzynski, R. (2011). ZnFe_2O_4 nanoparticles for ferrofluids: A combined XANES and XRD study. **Journal of Magnetism and Magnetic Materials**. 323: 1203.
- Hench, L.L., and West, J.K. (1990). **Principles of electronic ceramics**. New York: John Wiley and Sons.

- Hu, C.C., and Chu, C.H. (2001). Electrochemical impedance characterization of polyaniline-coated graphite electrodes for electrochemical capacitors. **Journal of Electroanalytical Chemistry**. 503: 105.
- Huang, X., and Chen, Z. (2004). Nickel ferrite on silica nanocomposites prepared by the sol-gel method. **Journal of Magnetism and Magnetic Materials**. 280: 37-43.
- Hsieh, C.T., and Lin, Y.T. (2006). Synthesis of mesoporous carbon composite and its electric double-layer formation behavior. **Microporous and Mesoporous Materials**. 93: 232-239.
- Henderson, C.M.B., Charnock, J.M., and Plant, D.A. (2007). Cation occupancies in Mg, Co, Ni, Zn, Al ferrite spinels a multi-element EXAFS study. **Journal of Physics: Condensed Matters**. 19: 1.
- Hafner, B. (2007). **Scanning electron microscopy primer. Characterization facility**. University of Minnesota-twin cities. 1-28.
- Heli, H., Yadegari, H., and Jabbari, A. (2012). Graphene nanosheets-poly (o-aminophenol) nanocomposite for supercapacitor applications. **Materials Chemistry and Physics**. 134: 21-25.
- He, P., Yang, K., Wang, W., Dong, F., Du, L., and Deng, Y. (2012). Reduced graphene oxide CoFe₂O₄ composites for supercapacitor electrode. **Russian Journal of Electrochemistry**. 49(4): 2013.
- Huixia, F., Baiyi, C., Deyi, Z., Jianqiang, Z., and Lin, T. (2014). Preparation and characterization of the cobalt ferrite nano-particles by reverse coprecipitation. **Journal of Magnetism and Magnetic Materials**. 356: 68-72.

- Inoue, H., Namba, Y., and Higuchi, E. (2010). Preparation and characterization of Ni-based positive electrodes for use in aqueous electrochemical capacitors. **Journal of Power Sources**. 195: 6239-6244.
- Inagaki, M., Konno, H., and Tanaike, O. (2010). Carbon materials for electrochemical capacitors. **Journal of Power Sources**. 195:7880-7903.
- Issa, B., Obaidat, I.M., Albiss, B.A., and Haik, Y. (2013). Magnetic nanoparticles: surface effects and properties related to biomedicine applications. **International Journal of Molecular Sciences**. 14: 21266-21305.
- Jacobs, I.S. and Bean, C.P. (1955). An approach to elongated fine-particle magnets. **Physical Review**. 100: 1060.
- Jiles, D. (1998). **Introduction to Magnetism and Magnetic Materials**. Chapman & Hall.
- Janes, A., Kurig, H., and Lust, E. (2007). Characterization of activated nanoporous carbon for supercapacitor electrode materials. **Carbon**. 45: 1226.
- Ju, Y.W., Park, J.H., Jung, H.R., Cho, S.J., and Lee, W.J. (2008). Fabrication and characterization of cobalt ferrite (CoFe_2O_4) nanofibers by electrospinning. **Materials Science and Engineering B**. 147: 7.
- Jayalakshmi, M., and Balasubramanian, K. (2008). Simple capacitor to supercapacitor: An overview. **International Journal of Electrochemical Science**. 3: 1196-1217.
- Ji, L.W., and Zhang, X.W. (2009). Geration of activated carbon nanofibers from electrospun polyacrylonitrile zinc chloride composites for use as anodes in lithium ion batteries. **Electrochemistry Communications**. 11: 684.

- Jiang, W., Liu, Y., Li, F., Chu, J., and Chen, K. (2010). Superparamagnetic cobalt ferrite-modified carbon nanotubes using a facile method. **Materials Science Engineering B**. 166: 132.
- Johannes, S., Thomas, S., and Renato, Z. (2011). Nanoscale chemical imaging of single layer graphene. **ACS Nano**. 5(10): 8442.
- Jin, Y.H., Seo, S.D., Shim, H.W., Park, K.S., and Kim, D.W. (2012). Synthesis of core/shell spinel ferrite/carbon nanoparticles with enhanced cycling stability for lithium ion battery anodes. **Nanotechnology**. 23: 125402.
- Klug, H.P., and Alexander, L.E. (1974). **X-ray diffraction procedures for polycrystalline and amorphous materials**. (2nd ed). New York: Wiley-Interscience.
- Krupicka, S., and Novak, P. (1982). **Oxide spinels (Ferromagnetic materials)** (3rded). Amsterdam: E P Wohlfarth.
- Knight, D.S., and White, W.B. (1989). Characterization of diamond films by Raman spectroscopy. **Journal of Materials Research**. 4: 385.
- Kinoshita, K. (1988). **Carbon: Electrochemical and physiochemical properties**. New York: Wiley-Interscience.
- Klabunde, K.J. (2001). **Nanoscale materials in chemistry** (1st ed). New York: Wiley-Interscience.
- Kim C., Choi, Y.O., Lee, W.J., and Yang, K.S. (2004). Supercapacitor performances of activated carbon fiber webs prepared by electrospinning of PMDA-ODA poly (amic acid) solutions. **Electrochimica Acta**. 50(2-3): 883.

- Kravtsov, E., Haskel, D., Cady, A., Yang, A., Vittoria, C., Zuo, X., and Harris, V.G. (2006). Site-specific local structure of Mn in artificial manganese ferrite films. **Physical Review B**. 74: 104114.
- Khomenko, V., Raymundo-Pinero, E., Frackowiak, E., and Beguin, F. (2006). High-voltage asymmetric supercapacitors operating in aqueous electrolyte. **Applied Physics A**. 82: 567-73.
- Kim, J.H., Lee, Y.S., Sharma, A.K., and Liu, C.G. (2006). Polypyrrole/carbon composite electrode for high-power electrochemical capacitors. **Electrochimica Acta**. 52: 1727-1732.
- Kuo, S.L., and Wu, N.L. (2006). Electrochemical characterization on MnFe₂O₄/carbon black composite aqueous supercapacitors. **Journal of Power Sources**. 162: 1437-1443.
- Kim, C., Ngoc, B.T.N., Yang, K.S., Kojima, M., Kim Y.A., Kim, Y.J., Endo, M., and Yang, C. (2007). Self sustained thin webs consisting of porous carbon nanofibers for supercapacitors via the electrospinning of polyacrylonitrile solutions containing zinc chloride. **Advanced Materials**. 19: 2341- 46.
- Kim, B.H., Bui, N., Yang, K.S., Cruz, M.E., and Ferraris, P. (2009). Electrochemical properties of activated polyacrylonitrile/pitch carbon fibers produced using electrospinning. **Bulletin of the Korean Chemical Society**. 30 (9): 1967.
- Kim, S.H., Kim, Y.I., Park, J.H., and Ko, J.M. (2009). Cobalt-Manganese oxide/carbon nanofiber composite electrodes for supercapacitors. **International Journal of Electrochemical Science**. 4: 1489-1496.

- Kameoka, S., Tanabe, T., and Tsai, A.P. (2010). Self-assembled porous nano composite with high catalytic performance by reduction of tetragonal spinel CuFe_2O_4 . **Applied Catalysis A: General**. 375: 163-171.
- Kim, B.H., Yang, K.S., Kim, Y.A., Kim, Y.J., An, B., and Oshida, K. (2011). Solvent induced porosity control of carbon nanofiber webs for supercapacitor. **Journal of Power Sources**. 196: 10496-10501.
- Kumbhar, V.S., Jagadale, A.D., Shinde, N.M., and Lokhande, C.D. (2012). Chemical synthesis of spinel cobalt ferrite (CoFe_2O_4) nano-flakes for supercapacitor application. **Applied Surface Science**. 259: 39-43.
- Kim, B.H., Kim, C.H., Yang, K.S., Rahy, A., and Yang, D.J. (2012). Electrospun vanadium pentoxide/carbon nanofiber composites for supercapacitor electrodes. **Electrochimica Acta**. 83: 335-340.
- Kim, B.H., and Yang, K.S. (2013). Enhanced electrical capacitance of porous carbon nanofibers derived from polyacrylonitrile and boron trioxide. **Electrochimica Acta**. 88: 597- 603.
- Kanagaraj, M., Sathishkumar, P., Kalai Selvan, G., Phebe Kokila, I., and Arumugam, S. (2014). Structural and magnetic properties of CuFe_2O_4 as prepared and thermally treated spinel nanoferrites. **Indian Journal of Pure & Applied Physics**. 52: 124-130.
- Krishnamoorthy, K., Veerasubramani, G., Radhakrishnan, S., and Kim, S.J. (2014). Supercapacitive behavior of hydrothermally synthesized flower like MoS_2 Nanostructures. **Materials Research Bulletin**. 50: 499-502.

- Liu, C., Zou, B., Rondinone, A.J., and Zhang, Z.J. (2000). Chemical control of superparamagnetic properties of magnesium and cobalt spinel ferrite nanoparticles through atomic level magnetic couplings. **Journal of the American Chemical Society**. 122: 6263.
- Liu, C., Rondinone, A.J., and Zhang, Z.J. (2000). Synthesis of magnetic spinel ferrite CoFe_2O_4 nanoparticles from ferric salt and characterization of the size dependent superparamagnetic properties. **Pure and Applied Chemistry**. 72: 37-45.
- Li, D., and Xia, Y. (2004). Direct fabrication of composite and ceramic hollow nanofiber by Electrospinning. **Advanced Materials**. 16: 1151-70.
- Lee, J.S., Choi, K.H., Ghim, H.D., Kim, S.S., Chun, D.H., Kim, H.Y., and Lyoo, W.S. (2004). Role of molecular weight of PVA in the structure and properties of PVA nanofabric prepared by electrospinning. **Journal of Applied Polymer Science**. 93: 1638-1646.
- Liu, C. (2005). Modeling the machining dynamics in peripheral milling. **Machine Tools and Manufacture**. 45:1301-1320.
- Lv, W.Z., Liu, B., Luo, Z.K., Ren, X.Z., and Zhang, P.X. (2008). XRD studies on the nanosized copper ferrite powders synthesized by sonochemical method. **Journal of Alloys and Compounds**. 465: 261.
- Li, G., Feng, Z., Zhong, J., Wang, Z., and Tong, Y. (2010). Electrochemical synthesis of polyaniline nanobelts with predominant electrochemical performances. **Macromolecules**. 43: 2178.

- Li, Z., Zhao, T., Zhan, X., Gao, D., Xiao, Q., and Lei, G. (2010). High capacity three-dimensional ordered macroporous CoFe_2O_4 as anode material for lithium ion batteries. **Electrochimica Acta**. 55(15): 4594-4598.
- Lu, T., Zhang, Y.P., Li, H.B., Pan, L.K., Li, Y.L., and Sun, Z. (2010). Electrochemical behaviors of graphene-ZnO and graphene- SnO_2 composite films for supercapacitors. **Electrochimica Acta**. 55: 4170.
- Laokul, P., Amornkitbamrung, V., Seraphin, S., and Maensiri, S. (2011). Characterization and magnetic properties of nanocrystalline CuFe_2O_4 , NiFe_2O_4 , ZnFe_2O_4 powders prepared by the Aloe vera extract solution. **Current Applied Physics**. 11: 101.
- Laforgue, A. (2001). All-textile flexible supercapacitors using electrospun poly (3, 4-ethylenedioxythiophene) nanofibers. **Journal of Power Sources**. 196: 559.
- Lekakou, C., Moudam, O., Markoulidis, F., Andrews, T., Watts, J.F., and Reed, G.T. (2011). Carbon based fibrous EDLCs capacitors and supercapacitors. **Journal of Nanotechnology**. 2011: 1.
- Liu, J., An, J., Ma, Y., Li, M., and Ma, R. (2012). Synthesis of a graphene-polypyrrole nanotube composite and its application in supercapacitor electrode. **Journal of the Electrochemical Society**. 159(6): A823-33.
- Mendelson, M.I. (1969). Average grain size in polycrystalline ceramics. **Journal of the American Ceramic Society**. 52(8): 443.
- Margulies, D.T., Parker, F.T., Spada, F.E., Goldman, R.S., Li, J., Sinclair, R., and Borkowitz, A.E. (1996). Anomalous moment and anisotropy behavior in Fe_3O_4 films. **Physical Review B**. 53: 9175.

- Ma, P., and Zhang, R. (1999). Synthetic nano scale fibrous extracellular matrix. **Journal of Biomedical Materials Research**. 46: 60-72.
- Merino, C., Soto, P., Ortego, E.V., Gomez de Salazar, J.M., Pico, F., and Rojo, J.M. (2005). Carbon nanofibres and activated carbon nanofibres as electrodes in supercapacitors. **Carbon**. 43: 551-557.
- Maensiri, S., and Nuansing, W. (2006). Thermoelectric oxide NaCo_2O_4 nanofibers fabricated by electrospinning. **Materials Chemistry and Physics**. 99: 104.
- Maaz, K., Mumtaz, A., Hasnain, S.K., and Ceylan, A. (2007). Synthesis and magnetic properties of cobalt ferrite (CoFe_2O_4) nanoparticles prepared by wet chemical route. **Journal of Magnetism and Magnetic Materials**. 308(2): 289.
- Maensiri, S., Masingboon, C., Boonchom, B., and Seraphin, S. (2007). A simple route to synthesize nickel ferrite (NiFe_2O_4) nanoparticles using egg white. **Scripta Materialia**. 56: 797-800.
- Maaz, K., Mumtaz, A., Hasanain, S.K., Liu, J., and Duan J.L. (2009). Synthesis and magnetic characterization of nickel ferrite nanoparticles prepared by co-precipitation route. **Journal of Magnetism and Magnetic Materials**. 321: 1838.
- Makovec, D., Kodre, A., Arcon, I., and Drogenik, M. (2009). Structure of manganese zinc ferrite spinel nanoparticles prepared with co-precipitation in reversed microemulsions. **Journal of Nanoparticle Research**. 11: 1145.
- Meher, S.K., Justin, P., Ranga Rao, G. (2010). Pine-cone morphology and pseudocapacitive behavior of nanoporous nickel oxide. **Electrochimica Acta**. 55: 8388-8396.

- Makovec, D., Kodre, A., Arcon, I., and Drofenik, M. (2011). The structure of compositionally constrained zinc-ferrite spinel nanoparticles. **Journal of Nanoparticle Research**. 13: 1781.
- Mahmouda, M.H., Elshahawya, A.M., Makhoulf, Salah A., and Hamdeh, H.H. (2013). Mössbauer and magnetization studies of nickel ferrite nanoparticles synthesized by the microwave-combustion method. **Journal of Magnetism and Magnetic Materials**. 343: 21-26.
- Ma, C., Li, Y., Shi, J., Song, Y., and Liu, L. (2014). High-performance supercapacitor electrodes based on porous flexible carbon nanofiber paper treated by surface chemical etching. **Chemical Engineering Journal**. 249: 216-225.
- Neel, L. (1948). Magnetic properties of ferrites: ferrimagnetism and anti-ferromagnetism. **Annales de Physique (Paris)**. 3: 137-198.
- Nemanich, R.J., and Solin, S.A. (1979). First and second-order Raman scattering from finite-size crystals of graphite. **Physical Review B**. 20: 392.
- Nathani, H., Misra, R.D.K. (2004). Surface effects on the magnetic behavior of nanocrystalline nickel ferrites and nickel ferrite-polymer nanocomposites. **Materials Science and Engineering B**. 113(3): 228-235.
- Nuli, Y.N., and Qin, Q.Z. (2005). Nanocrystalline transition metal ferrite thin films prepared by an electrochemical route for Li-ion batteries. **Journal of Power Sources**. 142: 292-297.
- Nawale, A.B., Kanhe, N.S., Patil, K.R., Bhoraskar, S.V., Mathe, V.L., and Das, A.K. (2011). Magnetic properties of thermal plasma synthesized nanocrystalline nickel. **Journal of Alloys and Compounds**. 509: 4404-4413.

- Niu, H., Zhang, J., Xie, Z., Wang, X., and Lin, T. (2011). Preparation, structure and supercapacitance of bonded carbon nanofiber electrode materials. **Carbon**. 49: 2380-2388.
- Ning, G.Q. Fan, Z.J., Wang, G., Gao, J.S., Qian, W.Z., and Wei, F. (2011). A three-dimensional carbon nanotube/graphene sandwich and its application as electrode in supercapacitors. **Chemical Communications**. 47: 5976.
- Natalia, M., Sudhakar, Y.N., and Selvakumar, M. (2013). Activated carbon derived from natural sources and electrochemical capacitance of double layer capacitor. **Indian Journal of Chemical Technology**. 20: 392-399.
- Nan, D., Huang, Z.H., Lv, R., Yang, L., Wang, J.G, Shen, W., Lin, Y., Yu, X., Ye, L., Sun, H., and Kang, F. (2014). Nitrogen-enriched electrospun porous carbon nanofiber networks as high-performance free-standing electrode materials. **Journal of Materials Chemistry A**. 2: 19678-19684.
- Okuno, S.T., Hashimoto, S., and Inomata, K. (1992). Preferred crystal orientation of cobalt ferrite thin films induced by ion bombardment during deposition. **Journal of Applied Physics**. 71: 5926.
- Ondarcuhu, T., and Joachim, C. (1998). Drawing a single nanofibre over hundreds of microns. **Europhysics Letters**. 42(2): 215-220.
- Pennycok, S.J., and Nellist, P.D. (1999). **In: Impact of electron and scanning probe microscopy on materials Research** (D.G. Rickerby, U. Valdré, and G. Valdré (Eds.)), The Netherlands: Kluwer Academic Publishers.

- Park, H.S., Hwang, S.J., and Choy, J.h. (2001). Relationship between chemical bonding character and electrochemical performance in nickel-substituted lithium manganese oxides. **Journal of Physical Chemistry B**. 105(21): 4860-4866.
- Pradeep, A., Priyadharsini, P., and Chandrasekaran, G. (2008). Production of single phase nano size NiFe_2O_4 particles using sol-gel auto combustion route by optimizing the preparation conditions. **Materials Chemistry and Physics**. 112(2): 572-576.
- Park, S.J., and Im, S.H. (2008). Electrochemical behaviors of PAN/Ag-based carbon nanofibers by electrospinning. **Bulletin of the Korean Chemical Society**. 29 (4): 777.
- Ponhan, W., and Maensiri, S. (2009). Fabrication and magnetic properties of electrospun copper ferrite (CuFe_2O_4) nanofibers. **Solid State Sciences**. 11: 479-484.
- Peng, Y.T., Chen, Z., and Wen, J. (2011). Hierarchical manganese oxide/carbon nanocomposites for supercapacitor electrodes. **Nano Research**. 4: 216-225.
- Patil, D.S., Shaikh, J.S., Pawar, S.A., Devan, R.S., Ma, Y.R., Moholkar, A.V., Kim, J.H., Kalubarme, R.S., Park, C.J., and Patil, P.S. (2012). Investigations on silver/polyaniline electrodes for electrochemical supercapacitors. **Physical Chemistry Chemical Physics**. 14: 11886.
- Patil, D.S., Pawar, S.A., Devan, R.S., Gang, M.G., Ma, Y.R., and Kimc, J.H. (2013). Electrochemical supercapacitor electrode material based on polyacrylic acid/polypyrrole/silver composite. **Electrochimica Acta**. 105: 569-577.

- Ponce, A.S., Chagas, E.F, Prado, R.J., Fernandes, C.H.M., Terezo, A.J., and Baggio-Saitovitch, E. (2013). High coercivity induced by mechanical milling in cobalt ferrite powders. **Journal of Magnetism and Magnetic Materials**. 344: 182-187.
- Peng, S., Lia, L., and Srinivasan, M. (2014). Electrospun CuFe_2O_4 nanotubes as anode for high-performance lithium-ion batteries. **Journal of Energy Chemistry**. 23: 301-307.
- Qu, D.Y., and Shi, H. (1998). Studies of activated carbons used in double-layer capacitors. **Journal of Power Sources**. 74: 99-107.
- Qi, J.Q., Chen, W.P., Leu, M., Wang, Y., Tian, H.Y., Li, L.T., and Chan, H.L. (2005). Fabrication of copper ferrite nanowalls on ceramic surfaces by an electrochemical method. **Nanotechnology** 16: 3097.
- Qu, Q.T. Wang, B., Yang, L.C., Shi, Y., Tian, S., and Wu, Y.P. (2008). Electrochemical performance of MnO_2 nanorods in neutral aqueous electrolytes as a cathode for asymmetric supercapacitors. **Electrochemistry Communications**. 10: 1652-1655.
- Rongier, A., Striebel, K.A., Wen, S.J., and Cairns, E.J. (1998). Cyclic voltammetry of pulsed laser deposited $\text{Li}_x\text{Mn}_2\text{O}_4$ thin films. **Journal of the Electrochemical Society**. 145: 2975.
- Ravel, B., and Newville, M. (2005). Athena, Artemis, Hephaestus: data analysis for X-ray absorption spectroscopy using IFEFFIT. **Journal of Synchrotron Radiation**. 12: 537-541.

- Ramakrisna, S., Fujihara, K., Teo, W.E., Lim, T.C., and Ma, Z. (2005). **An introduction to electrospinning and nanofibers**. Singapore: World Scientific Publishing.
- Raymundo-Pinero, E., Kierzek, K., Machnikowski, J., and Beguin, F. (2006). Relationship between the nanoporous texture of activated carbons and their capacitance properties in different electrolytes. **Carbon**. 44: 2498-2507.
- Roy, S., and Ghose, J. (2006). Massbauer study of nanocrystalline cubic CuFe_2O_4 synthesized by precipitation in polymer matrix, **Journal of Magnetism and Magnetic Materials**. 307: 32-37.
- Rabe, K.M. (2010). First-Principles calculations of complex metal-oxide materials. **Annual review of condensed matter physics** 1: 27.
- Rashad, M.M., Mohamed, R.M., Ibrahim, M.A., Ismail, L.F.M., and Abdel-Aal, E.A. (2012). Magnetic and catalytic properties of cubic copper ferrite nanopowders synthesized from secondary resources. **Advanced Powder Technology**. 23: 315-323.
- Ren, B., Fan, M., Liu, Q., Wang, J., Song, D., and Bai, X. (2013). Hollow NiO nanofibers modified by citric acid and the performances as supercapacitor electrode. **Electrochimica Acta**. 92: 197-204.
- Saito, F., Toyoda, T., Mori, T., Tanaka, M., Hirano, K., and Sasaki, S. (1999). Site and valence-selective study on the origin of Fe peaks in X-ray magnetic circular dichroism of Ni ferrites, $\text{Fe}[\text{Ni}_x\text{Fe}_{2-x}]\text{O}_4$. **Physica B**. 270: 35.
- Samsonidze, G.G., Saito, R., Jorio, A. Souza Filho, A.G., Dresselhaus, G., Pimenta, M.A., and Dresselhaus, M.S. (2003). Phonon trigonal warping effect in graphite and carbon nanotubes. **Physical Review Letters**. 90: 027403.

- Selvan, R.K., Kalaiselvi, N., Augustin, C.O., Doh, C.H., and Sanjeeviraja, C. (2006). $\text{CuFe}_2\text{O}_4/\text{SnO}_2$ nanocomposites as anodes for Li-ion batteries. **Journal of Power Sources**. 157: 522-527.
- Stankovich, S., Dikin, D.A., Dommett, G.H.B., Kohlhaas, K.M., Zimney, E.J., and Stach, E.A., (2006). Graphene-based composite materials. **Nature**. 442: 282.
- Stewart, S.J., Figueroa, S.J.A., Lopez, J.M.R., Marchetti, S.G., Bengoa, J.F., Prado, R.J., and Requejo, F.G. (2007). Cationic exchange in nanosized spinel revealed by experimental and simulated near-edge absorption structure. **Physical Review B**. 75: 073408.
- Sun, Z., Liu, L., Jia, D.Z., and Pan, W. (2007). Simple synthesis of CuFe_2O_4 nanoparticles as gassensing materials. **Sensors and Actuators B: Chemical**. 125: 144-148.
- Simon, P., and Gogotsi, Y. (2008). Materials for electrochemical capacitors. **Nature Materials**. 7: 845-854.
- Sakurai, S., Sasaki, S., Okube, M., Ohara, H., and Toyoda, T. (2008). Cation distribution and valence state in Mn-Zn ferrite examined by synchrotron X-rays. **Physica B**. 403: 3589-3595.
- Stoler, M.D., Park, S.J., Zhu, Y.W., An, J.H., and Ruoff, R.S. (2008). Graphene based ultracapacitors. **Nano Letters**. 8(10): 3498-3502.
- Sharma, R.K., Oh, H.S., Shul, Y.G., and Kim, H. (2008). Growth and characterization of carbon supported MnO_2 nanorods for supercapacitor electrode. **Physica B**. 403: 1763-1769.

- Shi, Y.F., Guo, B.K., Corr, S.A., Shi, Q.H., Hu, Y.S., Heier, K.R., Seshadri, R., Chen, L.Q., and Stucky, G.D. (2009). Ordered mesoporous metallic MoO₂ materials with highly reversible lithium storage capacity. **Nano Letters**. 9: 4215.
- Saito, Y., Verma, P., Masui, K., Inouye, Y., and Kawata, S. (2009). Nano-scale analysis of grapheme layers by tip-enhanced near-field Raman spectroscopy. **Journal of Raman Spectroscopy**. 40: 1434.
- Sharma, R.K., and Zhai, L. (2009). Multiwall carbon nanotube supported poly (3,4 ethylenedioxythiophene)/manganese oxide nano-composite electrode for super-capacitors. **Electrochimica Acta**. 54: 7148.
- Snook, G.A., Kao, P., and Best, A.S. (2011). Conducting-polymer-base supercapacitor devices and electrodes. **Journal of Power Sources**. 196: 1.
- Sahoo, S., Karthikeyan, G., Nayak, G.C., and Das, C.K. (2011). Facile synthesis of polypyrrole nanofiber and its enhanced electrochemical performances in different electrolytes. **Synthetic Metals**. 161(15-16): 1713-9.
- Salvati-Niasari, M., Davar, F., Seyghakar, H., Esmaeili, E., and Mir, N. (2001). Novel inorganic precursor in the controlled synthesis of zinc blend ZnS nanoparticles via TGA-assisted hydrothermal method. **Crystal Engineering Communications**. 13: 2948.
- Salavati-Niasari, M., Mahmoudi, T., Sabet, M., Soofivand, F., Tavakoli, F. and Hosseinpour-Mashkani, S.M. (2012). Synthesis and characterization of copper ferrite nanocrystals via coprecipitation. **Journal of Cluster Science**. 23:1003-1010.
- Taylor, G.I. (1966). The circulation produced in a drops by an electric field. **Proc R Soc London, Series A**. 291: 159.

- Tuinstra, E., and Koenig, J.L. (1970). Raman spectrum of graphite. **Journal of Chemical Physics**. 53: 1126.
- Thomsen, C., and Reich, S. (2000). Double resonant Raman scattering in graphite. **Physical Review Letters**. 85: 5214.
- Thang Pham, D., Rijnders, G., and Blank Dave, H.A. (2005). Spinel cobalt ferrite by complexometric synthesis. **Journal of Magnetism and Magnetic Materials**. 295: 251.
- Tang, W., Liu, L.L., Zhu, Y.S., Sun, H., Wu, Y.P., and Zhu, K. (2012). An aqueous rechargeable lithium battery of excellent rate capability based on a nanocomposite of MoO_3 coated with PPy and LiMn_2O_4 . **Energy Environmental Science**. 5: 6909.
- Tai, Z., Yan, X., Lang, J., and Xue, Q. (2012). Enhancement of capacitance performance of flexible carbon nanofiber paper by adding grapheme nanosheets. **Journal of Power Sources**. 199: 373-378.
- Tran, C., and Kalra, V. (2013). Fabrication of porous carbon nanofibers with adjustable pore sizes as electrodes for supercapacitors. **Journal of Power Sources**. 235: 289-296.
- Teymourian, H., Salimi, A., and Khezrian, S. (2013). Fe_3O_4 magnetic nanoparticles/reduced graphene oxide nanosheets as a novel electrochemical and bioelectrochemical sensing platform. **Biosensors and Bioelectronics**. 49: 1-8.

- Tangcharoen, T., Klysubun, W., Kongmark, C., and Pecharapa, W. (2014). Synchrotron X-ray absorption spectroscopy and magnetic characteristics studies of metal ferrites (metal=Ni, Mn, Cu) synthesized by sol-gel auto-combustion method. **Physica Status Solidi A**. 211(8): 1903-1911.
- Vidano, R.P., Fishbach, D.B., Willis, L.J., and Loehr, T.M. (1981). Observation of Raman band shifting with excitation wavelength for carbons and graphites. **Solid State Communications**. 39: 341.
- Varma, P.C.R., Manna, R.S., Banerjee, D., Varma, M.R., Suresh, K.G., and Nigamc, A.K. (2008). Magnetic properties of CoFe_2O_4 synthesized by solid state, citrate precursor and polymerized complex methods: a comparative study. **Journal of Alloys and Compounds**. 453: 298.
- Vivekchand, S.R.C., Rout, C.S., Subrahmanyam, K.S., Govindara, J.A., and Rao, C.N.R. (2008). Graphene based electrochemical supercapacitor. **Journal of Chemical Sciences**. 120(1): 9-13.
- Vidal-Abarca, C., Lavela, P., and Tirado, J.L. (2011). A ^{57}Fe Mossbauer spectroscopy study of cobalt ferrite conversion electrodes for Li-ion batteries. **Journal of Power Sources**. 196: 6978.
- Wei, Q.M., Li, J.B., Chen, Y.J., and Han, Y.S. (2001). X-ray study of cation distribution in $\text{NiMn}_{1-x}\text{Fe}_{2-x}\text{O}_4$ ferrites. **Materials Characterization**. 47(3-4): 247-252.
- Whitesides, G.M., and Grzybowski, B. (2002). Self assemble at all scales. **Science**. 295: 2418-2420.
- Wang, Y., Serrano, S., Jorge, J., and Aviles, S. (2003). Raman characterization of carbon nanofibers prepared using electrospinning. **Synthetic Metals**. 138: 423.

- Winter, M., and Brodd, R.J. (2004). What are batteries, fuel cells and supercapacitors?. **Chemical Review**. 104: 4245-4269.
- Wang, D.W., Li, F., Fang, H.T., Liu, M., Lu, G.Q., and Cheng, H.M. (2006). Effect of pore packing defects in 2-D ordered mesoporous carbons on ionic transport. **Journal of Physical Chemistry B**. 110: 8570.
- Wang, H., Zhang, F., Zhang, W., Wang, X., Lu, Z., Qian, Z., Sui, Y., Dong, D., and Su, W. (2006). The effect of surface modification on the morphology and magnetic properties of NiFe₂O₄ nanoparticles. **Journal of Crystal Growth**. 293: 169-174.
- Wang, L., Yu, Y., Chen, P.C., Zhang, D.W., and Chen, C.H. (2008). Electrospinning synthesis of C/Fe₃O₄ composite nanofibers and their application for high performance lithium-ion batteries. **Journal of Power Source**. 183: 717-723.
- Wang, D.W., Li, F., and Cheng, H.M. (2008). Hierarchical porous nickel oxide and carbon as electrode materials for asymmetric supercapacitor **Journal of Power Sources**. 185: 1563-1568.
- Wen, Z.B, Qu, Q.T., Gao, Q., Hu, Z.H., Wu, Y.P., Zheng, X.W., Liu, Y.F., and Wang, X.J. (2009). An activated carbon with high capacitance from carbonization of a resorcinol–formaldehyde resin. **Electrochemistry Communications**. 11: 715-718.
- Wang, H., Hao, Q., Yang, X., Lu, L., and Wang, X. (2010). A nanostructured graphene/polyaniline hybrid material for supercapacitors. **Nanoscale**. 2(10): 2164-70.

- Wu, Z.S., Ren, W.C., Wang, D.W., Li, F., Liu, B.L., and Cheng, H.M. (2010). High energy MnO₂ nanowire/graphene and graphene asymmetric electrochemical capacitors. **ACS Nano**. 4: 5835-5842.
- Wang, W., Liu, P., Zhang, M., Hu, J., and Xing, F. (2012). The pore structure of phosphoaluminate cement. **Open Journal of Composite Materials**. 2: 104-112.
- Wang, J.G., Yang, Y., Huang, Z.H., and Kang, F. (2012). Interfacial synthesis of mesoporous MnO₂/polyaniline hollow spheres and their application in electrochemical capacitors. **Journal of Power Sources**. 204: 236-43.
- Wang, J.G., Yang, Y., Huang, Z.H., and Kang, F. (2013). A high-performance asymmetric supercapacitor based on carbon and carbon-MnO₂ nanofiber electrodes. **Carbon**. 61: 190-199.
- Wang, Q.H., Jiao, L.F., Du, H.M., Wang, Y.J., and Yuan, H.T. (2014). Fe₃O₄ nanoparticles grown on graphene as advanced electrode materials for supercapacitors, **Journal of Power Sources**. 245: 101-106.
- Xu, M.W., Zhao, D.D., Bao, S.J., and Li, H.L. (2007). Mesoporous amorphous MnO₂ as electrode material for supercapacitor. **Journal of Solid State Electrochemistry**. 11: 1101.
- Xia, H., Zhua, D., Fub, Y., and Wang, X. (2012). CoFe₂O₄-graphene nanocomposite as a high-capacity anode material for lithium-ion batteries. **Electrochimica Acta**. 83: 166-174.
- Xing, Z., Ju, Z.C., Yang, J., Xu, H.Y., and Qian, Y.T. (2013). One-step solid state reaction to selectively fabricate cubic and tetragonal CuFe₂O₄ anode material for high power lithium ion batteries. **Electrochimica Acta**. 102: 51.

- Xiong, Q.Q., Tu, J.P., Shi, S.J., Liu, X.Y., Wang, X.L., and Gu, C.D. (2014). Ascorbic acid-assisted synthesis of cobalt ferrite (CoFe_2O_4) hierarchical flower-like microspheres with enhanced lithium storage properties. **Journal of Power Sources**. 256: 153-159.
- Ye, C., Lin, Z.M., and Hui, S.Z. (2005). Electrochemical and capacitance properties of rod-shaped MnO_2 for supercapacitor, **Journal of the Electrochemical Society**. 152: A1272.
- Yuan, D.S., Chen, J.X., Zeng, J.H., and Tan, S.X. (2008). Preparation of monodisperse carbon nanospheres for electrochemical capacitors. **Electrochemistry Communications**. 10: 1067.
- Yang, X., Wu, D., Chen, X., and Fu, R. (2010). Nitrogen-enriched nanocarbons with a 3-D continuous mesopore structure from polyacrylonitrile for supercapacitor application. **Journal of Physical Chemistry C**. 114: 8581-8586.
- Yan, X., Tai, Z., Chen, J., and Xue, Q. (2011). Fabrication of carbon nanofiber polyaniline composite flexible paper for supercapacitor. **Nanoscale**. 3: 212-216.
- Yang, L., Cheng, S., Ding, Y., Zhu, X., Wang, Z.L., and Liu, M. (2011). Hierarchical network architectures of carbon fiber paper supported cobalt oxide nanonet for high-capacity pseudocapacitors. **Nano Letters**. 12: 321-5.
- Yu, G., Hu, L., Liu, N., Wang, H., Vosgueritchian, M., and Yang, Y. (2011). Enhancing the supercapacitor performance of graphene/ MnO_2 nanostructured electrodes by conductive wrapping. **Nano Letters**. 11: 4438-42.

- Yang, S., Guo, Z., Sheng, G., and Wang, X. (2012). Application of a novel plasma induced CD/MWCNT/Iron oxide composite in zinc decontamination. **Carbohydrate Polymers**. 90: 1100.
- Zhang, G.Q., Zhao, Y.Q., and Tao, F. (2006). Electrochemical characteristics and impedance spectroscopy studies of nano-cobalt silicate hydroxide for supercapacitor. **Journal of Power Sources**. 161: 723.
- Zou, G.F., Zhang, D.W., Dong, C., Li, H., Xiong, K., Fei, L.F., and Qian, Y.T. (2006). Carbon nanofibers: synthesis, characterization, and electrochemical properties. **Carbon**. 44: 828.
- Zhao, H., Zheng, Z., Wong, K.W., Wang, S., Huang, B., and Li, D. (2007). Fabrication and electrochemical performance of nickel ferrite nanoparticles as anode material in lithium ion batteries. **Electrochemistry Communications**. 9: 2606-2610.
- Zhao, L.J., Zhang, H.J., Xing, Y., Song, S.Y., Yu, S.Y., Shi, W.D., Guo, Yang, J.H., Lei, Y.Q., and Cao, F. (2008). Studies on the magnetism of cobalt ferrite nanocrystals synthesized by hydrothermal method. **Journal of Solid State Chemistry**. 181: 245.
- Zhang, D., Karki, A.B., Rutman, D., Young, D.P., Wang, A., Cocke, D., Ho, T.H., and Guo, Z. (2009). Electrospun polyacrylonitrile nanocomposite fibers reinforced with Fe_3O_4 nanoparticles: Fabrication and property analysis. **Polymer**. 50: 4189.
- Zhang, Z., Zhou, T., Lu, M., Wei, A., Poh, C., and Piramanayagam, S.N. (2009). Cobalt nanomaterials: Synthesis and characterization. **Nanomaterials for the Life Sciences**. 4.

- Zhang, L.L., and Zhao, X.S. (2009). Carbon-based materials as supercapacitor electrodes. **Chemical Society Reviews**. 38: 2520-2531.
- Zhou, Z., Lai, C., Zhang, L., Qian, Y., Hou, H., and Reneker, D.H. (2009). Development of carbon nanofibers from aligned electrospun polyacrylonitrile nanofiber bundles and characterization of their microstructural, electrical, and mechanical properties. **Polymer**. 50: 2999-3006.
- Zhu, X.J., Zhu, Y.W., Murali, S., Stoller, M.D., and Ruoff, R.S. (2011). Nanostructure reduced graphene oxide/Fe₂O₃ composite as a high performance anode material for lithium ion batteries. **ACS Nano**. 5: 3333.
- Zhang, J., Jiang, J., and Zhao, X.S. (2011). Synthesis and capacitive properties of manganese oxide nanosheets dispersed on functionalized graphene sheets, **Journal of Physical Chemistry C**. 115: 6448.
- Zhi, M., Manivannan, A., Meng, F., and Wu, N. (2012). Highly conductive electrospun carbon nanofiber/MnO₂ coaxial nano-cables for high energy and power density supercapacitor. **Journal of Power Sources**. 208: 345-353.
- Zhengping, Z., and Xiang-Fa, W. (2013). Graphene-beaded carbon nanofibers for use in supercapacitor electrodes: synthesis and electrochemical characterization. **Journal of Power Sources**. 222: 410-416.
- Zhuang, X., Jia, K., Cheng, B., Feng, X., Shi, S., and Zhang, B. (2014). Solution blowing of continuous carbon nanofiber yarn and its electrochemical performance for supercapacitors. **Chemical Engineering Journal**. 237: 308-311.

APPENDIX



APPENDIX

PUBLICATIONS AND PRESENTATIONS

B.1 List of publications

Nilmoung, S., Kidkhunthod, P., Pinitsoontorn, S., Rujirawat, S., Yimnirun, R., Maensiri, S. (2015). Fabrication, structure, and magnetic properties of electrospun carbon/cobalt ferrite (C/CoFe₂O₄) composite nanofibers. **Applied Physics A**. 119(1). 141-154.

Nilmoung, S., Kidkhunthod, P., Maensiri, S. Local structure determination of Carbon/Nickel Ferrite composite nanofibers probed by X-ray absorption spectroscopy. Journal of Nanoscience and Nanotechnology. (**Accepted**)

B.2 List of oral presentations

Nilmoung, S., Yimnirun, R., Rujirawat, S., Maensiri, S. (July 2014). Fabrication and Characterization of C/CuFe₂O₄ Composite Nanofiber for Electrochemical capacitors. In **The 12th International Nanotech Symposium & Nano-Convergence Expo**. Coex, Seoul, Korea.

Nilmoung, S., Yimnirun, R., Rujirawat, S., Maensiri, S. (November 2014). Fabrication and Characterization of C/MFe₂O₄ (M=Ni, Cu) Composite Nanofiber by electrospinning and heat treatment process. In **The 4th Thailand International Nanotechnology Conference 2014**. Convention Center, Thailand Science Park, Pathumthani, Thailand.

B.3 List of poster presentations

Nilmoung, S., Yimnirun, R., Rujirawat, S., Maensiri, S. (November 2013). Fabrication and Characterization of C/ZnFe₂O₄ composite nanofibers by electrospinning. In **The 3rd Academic Conference on Natural Science of Master and PhD. Students from ASEAN countries (CASEAN-2013)**. Phnom Penh, Cambodia.

Nilmoung, S., Yimnirun, R., Rujirawat, S., Maensiri, S. (August 2011). Fabrication, Structure, and Magnetic Properties of Carbon/Nickel ferrite (NiFe₂O₄) composite nanofibers. **The 18th International Conference on Composite Materials**. ICC Jeju, Korea.

CURRICULUM VITAE

Name Miss Sukanya Nilmoung

Date of Birth June 9, 1978

Place of Birth 39 Moo 12 Tambol Nadee, Muang Surin District, Surin Province, 32000, Thailand.

Education

1996 -2000 Maharakham University, Maharakham, Thailand.
B.S. in Appiled Physics.

2001 -2003 Suranaree University of Technology, Nakhon Ratchasima, Thailand,
M.Sc. in Physics

2010-2014 Suranaree University of Technology, Nakhon Ratchasima, Thailand,
Ph.D. in Physics

Position and Place of Work Department of Physics, Faculty of Science and
Library Art, Rajamangala University of
Technology Isan, Nakhon Ratchasima, Thailand.